

1 **The Sensitivity to Oscillation Parameters**
2 **from a Simultaneous Beam and**
3 **Atmospheric Neutrino Analysis that**
4 **combines the T2K and SK Experiments**



6 Daniel Robert Clement Barrow
7 Magdalen College
8 University of Oxford

9 A thesis submitted for the degree of
10 *Doctor of Philosophy*
11 Trinity 2022

Abstract

12

13 Super-Kamiokande (SK) is a large water Cherenkov detector which observes a
14 flux of atmospheric neutrinos originating from the primary and secondary decays
15 of cosmic rays. It is also situated as the far detector of the Tokai-to-Kamioka (T2K)
16 experiment, with a baseline of 295km, and observes the flux of beam neutrinos
17 (or antineutrinos) produced at the J-PARC facility. This makes the detector the
18 ideal candidate for a joint beam-atmospheric oscillation analysis.

19 This thesis presents the first simultaneous beam and atmospheric oscillation
20 analysis to be supported by the two collaborations. This leverages the different
21 energies and baselines of the two experiments and provides strong sensitivities
22 on δ_{CP} , $\sin^2(\theta_{23})$ and Δm_{32}^2 . To do this, a Bayesian Markov Chain Monte Carlo
23 technique is utilised to generate parameter estimates and credible intervals.
24 Constraints from the T2K near detector are also used to constrain the uncertainties
25 of both beam and atmospheric predictions.

26 For a known set of oscillation parameters close to the preferred values from
27 a T2K-only data fit, the sensitivity of the joint analysis to $\sin^2(\theta_{23})$ is increased
28 compared to the beam-only analysis. Furthermore, the sensitivity of the joint
29 analysis to select the correct mass hierarchy hypothesis is drastically increased
30 compared to the beam-only analysis, culminating in a substantial preference as
31 classified by Jeffrey's scale. This statement is stronger than the sensitivity of
32 the beam analysis, either with or without external constraints on $\sin^2(\theta_{13})$. The
33 sensitivities of the beam-only and joint beam-atmospheric analyses have also been
34 compared for a known set of oscillation parameters which are CP-conserving.
35 The joint analysis displays an improved ability to select the correct phase of δ_{CP}
36 and octant of $\sin^2(\theta_{23})$ compared to the beam-only analysis. This thesis illustrates
37 the benefit of the combined beam and atmospheric analysis, which could also be
38 extended for use in the next-generation Hyper-Kamiokande experiment.

Acknowledgements

40 Personal

41 This is where you thank your advisor, colleagues, and family and friends.

42 Lorem ipsum dolor sit amet, consectetur adipiscing elit. Vestibulum feugiat
43 et est at accumsan. Praesent sed elit mattis, congue mi sed, porta ipsum. In
44 non ullamcorper lacus. Quisque volutpat tempus ligula ac ultricies. Nam sed
45 erat feugiat, elementum dolor sed, elementum neque. Aliquam eu iaculis est,
46 a sollicitudin augue. Cras id lorem vel purus posuere tempor. Proin tincidunt,
47 sapien non dictum aliquam, ex odio ornare mauris, ultrices viverra nisi magna
48 in lacus. Fusce aliquet molestie massa, ut fringilla purus rutrum consectetur.
49 Nam non nunc tincidunt, rutrum dui sit amet, ornare nunc. Donec cursus
50 tortor vel odio molestie dignissim. Vivamus id mi erat. Duis porttitor diam
51 tempor rutrum porttitor. Lorem ipsum dolor sit amet, consectetur adipiscing
52 elit. Sed condimentum venenatis consectetur. Lorem ipsum dolor sit amet,
53 consectetur adipiscing elit.

54 Aenean sit amet lectus nec tellus viverra ultrices vitae commodo nunc. Mauris
55 at maximus arcu. Aliquam varius congue orci et ultrices. In non ipsum vel
56 est scelerisque efficitur in at augue. Nullam rhoncus orci velit. Duis ultricies
57 accumsan feugiat. Etiam consectetur ornare velit et eleifend.

58 Suspendisse sed enim lacinia, pharetra neque ac, ultricies urna. Phasellus sit
59 amet cursus purus. Quisque non odio libero. Etiam iaculis odio a ex volutpat, eget
60 pulvinar augue mollis. Mauris nibh lorem, mollis quis semper quis, consequat
61 nec metus. Etiam dolor mi, cursus a ipsum aliquam, eleifend venenatis ipsum.
62 Maecenas tempus, nibh eget scelerisque feugiat, leo nibh lobortis diam, id laoreet
63 purus dolor eu mauris. Pellentesque habitant morbi tristique senectus et netus
64 et malesuada fames ac turpis egestas. Nulla eget tortor eu arcu sagittis euismod
65 fermentum id neque. In sit amet justo ligula. Donec rutrum ex a aliquet egestas.

66 Institutional

67 If you want to separate out your thanks for funding and institutional support,
68 I don't think there's any rule against it. Of course, you could also just remove
69 the subsections and do one big traditional acknowledgement section.

⁷⁰ Lorem ipsum dolor sit amet, consectetur adipiscing elit. Ut luctus tempor ex at
⁷¹ pretium. Sed varius, mauris at dapibus lobortis, elit purus tempor neque, facilisis
⁷² sollicitudin felis nunc a urna. Morbi mattis ante non augue blandit pulvinar.
⁷³ Quisque nec euismod mauris. Nulla et tellus eu nibh auctor malesuada quis
⁷⁴ imperdiet quam. Sed eget tincidunt velit. Cras molestie sem ipsum, at faucibus
⁷⁵ quam mattis vel. Quisque vel placerat orci, id tempor urna. Vivamus mollis,
⁷⁶ neque in aliquam consequat, dui sem volutpat lorem, sit amet tempor ipsum felis
⁷⁷ eget ante. Integer lacinia nulla vitae felis vulputate, at tincidunt ligula maximus.
⁷⁸ Aenean venenatis dolor ante, euismod ultrices nibh mollis ac. Ut malesuada
⁷⁹ aliquam urna, ac interdum magna malesuada posuere.

80

Statement of Originality

81 The work, and associated interpretation, presented within this thesis are
82 my own and were produced by myself. Where applicable, results and figures
83 taken from others have been attributed and referenced. This work has not been
84 submitted for any other qualification, at this university or any other.

85 The background of neutrino physics history and a description of the T2K and
86 SK experiments are provided in Chapters 2 and 3, respectively. The Bayesian
87 fitting techniques and MaCh3 framework used throughout this analysis are de-
88 tailed in Chapter 4. These chapters present entirely background knowledge
89 relevant for understanding the work presented within this thesis. Chapter 5
90 documents the simulation and reconstruction of neutrino events. This includes a
91 section of work done by myself to validate the `fiTQun` reconstruction software
92 for use on SK-V data.

93 Chapter 6 details the event selections and systematics used within this oscilla-
94 tion analysis. The selections were developed by others within the T2K and SK
95 collaborations and have been appropriately referenced. The implementation and
96 validation of the simultaneous support for the beam and atmospheric samples
97 selected by the SK detector, in the MaCh3 fitting framework, has been entirely my
98 own work. The systematic models invoked within this analysis were developed
99 by others, and relevant references have been included. The implementation
100 of these systematics within the MaCh3 fitting framework has been entirely my
101 own work and includes generating the systematic response functions for each
102 systematic from the Super-Kamiokande Monte Carlo. The implementation
103 and validation of the near detector sample and systematics were performed
104 by Clarence Wret on behalf of the MaCh3 working group.

105 Chapter 7 documents a new method of calculating the oscillation probabilities
106 for atmospheric neutrinos at SK. The method and validation of the ‘smearing’
107 technique were entirely my own. The methodology for including effects from
108 production height systematics was developed by others but the implementation
109 and validation were my own. Several performance increases, including the
110 interfacing of alternative oscillation calculation engines, were my own work.
111 The sensitivities, and interpretation, provided within Chapter 8 are produced
112 entirely by myself.

Contents

113

114	1 Introduction	1
115	2 Neutrino Oscillation Physics	4
116	2.1 Discovery of Neutrinos	5
117	2.2 Theory of Neutrino Oscillation	6
118	2.3 Neutrino Oscillation Measurements	10
119	2.4 Summary Of Oscillation Parameter Measurements	20
120	2.5 Overview of Oscillation Effects	21
121	3 T2K and SK Experiment Overview	29
122	3.1 The Super-Kamiokande Experiment	29
123	3.2 The Tokai to Kamioka Experiment	40
124	4 Bayesian Statistics and Markov Chain Monte Carlo Techniques	55
125	4.1 Bayesian Statistics	56
126	4.2 Monte Carlo Simulation	58
127	4.3 Understanding the MCMC Results	66
128	5 Simulation, Reconstruction, and Event Reduction	71
129	5.1 Simulation	71
130	5.2 Event Reconstruction at SK	77
131	5.3 Event Reduction at SK	88
132	6 Sample Selections and Systematics	93
133	6.1 Atmospheric Samples	95
134	6.2 Near Detector Beam Samples	103
135	6.3 Far Detector Beam Samples	105
136	6.4 Systematic Uncertainties	111
137	6.5 Likelihood Calculation	132
138	7 Oscillation Probability Calculation	135
139	7.1 Treatment of Fast Oscillations	136
140	7.2 Calculation Engine	143
141	7.3 Matter Density Profile	147
142	7.4 Production Height Averaging	152

¹⁴³	8 Oscillation Analysis	155
¹⁴⁴	8.1 Monte Carlo Prediction	156
¹⁴⁵	8.2 Likelihood Scans	157
¹⁴⁶	8.3 Sensitivity Studies	169
¹⁴⁷	8.4 Summary of Sensitivity Studies	221
¹⁴⁸	9 Conclusions and Outlook	223

1

149

150

Introduction

151 Current astrophysical measurements show that the universe is matter-dominated,
152 despite current theoretical models suggesting that an equal amount of matter
153 and antimatter were created in the Big Bang. For an imbalance to occur, the
154 Sakharov conditions [1] require the violation of charge parity (CP) symmetries.
155 CP violation has been observed in quark mixing but is insufficient to explain
156 the observed asymmetry. As the Standard Model relates the neutrino and the
157 antineutrino through these symmetries, CP violation could be found in the
158 neutrino sector. This would be observed as a difference between neutrino and
159 antineutrino oscillation. Current neutrino oscillation measurements contain hints
160 of CP violation [2] but no conclusive measurement has been achieved. One of the
161 main goals of neutrino oscillation experiments is to continue the search for CP
162 violation, requiring a precise measurement of all oscillation parameters.

163 The Super-Kamiokande (SK) detector observes atmospheric neutrinos emitted
164 from the subsequent decays of cosmic rays. It is also situated as the far detector
165 of the Tokai-to-Kamioka (T2K) experiment and measures the interactions of
166 neutrinos produced from the J-PARC (anti-)neutrino beam facility. Previous
167 oscillation analyses published by these two experiments have treated the datasets
168 independently. However, due to the different energies, path lengths, and density
169 of matter in which the neutrinos pass through, a combined analysis can leverage

170 the constraints from both datasets and be able to improve measurements of
171 neutrino oscillation parameters.

172 This thesis introduces a joint beam and atmospheric neutrino analysis using
173 beam samples observed at the near and far detectors of the T2K experiment and
174 atmospheric samples present in SK. It combines the beam analysis presented in
175 [2] and the atmospheric analysis documented in [3]. This corresponds to run1-10
176 of the T2K experiment with approximately equal exposure taken in neutrino
177 and antineutrino beam modes, alongside more than 3000 days of atmospheric
178 events. This results in this thesis are presented as sensitivities to the δ_{CP} , $\sin^2(\theta_{13})$,
179 $\sin^2(\theta_{23})$, and Δm_{32}^2 oscillation parameters. Crucially, the combination of beam
180 and atmospheric neutrinos gives strong sensitivity to the mass hierarchy due to
181 the correlation between the matter resonance and $\sin^2(\theta_{23})$. The sensitivities are
182 generated by the MaCh3 Bayesian Markov Chain Monte Carlo fitting framework.

183 Chapter 2 provides a concise overview of neutrino physics history including
184 the discovery of the neutrino along with the first evidence for neutrino oscillation.
185 It also includes a brief discussion of the theory underpinning the PMNS formal-
186 ism of neutrino oscillation alongside a summary of the current measurements
187 of each oscillation parameter.

188 The T2K and SK experiments are detailed in Chapter 3. This includes the
189 design and calibration of the SK detector along with a brief description of the
190 composition and detection techniques of T2K's two near detectors. The neutrino
191 beamline, and the 'off-axis' technique, are also briefly summarised.

192 This thesis presents a Bayesian neutrino oscillation analysis that uses Markov
193 Chain Monte Carlo techniques. This analysis strategy, along with a summary
194 of the fundamental concepts of Bayesian inference, is described in Chapter 4.
195 This includes a discussion about the conditions that are required to correctly
196 sample the parameter space along with the methods used to calculate parameter
197 estimations and build credible intervals.

198 Chapter 5 details the simulations and reconstruction tools used to build Monte
199 Carlo predictions of each sample used within this analysis. This includes the

200 models used to provide flux predictions of the beam and atmospheric neutrinos
201 as well as the models invoked with this analysis to simulate neutrino interactions.
202 Validation of the far detector’s reconstruction tools has been documented which
203 compares the change in detector response between two different periods of SK.

204 A description of the beam samples used at the near and far detector and the
205 atmospheric samples used at the SK detector is presented in Chapter 6. These
206 include energy and interaction mode comparisons along with documenting the
207 event selection cuts. This chapter also includes the systematic models used
208 to quantify the uncertainty in the flux predictions of both beam and atmo-
209 spheric neutrinos, the interaction models, and the response of the detectors
210 used within this analysis.

211 A novel atmospheric neutrino oscillation probability calculation method
212 is documented in Chapter 7. This is required to ensure reliable Monte Carlo
213 sampling of a rapidly varying region of oscillation parameter space. This chapter
214 also documents the uncertainties related to the Earth’s density as well as the
215 production height of neutrinos in the upper atmosphere.

216 Chapter 8 presents the sensitivities of this joint beam and atmospheric neu-
217 trino oscillation analysis. The results are provided for two different sets of known
218 values. The application of the external constraints on $\sin^2(\theta_{13})$ has also been
219 considered. The sensitivities of the joint analysis are compared to the beam-only
220 analysis and show the benefits of the combined analysis. These results have been
221 presented by the T2K and SK collaborations at the Neutrino 2022 conference [4].

222 A summarised discussion of the sensitivity results and the outlook for the
223 analysis, including the implications of analysis on the next generation of neutrino
224 experiments, is provided in Chapter 9.

2

225

226

Neutrino Oscillation Physics

227 When first proposed, neutrinos were expected to be approximately massless
228 fermions that only interact through weak and gravitational forces. This meant
229 they were very difficult to detect as they can pass through significant amounts
230 of matter without interacting. Despite this, experimental neutrino physics has
231 developed many different detection techniques and observed neutrinos from
232 both natural and artificial sources. In direct tension with Standard Model physics,
233 neutrinos have been determined to oscillate between different lepton flavours,
234 requiring them to have mass.

235 The observation techniques which led to the discovery of the neutrino are doc-
236 umented in section 2.1. The theory underpinning neutrino oscillation is described
237 in section 2.2 and includes the approximations which can be made to simplify
238 the understanding of neutrino oscillation in the two-flavour approximation. Past,
239 current, and future neutrino experiments are detailed in section 2.3, including the
240 reactor, atmospheric, and long-baseline accelerator neutrino sources that have
241 been used to successfully constrain oscillation parameters. Finally, the current
242 state of oscillation parameter measurements are summarised in section 2.4.

2.1 Discovery of Neutrinos

At the start of the 20th century, the electrons emitted from the β -decay of the nucleus were found to have a continuous energy spectrum [5, 6]. This observation seemingly broke the energy conservation invoked within that period's nuclear models. In 1930, Pauli provided a solution to this problem in the form of a new particle, the neutrino (originally termed "neutron"). It was theorized to be an electrically neutral spin-1/2 fermion with a mass smaller than that of the electron [7]. This neutrino was emitted with the electron in β -decay to alleviate the apparent breaking of energy conservation. As a predecessor of today's weak interaction model, Fermi's theory of β -decay developed the understanding by coupling the four constituent particles: electron, proton, neutron, and neutrino, into a quantitative model [8].

Whilst Pauli was not convinced of the ability to detect neutrinos, the first observations of the particle were made in the mid-1950s when neutrinos from a reactor were observed via the inverse β -decay (IBD) process, $\bar{\nu}_e + p \rightarrow n + e^+$ [9, 10]. The detector consisted of two parts: a neutrino interaction medium and a liquid scintillator. The interaction medium was built from two water tanks, loaded with cadmium chloride to allow for increased efficiency in the detection of neutron capture. The positron emitted from IBD annihilates, $e^+ + e^- \rightarrow 2\gamma$, generating a prompt signal and the neutron is captured on the cadmium via $n + ^{108}Cd \rightarrow ^{109*}Cd \rightarrow ^{109}Cd + \gamma$, producing a delayed signal. An increase in the coincidence rate was observed when the reactor was operating which was interpreted as interactions from neutrinos generated in the reactor.

After the discovery of the ν_e , the question of how many flavours of neutrino exist was asked. In 1962, a measurement of the ν_μ was conducted at the Brookhaven National Laboratory [11]. A proton beam was directed at a beryllium target, generating pions which then decayed via $\pi^\pm \rightarrow \mu^\pm + (\nu_\mu, \bar{\nu}_\mu)$, and the subsequent interactions of the ν_μ were observed. As the subsequent interaction of the neutrino generated muons rather than electrons, it was determined that

the ν_μ was fundamentally different from ν_e . The final observation to be made was that of the ν_τ from the DONUT experiment [12]. Three neutrinos seem the obvious solution as it mirrors the known number of charged leptons (as they form weak isospin doublets) but there could be evidence of more. Several neutrino experiments have found anomalous results [13, 14] which could be attributed to “sterile” neutrinos. These hypothesised particles are not affected by gauge interactions in the Standard Model so their presence can only be inferred through the observation of non-standard oscillation modes. However, cosmological observations indicate the number of neutrino species $N_{eff} = 2.99 \pm 0.17$ [15], as measured from the cosmic microwave background power spectrum. LEP also measured the number of active neutrino flavours to be $N_\nu = 2.9840 \pm 0.0082$ [16] from measurements of the Z-decay width, but this does not strongly constrain the number of sterile neutrinos.

2.2 Theory of Neutrino Oscillation

A neutrino generated with lepton flavour α can change into a different lepton flavour β after propagating some distance. This phenomenon is called neutrino oscillation and requires that neutrinos must have a non-zero mass. This behaviour has been characterised by the Pontecorvo-Maki-Nakagawa-Sakata (PMNS) [17–19] mixing matrix which describes how the flavour and mass of neutrinos are associated. This is analogous to the Cabibbo-Kobayashi-Maskawa (CKM) [20] matrix measured in quark physics.

2.2.1 Three Flavour Oscillations

The PMNS parameterisation defines three flavour eigenstates, ν_e , ν_μ and ν_τ (indexed ν_α), which are eigenstates of the weak interaction and three mass eigenstates, ν_1 , ν_2 and ν_3 (indexed ν_i). Each mass eigenstate is the superposition

²⁹⁷ of all three flavour states,

$$|\nu_i\rangle = \sum_{\alpha} U_{\alpha i} |\nu_{\alpha}\rangle. \quad (2.1)$$

²⁹⁸ Where U is the 3×3 PMNS matrix which is unitary and connects the mass
²⁹⁹ and flavour eigenstates.

³⁰⁰ The weak interaction, when interacting via a W^{\pm} boson, couples to flavour
³⁰¹ eigenstates so neutrinos interact with leptons of the same flavour. The prop-
³⁰² agation of a neutrino flavour eigenstate, in a vacuum, can be re-written as a
³⁰³ plane-wave solution to the time-dependent Schrödinger equation,

$$|\nu_{\alpha}(t)\rangle = \sum_i U_{\alpha i}^{*} |\nu_i\rangle e^{-i\phi_i}. \quad (2.2)$$

³⁰⁴ The ϕ_i term can be expressed in terms of the energy, E_i , and magnitude of the
³⁰⁵ three momenta, p_i , of the neutrino, $\phi_i = E_i t - p_i x$ (t and x being time and position
³⁰⁶ coordinates). The probability of observing a neutrino of flavour eigenstate β from
³⁰⁷ one which originated as flavour α can be calculated as,

$$P(\nu_{\alpha} \rightarrow \nu_{\beta}) = |\langle \nu_{\beta} | \nu_{\alpha}(t) \rangle|^2 = \sum_{i,j} U_{\alpha i}^{*} U_{\beta i} U_{\alpha j} U_{\beta j}^{*} e^{-i(\phi_j - \phi_i)}. \quad (2.3)$$

³⁰⁸ The term within the exponential can be represented as,

$$\phi_j - \phi_i = E_j t - E_i t - p_j x + p_i x. \quad (2.4)$$

³⁰⁹ For a relativistic particle, $E_i \gg m_i$, a Taylor series expansion means,

$$p_i = \sqrt{E_i^2 - m_i^2} \approx E_i - \frac{m_i^2}{2E_i}. \quad (2.5)$$

³¹⁰ Making the approximations that neutrinos are relativistic, the mass eigenstates
³¹¹ were created with the same energy and that $x = L$, where L is the distance
³¹² travelled by the neutrino, Equation 2.4 then becomes

$$\phi_j - \phi_i = \frac{\Delta m_{ij}^2 L}{2E}, \quad (2.6)$$

313 where $\Delta m_{ij}^2 = m_i^2 - m_j^2$. This, combined with further use of unitarity relations
314 results in Equation 2.3 becoming

$$\begin{aligned} P(\nu_\alpha \rightarrow \nu_\beta) &= \delta_{\alpha\beta} - 4 \sum_{i>j} \Re \left(U_{\alpha i}^* U_{\beta i} U_{\alpha j} U_{\beta j}^* \right) \sin^2 \left(\frac{\Delta m_{ij}^2 L}{4E} \right) \\ &\quad + (-) 2 \sum_{i>j} \Im \left(U_{\alpha i}^* U_{\beta i} U_{\alpha j} U_{\beta j}^* \right) \sin \left(\frac{\Delta m_{ij}^2 L}{2E} \right). \end{aligned} \quad (2.7)$$

315 Where $\delta_{\alpha\beta}$ is the Kronecker delta function and the negative sign on the last
316 term is included for the oscillation probability of antineutrinos. As an important
317 point to note, the observation of oscillation probability requires a non-zero value
318 of Δm_{ij}^2 , which in turn requires that neutrinos have differing masses.

319 Typically, the PMNS matrix is parameterised into three mixing angles, a
320 charge parity (CP) violating phase δ_{CP} , and two Majorana phases $\alpha_{1,2}$,

$$U = \underbrace{\begin{pmatrix} 1 & 0 & 0 \\ 0 & c_{23} & s_{23} \\ 0 & -s_{23} & c_{23} \end{pmatrix}}_{\text{Atmospheric, Accelerator}} \underbrace{\begin{pmatrix} c_{13} & 0 & s_{13}e^{-i\delta_{CP}} \\ 0 & 1 & 0 \\ -s_{13}e^{-i\delta_{CP}} & 0 & c_{13} \end{pmatrix}}_{\text{Reactor, Accelerator}} \times \underbrace{\begin{pmatrix} c_{12} & s_{12} & 0 \\ -s_{12} & c_{12} & 0 \\ 0 & 0 & 1 \end{pmatrix}}_{\text{Reactor, Solar}} \underbrace{\begin{pmatrix} e^{i\alpha_1/2} & 0 & 0 \\ 0 & e^{i\alpha_2/2} & 0 \\ 0 & 0 & 1 \end{pmatrix}}_{\text{Majorana}}. \quad (2.8)$$

321 Where $s_{ij} = \sin(\theta_{ij})$ and $c_{ij} = \cos(\theta_{ij})$. The oscillation parameters are often
322 grouped: (1,2) as “solar”, (2,3) as “atmospheric” and (1,3) as “reactor”. Many
323 neutrino experiments aim to measure the PMNS parameters from a wide array
324 of origins, as is the purpose of this thesis.

325 The Majorana phase, $\alpha_{1,2}$, included within the fourth matrix in Equation 2.8
326 is only included for completeness. For an oscillation analysis experiment, any
327 terms containing this phase disappear due to taking the expectation value of the
328 PMNS matrix. Measurements of these phases can be performed by experiments
329 searching for neutrino-less double β -decay [21].

330 A two-flavour approximation can be obtained when one assumes the third
331 mass eigenstate is degenerate with another. This results in the two-flavour
332 approximation being reasonable for understanding the features of the oscillation.
333 In this two-flavour case, the mixing matrix becomes,

$$U_{2\text{ Flav.}} = \begin{pmatrix} \cos(\theta) & \sin(\theta) \\ -\sin(\theta) & \cos(\theta) \end{pmatrix}. \quad (2.9)$$

334 This culminates in the oscillation probability,

$$\begin{aligned} P(\nu_\alpha \rightarrow \nu_\alpha) &= 1 - \sin^2(2\theta) \sin^2\left(\frac{\Delta m^2 L}{4E}\right), \\ P(\nu_\alpha \rightarrow \nu_\beta) &= \sin^2(2\theta) \sin^2\left(\frac{\Delta m^2 L}{4E}\right). \end{aligned} \quad (2.10)$$

335 Where $\alpha \neq \beta$. For a fixed neutrino energy, the oscillation probability is
336 a sinusoidal function depending upon the distance over which the neutrino
337 propagates. The frequency and amplitude of oscillation are dependent upon
338 $\Delta m^2/4E$ and $\sin^2 2\theta$, respectively. The oscillation probabilities presented thus far
339 assume $c = 1$, where c is the speed of light in a vacuum. In more familiar units, the
340 maximum oscillation probability for a fixed value of θ is given at $L[\text{km}] / E[\text{GeV}] \sim$
341 $1.27/\Delta m^2$. It is this calculation that determines the best L/E value for a given
342 experiment to be designed around for measurements of a specific value of Δm^2 .

343 2.2.2 The MSW Effect

344 The theory of neutrino oscillation in a vacuum has been described in subsec-
345 tion 2.2.1. However, the beam neutrinos and atmospheric neutrinos originating
346 from below the horizon propagate through the matter in the Earth. The coherent
347 scattering of neutrinos from a material target modifies the Hamiltonian of the
348 system which results in a change in the oscillation probability. This modification
349 is termed the Mikheyev-Smirnov-Wolfenstein (MSW) effect [22–24]. This occurs
350 because charged current scattering ($\nu_e + e^- \rightarrow \nu_e + e^-$, propagated by a W boson)
351 only affects electron neutrinos whereas the neutral current scattering ($\nu_l + l^- \rightarrow$

³⁵² $\nu_l + l^-$, propagated by a Z^0 boson) interacts through all neutrino flavours equally.
³⁵³ In the two-flavour approximation, the effective mixing parameter becomes

$$\sin^2(2\theta) \rightarrow \sin^2(2\theta_m) = \frac{\sin^2(2\theta)}{(A/\Delta m^2 - \cos(2\theta))^2 + \sin^2(2\theta)}, \quad (2.11)$$

³⁵⁴ where $A = 2\sqrt{2}G_F N_e E$, N_e is the electron density of the medium and G_F
³⁵⁵ is Fermi's constant. It is clear that there exists a value of $A = \Delta m^2 \cos(2\theta)$ for
³⁵⁶ $\Delta m^2 > 0$, which results in a divergent mixing parameter, colloquially called the
³⁵⁷ matter resonance. This resonance regenerates the electron neutrino component of
³⁵⁸ the neutrino flux [22–24]. The density at which the resonance occurs is given by

$$N_e = \frac{\Delta m^2 \cos(2\theta)}{2\sqrt{2}G_F E}. \quad (2.12)$$

³⁵⁹ At densities lower than this critical value, the oscillation probability will
³⁶⁰ be much closer to that of vacuum oscillation. For antineutrinos, $N_e \rightarrow -N_e$
³⁶¹ [25]. The resonance occurring from the MSW effect depends on the sign of Δm^2 .
³⁶² Therefore, any neutrino oscillation experiment which observes neutrinos and
³⁶³ antineutrinos which have propagated through matter can have some sensitivity
³⁶⁴ to the ordering of the neutrino mass eigenstates.

³⁶⁵ 2.3 Neutrino Oscillation Measurements

³⁶⁶ As evidence of beyond Standard Model physics, the 2015 Nobel Prize in Physics
³⁶⁷ was awarded to the Super-Kamiokande (SK) [26] and Sudbury Neutrino Ob-
³⁶⁸ servatory (SNO) [27] collaborations for the first definitive observation of solar
³⁶⁹ and atmospheric neutrino oscillation [28]. Since then, the field has seen a wide
³⁷⁰ array of oscillation measurements from a variety of neutrino sources. As seen
³⁷¹ in subsection 2.2.1, the neutrino oscillation probability is dependent on the ratio
³⁷² of the propagation baseline, L , to the neutrino energy, E . It is this ratio that
³⁷³ determines the type of neutrino oscillation a particular experiment is sensitive to.

³⁷⁴ As illustrated in Figure 2.1, there are many neutrino sources that span a
³⁷⁵ wide range of energies. The least energetic neutrinos are from reactor and

³⁷⁶ terrestrial sources at $O(1)$ MeV whereas the most energetic neutrinos originate
³⁷⁷ from atmospheric and galactic neutrinos of $> O(1)$ TeV.

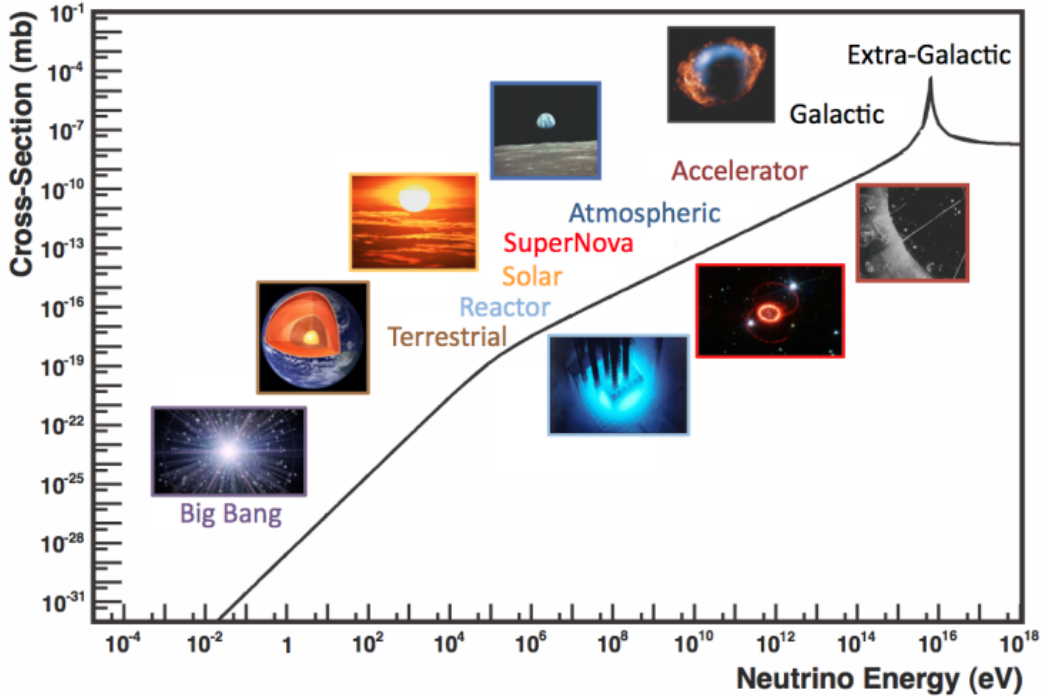


Figure 2.1: The electro-weak cross-section for $\bar{\nu}_e + e^- \rightarrow \bar{\nu}_e + e^-$ scattering on free electrons from various natural and man-made neutrino sources, as a function of neutrino energy. Taken from [29]

³⁷⁸ 2.3.1 Solar Neutrinos

³⁷⁹ Solar neutrinos are emitted from fusion reaction chains at the centre of the Sun.
³⁸⁰ The solar neutrino flux, given as a function of neutrino energy for different
³⁸¹ fusion and decay chains, is illustrated in Figure 2.2. Whilst proton-proton fusion
³⁸² generates the largest flux of neutrinos, the neutrinos are low energy and are
³⁸³ difficult to reconstruct due to the IBD interaction threshold of 1.8MeV [30].
³⁸⁴ Consequently, most experiments focus on the neutrinos from the decay of 8B
³⁸⁵ (via $^8B \rightarrow ^8Be^* + e^+ + \nu_e$), which are higher energy.

³⁸⁶ The first measurements of solar neutrinos observed a significant reduction in
³⁸⁷ the event rate compared to predictions from the Standard Solar Model [32, 33]. A
³⁸⁸ proposed solution to this “solar neutrino problem” was $\nu_e \leftrightarrow \nu_\mu$ oscillations in a

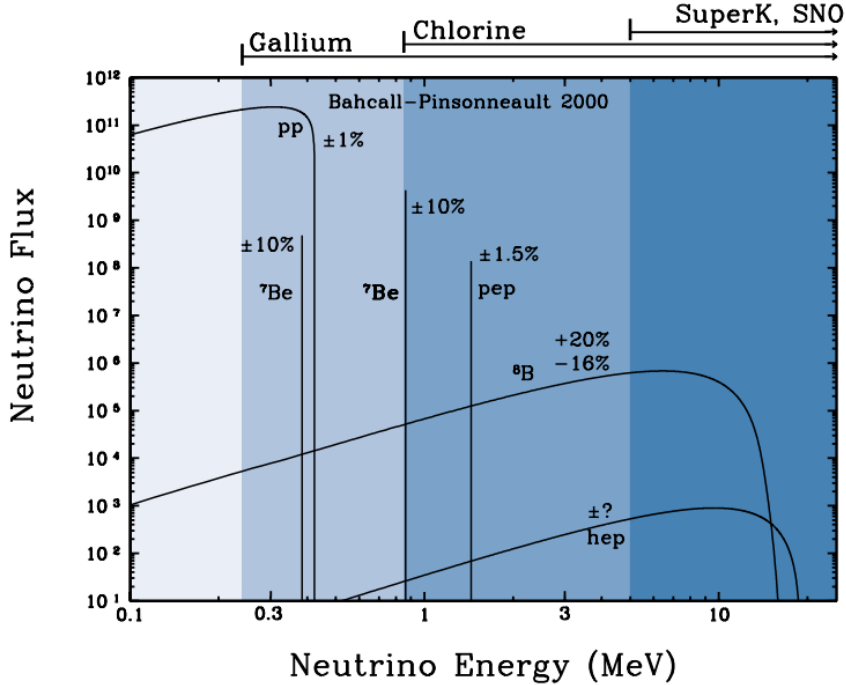


Figure 2.2: The solar neutrino flux as a function of neutrino energy for various fusion reactions and decay chains as predicted by the Standard Solar Model. Taken from [31].

389 precursory version of the PMNS model [34]. The Kamiokande [35], Gallex [36]
 390 and Sage [37] experiments confirmed the ~ 0.5 factor deficit of solar neutrinos.

391 The conclusive solution to this problem was determined by the SNO col-
 392 laboration [27]. Using a deuterium water target to observe 8B neutrinos, the
 393 event rate of charged current (CC), neutral current (NC), and elastic scattering
 394 (ES) interactions (Given in Equation 2.13) was simultaneously measured. CC
 395 events can only occur for electron neutrinos, whereas the NC channel is agnostic
 396 to neutrino flavour, and the ES reaction has a small excess sensitivity for the
 397 detection of electron neutrino interactions. This meant that there were direct
 398 measurements of the ν_e and ν_x neutrino flux. It was concluded that the CC and
 399 ES interaction rates were consistent with the deficit previously observed. Most
 400 importantly, the NC reaction rate was only consistent with the others under the

401 hypothesis of flavour transformation.

$$\begin{aligned} \nu_e + d &\rightarrow p + p + e^- & (CC) \\ \nu_x + d &\rightarrow p + n + \nu_x & (NC) \\ \nu_x + e^- &\rightarrow \nu_x + e^- & (ES) \end{aligned} \quad (2.13)$$

402 Since the SNO measurement, many experiments have since measured the
403 neutrino flux of different interaction chains within the sun [38–40]. The most
404 recent measurement was that of CNO-cycle neutrinos which were recently
405 observed with 5σ significance by the Borexino collaboration [38].

406 2.3.2 Accelerator Neutrinos

407 The concept of using an artificial “neutrino beam” was first realised in 1962 [11].
408 Since then, many experiments have adopted the same fundamental concepts.
409 Typically, a proton beam is aimed at a target producing charged mesons that
410 decay to neutrinos. The mesons can be sign-selected by the use of magnetic
411 focusing horns to generate a neutrino or antineutrino beam. Pions are the primary
412 mesons that decay and depending on the orientation of the magnetic field, a
413 muon (anti-)neutrino beam is generated via $\pi^+ \rightarrow \mu^+ + \nu_\mu$ or $\pi^- \rightarrow \mu^- + \bar{\nu}_\mu$.
414 The decay of muons and kaons results in an irreducible intrinsic electron neutrino
415 background. In T2K, this background contamination is $O(< 1\%)$ [41]. There is
416 also an approximately $\sim 5\%$ “wrong-sign” neutrino background of $\bar{\nu}_\mu$ generated
417 via the same decays. As the beam is generated by proton interactions (rather
418 than anti-proton interactions), the wrong-sign component in the antineutrino
419 beam is larger when operating in neutrino mode.

420 Tuning the proton energy in the beam and using beam focusing techniques
421 allows the neutrino energy to be set to a value that maximises the disappear-
422 ance oscillation probability in the L/E term in Equation 2.10. This means that
423 accelerator experiments are typically more sensitive to the mixing parameters as
424 compared to a natural neutrino source. However, the disadvantage compared
425 to atmospheric neutrino experiments is the cost of building a facility to provide

⁴²⁶ high-energy neutrinos, with a high flux, which is required for longer baselines.
⁴²⁷ Consequently, there is typically less sensitivity to matter effects and the ordering
⁴²⁸ of the neutrino mass eigenstates.

⁴²⁹ A neutrino experiment measures

$$R(\vec{x}) = \Phi(E_\nu) \times \sigma(E_\nu) \times \epsilon(\vec{x}) \times P(\nu_\alpha \rightarrow \nu_\beta), \quad (2.14)$$

⁴³⁰ where $R(\vec{x})$ is the event rate of neutrinos at position \vec{x} , $\Phi(E_\nu)$ is the flux of
⁴³¹ neutrinos with energy E_ν , $\sigma(E_\nu)$ is the cross-section of the neutrino interaction and
⁴³² $\epsilon(\vec{x})$ is the efficiency and resolution of the detector. In order to leverage the most
⁴³³ out of an accelerator neutrino experiment, the flux and cross-section systematics
⁴³⁴ need to be constrained. This is typically done via the use of a “near detector”,
⁴³⁵ situated at a baseline of $O(1)$ km. This detector observes the unoscillated neutrino
⁴³⁶ flux and constrains the parameters used within the flux and cross-section model.

⁴³⁷ The first accelerator experiments to precisely measure oscillation parameters
⁴³⁸ were MINOS [42] and K2K [43]. These experiments confirmed the ν_μ disappear-
⁴³⁹ ance seen in atmospheric neutrino experiments by finding consistent parameter
⁴⁴⁰ values for $\sin^2(\theta_{23})$ and Δm_{32}^2 . The current generation of accelerator neutrino
⁴⁴¹ experiments, T2K and NO ν A extended this field by observing $\bar{\nu}_\mu \rightarrow \bar{\nu}_e$ and lead
⁴⁴² the sensitivity to atmospheric mixing parameters as seen in Figure 2.6 [44]. The
⁴⁴³ two experiments differ in their peak neutrino energy, baseline, and detection tech-
⁴⁴⁴ nique. The NO ν A experiment is situated at a baseline of 810km from the NuMI
⁴⁴⁵ beamline which delivers 2GeV neutrinos. The T2K neutrino beam is peaked
⁴⁴⁶ around 0.6GeV and propagates 295km [45]. Additionally, the NO ν A experiment
⁴⁴⁷ uses functionally identical detectors (near and far) whereas T2K uses a plastic
⁴⁴⁸ scintillator technique at the near detector and a water Cherenkov far detector.
⁴⁴⁹ The future generation experiments DUNE [46] and Hyper-Kamiokande [47]
⁴⁵⁰ will succeed these experiments as the high-precision era of neutrino oscillation
⁴⁵¹ parameter measurements develops.

⁴⁵² Several anomalous results have been observed in the LSND [13] and Mini-
⁴⁵³ BooNE [14] detectors which were designed with purposefully short baselines.

454 Parts of the neutrino community attributed these results to oscillations induced
455 by a fourth “sterile” neutrino [48] but several searches in other experiments,
456 MicroBooNE [49] and KARMEN [50], found no hints of additional neutrino
457 species. The solution to the anomalous results is still being determined.

458 2.3.3 Atmospheric Neutrinos

459 The interactions of primary cosmic ray protons in the Earth’s upper atmosphere
460 generate showers of energetic hadrons. These are mostly pions and kaons that
461 decay to produce a natural source of neutrinos spanning energies of MeV to
462 TeV [51]. The main decay is via,

$$\begin{aligned} \pi^\pm &\rightarrow \mu^\pm + (\nu_\mu, \bar{\nu}_\mu), \\ \mu^\pm &\rightarrow e^\pm + (\nu_e, \bar{\nu}_e) + (\nu_\mu, \bar{\nu}_\mu), \end{aligned} \tag{2.15}$$

463 such that for a single pion decay, three neutrinos can be produced. The
464 atmospheric neutrino flux energy spectra as predicted by the Bartol [52], Honda
465 [53–55], and FLUKA [56] models are illustrated in Figure 2.3. The flux distribution
466 peaks at an energy of $O(10)$ GeV. The uncertainties associated with these models
467 are dominated by the hadronic production of kaon and pions as well as the
468 primary cosmic flux.

469 Unlike long-baseline experiments which have a fixed baseline, the distance
470 atmospheric neutrinos propagate is dependent upon the zenith angle at which
471 they interact. This is illustrated in Figure 2.4. Neutrinos that are generated
472 directly above the detector ($\cos(\theta) = 1.0$) have a baseline equivalent to the
473 height of the atmosphere, whereas neutrinos that interact directly below the
474 detector ($\cos(\theta) = -1.0$) have to travel a length equal to the diameter of the Earth.
475 This means atmospheric neutrinos have a baseline that varies from $O(20)$ km to
476 $O(6 \times 10^3)$ km. Any neutrino generated at or below the horizon will be subject
477 to MSW matter resonance as they propagate through the Earth.

478 Figure 2.5 highlights the neutrino flux as a function of the zenith angle for
479 different slices of neutrino energy. For medium to high-energy neutrinos (and to

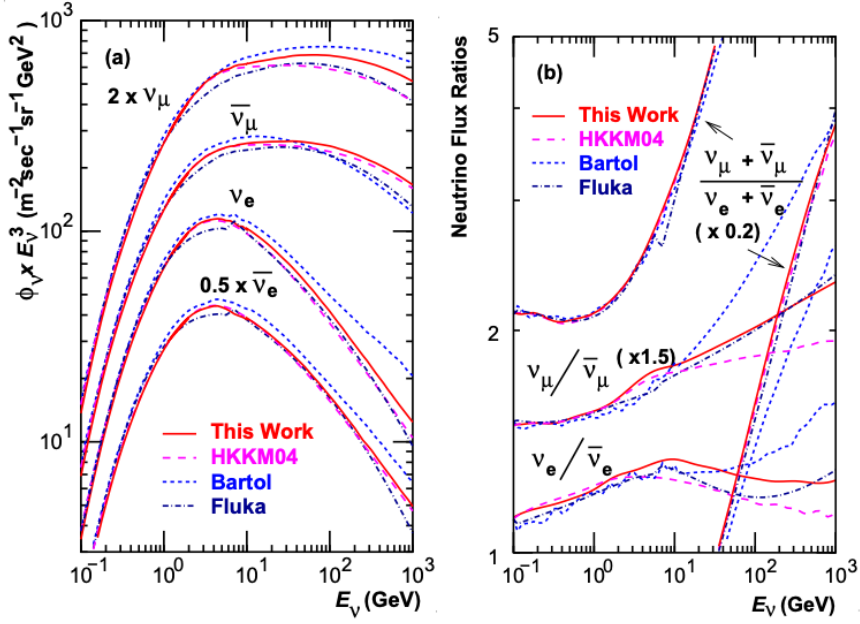


Figure 2.3: Left panel: The atmospheric neutrino flux for different neutrino flavours as a function of neutrino energy as predicted by the 2007 Honda model (“This work”) [53], the 2004 Honda model (“HKKM04”)[54], the Bartol model [52] and the FLUKA model [56]. Right panel: The ratio of the muon to electron neutrino flux as predicted by all the quoted models. Both figures taken from [53].

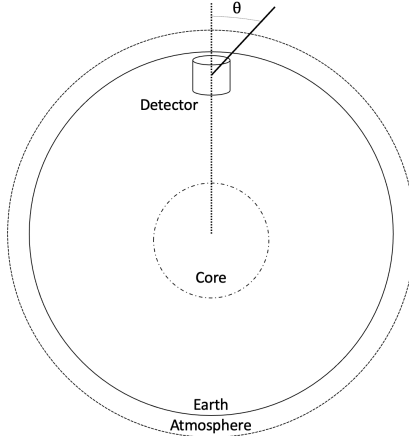


Figure 2.4: A diagram illustrating the definition of zenith angle as used in the Super Kamiokande experiment [57].

480 a lesser degree for low-energy neutrinos), the flux is approximately symmetric
 481 around $\cos(\theta) = 0$. To the accuracy of this approximation, the systematic
 482 uncertainties associated with atmospheric flux for comparing upward-going
 483 and down-going neutrino cancels. This allows the down-going events, which are

- ⁴⁸⁴ mostly insensitive to oscillation probabilities, to act as an unoscillated prediction
⁴⁸⁵ (similar to a near detector in an accelerator neutrino experiment).

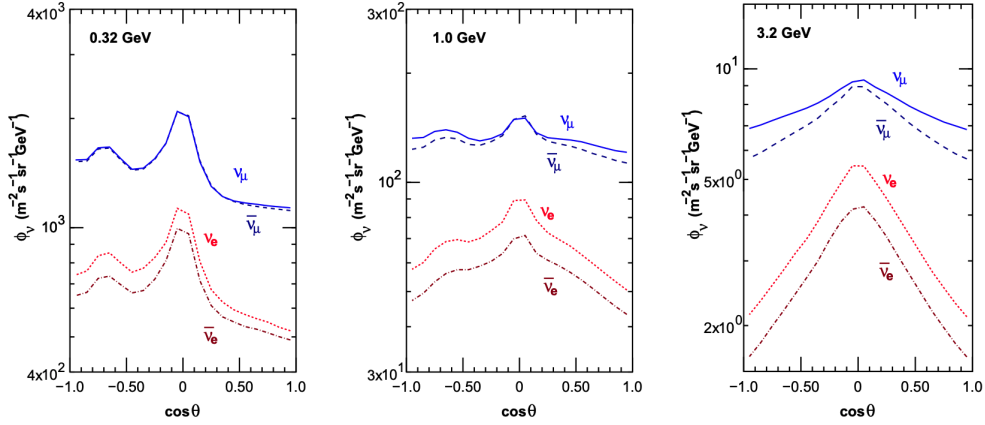


Figure 2.5: Prediction of ν_e , $\bar{\nu}_e$, ν_μ , $\bar{\nu}_\mu$ fluxes as a function of zenith angle as calculated by the HKKM model [55]. The left, middle and right panels represent three values of neutrino energy, 0.32GeV, 1.0GeV and 3.2GeV respectively. Predictions for other models including Bartol [52], Honda [53] and FLUKA [56] are given in [57].

⁴⁸⁶ Precursory hints of atmospheric neutrinos were observed in the mid-1960s
⁴⁸⁷ searching for $\nu_\mu + X \rightarrow X^* + \mu^\pm$ [58]. This was succeeded by the IMB-3 [59]
⁴⁸⁸ and Kamiokande [60] experiments which measured the double ratio of muon
⁴⁸⁹ to electron neutrinos in data to Monte Carlo, $R(\nu_\mu/\nu_e) = (\mu/e)_{Data}/(\mu/e)_{MC}$.
⁴⁹⁰ Both experiments were found to have a consistent deficit of muon neutrinos,
⁴⁹¹ with $R(\nu_\mu/\nu_e) = 0.67 \pm 0.17$ and $R(\nu_\mu/\nu_e) = 0.658 \pm 0.016 \pm 0.035$, respectively.
⁴⁹² Super-Kamiokande (SK) [57] extended this analysis by fitting oscillation pa-
⁴⁹³ rameters in $P(\nu_\mu \rightarrow \nu_\tau)$ which found best fit parameters $\sin^2(2\theta) > 0.92$ and
⁴⁹⁴ $1.5 \times 10^{-3} < \Delta m^2 < 3.4 \times 10^{-3} eV^2$.

⁴⁹⁵ Since then, atmospheric neutrino experiments have been making precision
⁴⁹⁶ measurements of the $\sin^2(\theta_{23})$ and Δm^2_{32} oscillation parameters. Atmospheric
⁴⁹⁷ neutrino oscillation is dominated by $P(\nu_\mu \rightarrow \nu_\tau)$, where SK observed a 4.6σ
⁴⁹⁸ discovery of ν_τ appearance [61]. Figure 2.6 illustrates the current estimates on
⁴⁹⁹ the atmospheric mixing parameters, from a wide range of atmospheric and
⁵⁰⁰ accelerator neutrino observatories.

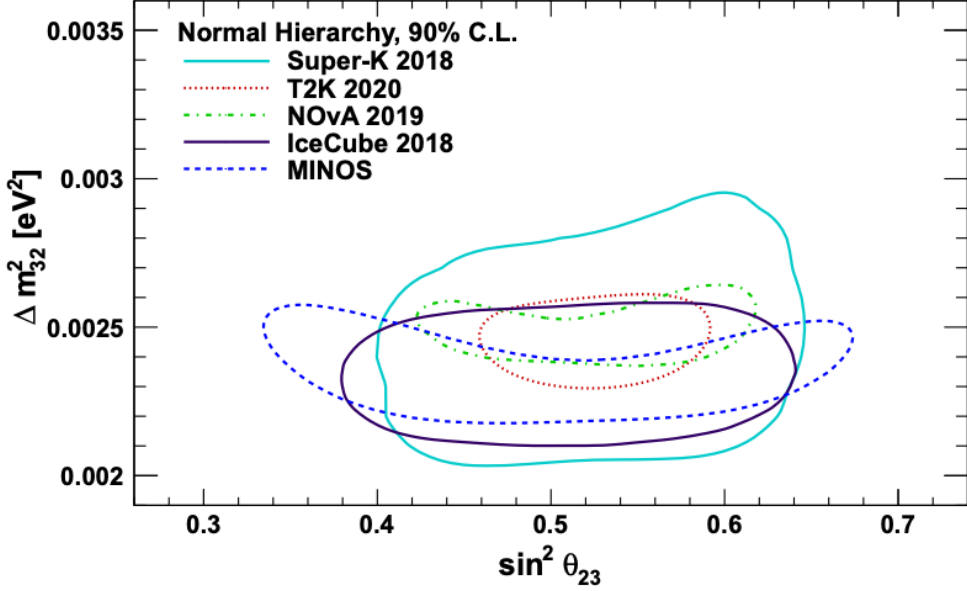


Figure 2.6: Constraints on the atmospheric oscillation parameters, $\sin^2(\theta_{23})$ and Δm_{32}^2 , from atmospheric and long-baseline experiments: SK [62], T2K [63], NOvA [64], IceCube [65] and MINOS [66]. Figure taken from [67].

2.3.4 Reactor Neutrinos

As illustrated in the first discovery of neutrinos (section 2.1), nuclear reactors are a very useful artificial source of electron antineutrinos. For reactors that use low-enriched uranium ^{235}U as fuel, the antineutrino flux is dominated by the β -decay fission of ^{235}U , ^{238}U , ^{239}Pu and ^{241}Pu [68] as illustrated in Figure 2.7.

Due to their low energy, reactor electron antineutrinos predominantly interact via the inverse β -decay (IBD) interaction. The typical signature contains two signals delayed by $O(200)\mu\text{s}$; firstly the prompt photons from positron annihilation, and secondly the photon emitted ($E_{tot}^\gamma = 2.2\text{MeV}$) from de-excitation after neutron capture on hydrogen. Searching for both signals improves the detector's ability to distinguish between background and signal events [69].

There are many short baseline experiments ($L \sim O(1)\text{km}$) that have measured the $\sin^2(\theta_{13})$ and Δm_{32}^2 oscillation parameters. Daya Bay [70], RENO [71] and Double Chooz [72] have all provided precise measurements, with the first discovery of a non-zero θ_{13} made by Daya Bay and RENO (and complemented by T2K [72]). The constraints on $\sin^2(\theta_{13})$ by the reactor experiments lead the field. They

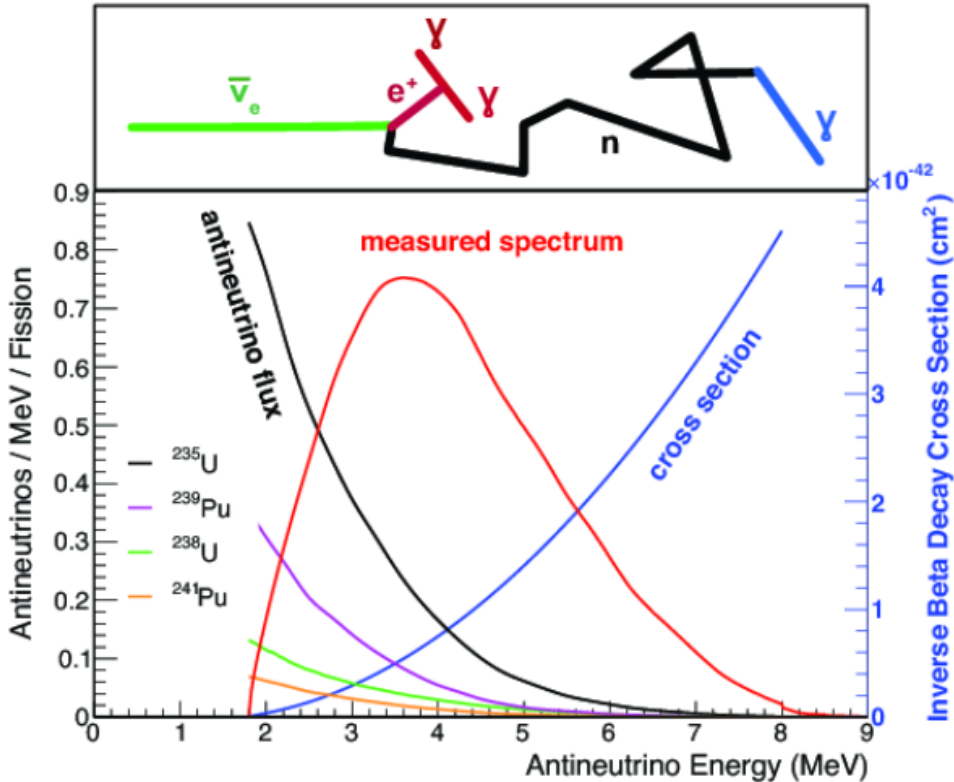


Figure 2.7: Reactor electron antineutrino fluxes for ^{235}U (Black), ^{238}U (Green), ^{239}Pu (Purple), and ^{241}Pu (Orange) isotopes. The inverse β -decay cross-section (Blue) and corresponding measurable neutrino spectrum (Red) are also given. Top panel: Schematic of Inverse β -decay interaction including the eventual capture of the emitted neutron. This capture emits a γ -ray which provides a second signal of the event. Taken from [67].

are often used as external inputs to accelerator neutrino experiments to improve their sensitivity to δ_{CP} and mass hierarchy determination. JUNO-TAO [73], a small collaboration within the larger JUNO experiment, is a next-generation reactor experiment that aims to precisely measure the isotopic antineutrino yields from the different fission chains.

Kamland [74] is the only experiment to have observed reactor neutrinos using a long baseline (flux weighted averaged baseline of $L \sim 180\text{km}$) which allows it to have sensitivity to Δm_{21}^2 . Combined with the SK solar neutrino experiment, the combined analysis puts the most stringent constraint on Δm_{21}^2 [75].

2.4 Summary Of Oscillation Parameter Measurements

Since the first evidence of neutrino oscillations, numerous measurements of the mixing parameters have been made. Many experiments use neutrinos as a tool for the discovery of new physics (diffuse supernova background, neutrinoless double beta decay and others) so the PMNS parameters are summarised in the Particle Data Group (PDG) review tables. The analysis presented in this thesis focuses on the 2020 T2K oscillation analysis presented in [2] which the 2020 PDG constraints [76] were used. These constraints are outlined in Table 2.1.

Parameter	2020 Constraint
$\sin^2(\theta_{12})$	0.307 ± 0.013
Δm_{21}^2	$(7.53 \pm 0.18) \times 10^{-5} \text{ eV}^2$
$\sin^2(\theta_{13})$	$(2.18 \pm 0.07) \times 10^{-2}$
$\sin^2(\theta_{23})$ (I.H.)	0.547 ± 0.021
$\sin^2(\theta_{23})$ (N.H.)	0.545 ± 0.021
Δm_{32}^2 (I.H.)	$(-2.546^{+0.034}_{-0.040}) \times 10^{-3} \text{ eV}^2$
Δm_{32}^2 (N.H.)	$(2.453 \pm 0.034) \times 10^{-3} \text{ eV}^2$

Table 2.1: The 2020 Particle Data Group constraints of the oscillation parameters taken from [76]. The value of Δm_{32}^2 is given for both normal hierarchy (N.H.) and inverted hierarchy (I.H.) and $\sin^2(\theta_{23})$ is broken down by whether its value is below (Q1) or above (Q2) 0.5.

The $\sin^2(\theta_{13})$ measurement stems from the electron antineutrino disappearance, $P(\bar{\nu}_e \rightarrow \bar{\nu}_e)$, and is taken as the average best-fit from the combination of Daya Bay, Reno and Double Chooz. It is often used as a prior uncertainty within other neutrino oscillation experiments, typically termed the reactor constraint. The $\sin^2(\theta_{12})$ parameter is predominantly measured through electron neutrino disappearance, $P(\nu_e \rightarrow \nu_{\mu,\tau})$, in solar neutrino experiments. The long-baseline reactor neutrino experiment Kamland also has a sensitivity to this parameter and is used in a joint fit to solar data from SNO and SK, using the reactor constraint. Measurements of $\sin^2(\theta_{23})$ are made by long-baseline and atmospheric neutrino experiments. The PDG value is a joint fit of T2K, NO ν A, MINOS and IceCube DeepCore experiments. The latest T2K-only measurement, provided at Neutrino2020 and is the basis of this thesis, is given as $\sin^2(\theta_{23}) = 0.546^{+0.024}_{-0.046}$ [2].

The PDG constraint on Δm_{21}^2 is provided by the KamLAND experiment using solar and geoneutrino data. This measurement utilised a $\sin^2(\theta_{13})$ constraint from accelerator (T2K, MINOS) and reactor neutrino (Daya Bay, RENO, Double Chooz) experiments. Accelerator measurements make some of the most stringent constraints on Δm_{32}^2 although atmospheric experiments have more sensitivity to the mass hierarchy determination. The PDG performs a joint fit of accelerator and atmospheric data, in both normal and inverted hierarchies separately. The latest T2K-only result is $\Delta m_{32}^2 = 2.49^{+0.058}_{-0.082} \times 10^{-3} \text{ eV}^2$ favouring normal hierarchy [2]. The value of δ_{CP} is largely undetermined. CP-conserving values of 0 and π were rejected with $\sim 2\sigma$ intervals, as published in Nature, although more recent analyses have reduced the credible intervals to 90%. Since the 2020 PDG publication, there has been a new measurement of $\sin^2(\theta_{13}) = (2.20 \pm 0.07) \times 10^{-2}$ [77], alongside updated Δm_{32}^2 and $\sin^2(\theta_{23})$ measurements.

Throughout this thesis, several sample spectra predictions and contours are presented, which require oscillation parameters to be assumed. Table 2.2 defines two sets of oscillation parameters, with “Asimov A” set being close to the preferred values from a previous T2K-only fit [78] and “Asimov B” being CP-conserving and further from maximal θ_{23} mixing.

Parameter	Asimov A	Asimov B
Δm_{12}^2	$7.53 \times 10^{-5} \text{ eV}^2$	
Δm_{32}^2	$2.509 \times 10^{-3} \text{ eV}^2$	
$\sin^2(\theta_{12})$	0.304	
$\sin^2(\theta_{13})$	0.0219	
$\sin^2(\theta_{23})$	0.528	0.45
δ_{CP}	-1.601	0.0

Table 2.2: Reference values of the neutrino oscillation parameters for two different oscillation parameter sets.

2.5 Overview of Oscillation Effects

The analysis presented within this thesis focuses on the determination of oscillation parameters from atmospheric and beam neutrinos. Whilst subject to the

567 same oscillation formalism, the way in which the two samples have sensitivity
 568 to the different oscillation parameters differs significantly.

569 Atmospheric neutrinos have a varying baseline, or “path length” L , such that
 570 the distance each neutrino travels before interacting is dependent upon the zenith
 571 angle, θ_Z . As primary cosmic rays can interact anywhere between the Earth’s
 572 surface and $\sim 50\text{km}$ above that, the height, h , in the atmosphere at which the
 573 neutrino was generated also affects the path length,

$$L = \sqrt{(R_E + h)^2 - R_E^2(1 - \cos^2(\theta_Z))} - R_E \cos(\theta_Z). \quad (2.16)$$

574 Where $R_E = 6,371\text{km}$ is the Earth’s radius. This assumes a spherically
 575 symmetric Earth model. Therefore, the oscillation probability is dependent upon
 576 two parameters, $\cos(\theta_Z)$ and E_ν .

577 The oscillation probability used within this analysis is based on [25]. The
 578 neutrino wavefunction in the vacuum Hamiltonian evolves in each layer of
 579 constant matter density via

$$i \frac{d\psi_j(t)}{dt} = \frac{m_j^2}{2E_\nu} \psi_j(t) - \sum_k \sqrt{2} G_F N_e U_{ej} U_{ke}^\dagger \psi_k(t), \quad (2.17)$$

580 where m_j^2 is the square of the j^{th} vacuum eigenstate mass, E_ν is the neutrino
 581 energy, G_F is Fermi’s constant, N_e is the electron number density and U is the
 582 PMNS matrix. The transformation $N_e \rightarrow -N_e$ and $\delta_{CP} \rightarrow -\delta_{CP}$ is applied for
 583 antineutrino propagation. Thus, a model of the Earth’s density is required for
 584 neutrino propagation. Following the official SK-only methodology [79], this
 585 analysis uses the Preliminary Reference Earth Model (PREM) [80] which provides
 586 piecewise cubic polynomials as a function of the Earth’s radius. This density
 587 profile is illustrated in Figure 2.8. As the propagator requires layers of constant
 588 density, the SK methodology approximates the PREM model by using four layers
 589 of constant density [79], detailed in Table 2.3.

590 The atmospheric neutrino oscillation probabilities can be presented as two di-
 591 mensional “oscillograms” as illustrated in Figure 2.9. The distinct discontinuities,
 592 as a function of $\cos(\theta_Z)$, are due to the discontinuous density in the PREM model.

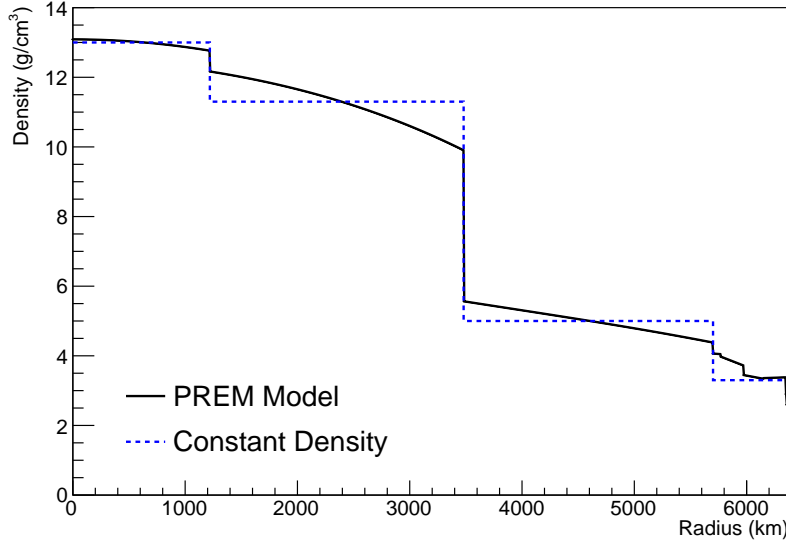


Figure 2.8: The density of the Earth given as a function of the radius, as given by the PREM model (Black), and the constant density four-layer approximation (Blue), as used in the official SK-only analysis.

Layer	Outer Radius [km]	Density [g/cm ³]	Chemical composition (Z/A)
Inner Core	1220	13	0.468 ± 0.029
Outer Core	3480	11.3	0.468 ± 0.029
Lower Mantle	5701	5.0	0.496
Transition Zone	6371	3.3	0.496

Table 2.3: Description of the four layers of the Earth invoked within the constant density approximation of the PREM model [80].

Atmospheric neutrinos have sensitivity to δ_{CP} through the overall event rate. Figure 2.10 illustrates the difference in oscillation probability between CP-conserving ($\delta_{CP} = 0.$) and a CP-violating ($\delta_{CP} = -1.601$) value taken from Asimov A oscillation parameter set (Table 2.2). The result is a complicated oscillation pattern in the appearance probability for sub-GeV upgoing neutrinos. The detector does not have sufficient resolution to resolve these individual patterns so the sensitivity to δ_{CP} for atmospheric neutrinos comes via the overall normalisation of these events.

The presence of matter means that the effect δ_{CP} has on the oscillation probability is not equal between neutrinos and antineutrinos. Furthermore, the interaction cross-section for neutrinos is larger than for antineutrinos so the two

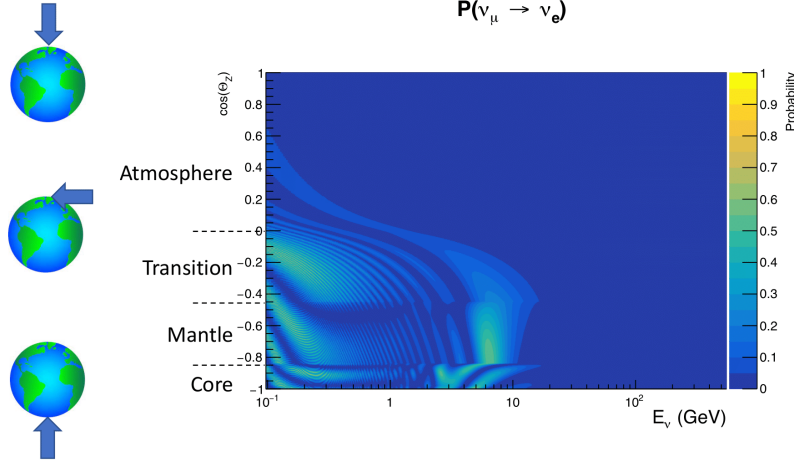


Figure 2.9: An “oscillogram” that depicts the $P(\nu_\mu \rightarrow \nu_e)$ oscillation probability as a function of neutrino energy and cosine of the zenith angle. The zenith angle is defined such that $\cos(\theta_Z) = 1.0$ represents neutrinos that travel from directly above the detector. The four-layer constant density PREM model approximation is used and Asimov A oscillation parameters are assumed (Table 2.2).

604 effects have to be disentangled. These effects are further convoluted by detector
 605 efficiencies as SK cannot distinguish neutrinos and antineutrinos well. All of
 606 these effects lead to a difference in the number of neutrinos detected compared
 607 to antineutrinos. This changes how the δ_{CP} normalisation term is observed,
 608 resulting in a very complex sensitivity to δ_{CP} .

609 The vacuum and matter oscillation probabilities for $P(\nu_e \rightarrow \nu_e)$ and $P(\bar{\nu}_e \rightarrow$
 610 $\bar{\nu}_e)$ are presented in Figure 2.11, where the PREM model has been assumed. The
 611 oscillation probability for both neutrinos and antineutrinos is affected in the
 612 presence of matter. However, the resonance effects around $O(5)\text{GeV}$ only occur
 613 for neutrinos in the normal mass hierarchy and antineutrinos in the inverse mass
 614 hierarchy. The exact position and amplitude of the resonance depend on $\sin^2(\theta_{23})$,
 615 further increasing the atmospheric neutrinos’ sensitivity to the parameter.

616 As the T2K beam flux is centered at the first oscillation maximum ($E_\nu =$
 617 0.6GeV) [45], the sensitivity to δ_{CP} is predominantly observed as a change in the
 618 event-rate of e-like samples in $\nu/\bar{\nu}$ modes. Figure 2.12 illustrates the $P(\nu_\mu \rightarrow \nu_e)$
 619 oscillation probability for a range of δ_{CP} values. A circular modulation of the

$$\mathbf{P}(\nu_\mu \rightarrow \nu_e; \delta_{CP} = -1.601) - \mathbf{P}(\nu_\mu \rightarrow \nu_e; \delta_{CP} = 0.)$$

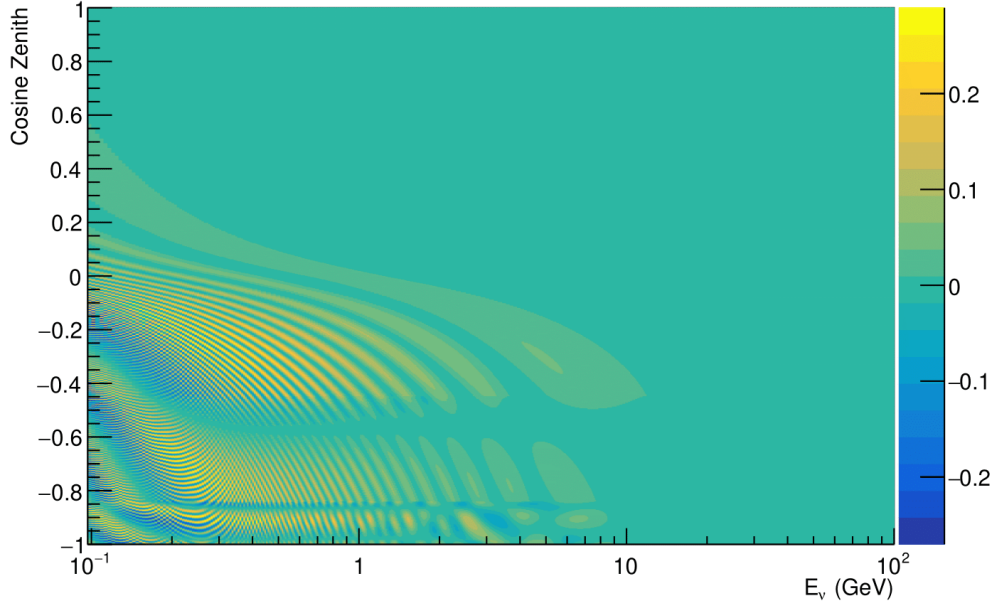


Figure 2.10: The effect of δ_{CP} for atmospheric neutrinos given in terms of the neutrino energy and zenith angle. This oscillogram compares the $P(\nu_\mu \rightarrow \nu_e)$ oscillation probability for a CP conserving ($\delta_{CP} = 0.0$) and a CP violating ($\delta_{CP} = -1.601$) value taken from the Asimov A parameter set. The other oscillation parameters assume the Asimov A oscillation parameter set given in Table 2.2.

first oscillation peak (in both magnitude and position) is observed when varying throughout the allowable values of δ_{CP} . The CP-conserving values of $\delta_{CP} = 0, \pi$ have a lower(higher) oscillation maximum than the CP-violating values of $\delta_{CP} = -\pi/2 (\delta_{CP} = \pi/2)$. A sub-dominant shift in the energy of the oscillation peak is also present, which aids in separating the two CP-conserving values of δ_{CP} .

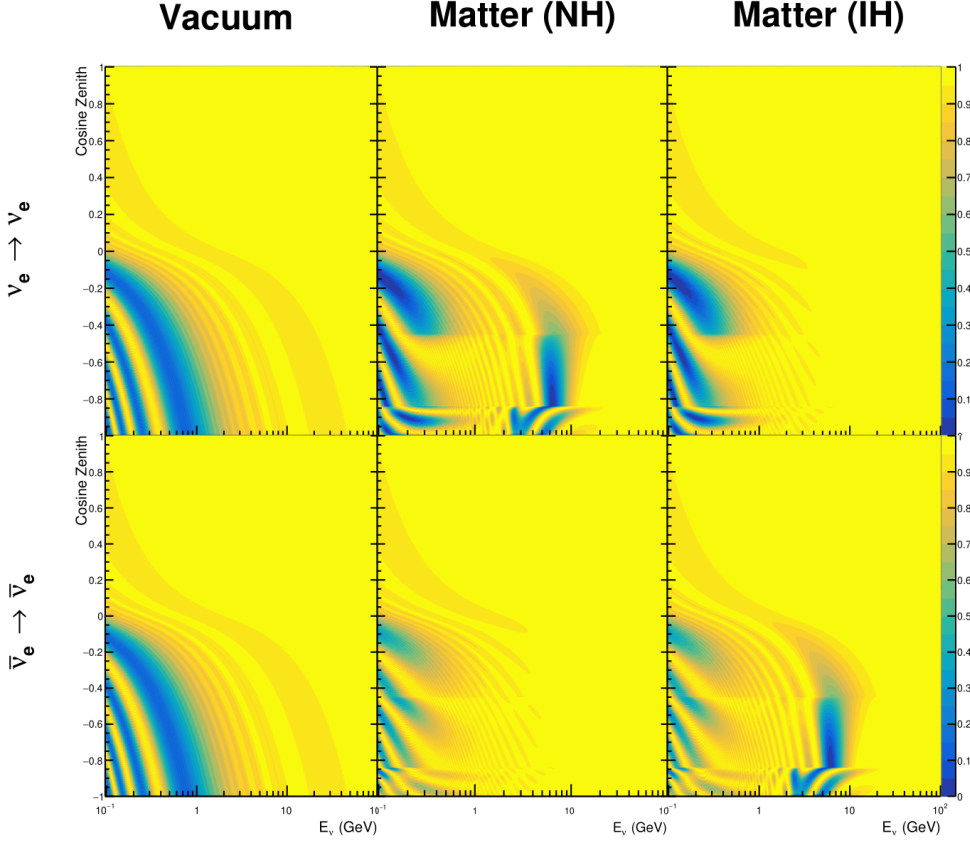


Figure 2.11: An illustration of the matter-induced effects on the oscillation probability, given as a function of neutrino energy and zenith angle. The top row of panels gives the $P(\nu_e \rightarrow \nu_e)$ oscillation probability and the bottom row illustrates the $P(\bar{\nu}_e \rightarrow \bar{\nu}_e)$ oscillation probability. The left column highlights the oscillation probability in a vacuum, whereas the middle and right column represents the oscillation probabilities when the four-layer fixed density PREM model is assumed. All oscillation probabilities assume the “Asimov A” set given in Table 2.2, but importantly, the right column sets an inverted mass hierarchy. The “matter resonance” effects at $E_\nu \sim 5\text{GeV}$ can be seen in the $P(\nu_e \rightarrow \nu_e)$ for normal mass hierarchy and $P(\bar{\nu}_e \rightarrow \bar{\nu}_e)$ for inverted hierarchy.

625 T2K’s sensitivity to $\sin^2(\theta_{23})$ and Δm_{32}^2 is observed as a shape-based variation
 626 of the muon-like samples, as illustrated in Figure 2.12. The value of Δm_{32}^2 laterally
 627 shifts the position of the oscillation dip (around $E_\nu \sim 0.6\text{GeV}$) in the $P(\nu_\mu \rightarrow \nu_\mu)$
 628 oscillation probability. A variation of $\sin^2(\theta_{23})$ is predominantly observed as
 629 a vertical shift of the oscillation dip with second-order horizontal shifts being
 630 due to matter effects. The beam neutrinos have limited sensitivity to matter
 631 effects due to the relatively shorter baseline as well as the Earth’s mantle being

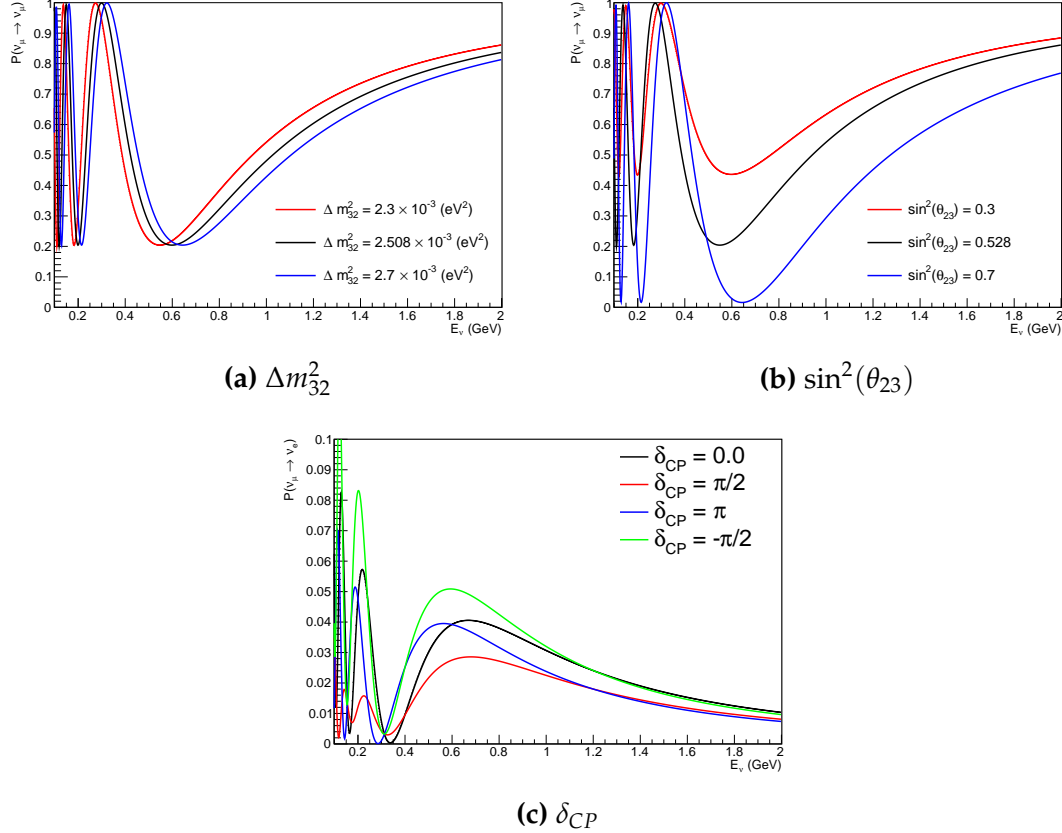


Figure 2.12: The oscillation probability for beam neutrino events given as a function of neutrino energy. All oscillation parameters assume the “Asimov A” set given in Table 2.2 unless otherwise stated. A path-length of 295km is assumed. Each panel represents a change in one of the oscillation parameters whilst keeping the remaining parameters fixed.

632 a relatively low-density material (as compared to the Earth’s core). For some
 633 values of δ_{CP} , the degeneracy in the number of e-like events allows the mass
 634 hierarchy to be broken. This leads to a δ_{CP} -dependent mass hierarchy sensitivity
 635 which can be seen in Figure 2.13.

636 Whilst all oscillation channels should be included for completeness, the
 637 computational resources required to run a fit are limited and any reasonable
 638 approximations which reduce the number of oscillation probability calculations
 639 that need to be made should be applied. The $\nu_e \rightarrow \nu_{e,\mu,\tau}$ (and antineutrino
 640 equivalent) oscillations can be ignored for beam neutrinos as the $\nu_e/\bar{\nu}_e$ fluxes are
 641 approximately two orders of magnitude smaller than the corresponding $\nu_\mu/\bar{\nu}_\mu$
 642 flux. Furthermore, as the peak neutrino energy of the beam is well below the

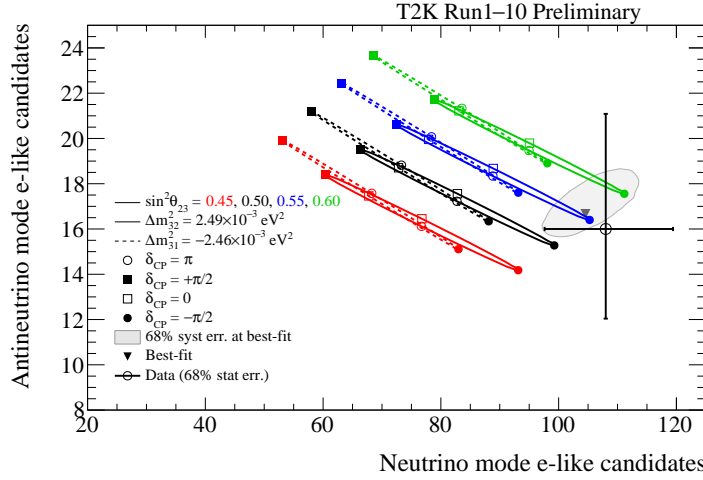


Figure 2.13: The number of electron-like events in the FHC and RHC operating mode of the beam, as a function of the oscillation probabilities. Both normal hierarchy (Solid) and inverse hierarchy (Dashed) values of Δm_{32}^2 are given.

threshold for charged current tau production ($E_\nu = 3.5\text{GeV}$ [61]), only a small proportion of the neutrinos produced in the beam have the required energy. For the few neutrinos that have sufficient energy, the oscillation probability is very small due to their energy being well above the oscillation maximum (small value of L/E). Whilst these approximations have been made for the beam neutrinos, the atmospheric flux of ν_e is of the same order of magnitude as the ν_μ flux and the energy distribution of atmospheric neutrinos extends well above the tau production threshold. These events can have non-negligible oscillation probabilities due to the further distance they travel.

3

652

653

T2K and SK Experiment Overview

654 As the successor of the Kamiokande experiment, the Super-Kamiokande (SK)
655 collaboration has been leading atmospheric neutrino oscillation analyses for
656 over two decades. The detector has provided some of the strongest constraints
657 on proton decay and the first precise measurements of the Δm_{32}^2 and $\sin^2(\theta_{23})$
658 neutrino oscillation parameters. The history, detection technique, and operation
659 of the SK detector is described in section 3.1.

660 The Tokai-to-Kamioka (T2K) experiment was one of the first long-baseline
661 experiments to use both neutrino and antineutrino beams to precisely measure
662 charge parity violation within the neutrino sector. The T2K experiment observed
663 the first hints of a non-zero $\sin^2(\theta_{13})$ measurement and continues to lead the
664 field with the constraints it provides on $\sin^2(\theta_{13})$, $\sin^2(\theta_{23})$, Δm_{32}^2 and δ_{CP} . In
665 section 3.2, the techniques that T2K use to generate the neutrino beam and
666 constrain systematic parameter through near detector constraints are described.

667 3.1 The Super-Kamiokande Experiment

668 The SK experiment began taking data in 1996 [81] and has had many modifi-
669 cations throughout its operation. There have been seven defined periods of
670 data taking as noted in Table 3.1. Data taking began in SK-I which ran for five

years. Between the SK-I and SK-II periods, approximately 55% of the PMTs were damaged during maintenance [82]. Those that survived were equally distributed throughout the detector in the SK-II era, which resulted in a reduced 19% photo-coverage. From SK-III onwards, repairs to the detector meant the full suite of PMTs was operational recovering the 40% photo-coverage. Before the start of SK-IV, the data acquisition and electronic systems were upgraded. Between SK-IV and SK-V, a significant effort was placed into tank open maintenance and repair/replacement of defective PMTs in preparation for the Gadolinium upgrade; a task for which the author of this thesis was required. Consequently, the detector conditions were significantly changed from this point. SK-VI marked the start of the SK-Gd era, with the detector being doped with gadolinium at a concentration of 0.01% by concentration. SK-VII, which started during the writing of this thesis, has increased the gadolinium concentration to 0.03% for continued operation [83].

The oscillation analysis presented within this thesis focuses on the SK-IV period of running and the data taken within it. This follows from the recent SK analysis presented in [84]. Therefore, the information presented within this section focuses on that period.

Period	Start Date	End Date	Live-time (days)
I	April 1996	July 2001	1489.19
II	October 2002	October 2005	798.59
III	July 2006	September 2008	518.08
IV	September 2008	May 2018	3244.4
V	January 2019	July 2020	461.02
VI	July 2020	May 2022	583.3
VII	May 2022	Ongoing	N/A

Table 3.1: The various SK periods and their respective live-time. The SK-VI live-time is calculated until 1st April 2022. SK-VII started during the writing of this thesis.

3.1.1 The SK Detector

The basic structure of the Super-Kamiokande (SK) detector is a cylindrical tank with a diameter 39.3m and height 41.1m filled with ultrapure water [82]. A diagram of the significant components of the SK detector is given in Figure 3.1.

692 The SK detector is situated in the Kamioka mine in Gifu, Japan. The mine is under-
 693 ground with roughly 1km rock overburden (2.7km water equivalent overburden)
 694 [85]. At this depth, the rate of cosmic ray muons is significantly decreased to a
 695 value of $\sim 2\text{Hz}$ (net rate). The top of the tank is covered with stainless steel which
 696 is designed as a working platform for maintenance, calibration, and location for
 697 high voltage and data acquisition electronics.

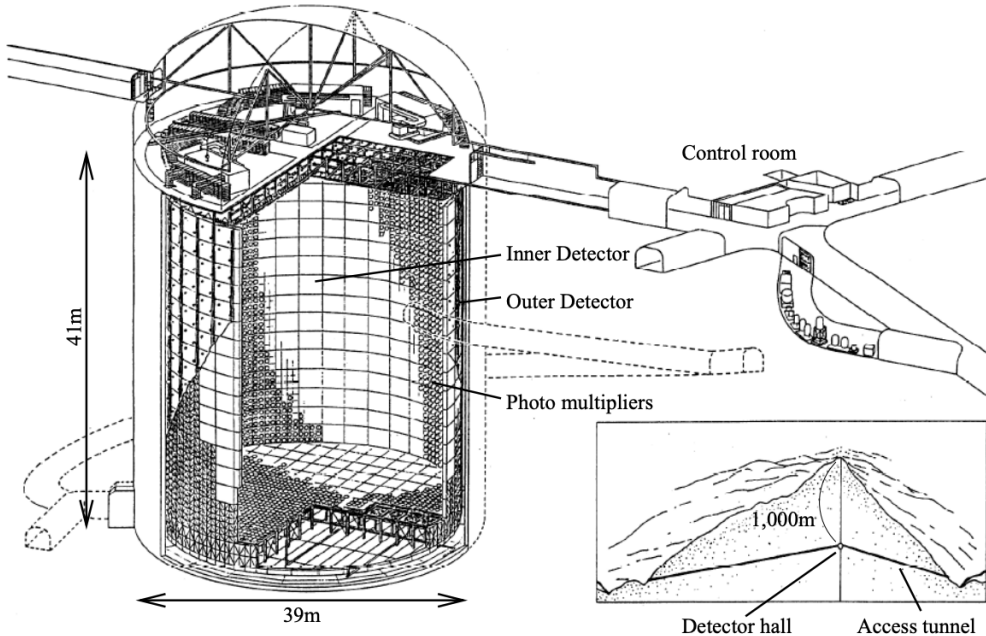


Figure 3.1: A schematic diagram of the Super-Kamiokande Detector. Taken from [86].

698 A smaller cylindrical structure (36.2m diameter, 33.8m height) is situated
 699 inside the tank, with an approximate 2m gap between this structure and the outer
 700 tank wall. The purpose of this structure is to support the photomultiplier tubes
 701 (PMTs). The volume inside and outside the support structure is referred to as the
 702 inner detector (ID) and outer detector (OD), respectively. In the SK-IV era, the
 703 ID and OD are instrumented by 11,129 50cm and 1,885 20cm PMTs respectively
 704 [82]. The ID contains a 32kton mass of water. Many analyses performed at SK
 705 use a “fiducial volume” defined by the volume of water inside the ID excluding
 706 some distance to the ID wall. This reduces the volume of the detector which is
 707 sensitive to neutrino events but reduces radioactive backgrounds and allows for

708 better reconstruction performance. The nominal fiducial volume is defined as the
709 area contained inside 2m from the ID wall for a total of 22.5kton water [3].

710 The two regions of the detector (ID and OD) are optically separated with
711 opaque black plastic hung from the support structure. The purpose of this is
712 to determine whether an event entered or exited the ID. This allows cosmic ray
713 muons and partially contained events to be tagged and separated from neutrino
714 events entirely contained within the ID. This black plastic is also used to cover
715 the area between the ID PMTs to reduce photon reflection from the ID walls.
716 Opposite to this, the OD is lined with a reflective material to allow photons to
717 reflect around inside the OD until collected by one of the PMTs. Furthermore,
718 each OD PMT is optically coupled with $50 \times 50\text{cm}$ plates of wavelength shifting
719 acrylic which increases the efficiency of light collection [85].

720 In the SK-IV data-taking period, the photocathode coverage of the detector, or
721 the fraction of the ID wall instrumented with PMTs, is $\sim 40\%$ [85]. The PMTs have
722 a quantum efficiency (the ratio of detected electrons to incident photons) of $\sim 21\%$
723 for photons with wavelengths of $360\text{nm} < \lambda < 390\text{nm}$ [87, 88]. The proportion
724 of photoelectrons that produce a signal in the dynode of a PMT, termed the
725 collection efficiency, is $> 70\%$ [85]. The PMTs used within SK are most sensitive
726 to photons with wavelength $300\text{nm} \leq \lambda \leq 600\text{nm}$ [85]. One disadvantage of
727 using PMTs as the detection media is that the Earth's geomagnetic field can
728 modify its response. Therefore, a set of compensation coils is built around the
729 inner surface of the detector to mitigate this effect [85].

730 The SK detector is filled with ultrapure water, which in a perfect world, con-
731 tains no impurities. However, bacteria and organic compounds can significantly
732 degrade the water quality. This decreases the attenuation length, which reduces
733 the total number of photons that hit a PMT. To combat this, a sophisticated water
734 treatment system has been developed [85, 89]. UV lights, mechanical filters, and
735 membrane degasifiers are used to reduce the bacteria, suspended particulates,
736 and radioactive materials from the water. The flow of water within the tank
737 is also critical as it can remove stagnant bacterial growth or build-up of dust

738 on the surfaces within the tank. Gravity drifts impurities in the water towards
739 the bottom of the tank which, if left uncontrolled, can create asymmetric water
740 conditions between the top and bottom of the tank. Typically, the water entering
741 the tank is cooled below the ambient temperature of the tank to control convection
742 and inhibit bacteria growth. Furthermore, the rate of dark noise hits within PMTs
743 is sensitive to the PMT temperature [90]. Therefore controlling the temperature
744 gradients within the tank is beneficial for stable measurements.

745 SK-VI is the first phase of the SK experiment to use gadolinium dopants
746 within the ultrapure water [83]. As such, the SK water system had to be replaced
747 to avoid removing the gadolinium concentrate from the ultrapure water [69]. For
748 an inverse β -decay (IBD) interaction on a water target, the emitted neutron is
749 thermally captured on hydrogen. This process releases a 2.2MeV γ ray which is
750 difficult to detect as the resulting Compton scattered electrons are very close to the
751 Cherenkov threshold, limiting detection capability. Thermal capture of neutrons
752 on gadolinium generates γ rays with higher energy (8MeV [69]) meaning they
753 are more easily detected and reconstructed. SK-VI has 0.01% Gd loading (0.02%
754 gadolinium sulphate by mass) which causes \approx 50% of neutrons emitted by IBD
755 to be captured on gadolinium[91]. Whilst predominantly useful for low energy
756 analyses, Gd loading allows better $\nu/\bar{\nu}$ separation for atmospheric neutrino
757 event selections [92]. Efforts are currently in place to increase the gadolinium
758 concentrate to 0.03% for \approx 75% neutron capture efficiency on gadolinium [93].
759 The final stage of loading targets 0.1% concentrate for \approx 90% neutron capture
760 efficiency on gadolinium.

761 3.1.2 Calibration

762 The calibration of the SK detector is documented in [82] and summarised below.
763 The analysis presented within this thesis is dependent upon ‘high energy events’
764 (Charged particles with $O(> 100)$ MeV momenta). These are events that are
765 expected to generate a larger number of photons such that each PMT will
766 be hit with multiple photons. The reconstruction of these events depends

upon the charge deposited within each PMT and the timing response of each individual PMT. Therefore, the most relevant calibration techniques to this thesis are outlined.

Before installation, 420 PMTs were calibrated to have identical charge responses and then distributed throughout the tank in a cross-shape pattern (As illustrated by Figure 3.2). These are used as a standardised measure for the rest of the PMTs installed at similar geometric positions within SK to be calibrated against. To perform this calibration, a xenon lamp is located at the center of the SK tank which flashes uniform light at 1Hz. This allows for geometrical effects, water quality variation, and timing effects to be measured in situ throughout normal data-taking periods.

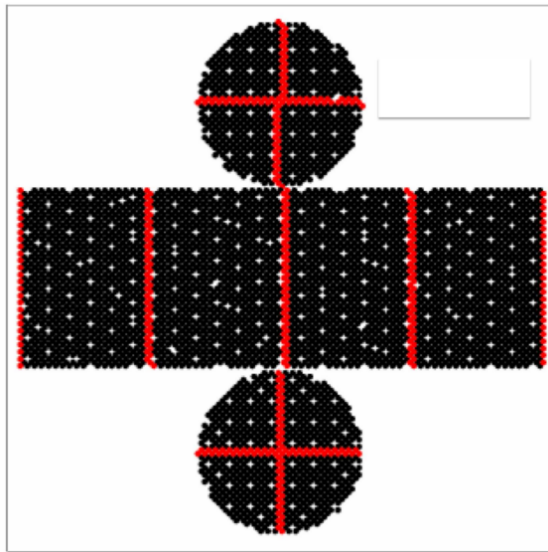


Figure 3.2: The location of “standard PMTs” (red) inside the SK detector. Taken from [82].

When specifically performing calibration of the detector (in out-of-data taking mode), the water in the tank was circulated to avoid top/bottom asymmetric water quality. Any non-uniformity within the tank significantly affects the PMT hit probability through scattering or absorption. This becomes a dominant effect for very low-intensity light sources that are designed such that only one photon is incident upon a given PMT.

The gain of a PMT is defined as the ratio of the total charge of the signal produced compared to the charge of photoelectrons emitted by the photocathodes within the PMT. To calibrate the signal of each PMT, the “relative” and “absolute” gain values are measured. The relative gain is the variation of gain among each of the PMTs whereas the absolute gain is the average gain of all PMTs.

The relative gain is calibrated as follows. A laser is used to generate two measurements: a high-intensity flash that illuminates every PMT with a sufficient number of photons, and a low-intensity flash in which only a small number of PMTs collect light. The first measurement creates an average charge, $Q_{obs}(i)$ on PMT i , whereas the second measurement ensures that each hit PMT only generates a single photoelectron. For the low-intensity measurement, the number of times each PMT records a charge larger than 1/4 photoelectrons, $N_{obs}(i)$, is counted. The values measured can be expressed as

$$\begin{aligned} Q_{obs}(i) &\propto I_H \times f(i) \times \epsilon(i) \times G(i), \\ N_{obs}(i) &\propto I_L \times f(i) \times \epsilon(i). \end{aligned} \tag{3.1}$$

Where I_H and I_L is the intensity of the high and low flashes, $f(i)$ is the acceptance efficiency of the i^{th} PMT, $\epsilon(i)$ is the product of the quantum and collection efficiency of the i^{th} PMT and $G(i)$ is the gain of the i^{th} PMT. The relative gain for each PMT can be determined by taking the ratio of these quantities.

The absolute gain calibration is performed by observing fixed energy γ -rays of $E_\gamma \sim 9\text{MeV}$ emitted isotropically from neutron capture on a NiCf source situated at the center of the detector. This generates a photon yield of about 0.004 photoelectrons/PMT/event, meaning that $> 99\%$ of PMT signals are generated from single photoelectrons. A charge distribution is generated by performing this calibration over all PMTs, and the average value of this distribution is taken to be the absolute gain value.

As mentioned in subsection 3.1.1, the average quantum and collection efficiency for the SK detector PMTs is $\sim 21\%$ and $> 70\%$ respectively. However, these values do differ between each PMT and need to be calibrated accordingly.

Consequently, the NiCf source is also used to calibrate the “quantum \times collection” efficiency (denoted “QE”) value of each PMT. The NiCf low-intensity source is used as the PMT hit probability is proportional to the QE ($N_{obs}(i) \propto \epsilon(i)$ in Equation 3.1). A Monte Carlo prediction which includes photon absorption, scattering, and reflection is made to estimate the number of photons incident on each PMT and the ratio of the number of predicted to observed hits is calculated. The difference is attributed to the QE efficiency of that PMT. This technique is extended to calculate the relative QE efficiency by normalizing the average of all PMTs which removes the dependence on the light intensity.

Due to differing cable lengths and readout electronics, the timing response between a photon hitting the PMT and the signal being captured by the data acquisition can be different between each PMT. Due to threshold triggers (Described in subsection 3.1.3), the time at which a pulse reaches a threshold is dependent upon the size of the pulse. This is known as the ‘time-walk’ effect and also needs to be accounted for in each PMT. To calibrate the timing response, a pulse of light with width 0.2ns is emitted into the detector through a diffuser. Two-dimensional distributions of time and pulse height (or charge) are made for each PMT and are used to calibrate the timing response. This is performed in-situ during data taking with the light source pulsing at 0.03Hz.

The top/bottom water quality asymmetry is measured using the NiCf calibration data and cross-referencing these results to the “standard PMTs”. The water attenuation length is continuously measured by the rate of vertically-downgoing cosmic-ray muons which enter via the top of the tank.

Dark noise is where a PMT registers a pulse that is consistent with a single photoelectron emitted from photon detection despite the PMT being in complete darkness. This is predominately caused by two processes. Firstly there is intrinsic dark noise which is where photoelectrons gain enough thermal energy to be emitted from the photocathode, and secondly, the radioactive decay of contaminants inside the structure of the PMT. Typical dark noise rate for PMTs used within SK are $O(3)$ kHz [85]. This is lower than the expected number of

841 photons generated for a ‘high energy event’ (As described in subsection 3.1.4)
842 but instability in this value can cause biases in reconstruction. Dark noise is
843 related to the gain of a PMT and is calibrated using hits inside a time window
844 recorded before an event trigger [94].

845 3.1.3 Data Acquisition and Triggering

846 As the analysis presented in this thesis will only use the SK-IV period of the
847 SK experiment so this subsection focuses on the relevant points of the data
848 acquisition and triggering systems to that SK period. The earlier data acquisition
849 and triggering systems are documented in [95, 96].

850 Before the SK-IV period started, the existing front-end electronics were re-
851 placed with “QTC-Based Electronics with Ethernet, QBEE” systems [97]. When
852 the QBEE observes a signal above a 1/4 photoelectron threshold, the charge-to-
853 time (QTC) converter generates a rectangular pulse. The start of the rectangular
854 pulse indicates the time at which the analog photoelectron signal was received
855 and the width of the pulse indicates the total charge integrated throughout the
856 signal. This is then digitized by time-to-digital converters and sent to the “front-
857 end” PCs. The digitized signal from every QBEE is then chronologically ordered
858 and sent to the “merger” PCs. It is the merger PCs that apply the software trigger.
859 Any triggered events are passed to the “organizer” PC. This sorts the data stream
860 of multiple merger PCs into chronologically ordered events, which are then saved
861 to disk. The schematic of data flow from PMTs to disk is illustrated in Figure 3.3.

862 The software trigger (described in [99]) operates by determining the number
863 of PMT hits within a 200ns sliding window, N_{200} . This window coincides with the
864 maximum time that a Cherenkov photon would take to traverse the length of the
865 SK tank [96]. For lower energy events that generate fewer photons, this technique
866 is useful for eliminating background processes like dark noise and radioactive
867 decay which would be expected to be separated in time. When the value of
868 N_{200} exceeds some pre-defined threshold, a software trigger is issued. There are
869 several trigger thresholds used within the SK-IV period which are detailed in

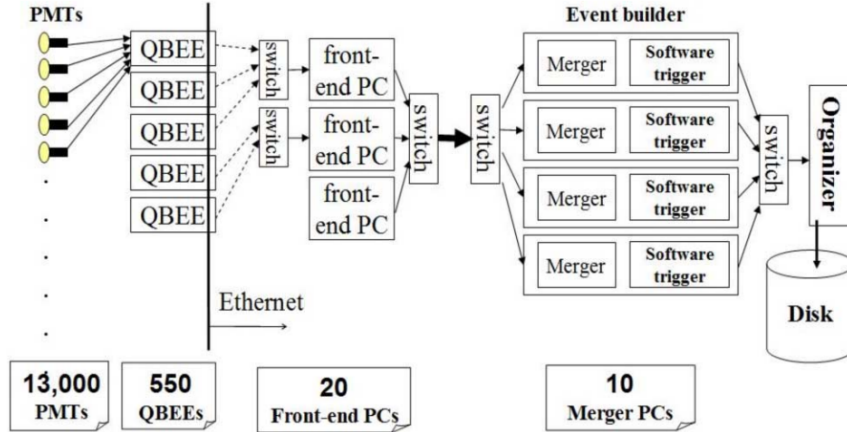


Figure 3.3: Schematic view of the data flow through the data acquisition and online system. Taken from [98].

870 Table 3.2. If one of these thresholds is met, the PMT hits within an extended time
 871 window are also read out and saved to disk. In the special case of an event that
 872 exceeds the SHE trigger but does not exceed the OD trigger, the AFT trigger looks
 873 for delayed coincidences of 2.2MeV gamma rays emitted from neutron capture in
 874 a $535\mu\text{s}$ window after the SHE trigger. A similar but more complex “Wideband
 875 Intelligent Trigger (WIT)” has been deployed and is described in [100].

Trigger	Acronym	Condition	Extended time window (μs)
Super Low Energy	SLE	>34/31 hits	1.3
Low Energy	LE	>47 hits	40
High Energy	HE	>50 hits	40
Super High Energy	SHE	>70/58 hits	40
Outer Detector	OD	>22 hits in OD	N/A

Table 3.2: The trigger thresholds and extended time windows saved around an event which were utilised throughout the SK-IV period. The exact thresholds can change and the values listed here represent the thresholds at the start and end of the SK-IV period.

3.1.4 Cherenkov Radiation

876 Cherenkov light is emitted from any highly energetic charged particle traveling
 877 with relativistic velocity, β , greater than the local speed of light in a medium [101].

⁸⁷⁹ Cherenkov light is formed at the surface of a cone with a characteristic pitch angle,

$$\cos(\theta) = \frac{1}{\beta n}. \quad (3.2)$$

⁸⁸⁰ Where n is the refractive index of the medium. Consequently, the Cherenkov
⁸⁸¹ momentum threshold, P_{thres} , is dependent upon the mass, m , of the charged
⁸⁸² particle moving through the medium,

$$P_{thres} = \frac{m}{\sqrt{n^2 - 1}}. \quad (3.3)$$

⁸⁸³ For water, where $n = 1.33$, the Cherenkov threshold momentum and energy
⁸⁸⁴ for various particles are given in Table 3.3. In contrast, γ -rays are detected
⁸⁸⁵ indirectly via the combination of photons generated by Compton scattering
⁸⁸⁶ and pair production. The threshold for detection in the SK detector is typically
⁸⁸⁷ higher than the threshold for photon production. This is due to the fact that the
⁸⁸⁸ attenuation of photons in the water means that typically $\sim 75\%$ of Cherenkov
⁸⁸⁹ photons reach the ID PMTs. Then the collection and quantum efficiencies
⁸⁹⁰ described in subsection 3.1.1 result in the number of detected photons being
⁸⁹¹ lower than the number of photons which reach the PMTs.

Particle	Threshold Momentum (MeV)	Threshold Energy (MeV)
Electron	0.5828	0.7751
Muon	120.5	160.3
Pion	159.2	211.7
Proton	1070.0	1423.1

Table 3.3: The threshold momentum and total energy for a particle to generate Cherenkov light in ultrapure water, as calculated in Equation 3.2 in ultrapure water which has refractive index $n = 1.33$.

⁸⁹² The Frank-Tamm equation [102] describes the relationship between the num-
⁸⁹³ ber of Cherenkov photons generated per unit length, dN/dx , the wavelength of
⁸⁹⁴ the photons generated, λ , and the relativistic velocity of the charged particle,

$$\frac{d^2N}{dxd\lambda} = 2\pi\alpha \left(1 - \frac{1}{n^2\beta^2}\right) \frac{1}{\lambda^2}. \quad (3.4)$$

895 where α is the fine structure constant. For a 100MeV momentum electron,
 896 approximately 330 photons will be produced per centimeter in the $300\text{nm} \leq \lambda \leq$
 897 700nm region which the ID PMTs are most sensitive to [85].

898 3.2 The Tokai to Kamioka Experiment

899 The Tokai to Kamioka (T2K) experiment is a long-baseline neutrino oscillation
 900 experiment located in Japan. Proposed in the early 2000s [86, 103] to replace
 901 K2K [104], T2K was designed to observe electron neutrino appearance whilst
 902 precisely measuring the oscillation parameters associated with muon neutrino
 903 disappearance [105]. The experiment consists of a neutrino beam generated
 904 at the Japan Proton Accelerator Research Complex (J-PARC), a suite of near
 905 detectors situated 280m from the beam target, and the Super Kamiokande far
 906 detector positioned at a 295km baseline. The cross-section view of the T2K
 907 experiment is drawn in Figure 3.4.

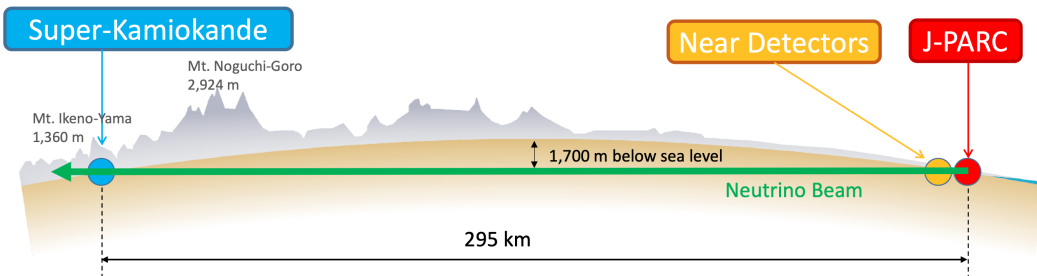


Figure 3.4: The cross-section view of the Tokai to Kamioka experiment illustrating the beam generation facility at J-PARC, the near detector situated at a baseline of 280m and the Super Kamiokande far detector situated 295km from the beam target.

908 The T2K collaboration makes world-leading measurements of the $\sin^2(\theta_{23})$,
 909 Δm_{32}^2 , and δ_{CP} oscillation parameters. Improvements in the precision and accu-
 910 racy of parameter estimates are still being made by including new data samples
 911 and developing the models which describe the neutrino interactions and detector
 912 responses [4]. Electron neutrino appearance was first observed at T2K in 2014
 913 [106] with 7.3σ significance.

914 The near detectors provide constraints on the beam flux and cross-section
 915 model parameters used within the oscillation analysis by observing the unoscil-
 916 lated neutrino beam. There are a host of detectors situated in the near detector hall
 917 (As illustrated in Figure 3.5): ND280 (subsection 3.2.3), INGRID (subsection 3.2.4),
 918 NINJA [107], WAGASCI [108], and Baby-MIND [109]. The latter three are not
 919 currently used within the oscillation analysis presented in this thesis.

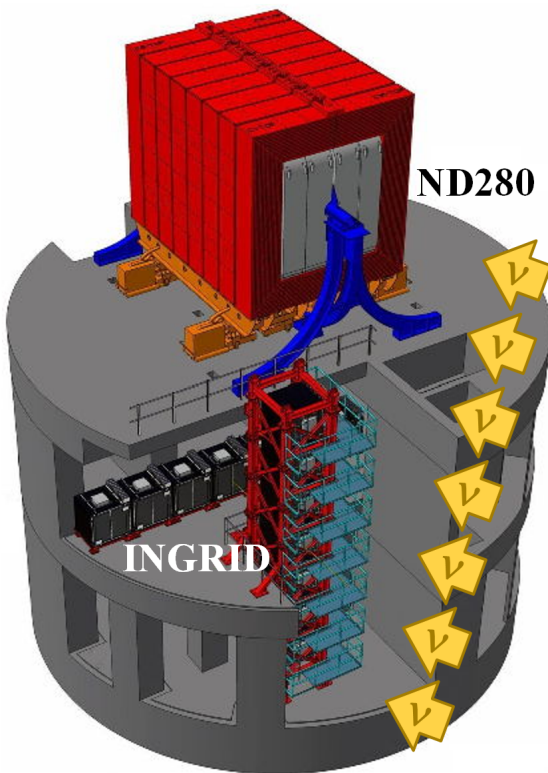


Figure 3.5: The near detector suite for the T2K experiment showing the ND280 and INGRID detectors. The distance between the detectors and the beam target is 280m.

920 Whilst this thesis presents the ND280 in terms of its purpose for the oscillation
 921 analysis, the detector can also make many cross-section measurements at neutrino
 922 energies of $O(1)$ GeV for the different targets within the detector [110, 111]. These
 923 measurements are of equal importance as they can lead the way in determining
 924 the model parameters used in the interaction models for the future high-precision
 925 era of neutrino physics.

3.2.1 Analysis Overview

There are two independent fitters, MaCh3 and BANFF, which perform the near detector fit. MaCh3 uses a bayesian Markov Chain Monte Carlo fitting technique, whereas BANFF uses a frequentist gradient descent technique. The output of each fitter is compared as a method of cross-checking the behaviour of the two fitters. This is done by comparing: the Monte Carlo predictions using various tunes, the likelihood that is calculated in each fitter and the post-fit constraint associated with every parameter used in the fit. Once validated, the output converted into a covariance matrix to describe the error and correlations between all the flux and cross-section parameters. This is then propagated to the far-detector oscillation analysis group.

The far detector group has three independent fitters: P-Theta, VALOR and MaCh3. The first two fitters use a hybrid frequentist fitting technique where the likelihood is minimised with respect to the parameters of interest and marginalised over all other parameters. These fitters use the covariance provided by the near detector fitters as a basis for implementing the near detector constraints. The MaCh3 fitter uses a simultaneous fit of all near and far detector samples. This removes any Gaussian assumptions when making the covariance matrix from the near detector results. The results for all three fitters are compares using a technique similar to the validation of the near detector fitters.

There are three particular tunes of the T2K flux and low energy cross section model typically considered. Firstly, the “generated” tune which is the set of dial values with which the Monte Carlo was generated. Secondly, the set of dial values which are taken from external data measurements and used as inputs. These are the “pre-fit” dial values. The reason these two sets of dial values are different is that the external data measurements are continually updated but it is very computationally intensive to regenerate a Monte Carlo prediction after each update. The final tune is the “post-fit”, “post-ND fit” or “post-BANFF” dial values. These are the values taken from the constraints provided by the near detector.

3.2.2 The Neutrino Beam

The neutrino beam used within the T2K experiment is described in [41, 45] and summarised below. The accelerator facility at J-PARC is composed of two sections; the primary and secondary beamlines. Figure 3.6 illustrates a schematic of the beamline, focusing mostly on the components of the secondary beamline. The primary beamline has three accelerators that progressively accelerate protons; a linear accelerator, a rapid-cycling synchrotron, and the main-ring (MR) synchrotron. Once fully accelerated by the MR, the protons have a kinetic energy of 30GeV. Eight bunches of these protons, separated by 500ns, are extracted per “spill” from the MR and directed towards a graphite target (a rod of length 91.4cm and diameter 2.6cm). Spills are extracted at 0.5Hz with $\sim 3 \times 10^{14}$ protons contained per spill.

The secondary beamline consists of three main components: the target station, the decay volume, and the beam dump. The target station is comprised of the target, beam monitors, and three magnetic focusing horns. The proton beam interacts with the graphite target to form a secondary beam of mostly pions and kaons. The secondary beam travels through a 96m long decay volume, generating neutrinos through the following decays [41],

$$\begin{array}{ll}
\pi^+ \rightarrow \mu^+ + \nu_\mu & \pi^- \rightarrow \mu^- + \bar{\nu}_\mu \\
K^+ \rightarrow \mu^+ + \nu_\mu & K^- \rightarrow \mu^- + \bar{\nu}_\mu \\
\rightarrow \pi^0 + e^+ + \nu_e & \rightarrow \pi^0 + e^- + \bar{\nu}_e \\
\rightarrow \pi^0 + \mu^+ + \nu_\mu & \rightarrow \pi^0 + \mu^- + \bar{\nu}_\mu \\
K_L^0 \rightarrow \pi^- + e^+ + \nu_e & K_L^0 \rightarrow \pi^+ + e^- + \bar{\nu}_e \\
\rightarrow \pi^- + \mu^+ + \nu_\mu & \rightarrow \pi^+ + \mu^- + \bar{\nu}_\mu \\
\mu^+ \rightarrow e^+ + \bar{\nu}_\mu + \nu_e & \mu^- \rightarrow e^- + \nu_\mu + \bar{\nu}_e.
\end{array}$$

The electrically charged component of the secondary beam is focused towards the far detector by the three magnetic horns. These horns direct charged particles of a particular polarity towards SK whilst defocusing the oppositely charged particles. This allows a mostly neutrino or mostly antineutrino beam to be used within the experiment, denoted as “forward horn current (FHC)” or “reverse horn current (RHC)” respectively.

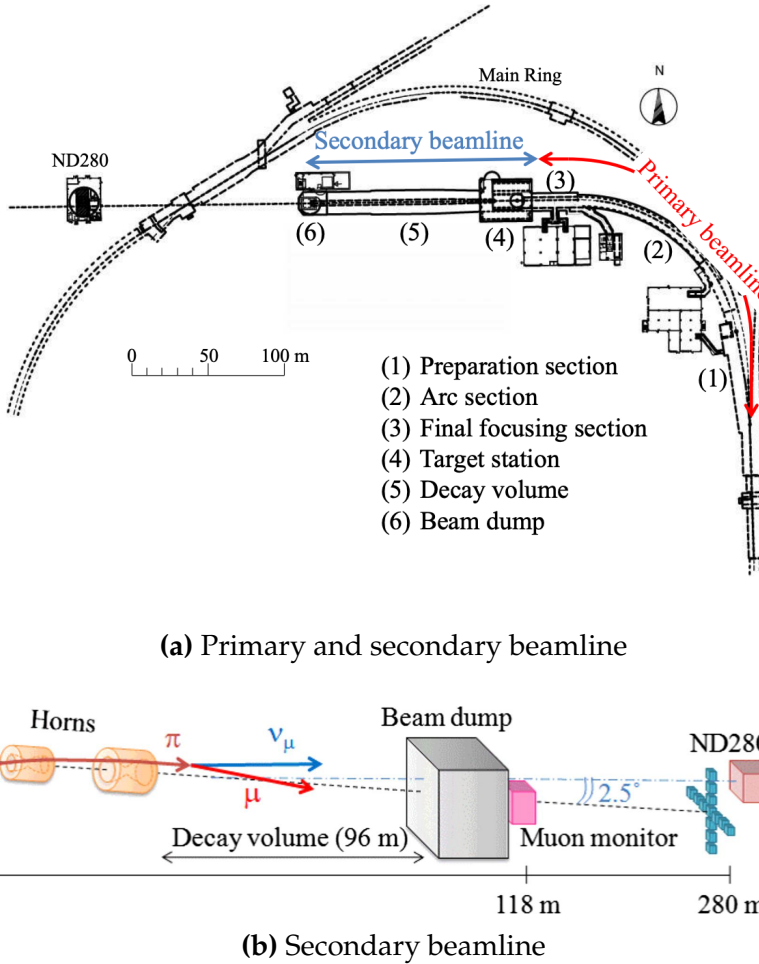


Figure 3.6: Top panel: Bird's eye view of the most relevant part of primary and secondary beamline used within the T2K experiment. The primary beamline is the main-ring proton synchrotron, kicker magnet, and graphite target. The secondary beamline consists of the three focusing horns, decay volume, and beam dump. Figure taken from [45]. Bottom panel: The side-view of the secondary beamline including the focusing horns, beam dump and neutrino detectors. Figure taken from [112].

981 Figure 3.7 illustrates the different contributions to the FHC and RHC neutrino
 982 flux. The low energy flux is dominated by the decay of pions whereas kaon
 983 decay becomes the dominant source of neutrinos for $E_\nu > 3\text{GeV}$. The “wrong-
 984 sign” component, which is the $\bar{\nu}_\mu$ background in a ν_μ beam, and the intrinsic
 985 irreducible ν_e background, are predominantly due to muon decay for $E_\nu <$
 986 2GeV. As the antineutrino production cross-section is smaller than the neutrino
 987 cross-section, the wrong-sign component is more dominant in the RHC beam
 988 as compared to that in the FHC beam.

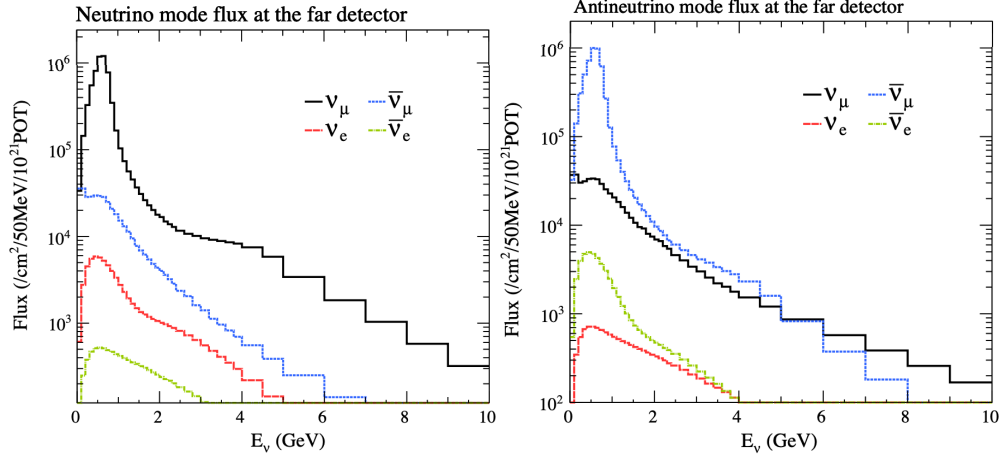


Figure 3.7: The Monte Carlo prediction of the energy spectrum for each flavour of neutrino (ν_e , $\bar{\nu}_e$, ν_μ and $\bar{\nu}_\mu$) in the neutrino dominated beam FHC mode (Left) and antineutrino dominated beam RHC mode (Right) expected at SK. Taken from [113].

989 The beam dump, situated at the end of the decay volume, stops all charged
 990 particles other than highly energetic muons ($p_\mu > 5\text{GeV}$). The MuMon detector
 991 monitors the penetrating muons to determine the beam direction and inten-
 992 sity which is used to constrain some of the beam flux systematics within the
 993 analysis [112, 114].

994 The T2K experiment uses an off-axis beam to narrow the neutrino energy
 995 distribution. This was the first implementation of this technique in a long-
 996 baseline neutrino oscillation experiment after its original proposal [115]. Pion
 997 decay, $\pi \rightarrow \mu + \nu_\mu$, is a two-body decay. Consequently, the neutrino energy,
 998 E_ν , can be determined based on the pion energy, E_π , and the angle at which
 999 the neutrino is emitted, θ ,

$$E_\nu = \frac{m_\pi^2 - m_\mu^2}{2(E_\pi - p_\pi \cos(\theta))}, \quad (3.5)$$

1000 where m_π and m_μ are the mass of the pion and muon respectively. For a fixed
 1001 energy pion, the neutrino energy distribution is dependent upon the angle at
 1002 which the neutrinos are observed from the initial pion beam direction. For the
 1003 295km baseline at T2K, $E_\nu = 0.6\text{GeV}$ maximises the electron neutrino appearance
 1004 probability, $P(\nu_\mu \rightarrow \nu_e)$, whilst minimising the muon disappearance probability,

1005 $P(\nu_\mu \rightarrow \nu_\mu)$. Figure 3.8 illustrates the neutrino energy distribution for a range of
1006 off-axis angles, as well as the oscillation probabilities most relevant to T2K.

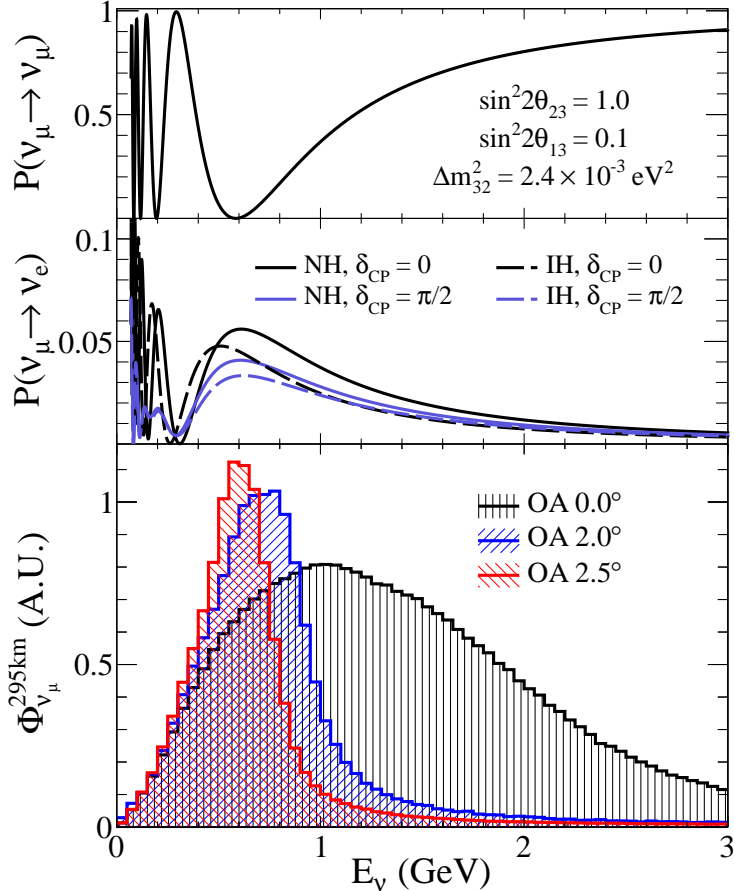


Figure 3.8: Top panel: T2K muon neutrino disappearance probability as a function of neutrino energy. Middle panel: T2K electron neutrino appearance probability as a function of neutrino energy. Bottom panel: The neutrino flux distribution for three different off-axis angles (Arbitrary units) as a function of neutrino energy.

1007 3.2.3 The Near Detector at 280m

1008 Whilst all the near detectors are situated in the same “pit” located at 280m from
1009 the beamline, the “ND280” detector is the off-axis detector which is situated at
1010 the same off-axis angle as the Super-Kamiokande far detector. It has two primary
1011 functions; firstly it measures the neutrino flux and secondly, it counts the event
1012 rates of different types of neutrino interactions. Both of these constrain the flux
1013 and cross-section systematics invoked within the model for a more accurate
1014 prediction of the expected event rate at the far detector.

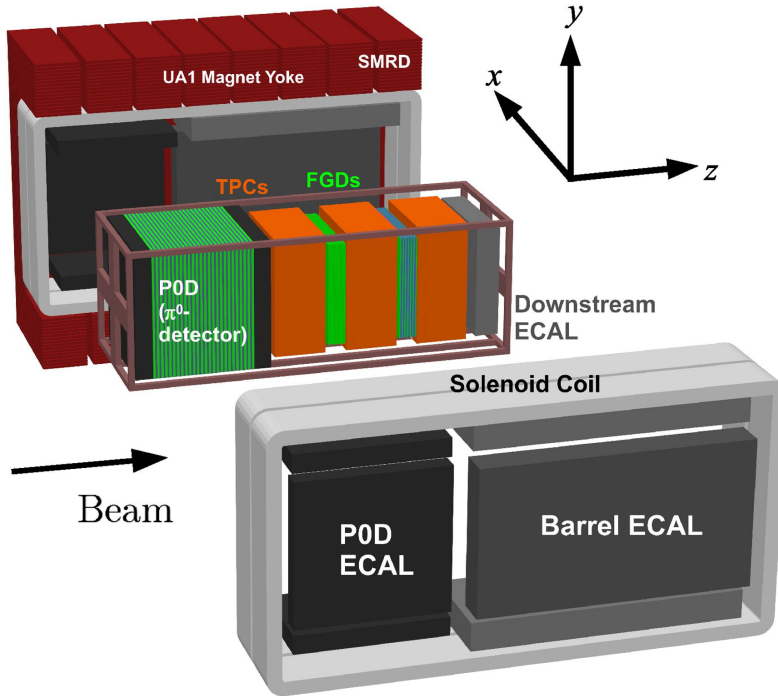


Figure 3.9: The components of the ND280 detector. The neutrino beam travels from left to right. Taken from [45].

As illustrated in Figure 3.9, the ND280 detector consists of several subdetectors. The most important part of the detector for this analysis is the tracker region. This is comprised of two-time projection chambers (TPCs) sandwiched between three fine grain detectors (FGDs). The FGDs contain both hydrocarbon plastics and water targets for neutrino interactions and provide track reconstruction near the interaction vertex. The emitted charged particles can then propagate into the TPCs which provide particle identification and momentum reconstruction. The FGDs and TPCs are further described in subsubsection 3.2.3.1 and subsubsection 3.2.3.2 respectively. The electromagnetic calorimeter (ECAL) encapsulates the tracker region alongside the π^0 detector (P0D). The ECAL measures the deposited energy from photons emitted from interactions within the FGD. The P0D constrains the cross-section of neutral current interactions which generate neutral pions, which is one of the largest backgrounds in the electron neutrino appearance oscillation channel. The P0D and ECAL detectors are detailed in subsubsection 3.2.3.3 and subsubsection 3.2.3.4 respectively. The entire detector is located within a large yoke magnet which produces a 0.2T magnetic field.

1031 field. This design of the magnet also includes a scintillating detector called the
1032 side muon range detector (SMRD), which is used to track high-angle muons as
1033 well as acting as a cosmic veto. The SMRD is described in subsubsection 3.2.3.5.

1034 **3.2.3.1 Fine Grained Detectors**

1035 The T2K tracker region is comprised of two fine-grained detectors (FGD) and
1036 three Time Projection Chambers (TPC). A detailed description of the FGD design,
1037 construction, and assembly is found in [116] and summarised below. The FGDS
1038 are the primary target for neutrino interactions with a mass of 1.1 tonnes per FGD.
1039 Alongside this, the FGDS are designed to be able to track short-range particles
1040 which do not exit the FGD. Typically, short-range particles are low momentum
1041 and are observed as tracks that deposit a large amount of energy per unit length.
1042 This means the FGD needs good granularity to resolve these particles. The
1043 FGDS have the best timing resolution ($\sim 3\text{ns}$) of any of the sub-detectors of the
1044 ND280 detector. As such, the FGDS are used for time of flight measurements
1045 to distinguish forward-going positively charged particles from backward-going
1046 negatively charged particles. Finally, any tracks which pass through multiple
1047 sub-detectors are required to be track matched to the FGD.

1048 Both FGDS are made from square scintillator planes of side length 186cm and
1049 width 2.02cm. Each plane consists of two layers of 192 scintillator bars in an
1050 X or Y orientation. A wavelength-shifting fiber is threaded through the center
1051 of each bar and is read out by a multi-pixel photon counter (MPPC). FGD1 is
1052 the most upstream of the two FGDS and contains 15 planes of carbon plastic
1053 scintillator which is a common target in external neutrino scattering data. As
1054 the far detector is a pure water target, 7 of the 15 scintillator planes in FGD2
1055 have been replaced with a hybrid water-scintillator target. Due to the complexity
1056 of the nucleus, nuclear effects can not be extrapolated between different nuclei.
1057 Therefore having the ability to take data on one target which is the same as
1058 external data and another target which is the same as the far detector target is
1059 beneficial for reliable model parameter estimates.

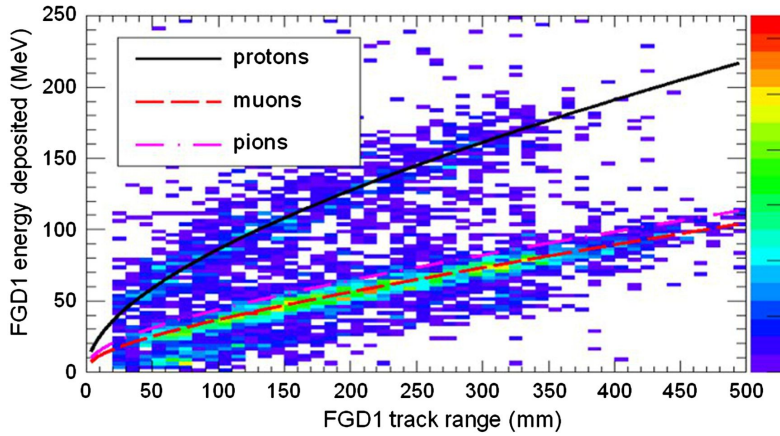


Figure 3.10: Comparison of data to Monte Carlo prediction of integrated deposited energy as a function of track length for particles that stopped in FGD1. Taken from [116].

1060 The integrated deposited energy is used for particle identification. The FGD
 1061 can distinguish protons from other charged particles by comparing the integrated
 1062 deposited energy from data to Monte Carlo prediction as seen in Figure 3.10.

1063 3.2.3.2 Time Projection Chambers

1064 The majority of particle identification and momentum measurements within
 1065 ND280 are provided by three Time Projection Chambers (TPCs) [117]. The
 1066 TPCs are located on either side of the FGDs. They are located inside of the
 1067 magnetic field meaning the momentum of a charged particle can be determined
 1068 from the bending of the track.

1069 Each TPC module consists of two gas-tight boxes, as shown in Figure 3.11,
 1070 which are made of non-magnetic material. The outer box is filled with CO₂ which
 1071 acts as an electrical insulator between the inner box and the ground. The inner box
 1072 forms the field cage which produces a uniform electric drift field of $\sim 275\text{V/cm}$
 1073 and is filled with an argon gas mixture. Charged particles moving through this
 1074 gas mixture ionize the gas and the ionised charge is drifted towards micromegas
 1075 detectors which measure the ionization charge. The time and position information
 1076 in the readout allows a three-dimensional image of the neutrino interaction.

1077 The particle identification of tracks that pass through the TPCs is performed
 1078 using dE/dx measurements. Figure 3.12 illustrates the data to Monte Carlo

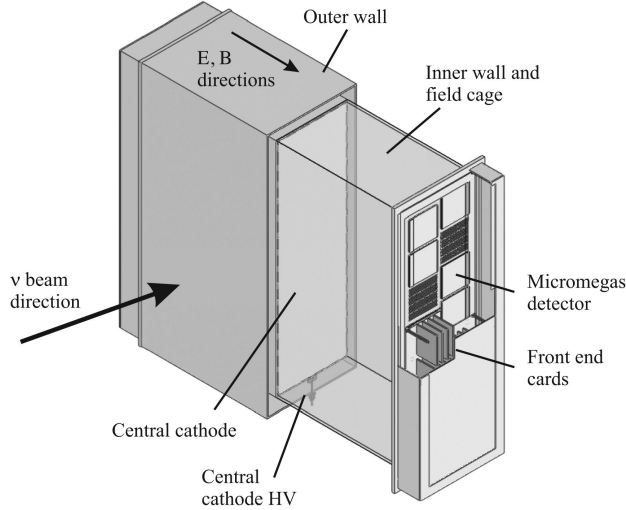


Figure 3.11: Schematic design of a Time Projection Chamber detector. Taken from [117].

1079 distributions of the energy lost by a charged particle passing through the TPC as
 1080 a function of the reconstructed particle momentum. The resolution is $7.8 \pm 0.2\%$
 1081 meaning that electrons and muons can be distinguished. This allows reliable
 1082 measurements of the intrinsic ν_e component of the beam.

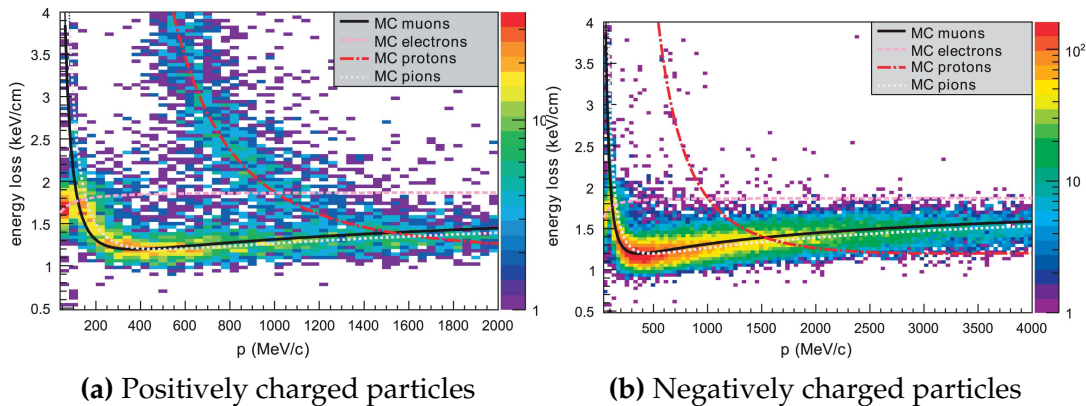


Figure 3.12: The distribution of energy loss as a function of reconstructed momentum for charged particles passing through the TPC, comparing data to Monte Carlo prediction. Taken from [117].

1083 **3.2.3.3 π^0 Detector**

1084 If one of the γ -rays from a $\pi^0 \rightarrow 2\gamma$ decay is missed at the far detector, the
 1085 reconstruction will determine that event to be a charge current ν_e -like event.
 1086 This is one of the main backgrounds hindering the electron neutrino appearance

1087 searches. The π^0 detector (P0D) measures the cross-section of the neutral current
1088 induced neutral pion production on a water target to constrain this background.

1089 The P0D is a cube of approximately 2.5m length consisting of layers of scin-
1090 tillating bars, brass and lead sheets, and water bags as illustrated in Figure 3.13.
1091 Two electromagnetic calorimeters are positioned at the most upstream and most
1092 downstream position in the sub-detector and the water target is situated in
1093 between them. The scintillator layers are built from two triangular bars orientated
1094 in opposite directions to form a rectangular layer. Each triangular scintillator bar
1095 is threaded with optical fiber which is read out by MPPCs. The high-Z brass and
1096 lead regions produce electron showers from the photons emitted in π^0 decay.

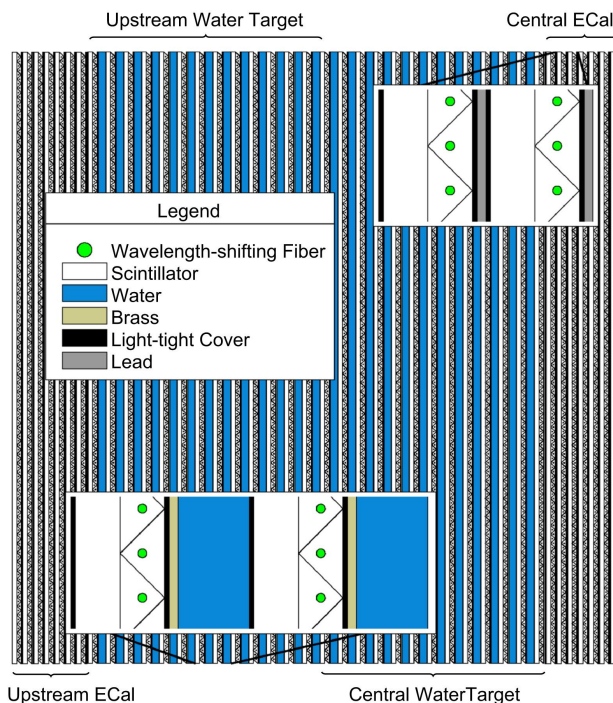


Figure 3.13: A schematic of the P0D side-view. Taken from [118].

1097 The sub-detector can generate measurements of NC1 π^0 cross-sections on a
1098 water target by measuring the event rate both with and without the water target,
1099 with the cross-section on a water target being determined as the difference. The to-
1100 tal active mass is 16.1 tonnes when filled with water and 13.3 tonnes when empty.

3.2.3.4 Electromagnetic Calorimeter

The electromagnetic calorimeter [119] (ECal) encapsulates the P0D and tracking sub-detectors. Its primary purpose is to aid π^0 reconstruction from any interaction in the tracker. To do this, it measures the energy and direction of photon showers from $\pi^0 \rightarrow 2\gamma$ decay. It can also distinguish pion and muon tracks depending on the shape of the photon shower deposited.

The ECal is comprised of three sections; the P0D ECal which surrounds the P0D, the barrel ECal which encompasses the tracking region, and the downstream ECal which is situated downstream of the tracker region. The barrel and downstream ECals are tracking calorimeters that focus on electromagnetic showers from high-angle particles emitted from the tracking sub-detectors. Particularly in the TPC, high-angle tracks (those which travel perpendicularly to the beam-axis) can travel along a single scintillator bar resulting in very few hits. The width of the barrel and downstream ECal corresponds to ~ 11 electron radiation lengths to ensure a significant amount of the π^0 energy is contained. As the P0D has its own calorimetry which reconstructs showers, the P0D ECal determines the energy which escapes the P0D.

Each ECal is constructed of multiple layers of scintillating bars sandwiched between lead sheets. The scintillating bars are threaded with optical fiber and read out by MPPCs. Each sequential layer of the scintillator is orientated perpendicular to the previous which allows a three-dimensional event reconstruction. The target mass of the P0D ECal, barrel ECal, and downstream ECal are 1.50, 4.80, and 6.62 tonnes respectively.

3.2.3.5 Side Muon Range Detector

As illustrated in Figure 3.9, the ECal, FGDs, P0D, and TPCs are enclosed within the UA1 magnet. Reconditioned after use in the UA1 [120] and NOMAD [121] experiments, this magnet provides a uniform horizontal magnetic field of 0.2T with an uncertainty of 2×10^{-4} T.

1129 Built into the UA1 magnet, the side muon range detector (SMRD)[122] monitors
1130 high-energy muons which leave the tracking region and permeate through
1131 the ECal. It additionally acts as a cosmic muon veto and trigger.

1132 **3.2.4 The Interactive Neutrino GRID**

1133 The Interactive Neutrino GRID (INGRID) detector is situated within the same
1134 “pit” as the other near detectors. It is aligned with the beam in the “on-axis”
1135 position and measures the beam direction, spread, and intensity. The detector
1136 was originally designed with 16 identical modules [45] (two modules have since
1137 been decommissioned) and a “proton” module. The design of the detector is 14
1138 modules oriented in a cross with length and height $10\text{m} \times 10\text{m}$, as illustrated
1139 in Figure 3.14.

1140 Each module is composed of iron sheets interlaced with eleven tracking
1141 scintillator planes for a total target mass of 7.1 tonnes per module. The scintillator
1142 design is an X-Y pattern of 24 bars in both orientations, where each bar contains
1143 wave-length shifting fibers which are connected to multi-pixel photon counters
1144 (MPPCs). Each module is encapsulated inside veto planes to aid the rejection
1145 of charged particles entering the module.

1146 The proton module is different from the other modules in that it consists
1147 of entirely scintillator planes with no iron target. The scintillator bars are also
1148 smaller than those used in the other modules to increase the granularity of
1149 the detector and improve tracking capabilities. The module sits in the center
1150 of the beamline and is designed to give precise measurements of quasi-elastic
1151 charged current interactions to evaluate the performance of the Monte Carlo
1152 simulation of the beamline.

1153 The INGRID detector can measure the beam direction to an uncertainty of
1154 0.4mrad and the beam centre within a resolution of 10cm [45]. The beam direction
1155 in both the vertical and horizontal directions is discussed in [123] and it is found
1156 to be in good agreement with the MUMON monitor described in subsection 3.2.2.

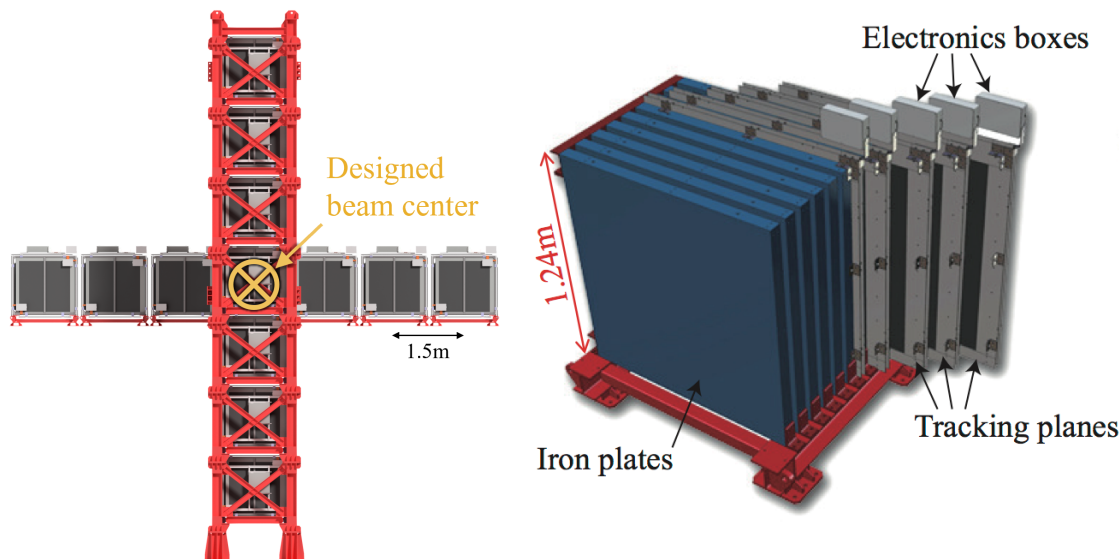


Figure 3.14: Left panel: The Interactive Neutrino GRID on-axis Detector. 14 modules are arranged in a cross-shape configuration, with the center modules being directly aligned with the on-axis beam. Right panel: The layout of a single module of the INGRID detector. Both figures are recreated from [45].

4

1157

1158

1159

Bayesian Statistics and Markov Chain Monte Carlo Techniques

1160 This thesis presents a Bayesian oscillation analysis. To extract the oscillation
1161 parameters, a Markov Chain Monte Carlo (MCMC) method is used. This chapter
1162 explains the theory of how parameter estimates can be determined using this
1163 technique and condenses the material found in the literature [124–127].

1164 The oscillation parameter determination presented here is built upon a si-
1165 multaneous fit to neutrino beam data in the near detector, beam data at SK, and
1166 atmospheric data at SK. In total, there are four oscillation parameters of interest
1167 ($\sin^2(\theta_{23})$, $\sin^2(\theta_{13})$, Δm_{32}^2 , and δ_{CP}), two oscillation parameters to which this
1168 study will not be sensitive ($\sin^2(\theta_{12})$, Δm_{21}^2) and many nuisance parameters that
1169 control the systematic uncertainty models.

1170 This analysis uses a Monte Carlo technique to generate a multi-dimensional
1171 probability distribution across all of the model parameters used in the fit. To
1172 determine an estimate for each parameter, this multi-dimensional object is in-
1173 tegrated over all other parameters. This process is called Marginalisation and
1174 is described in subsection 4.3.1. Monte Carlo techniques approximate the prob-
1175 ability distribution of each parameter within the limit of generating infinite
1176 samples. As ever, generating a large number of samples is time and resource-

1177 dependent. Therefore, an MCMC technique is utilised within this analysis to
1178 reduce the required number of steps to sufficiently sample the parameter space.
1179 This technique is described in further detail in subsection 4.2.1.

1180 The Bayesian analysis techniques used within this thesis are built within the
1181 MaCh3 framework [128]. This uses a custom MCMC library package exclusively
1182 supported and developed by the MaCh3 collaborators (which includes the author
1183 of this thesis).

1184 4.1 Bayesian Statistics

1185 Bayesian inference treats observable data, D , and model parameters, $\vec{\theta}$, on equal
1186 footing such that a probability model of both data and parameters is required.
1187 This is the joint probability distribution $P(D, \vec{\theta})$ and can be described by the
1188 prior distribution for model parameters $P(\vec{\theta})$ and the likelihood of the data given
1189 the model parameters $P(D|\vec{\theta})$,

$$P(D, \vec{\theta}) = P(D|\vec{\theta})P(\vec{\theta}). \quad (4.1)$$

1190 The prior distribution, $P(\vec{\theta})$, describes all previous knowledge about the
1191 parameters within the model. For example, if the risk of developing health
1192 problems is known to increase with age, the prior distribution would describe the
1193 increase. For the purpose of this analysis, the prior distribution is typically
1194 the best-fit values taken from external data measurements with a Gaussian
1195 uncertainty. The prior distribution can also contain correlations between model
1196 parameters. In an analysis using Monte Carlo techniques, the likelihood of
1197 measuring some data assuming some set of model parameters is calculated
1198 by comparing the Monte Carlo prediction generated at that particular set of
1199 model parameters to the data.

1200 It is parameter estimation that is important for this analysis and as such, Bayes'
1201 theorem [129] is applied to calculate the probability for each parameter to have a

1202 certain value given the observed data, $P(\vec{\theta}|D)$, which is known as the posterior
1203 distribution (often termed the posterior). This can be expressed as

$$P(\vec{\theta}|D) = \frac{P(D|\vec{\theta})P(\vec{\theta})}{\int P(D|\vec{\theta})P(\vec{\theta})d\vec{\theta}}. \quad (4.2)$$

1204 The denominator in Equation 4.2 is the integral of the joint probability distri-
1205 bution over all values of all parameters used within the fit. For brevity, the
1206 posterior distribution is

$$P(\vec{\theta}|D) \propto P(D|\vec{\theta})P(\vec{\theta}). \quad (4.3)$$

1207 For the purposes of this analysis, it is acceptable to neglect the normalisation
1208 term and focus on this proportional relationship.

1209 4.1.1 Application of Prior Knowledge

1210 The posterior distribution is proportional to the prior uncertainty applied to
1211 each parameter, as illustrated by Equation 4.3. This means that it is possible
1212 to change the prior after the posterior distribution has been determined. The
1213 prior uncertainty of a particular parameter can be ‘divided’ out of the posterior
1214 distribution and the resulting distribution can be reweighted using the new
1215 prior uncertainty that is to be applied. The methodology and implementation
1216 of changing the prior follows that described in [130].

1217 An example implementation that is useful for this analysis is the application
1218 of the “reactor constraint”. As discussed in section 2.4, an external constraint
1219 on $\sin^2(\theta_{13})$ is determined from measurements taken from reactor experiments.
1220 However, the sensitivities from just using the T2K and SK samples is equally
1221 as important. Without this technique, two fits would have to be run, doubling
1222 the required resources. Therefore, the key benefit for this analysis is the fact that
1223 only a single ‘fit’ has to be performed and can be used to build the two posterior
1224 distributions of the with and without reactor constraint applied.

1225 4.2 Monte Carlo Simulation

1226 Monte Carlo techniques are used to numerically solve a complex problem that
1227 does not necessarily have an analytical solution. These techniques rely on
1228 building a large ensemble of samples from an unknown distribution and then
1229 using the ensemble to approximate the properties of the distribution.

1230 An example that uses Monte Carlo techniques is to calculate the area under-
1231 neath a curve. For example, take the problem of calculating the area under a
1232 straight line with gradient $M = 0.4$ and intercept $C = 1.0$. Analytically, one can
1233 calculate the area under the line is equal to 30 units for $0 \leq x \leq 10$. Using Monte
1234 Carlo techniques, one can calculate the area under this line by throwing many
1235 random values for the x and y components of each sample and then calculating
1236 whether that point falls below the line. The area can then be calculated by the
1237 ratio of points below the line to the total number of samples thrown multiplied by
1238 the total area in which samples were scattered. The study is shown in Figure 4.1
1239 highlights this technique and finds the area under the curve to be 29.9 compared
1240 to an analytical solution of 30.0. The deviation of the numerical to analytical
1241 solution can be attributed to the number of samples used in the study. The
1242 accuracy of the approximation in which the properties of the Monte Carlo samples
1243 replicate those of the desired distribution is dependent on the number of samples
1244 used. Replicating this study with a differing number of Monte Carlo samples
1245 used in each study (As shown in Figure 4.2) highlights how the Monte Carlo
1246 techniques are only accurate within the limit of a high number of samples.

1247 Whilst the above example has an analytical solution, these techniques are just
1248 as applicable to complex solutions. Clearly, any numerical solution is only as
1249 useful as its efficiency. As discussed, the accuracy of the Monte Carlo technique is
1250 dependent upon the number of samples generated to approximate the properties
1251 of the distribution. Furthermore, if the positions at which the samples are
1252 evaluated are not ‘cleverly’ picked, the efficiency of the Monte Carlo technique
1253 significantly drops. Given the example in Figure 4.1, if the region in which the

1254 samples are scattered significantly extends passed the region of interest, many
1255 calculations will be calculated but do not add to the ability of the Monte Carlo
1256 technique to achieve the correct result. For instance, any sample evaluated at
1257 a $y \geq 5$ could be removed without affecting the final result. This does bring in
1258 an aspect of the ‘chicken and egg’ problem in that to achieve efficient sampling,
1259 one needs to know the distribution beforehand.

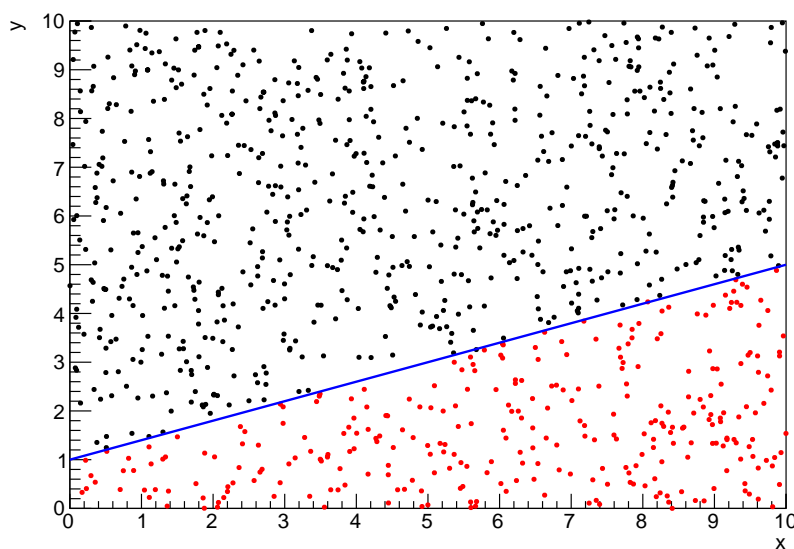


Figure 4.1: Example of using Monte Carlo techniques to find the area under the blue line. The gradient and intercept of the line are 0.4 and 1.0 respectively. The area found to be under the curve using one thousand samples is 29.9 units.

1260 4.2.1 Markov Chain Monte Carlo

1261 This analysis utilises a multi-dimensional probability distribution, with some
1262 dimensions being significantly more constrained than others. These constraints
1263 can be from prior knowledge of parameter distributions from external data or
1264 un-physical regions in which parameters can not exist. To maximise the efficiency
1265 of building the posterior distribution, a Markov Chain Monte Carlo (MCMC)
1266 technique is used. This employs a Markov chain to select the points at which
1267 to sample the posterior distribution. It performs a semi-random stochastic walk
1268 through the allowable parameter space. This builds a posterior distribution

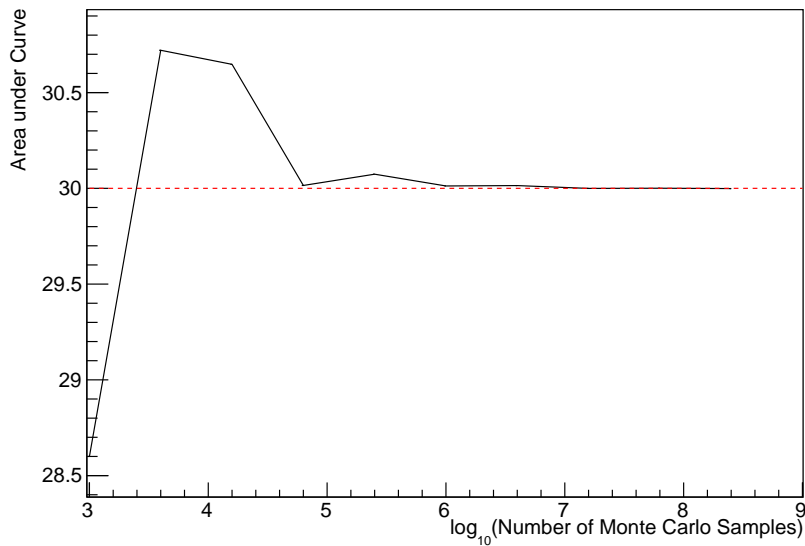


Figure 4.2: The area under a line of gradient 0.4 and intercept 1.0 for the range $0 \leq x \leq 10$ as calculated using Monte Carlo techniques as a function of the number of samples used in each repetition. The analytical solution to the area is 30 units as given by the red line.

1269 which has the property that the density of sampled points is proportional to the
 1270 probability density of that parameter. This means that the samples produced by
 1271 this technique are not statistically independent but they will cover the space
 1272 of the distribution.

1273 A Markov chain functions by selecting the position of step \vec{x}_{i+1} based on the
 1274 position of \vec{x}_i . The space in which the Markov chain selects samples is dependent
 1275 upon the total number of parameters utilised within the fit, where a discrete point
 1276 in this space is described by the N-dimensional space \vec{x} . In a perfectly operating
 1277 Markov chain, the position of the next step depends solely on the previous step
 1278 and not on the further history of the chain (\vec{x}_0, \vec{x}_1 , etc.). However, in solving
 1279 the multi-dimensionality of the fit used within this analysis, each step becomes
 1280 correlated with several of the steps preceding itself. Providing the MCMC chain is
 1281 well optimised, it will begin to converge towards a unique stationary distribution.
 1282 The period between the chain's initial starting point and the convergence to the
 1283 unique stationary distribution is colloquially known as the burn-in period. Once
 1284 the chain reaches the stationary distribution, all points sampled after that point

1285 will look like samples from that distribution.

1286 Further details of the theories underpinning MCMC techniques are discussed
1287 in [125] but can be summarised by the requirement that the chain satisfies the
1288 three ‘regularity conditions’:

- 1289 • Irreducibility: From every position in the parameter space \vec{x} , there must
1290 exist a non-zero probability for every other position in the parameter space
1291 to be reached.
- 1292 • Recurrence: Once the chain arrives at the stationary distribution, every step
1293 following from that position must be samples from the same stationary
1294 distribution.
- 1295 • Aperiodicity: The chain must not repeat the same sequence of steps at any
1296 point throughout the sampling period.

1297 The output of the chain after burn-in (i.e. the sampled points after the chain
1298 has reached the stationary distribution) can be used to approximate the posterior
1299 distribution and model parameters $\vec{\theta}$. To achieve the requirement that the unique
1300 stationary distribution found by the chain be the posterior distribution, one
1301 can use the Metropolis-Hastings algorithm. This guides the stochastic process
1302 depending on the likelihood of the current proposed step compared to that
1303 of the previous step.

1304 4.2.2 Metropolis-Hastings Algorithm

1305 As a requirement for MCMCs, the Markov chain implemented in this technique
1306 must have a unique stationary distribution that is equivalent to the posterior
1307 distribution. To ensure this requirement and that the regularity conditions are
1308 met, this analysis utilises the Metropolis-Hastings (MH) algorithm [131, 132].
1309 For the i^{th} step in the chain, the MH algorithm determines the position in the
1310 parameter space to which the chain moves to based on the current step, \vec{x}_i , and
1311 the proposed step, \vec{y}_{i+1} . The proposed step is randomly selected from some

1312 proposal function $f(\vec{x}_{i+1}|\vec{x}_i)$, which depends solely on the current step (ie. not
1313 the further history of the chain). The next step in the chain \vec{x}_{i+1} can be either the
1314 current step or the proposed step determined by whether the proposed step is
1315 accepted or rejected. To decide if the proposed step is selected, the acceptance
1316 probability, $\alpha(\vec{x}_i, \vec{y}_i)$, is calculated as

$$\alpha(\vec{x}_i, \vec{y}_{i+1}) = \min\left(1, \frac{P(\vec{y}_{i+1}|D)f(\vec{x}_i|\vec{y}_{i+1})}{P(\vec{x}_i|D)f(\vec{y}_{i+1}|\vec{x}_i)}\right). \quad (4.4)$$

1317 Where $P(\vec{y}_{i+1}|D)$ is the posterior distribution as introduced in section 4.1. To
1318 simplify this calculation, the proposal function is required to be symmetric such
1319 that $f(\vec{x}_i|\vec{y}_{i+1}) = f(\vec{y}_{i+1}|\vec{x}_i)$. In practice, a multi-variate Gaussian distribution
1320 centered on \vec{x}_i is used to throw parameter proposals. This reduces Equation 4.4 to

$$\alpha(\vec{x}_i, \vec{y}_{i+1}) = \min\left(1, \frac{P(\vec{y}_{i+1}|D)}{P(\vec{x}_i|D)}\right). \quad (4.5)$$

1321 After calculating this quantity, a random number, β , is generated uniformly
1322 between 0 and 1. If $\beta \leq \alpha(\vec{x}_i, \vec{y}_{i+1})$, the proposed step is accepted. Otherwise,
1323 the chain sets the next step equal to the current step. This procedure is repeated
1324 for subsequent steps. This can be interpreted as if the posterior probability
1325 of the proposed step is greater than that of the current step, ($P(\vec{y}_{i+1}|D) \geq$
1326 $P(\vec{x}_i|D)$), the proposed step will always be accepted. If the opposite is true,
1327 ($P(\vec{y}_{i+1}|D) \leq P(\vec{x}_i|D)$), the proposed step will be accepted with probability
1328 $P(\vec{x}_i|D)/P(\vec{y}_{i+1}|D)$. This ensures that the Markov chain does not get trapped
1329 in any local minima in the potentially non-Gaussian posterior distribution. The
1330 outcome of this technique is that the density of steps taken in a discrete region
1331 is directly proportional to the probability density in that region.

1332 4.2.3 MCMC Optimisation

1333 As discussed in subsection 4.2.2, the proposal function invoked within the MH
1334 algorithm can take any form and the chain will still converge to the stationary
1335 distribution. At each set of proposed parameter values, a prediction of the same
1336 spectra has to be generated which requires significant computational resources.

1337 Therefore, the number of steps taken before the unique stationary distribution
1338 is found should be minimised as only steps after convergence add information
1339 to the oscillation analysis. Furthermore, the chain should entirely cover the
1340 allowable parameter space to ensure that all values have been considered. Tuning
1341 the distance that the proposal function jumps between steps on a parameter-by-
1342 parameter basis can both minimise the length of the burn-in period and ensure
1343 that the correlation between step \vec{x}_i and \vec{x}_j is sufficiently small.

1344 The effect of changing the width of the proposal function is highlighted in
1345 Figure 4.3. Three scenarios, each with the same underlying stationary distribution
1346 (A Gaussian of width 1.0 and mean 0.), are presented. The only difference between
1347 the three scenarios is the width of the proposal function, colloquially known as
1348 the ‘step size σ ’. Each scenario starts at an initial parameter value of 10.0 which
1349 would be considered an extreme variation. For the case where $\sigma = 0.1$, it is
1350 clear to see that the chain takes a long time to reach the expected region of the
1351 parameter. This indicates that this chain would have a large burn-in period and
1352 does not converge to the stationary distribution until step ~ 500 . Furthermore,
1353 whilst the chain does move towards the expected region, each step is significantly
1354 correlated with the previous. Considering the case where $\sigma = 5.0$, the chain
1355 approaches the expected parameter region almost instantly meaning that the
1356 burn-in period is not significant. However, there are clearly large regions of steps
1357 where the chain does not move. This is likely due to the chain proposing steps
1358 in the tails of the distribution which have a low probability of being accepted.
1359 Consequently, this chain would take a significant number of steps to fully span
1360 the allowable parameter region. For the final scenario, where $\sigma = 0.5$, you can
1361 see a relatively small burn-in period of approximately 100 steps. Once the chain
1362 reaches the stationary distribution, it moves throughout the expected region of
1363 parameter values many times, sufficiently sampling the full parameter region.
1364 This example is a single parameter varying across a continuous distribution and
1365 does not fully reflect the difficulties in the many-hundred multi-variate parameter

1366 distribution used within this analysis. However, it does give a conceptual idea of
1367 the importance of selecting the proposal function and associated step size.

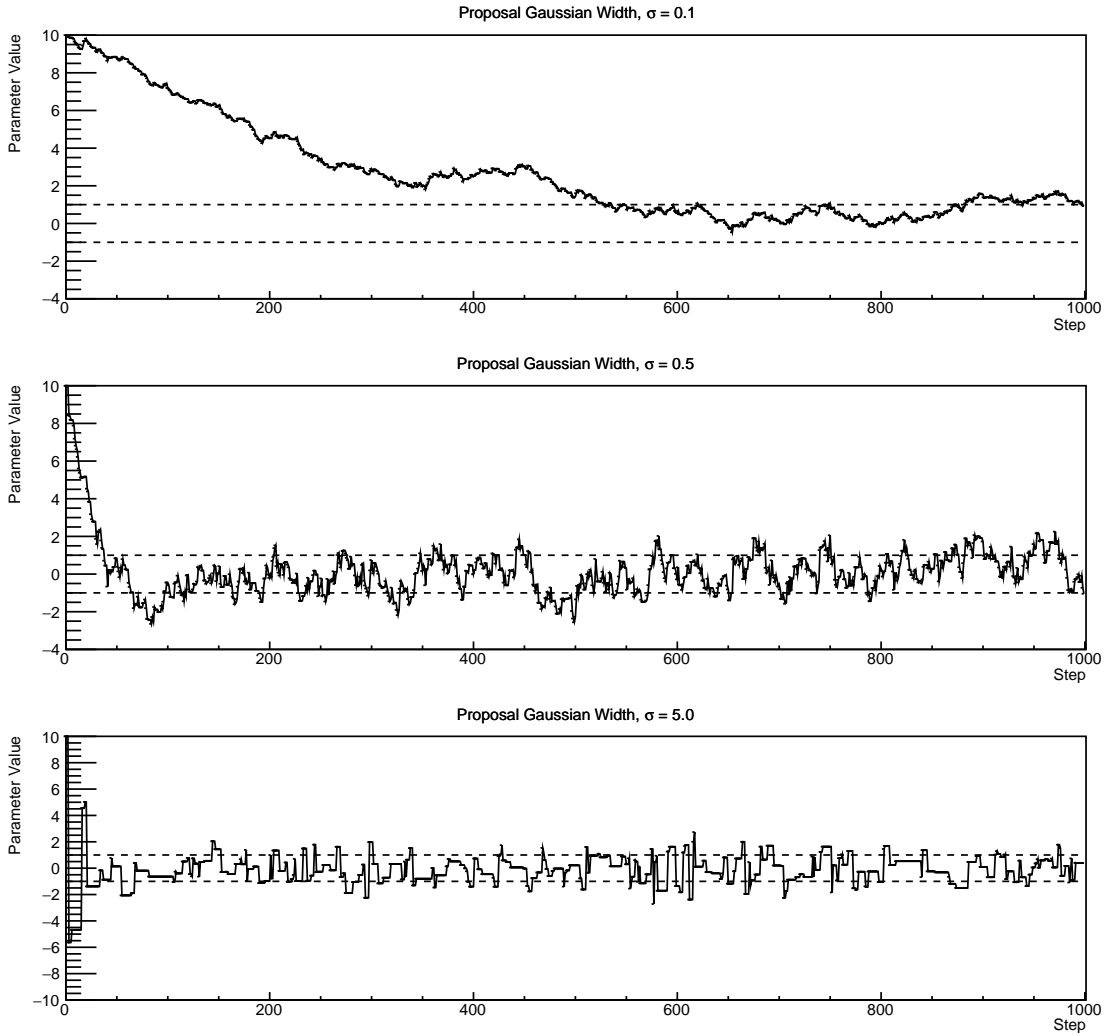


Figure 4.3: Three MCMC chains, each with a stationary distribution equal to a Gaussian centered at 0 and width 1 (As indicated by the black dotted lines). All of the chains use a Gaussian proposal function but have different widths (or ‘step size σ ’). The top panel has $\sigma = 0.1$, middle panel has $\sigma = 0.5$ and the bottom panel has $\sigma = 5.0$.

1368 As discussed, step size tuning directly correlates to the average step accep-
1369 tance rate. If the step size is too small, many steps will be accepted but the
1370 chain moves slowly. If the opposite is true, many steps will be rejected as the
1371 chain proposes steps in the tails of the distribution. Discussion in [133] suggests
1372 that the ‘ideal’ acceptance rate of a high dimension MCMC chain should be

1373 approximately $\sim 25\%$. An “ideal” step size [133] of

$$\sigma = \frac{2.4}{N_p}, \quad (4.6)$$

1374 where N_p is the number of parameters included in the MCMC fit. However,
1375 the complex correlations between systematics mean that some parameters have
1376 to be hand-tuned and many efforts have been taken to select a set of parameter-
1377 by-parameter step sizes to approximately reach the ideal acceptance rate.

1378 Figure 4.4 highlights the likelihood as calculated by the fit in subsection 8.3.4
1379 as a function of the number of steps in each chain. In practice, many independent
1380 MCMC chains are run simultaneously to parallelise the task of performing the
1381 fit. This figure overlays the distribution found in each chain. As seen, the
1382 likelihood decreases from its initial value and converges towards a stationary
1383 distribution after $\sim 1 \times 10^5$ steps.

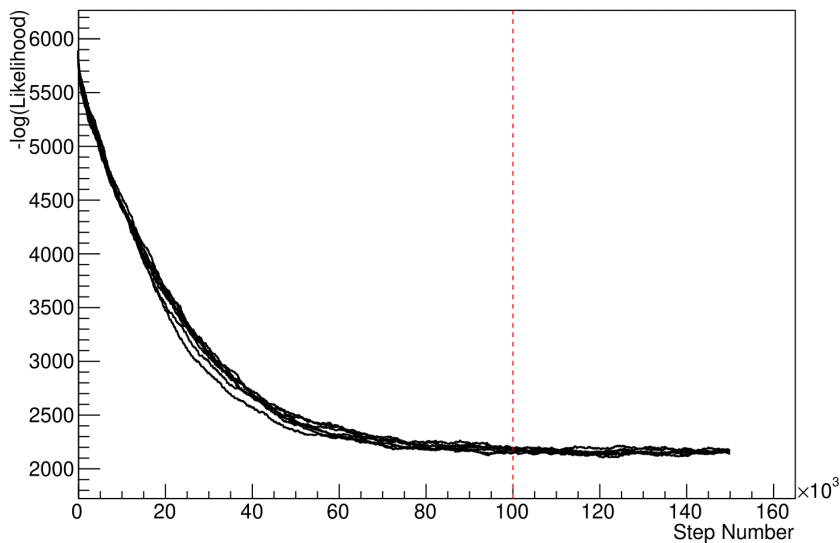


Figure 4.4: The log-likelihood from the fit detailed in subsection 8.3.4 as a function of the number of steps accumulated in each fit. Many independent MCMC chains were run in parallel and overlaid on this plot. The red line indicates the 1×10^5 step burn-in period after which the log-likelihood becomes stable.

1384 Multiple configurations of this analysis have been performed throughout this
1385 thesis where different samples or systematics have been used. For all of these con-
1386 figurations, it was found that a burnin period of 1×10^5 was sufficient in all cases.

1387 4.3 Understanding the MCMC Results

1388 The previous sections have described how to generate the posterior probability
1389 distribution using Bayesian MCMC techniques. However, this analysis focuses
1390 on oscillation parameter determination. The posterior distribution output from
1391 the chain is a high-dimension object, with as many dimensions as there are
1392 parameters included in the oscillation analysis. However, this multi-dimensional
1393 object is difficult to conceptualize so parameter estimations are often presented
1394 in one or two-dimensional projections of this probability distribution. To do
1395 this, marginalisation techniques are invoked.

1396 4.3.1 Marginalisation

1397 The output of the MCMC chain is a highly dimensional probability distribution
1398 which is very difficult to interpret. From the standpoint of an oscillation analysis
1399 experiment, the one or two-dimensional ‘projections’ of the oscillation parameters
1400 of interest are most relevant. Despite this, the best fit values and uncertainties on
1401 the oscillation parameters of interest should correctly encapsulate the correlations
1402 to the other systematic uncertainties (colloquially called ‘nuisance’ parameters).
1403 For this joint beam and atmospheric analysis, the oscillation parameters of
1404 interest are $\sin^2(\theta_{23})$, $\sin^2(\theta_{13})$, Δm_{32}^2 , and δ_{CP} . All other parameters (includ-
1405 ing the oscillation parameters this fit is insensitive to) are deemed nuisance
1406 parameters. To generate these projections, the posterior distribution is integrated
1407 over all nuisance parameters. This is called marginalisation. This technique
1408 also explains why it is acceptable to neglect the normalisation constant of the
1409 posterior distribution, which was discussed in section 4.1.

1410 A simple example of the marginalisation technique is to imagine the scenario
1411 where two coins are flipped. To determine the probability that the first coin
1412 returned a ‘head’, the exact result of the second coin flip is disregarded and
1413 simply integrated over. For the parameters of interest, $\vec{\theta}_i$, the marginalised

¹⁴¹⁴ posterior is calculated by integrating over the nuisance parameters, $\vec{\theta}_n$. In this
¹⁴¹⁵ case, Equation 4.2 becomes

$$P(\vec{\theta}_i|D) = \frac{\int P(D|\vec{\theta}_i, \vec{\theta}_n)P(\vec{\theta}_i, \vec{\theta}_n)d\vec{\theta}_n}{\int P(D|\vec{\theta})P(\vec{\theta})d\vec{\theta}}. \quad (4.7)$$

¹⁴¹⁶ Where $P(\vec{\theta}_i, \vec{\theta}_n)$ encodes the prior knowledge about the uncertainty and
¹⁴¹⁷ correlations between the parameters of interest and the nuisance parameters.
¹⁴¹⁸ In practice, this is simply taking the one or two-dimensional projection of the
¹⁴¹⁹ multi-dimensional probability distribution.

¹⁴²⁰ While in principle an easy solution to a complex problem, correlations be-
¹⁴²¹ tween the interesting and nuisance parameters can bias the marginalised results.
¹⁴²² A similar effect is found when the parameters being marginalised over have
¹⁴²³ non-Gaussian probability distributions. For example, Figure 4.5 highlights the
¹⁴²⁴ marginalisation bias in the probability distribution found for a parameter when
¹⁴²⁵ requiring a correlated parameter to have a positive parameter value. Due to
¹⁴²⁶ the complex nature of the oscillation parameter fit presented in this thesis, there
¹⁴²⁷ are correlations occurring between the oscillation parameters of interest and the
¹⁴²⁸ other nuisance parameters included in the fit.

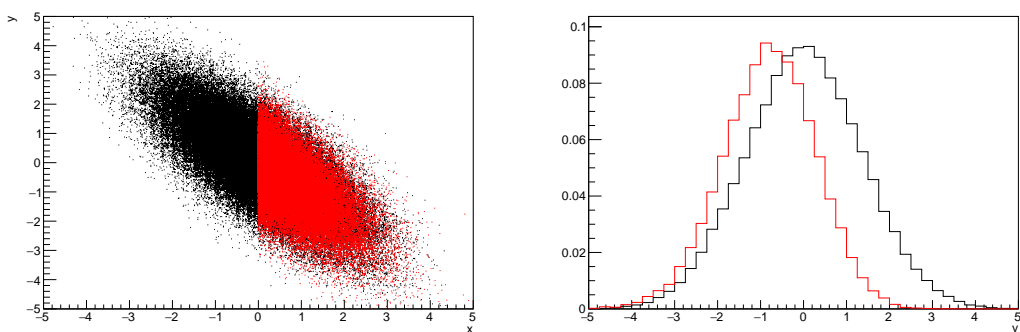


Figure 4.5: Left: The two-dimensional probability distribution for two correlated parameters x and y . The red distribution shows the two-dimensional probability distribution when $0 \leq x \leq 5$. Right: The marginalised probability distribution for the y parameter found when requiring the x to be bound between $-5 \leq x \leq 5$ and $0 \leq x \leq 5$ for the black and red distribution, respectively.

4.3.2 Parameter Estimation and Credible Intervals

The purpose of this analysis is to determine the best fit values for the oscillation parameters that the beam and atmospheric samples are sensitive to: $\sin^2(\theta_{23})$, $\sin^2(\theta_{13})$, Δm_{32}^2 , and δ_{CP} . The posterior probability density, taken from the output MCMC chain, is binned in these parameters. The parameter best-fit point is then taken to be the value that has the highest posterior probability. This is performed in both one and two-dimensional projections.

However, the single best-fit point in a given parameter is not of much use on its own. The uncertainty on the best-fit point must also be presented using credible intervals. The definition of the 1σ credible interval is that there is 68% belief that the parameter is within those bounds. For a more generalised definition, the credible interval is the region, R , of the posterior distribution that contains a specific fraction of the total probability, such that

$$\int_R P(\theta|D)d\theta = \alpha. \quad (4.8)$$

Where θ is the parameter being evaluated. This technique then calculates the $\alpha \times 100\%$ credible interval.

In practice, this analysis uses the highest posterior density (HPD) credible intervals which are calculated through the following method. First, the probability distribution is area-normalised such that it has an integrated area equal to 1.0. The bins of probability are then summed from the highest to lowest until the sum exceeds the 1σ level (0.68 in this example). This process is repeated for a range of credible intervals, notably the 1σ , 2σ and 3σ along with other levels where the critical values for each level can be found in [76]. This process can be repeated for the two-dimensional probability distributions by creating two-dimensional contours of credible intervals rather than a one-dimensional result.

1453 4.3.3 Bayesian Model Comparisons

1454 Due to the matter resonance, this analysis has some sensitivity to the mass
 1455 hierarchy of neutrino states (whether Δm_{32}^2 is positive or negative) and the
 1456 octant of $\sin^2(\theta_{23})$. The Bayesian approach utilised within this analysis gives an
 1457 intuitive method of model comparison by determining which hypothesis is most
 1458 favourable. Taking the ratio of Equation 4.3 for the two hypotheses of normal
 1459 hierarchy, NH , and inverted hierarchy, IH , gives

$$\frac{P(\vec{\theta}_{NH}|D)}{P(\vec{\theta}_{IH}|D)} = \frac{P(D|\vec{\theta}_{NH})}{P(D|\vec{\theta}_{IH})} \times \frac{P(\vec{\theta}_{NH})}{P(\vec{\theta}_{IH})}. \quad (4.9)$$

1460 The middle term defines the Bayes factor, $B(NH/IH)$, which is a data-driven
 1461 interpretation of how strong the data prefers one hierarchy to the other. For this
 1462 analysis, equal priors on both mass hierarchy hypotheses are chosen ($P(\vec{\theta}_{NH}) =$
 1463 $P(\vec{\theta}_{IH}) = 0.5$). In practice, the MCMC chain proposes a value of $|\Delta m_{32}^2|$ and
 1464 then applies a 50% probability that the value is sign flipped. Consequently,
 1465 the Bayes factor can be calculated from the ratio of the probability density in
 1466 either hypothesis. This equates to counting the number of steps taken in the
 1467 normal and inverted hierarchies and taking the ratio. The same approach can be
 1468 taken to compare the upper octant (UO) compared to the lower octant (LO)
 1469 hypothesis of $\sin^2(\theta_{23})$.

$\log_{10}(B_{AB})$	B_{AB}	Strength of Preference
< 0.0	< 1	No preference for hypothesis A (Supports hypothesis B)
0.0 – 0.5	1.0 – 3.16	Preference for hypothesis A is weak
0.5 – 1.0	3.16 – 10.0	Preference for hypothesis A is substantial
1.0 – 1.5	10.0 – 31.6	Preference for hypothesis A is strong
1.5 – 2.0	31.6 – 100.0	Preference for hypothesis A is very strong
> 2.0	> 100.0	Decisive preference for hypothesis A

Table 4.1: Jeffreys scale for strength of preference for two models A and B as a function of the calculated Bayes factor ($B_{AB} = B(A/B)$) between the two models [134]. The original scale is given in terms of $\log_{10}(B(A/B))$ but converted to linear scale for easy comparison throughout this thesis.

1470 Whilst the value of the Bayes factor should always be shown, the Jeffreys scale
 1471 [134] (highlighted in Table 4.1) gives an indication of the strength of preference

¹⁴⁷² for one model compared to the other. Other interpretations of the strength of
¹⁴⁷³ preference of a model exist, e.g. the Kass and Raferty Scale [135].

¹⁴⁷⁴ 4.3.4 Comparison of MCMC Output to Expectation

¹⁴⁷⁵ To ensure the fit is performing well, a best-fit spectrum is produced using the
¹⁴⁷⁶ posterior probability distribution and compared with the data, allowing easy
¹⁴⁷⁷ by-eye comparisons to be made. A simple method of doing this is to perform a
¹⁴⁷⁸ comparison in the fitting parameters (e.g. the reconstructed neutrino energy for
¹⁴⁷⁹ T2K far detector beam samples) of the spectra generated by the MCMC chain to
¹⁴⁸⁰ ‘data’. This ‘data’ could be true data or some variation of Monte Carlo prediction.
¹⁴⁸¹ This allows easy comparison of the MCMC probability distribution to the data. To
¹⁴⁸² perform this, N steps from the post-burnin MCMC chain are randomly selected.
¹⁴⁸³ From these, the Monte Carlo prediction at each step is generated by reweighting
¹⁴⁸⁴ the model parameters to the values specified at that step. Due to the probability
¹⁴⁸⁵ density being directly correlated with the density of steps in a certain region,
¹⁴⁸⁶ parameter values close to the best fit value are most likely to be selected.

¹⁴⁸⁷ In practice, for each bin of the fitting parameters has a probability distribution
¹⁴⁸⁸ of event rates, with one entry per sampled MCMC step. This distribution is
¹⁴⁸⁹ binned where the bin with the highest probability is selected as the mean and an
¹⁴⁹⁰ error on the width of this probability distribution is calculated using the approach
¹⁴⁹¹ highlighted in subsection 4.3.2. Consequently, the best fit distribution in the fit
¹⁴⁹² parameter is not necessarily that which would be attained by reweighting the
¹⁴⁹³ Monte Carlo prediction to the most probable parameter values.

¹⁴⁹⁴ A similar study can be performed to illustrate the freedom of the model
¹⁴⁹⁵ parameter space prior to the fit. This can be done by throwing parameter values
¹⁴⁹⁶ from the prior uncertainty of each parameter.

5

1497

1498

1499

Simulation, Reconstruction, and Event Reduction

1500 As a crucial part of the oscillation analysis, an accurate prediction of the expected
1501 neutrino spectrum at the far detector is required. This includes modeling the
1502 flux generation, neutrino interactions, and detector effects. All of the simulation
1503 packages required to do this are briefly described in section 5.1. The reconstruc-
1504 tion of neutrino events in the far detector, including the `fitQun` algorithm, is
1505 documented in section 5.2. This also includes data quality checks of the SK-V
1506 data which the author performed for the T2K oscillation analysis presented at the
1507 Neutrino 2020 conference [2]. Finally, section 5.3 describes the steps taken in the
1508 SK detector to trigger on events of interest whilst removing the comparatively
1509 large rate of cosmic ray muon events.

1510 5.1 Simulation

1511 In order to generate a Monte Carlo prediction of the expected event rate at
1512 the far detector, all the processes in the beam and atmospheric fluxes, neutrino
1513 interaction, and detector need to be modeled.

5.1.1 Neutrino Flux

The beamline simulation consists of three distinct parts: the initial hadron interaction modeled by FLUKA [136], the target station geometry and particle tracking performed by JNUBEAM, [41, 137] and any hadronic re-interactions simulated by GCALOR [138]. The primary hadronic interactions are $O(10)\text{GeV}$, where FLUKA matches external cross-section data better than GCALOR [139]. However, FLUKA is not very adaptable so a small simulation is built to model the interactions in the target and the output is then passed to JNUBEAM and GCALOR for propagation. The hadronic interactions are tuned to data from the NA61/SHINE [140–142] and HARP [143] experiments. The tuning is done by reweighting the FLUKA and GCALOR predictions to match the external data multiplicity and cross-section measurements, based on final state particle kinematics [139]. The culmination of this simulation package generates the predicted flux for neutrino and antineutrino beam modes which are illustrated in Figure 3.7.

The atmospheric neutrino flux is simulated by the HKKM model [53, 55]. The primary cosmic ray flux is tuned to AMS [144] and BESS [145] data assuming the US-standard atmosphere '76 [146] density profile and includes geomagnetic field effects. The primary cosmic rays interact to generate pions and muons. The interaction of these secondary particles to generate neutrinos is handled by DPMJET-III [147] for energies above 32GeV and JAM [55, 148] for energies below that value [51]. These hadronic interactions are tuned to BESS and L3 data [149, 150] using the same methodology as the tuning of the beamline simulation. The energy and cosine zenith predictions of $\nu_e, \bar{\nu}_e, \nu_\mu, \bar{\nu}_\mu$ flux are given in Figure 2.3 and Figure 2.5, respectively. The flux is approximately symmetrical and peaked around the horizon ($\cos(\theta_Z) = 0.0$). This is because horizontally-going pions and kaons can travel further than their vertically-going counterparts resulting in a larger probability of decaying to neutrinos. The symmetry is broken in lower-energy neutrinos due to geomagnetic effects, which modify the track of the primary cosmic rays. Updates to the HKKM model are currently ongoing [151].

1543 5.1.2 Neutrino Interaction

1544 Once a flux prediction has been made for all three detectors, NEUT 5.4.0 [152, 153]
 1545 models the interactions of the neutrinos in the detectors. For the purposes of this
 1546 analysis, quasi-elastic (QE), meson exchange (MEC), single meson production
 1547 (PROD), coherent pion production (COH), and deep inelastic scattering (DIS)
 1548 interactions are simulated. These interaction categories can be further broken
 1549 down by whether they were propagated via a W^\pm boson in Charged Current
 1550 (CC) interactions or via a Z^0 boson in Neutral Current (NC) interactions. CC
 1551 interactions have a charged lepton in the final state, which can be flavour-tagged
 1552 in reconstruction to determine the flavour of the neutrino. In contrast, NC
 1553 interactions have a neutrino in the final state so no flavour information can be
 1554 determined from the observables left in the detector after an interaction. This
 1555 is the reason why neutrinos that interact through NC modes are assumed to
 1556 not oscillate within this analysis. Both CC and NC interactions are modeled
 1557 for all the above interaction categories, other than MEC interactions which are
 1558 only modeled for CC events.

1559 As illustrated in Figure 5.1, CCQE interactions dominate the cross-section of
 1560 neutrino interactions around $E_\nu \sim 0.5\text{GeV}$. The NEUT implementation adopts
 1561 the Llewellyn Smith [154] model for neutrino-nucleus interactions, where the
 1562 nuclear ground state of any bound nucleons (neutrino-oxygen interactions) is
 1563 approximated by a spectral-function [155] model that simulates the effects of
 1564 Fermi momentum and Pauli blocking. The cross-section of QE interactions is
 1565 controlled by vector and axial-vector form factors parameterised by the BBBA05
 1566 [156] model and a dipole form factor with $M_A^{QE} = 1.21\text{GeV}$ fit to external data
 1567 [157], respectively. NEUT implements the Valencia [158] model to simulate MEC
 1568 events, where two nucleons and two holes in the nuclear target are produced
 1569 (often called 2p2h interactions).

1570 For neutrinos of energy $O(1)\text{GeV}$, PROD interactions become dominant.
 1571 These predominantly produce charged and neutral pions although γ , kaon,

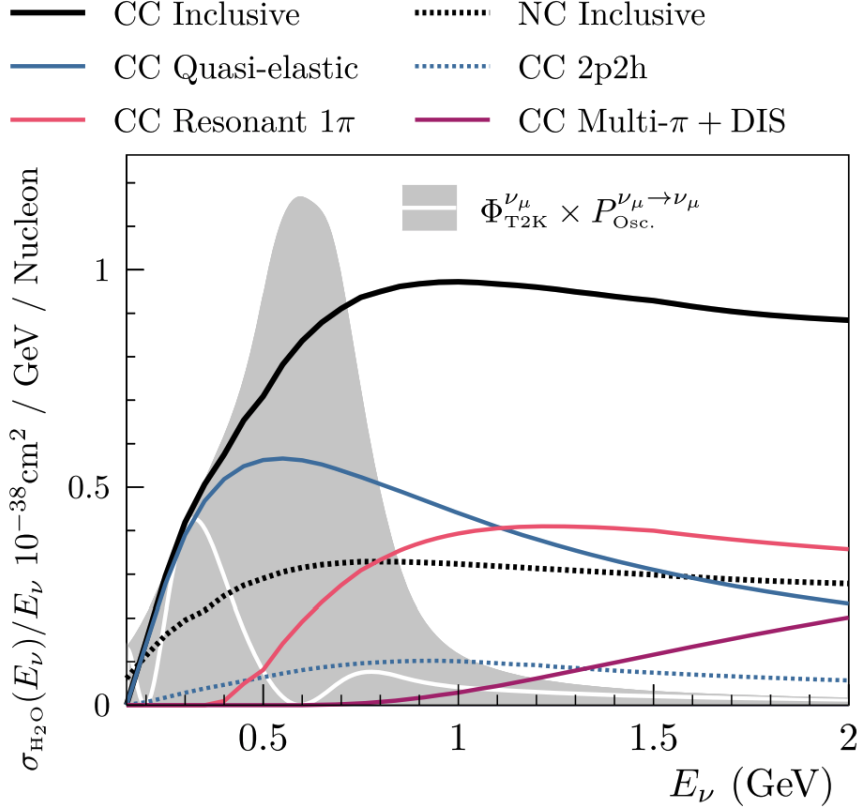


Figure 5.1: The NEUT prediction of the ν_μ -H₂O cross-section overlaid on the T2K ν_μ flux. The charged current (black, solid) and neutral current (black, dashed) inclusive, charged current quasi-elastic (blue, solid), charged current 2p2h (blue, dashed), charged current single pion production (pink), and charged current multi- π and DIS (Purple) cross-sections are illustrated. Figure taken from [152].

and η production is also considered. To simulate these interactions, the Berger-Sehgal [159] model is implemented within NEUT. It simulates the excitation of a nucleon from a neutrino interaction, production of an intermediate baryon, and the subsequent decay to a single meson or γ . Pions can also be produced through COH interactions, which occur when the incoming neutrino interacts with the entire oxygen nucleus leaving a single pion outside of the nucleus. NEUT utilises the Berger-Sehgal [160] model to simulate these COH interactions.

DIS and multi- π producing interactions become the most dominant for energies $> O(5)$ GeV. PYTHIA [161] is used to simulate any interaction with invariant mass $W > 2\text{GeV}/c^2$, which produces at least one meson. For any interaction which produces at least two mesons but has $W < 2\text{GeV}/c^2$, the

₁₅₈₃ Bronner model is used [162]. Both of these models use Parton distribution
₁₅₈₄ functions based on the Bodek-Yang model [163–165].

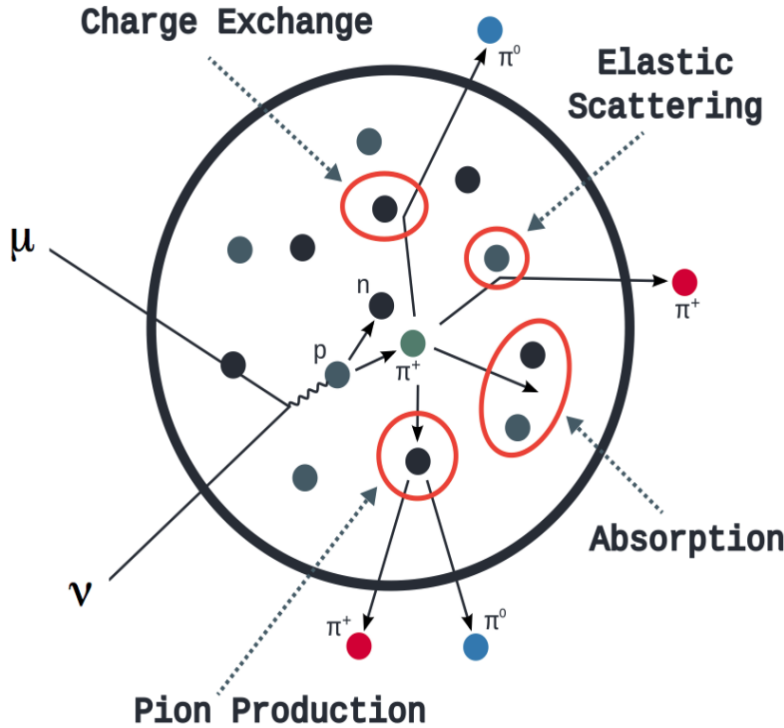


Figure 5.2: Illustration of the various processes which a pion can undergo before exiting the nucleus. Taken from [166].

₁₅₈₅ Any pion that is produced within the nucleus can re-interact through final
₁₅₈₆ state interactions before it exits, as illustrated by the scattering, absorption,
₁₅₈₇ production, and exchange interactions in Figure 5.2. These re-interactions alter
₁₅₈₈ the observable particles within the detector. For instance, if the charged pion
₁₅₈₉ from a CC PROD interaction is absorbed, the observables would mimic a CC QE
₁₅₉₀ interaction. To simulate these effects, NEUT uses a semi-classical intranuclear
₁₅₉₁ cascade model [152]. This cascade functions by stepping the pion through the
₁₅₉₂ nucleus in fixed-length steps equivalent to $dx = R_N/100$, where R_N is the radius
₁₅₉₃ of the nucleus. At each step, the simulation allows the pion to interact through
₁₅₉₄ scattering, charged exchange, absorption, or production with an interaction-
₁₅₉₅ dependent probability calculated from a fit to external data [167]. This cascade
₁₅₉₆ continues until the pion is absorbed or exits the nucleus.

1597 5.1.3 Detector

1598 Once the final state particle kinematics have been determined by NEUT, they
1599 are passed into the detector simulation. The near detectors, ND280 and INGRID,
1600 are simulated using a GEANT4 package [45, 168] to simulate the detector geom-
1601 etry, particle tracking, and energy deposition. The response of the detectors is
1602 simulated using the elecSim package [45].

1603 The far detector simulation is based upon the original Kamiokande experi-
1604 ment software which uses the GEANT3-based SKDETSIM [45, 169] package. This
1605 simulates the interactions of particles in the water as well as Cherenkov light
1606 production. The water quality and PMT calibration measurements detailed in
1607 subsection 3.1.2 are also used within this simulation to make accurate predictions
1608 of the detector response.

1609 Any event which generates optical photons that occurs in SK will be observed
1610 by the PMT array, where each PMT records the time and accumulated charge.
1611 This recorded information is shown in event displays similar to those illustrated
1612 in Figure 5.3 for simulated Monte Carlo events. To be useful for physics analyses,
1613 this series of PMT hit information needs to be reconstructed to determine the
1614 number and identity of particles and their kinematics (or track parameters): four-
1615 vertex, direction, and momentum. The reconstruction uses the fact that the charge
1616 and timing distribution of photons generated by a particular particle in an event is
1617 dependent upon its initial kinematics. Electron and muon rings are distinguished
1618 by their “fuzziness”. Muons are heavier and less affected by scattering or
1619 showering meaning they typically produce “crisp” rings. Electrons are more
1620 likely to interact via electromagnetic showering or scattering which results in
1621 larger variations of their direction from the initial direction. Consequently,
1622 electrons typically produce “fuzzier” rings compared to muons.

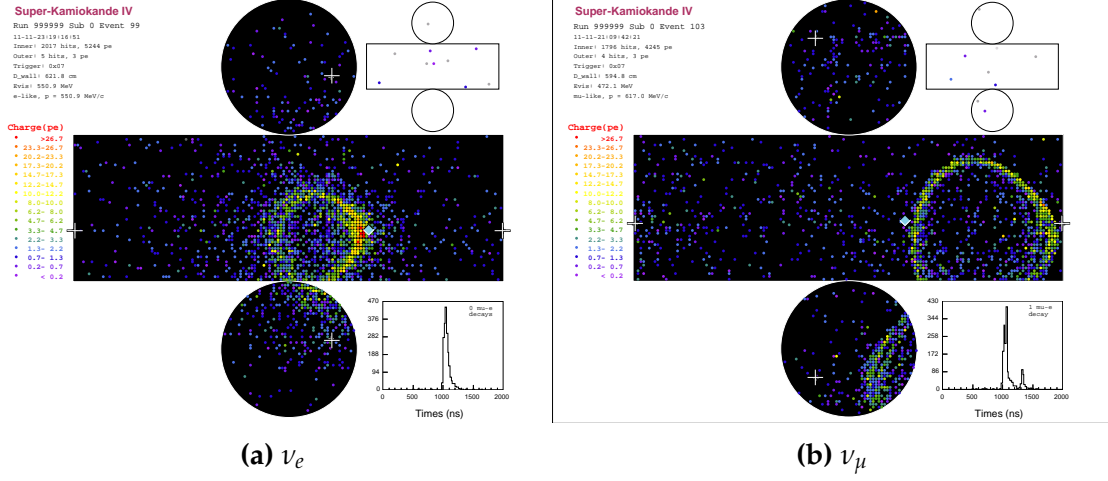


Figure 5.3: Event displays from Monte Carlo simulation at Super Kamiokande illustrating the “crisp” ring from a muon and the typically “fuzzy” electron ring. Each pixel represents a PMT and the color scheme denotes the accumulated charge deposited on that PMT. Figures taken from [170].

5.2 Event Reconstruction at SK

For the purposes of this analysis, the `fitQun` reconstruction algorithm [171] is utilised. Its core function is to compare a prediction of the accumulated charged and timing distribution from each PMT, generated for a particular particle identity and track parameters, to that observed in the neutrino event. It determines the preferred values by maximising a likelihood function (or minimising a log-likelihood function) which includes information from PMTs which were hit and those that were not hit. The `fitQun` algorithm is based on the key concepts of the MiniBooNE reconstruction algorithm [172].

The `fitQun` algorithm improves upon the previous `APFit` algorithm [173] which has been used for many previous SK analyses. `APFit` fits the vertex from timing information and then fits the direction of the particle from PMT hits within a 43 deg Cherenkov cone (assuming an ultra-relativistic particle) using a fitting estimator. A Hough transformation is used to find the radius of a ring (related to the momentum through Equation 3.2) as well as the number of rings contained within the event. The analysis presented here uses the `fitQun` algorithm as it improves both the accuracy of the fit parameters and the rejection of neutral

1640 current π^0 events as compared to APFit [174, 175].

1641 Any event in SK can consist of prompt (or primary) and decay (or secondary)
1642 particles. For example, a charged current muon neutrino interaction can gen-
1643 erate two particles that have the potential of generating Cherenkov photons
1644 (assuming the proton is below the Cherenkov threshold): the prompt muon,
1645 and the secondary decay-electron from the muon, approximately $2\mu\text{s}$ later. To
1646 reconstruct all particles within an event, it is divided into time clusters which are
1647 called “subevents”. Subevents after the primary subevent are considered to
1648 be decay electrons.

1649 The main steps of the `fitQun` reconstruction algorithm are:

- 1650 • **Vertex pre-fitting:** An estimate of the vertex is made using a goodness-of-fit
1651 metric based on PMT hit times
- 1652 • **Peak finding:** The initial time of each subevent is determined by clustering
1653 events by time residuals
- 1654 • **Single-ring fits:** Given the pre-fit vertex and estimated time of interaction,
1655 a maximum likelihood technique searches for a single particle generating
1656 light. Electron, muon, charged pion, and proton hypotheses are considered
- 1657 • **Multi-ring fits:** Seeded from the single-ring fits, hypotheses with multiple
1658 light-producing particles are considered using the same maximum likeli-
1659 hood technique. Electron-like or charged pion-like rings are added until
1660 the likelihood stops improving

1661 To find all the subevents in an event, a vertex goodness metric is calculated
1662 for some vertex position \vec{x} and time t ,

$$G(\vec{x}, t) = \sum_i^{\text{hit PMTs}} \exp \left(-\frac{1}{2} \left(\frac{T_{Res}^i(\vec{x}, t)}{\sigma} \right)^2 \right), \quad (5.1)$$

1663 where

$$T_{Res}^i(\vec{x}, t) = t^i - t - |R_{PMT}^i - \vec{x}| / c_n, \quad (5.2)$$

1664 is the residual hit time. It is the difference in time between the PMT hit time
 1665 t^i , of the i^{th} PMT, and the expected time of the PMT hit if the photon was at
 1666 the vertex. R_{PMT}^i is the position of the i^{th} PMT, c_n is the speed of light in water
 1667 and $\sigma = 4\text{ns}$ which is comparable to the time resolution of the PMT. When the
 1668 proposed fit values of time and vertex are close to the true values, $T_{Res}^i(\vec{x}, t)$ tends
 1669 to zero resulting in subevents appearing as spikes in the goodness metric. The
 1670 proposed fit vertex and time are grid-scanned, and the values which maximise
 1671 the goodness metric are selected as the “pre-fit vertex”. Whilst this predicts a
 1672 vertex for use in the clustering algorithm, the final vertex is fit using the higher-
 1673 precision maximum likelihood method described below.

1674 Once the pre-fit vertex has been determined, the goodness metric is scanned as
 1675 a function of t to determine the number of subevents. A peak-finding algorithm
 1676 is then used on the goodness metric, requiring the goodness metric to exceed
 1677 some threshold and drop below a reduced threshold before any subsequent
 1678 additional peaks are considered. The thresholds are set such that the rate of
 1679 false peak finding is minimised while still attaining good data to Monte Carlo
 1680 agreement. To improve performance, the pre-fit vertex for each delayed subevent
 1681 is re-calculated after PMT hits from the previous subevent are masked. This
 1682 improves the decay-electron tagging performance. Once all subevents have
 1683 been determined, the time window around each subevent is then defined by the
 1684 earliest and latest time which satisfies $-180 < T_{Res}^i < 800\text{ns}$. The subevents and
 1685 associated time windows are then used as seeds for further reconstruction.

1686 For a given subevent, the `fitQun` algorithm constructs a likelihood based on
 1687 the accumulated charge q_i and time information t_i from the i^{th} PMT,

$$L(\Gamma, \vec{\theta}) = \prod_j^{\text{unhit}} P_j(\text{unhit}|\Gamma, \vec{\theta}) \prod_i^{\text{hit}} \{1 - P_i(\text{unhit}|\Gamma, \vec{\theta})\} f_q(q_i|\Gamma, \vec{\theta}) f_t(t_i|\Gamma, \vec{\theta}). \quad (5.3)$$

1688 Where $\vec{\theta}$ defines the track parameters; vertex position, direction vector and
 1689 momenta, and Γ represents the particle hypothesis. $P_i(\text{unhit}|\Gamma, \vec{\theta})$ is the proba-
 1690 bility of the i^{th} tube to not register a hit given the track parameters and particle
 1691 hypothesis. The charge likelihood, $f_q(q_i|\Gamma, \vec{\theta})$, and time likelihood, $f_t(t_i|\Gamma, \vec{\theta})$,
 1692 represents the probability density function of observing charge q_i and time t_i on
 1693 the i^{th} PMT given the specified track parameters and particle hypothesis.

1694 The predicted charge is calculated based on contributions from both the
 1695 direct light and the scattered light. The direct light contribution is determined
 1696 based on the integration of the Cherenkov photon profile along the track. PMT
 1697 angular acceptance, water quality, and calibration measurements discussed in
 1698 subsection 3.1.2 are included to accurately predict the charge probability density
 1699 at each PMT. The scattered and reflected light is calculated in a similar way,
 1700 although it includes a scattering function that depends on the vertex of the
 1701 particle and the position of the PMT. The charge likelihood is calculated by
 1702 comparing the prediction to the observed charge in the PMT which is tuned
 1703 to the PMT simulation.

1704 The time likelihood is approximated to depend on the vertex \vec{x} , direction \vec{d} ,
 1705 and time t of the track as well as the particle hypothesis. The expected time
 1706 for PMT hits is calculated by assuming unscattered photons being emitted from
 1707 the midpoint of the track, S_{mid} ,

$$t_{\text{exp}}^i = t + S_{\text{mid}}/c + |R_{\text{PMT}}^i - \vec{x} - S_{\text{mid}}\vec{d}|/c_n, \quad (5.4)$$

1708 where c is the speed of light in a vacuum. The time likelihood is then expressed
 1709 in terms of the residual difference between the PMT hit time and the expected
 1710 hit time, $t_{\text{Res}}^i = t^i - t_{\text{exp}}^i$. The particle hypothesis and momentum also affect the
 1711 Cherenkov photon distribution. These parameters modify the shape of the time
 1712 likelihood density since in reality not all photons are emitted at the midpoint of
 1713 the track. As with the charge likelihood, the contributions from both the direct
 1714 and scattered light to the time likelihood density are calculated separately, which
 1715 are both calculated from particle gun Monte Carlo studies.

The track parameters and particle identity which maximise $L(\Gamma, \vec{\theta})$ are defined as the best-fit parameters. In practice MINUIT [176] is used to minimise the value of $-\ln L(\Gamma, \vec{\theta})$. The `fiTQun` algorithm considers an electron-like, muon-like, and charged pion-like hypothesis for events with a single final state particle, denoted “single-ring events”. The particle’s identity is determined by taking the ratio of the likelihood of each of the hypotheses. For instance, electrons and muons are distinguished by considering the value of $\ln(L(e, \vec{\theta}_e)/L(\mu, \vec{\theta}_\mu))$ in comparison to the reconstructed momentum of the electron hypothesis, as illustrated by Figure 5.4. The coefficients of the discriminator between electron-like and muon-like events are determined from Monte Carlo studies [171]. Similar distributions exist for distinguishing electron-like events from π^0 -like events, and muon-like events from pion-like events. The cuts are defined as,

$$\begin{aligned} \text{Electron/Muon} : & \ln(L_e/L_\mu) > 0.2 \times p_e^{rec} [\text{MeV}], \\ \text{Electron}/\pi^0 : & \ln(L_e/L_{\pi^0}) < 175 - 0.875 \times m_{\gamma\gamma} [\text{MeV}], \\ \text{Muon/Pion} : & \ln(L_\mu/L_{\pi^\pm}) < 0.15 \times p_\mu^{rec} [\text{MeV}], \end{aligned} \quad (5.5)$$

as taken from [177], where p_e^{rec} and p_μ^{rec} are the reconstructed momentum of the single-ring electron and muon fits, respectively. $m_{\gamma\gamma}$ represents the reconstructed invariant mass of the two photons emitted from π^0 decay. Typically, the distance between a particular entry in these two-dimensional distributions and the cut-line is termed the PID parameter and is illustrated in Figure 5.5.

The `fiTQun` algorithm also considers a π^0 hypothesis. To do this, it performs a fit looking for two standard electron-hypothesis tracks which point to the same four-vertex. This assumes the electron tracks are generated from photon-conversion so the electron tracks actually appear offset from the proposed π^0 vertex. For these fits, the conversion length, direction, and momentum of each photon are also considered as track parameters which are then fit in the same methodology as the standard single-ring hypotheses.

Whilst lower energy events are predominantly single-ring events, higher energy neutrino events can generate final states with multiple particles which

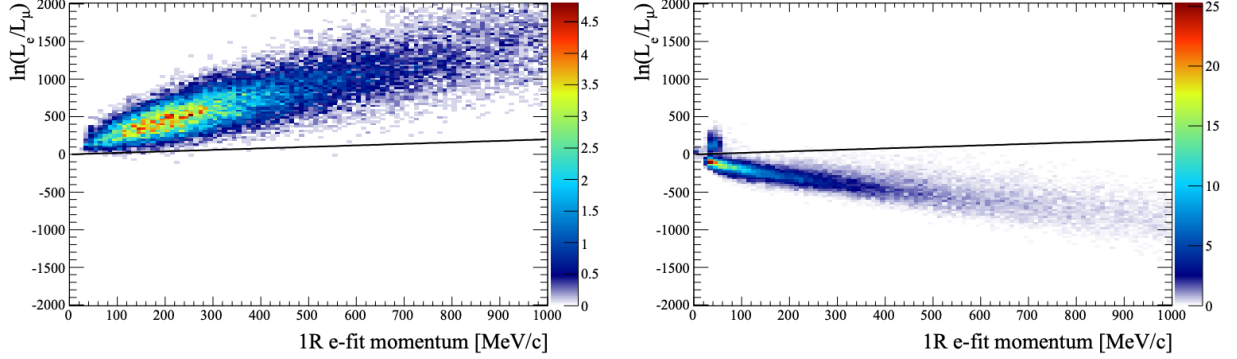


Figure 5.4: The difference of the electron-like and muon-like log-likelihood compared to the reconstructed single-ring fit momentum for atmospheric ν_e (left) and ν_μ (right) samples. The black line represents the cut used to discriminate electron-like and muon-like events, with coefficients obtained from Monte Carlo studies. Figures from [171].

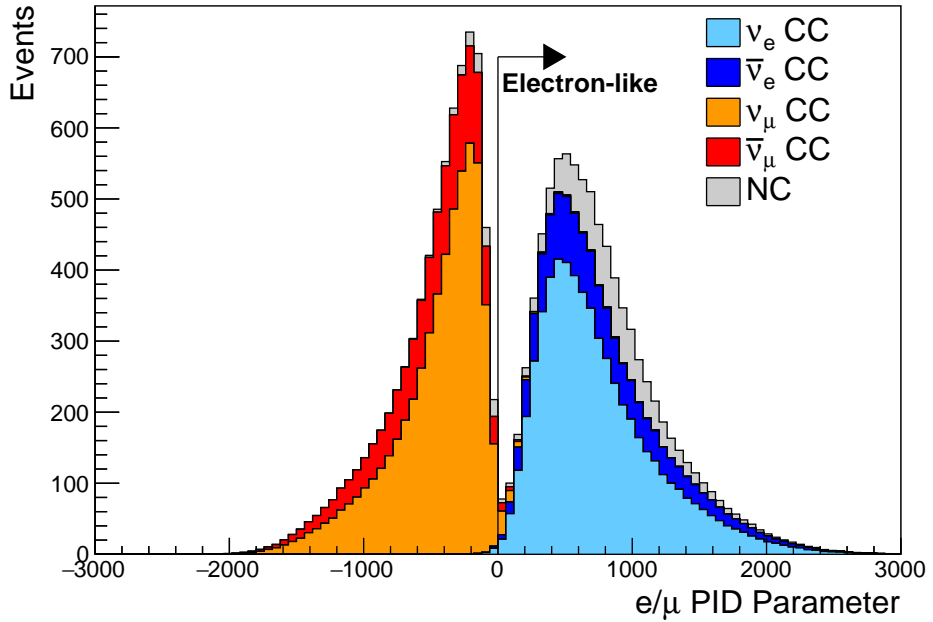


Figure 5.5: The electron/muon PID separation parameter for all sub-GeV single-ring events in SK-IV. The charged current (CC) component is broken down in four flavours of neutrino (ν_μ , $\bar{\nu}_\mu$, ν_e and $\bar{\nu}_e$). Events with positive values of the parameter are determined to be electron-like.

1742 generate Cherenkov photons. These “multi-ring” hypotheses are also considered
 1743 in the `fitQun` algorithm. When calculating the charge likelihood density, the
 1744 predicted charge associated with each ring is calculated separately and then
 1745 summed to calculate the total accumulated charge on each PMT. Similarly, the
 1746 time likelihood for the multi-ring hypothesis is calculated assuming each ring

is independent. Each track is time-ordered based on the time of flight from the center of the track to the PMT and the direct light from any ring incident on the PMT is assumed to arrive before any scattered light. To reduce computational resource usage, the multi-ring fits only consider electron-like and charged pion-like rings as the pion fit can be used as a proxy for a muon fit due to their similar mass. Due to the pions ability to interact through the strong force, they are more likely to hard-scatter. That means a single charged pion can produce multiple rings in different directions. There is an additional freedom, the fraction of kinetic energy lost in a single ring segment, which is added into the `fitQun` pion fit to cover this difference. Pion and muon rings are indistinguishable when this fraction tends to unity.

Multi-ring fits proceed by proposing another ring to the previous fit and then fitting the parameters in the method described above. Typically, multi-ring fits have the largest likelihood because of the additional degrees of freedom introduced. A likelihood value is calculated for the n -ring and $(n + 1)$ -ring hypotheses, where the additional ring is only included if the likelihood value is above 9.35, based on Monte Carlo studies in [178].

5.2.1 Validation of Reconstruction in SK-V

Understanding how the modelling of the detector conditions and stability effects the reconstruction is critical for ensuring accurate measurements. It is important to note that the detector systematics used in the 2020 T2K-only [2] oscillation analysis are determined using data-to-Monte Carlo comparisons of the SK-IV data [179]. Due to tank-open maintenance occurring between SK-IV and SK-V, the dark rate of each PMT was observed to increase in SK-V due to light exposure for a significant time during the repairs. This increase can be seen in Figure 5.6. Run-10 of the T2K experiment was conducted in the SK-V period, so the consistency of SK-IV and SK-V data needs to be studied to determine whether the SK-IV-defined systematics can be applied to the run-10 data. Consequently, the author of this thesis assessed the quality of `fitQun` event reconstruction for SK-V data.

This comparison study was performed using the stopping muon data set for both the SK-IV and SK-V periods. This data sample is used due to the high rate of interactions ($O(200)$ events per hour) as well as having similar energies to muons from CCQE ν_μ interactions from beam interactions. The rate of cosmic muons does depend on the solar activity cycle [180] but has been neglected in this comparison study. This is because the shape of the distributions is most important for the purposes of being compared to the detector systematics. The SK-IV and SK-V data samples consist of 2398.42 and 626.719 hours of data which equates to 686k and 192k events respectively. These samples do not correspond to the full data sets of either period but do contain enough events to be systematics limited rather than statistics limited.

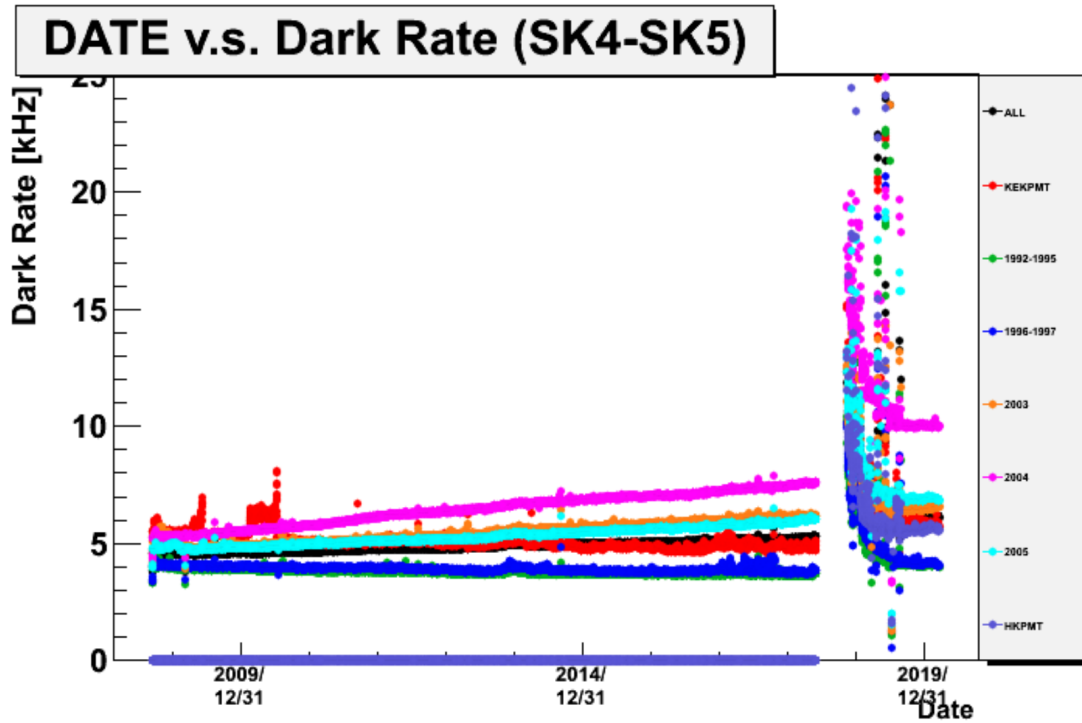


Figure 5.6: The variation of the measured dark rate as a function of date, broken down by PMT type. The SK-IV and SK-V periods span September 2008 to May 2018 and January 2019 to July 2020, respectively. The break in measurement in 2018 corresponds to the period of tank repair and refurbishment. Figure adapted from [179].

The predicted charge calculated in the `fitQun` algorithm includes a contribution from the photoelectron emission due to dark noise. Therefore, the increase

in the SK-V dark rate needs to be accounted for. In practice, the average dark rate in each SK period is calculated and used as an input in the reconstruction. This is calculated by averaging the dark rate per run for each period separately, using the calibration measurements detailed in subsection 3.1.2. The average dark rate from SK-IV and SK-V were found to be 4.57kHz and 6.30kHz, respectively. The charges associated with the muon and decay electron subevents are illustrated in Figure 5.7. The photoelectron emission from dark noise is more significant for events that have lower energy. This is because this contribution becomes more comparable to the number of photoelectrons emitted from incident photons in lower-energy events. This behaviour is observed in the data, where the charge deposited by the muon subevent is mostly unaffected by the increase in dark rate, whilst the charge associated with the decay-electron is clearly affected.

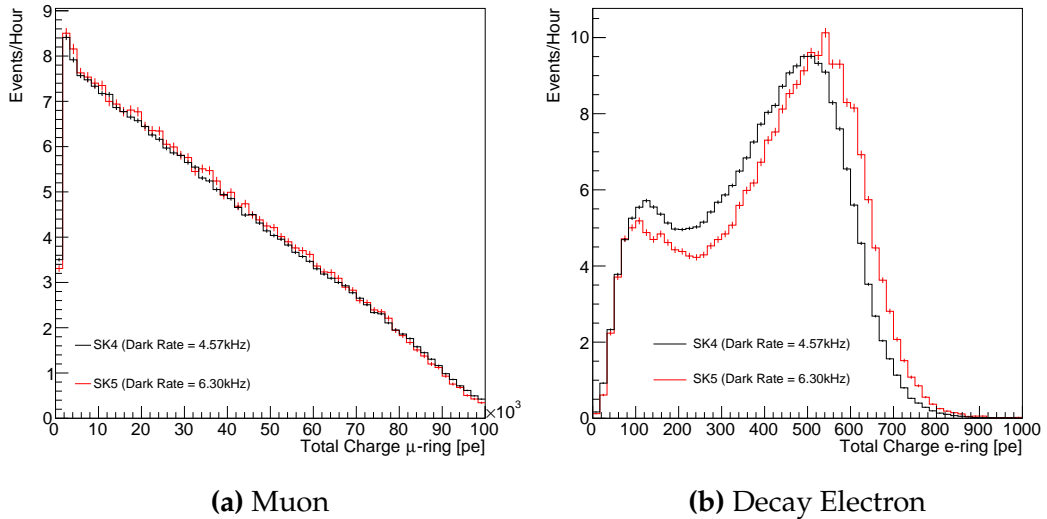


Figure 5.7: Comparison of the measured raw charge deposited per event from the stopping muon data samples between SK-IV (Blue) and SK-V (Red), split by the primary muon subevent (left) and the associated decay electron subevent (right).

The energy scale systematic is estimated from data-to-Monte Carlo differences in the stopping muon sample in [62] and found to be 2.1%. To determine the consistency of SK-IV and SK-V with respect to the energy scale systematic, the muon momentum distribution is compared between the two SK periods. As the total number of Cherenkov photons is integrated across the track length,

₁₈₀₆ the reconstructed momentum divided by track length (or range) is compared
₁₈₀₇ between SK-IV and SK-V as illustrated in Figure 5.8.

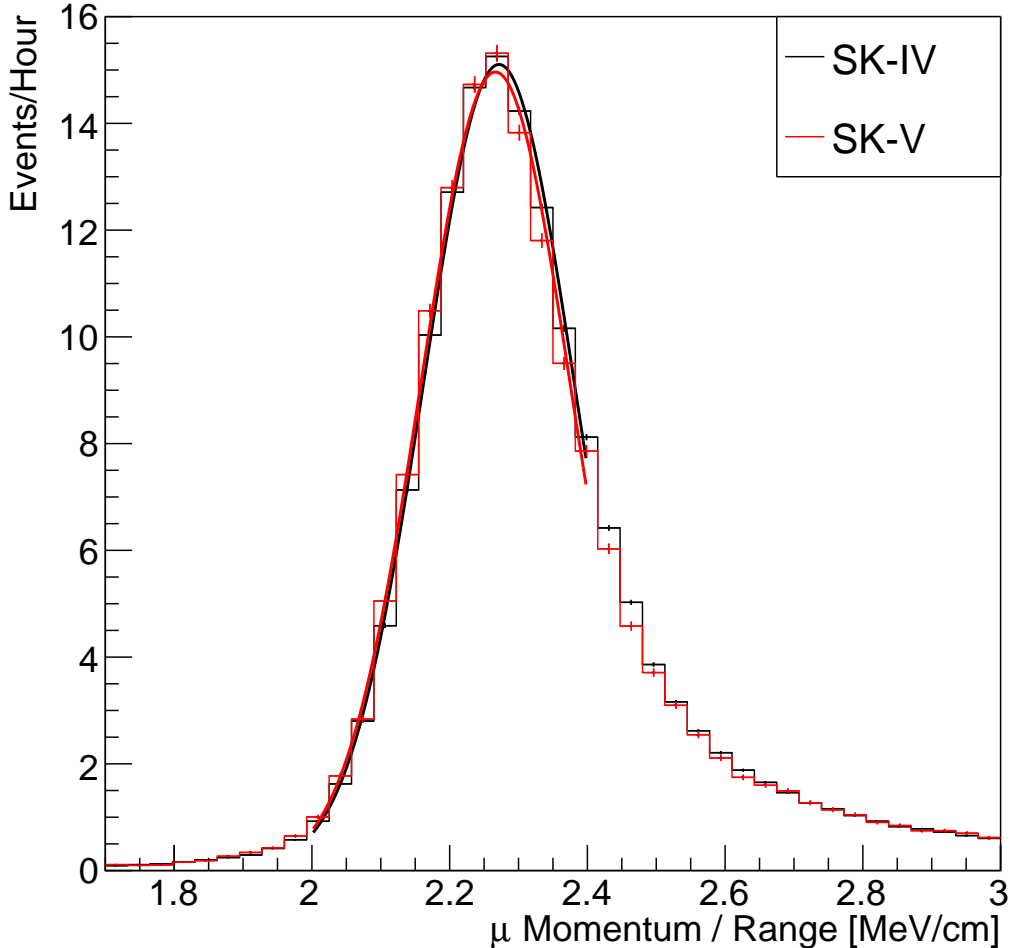


Figure 5.8: The distribution of the reconstructed momentum from the muon ring divided by the distance between the reconstructed muon and decay electron vertices as found in the stopping muon data sets of SK-IV (Black) and SK-IV (Red). Only events with one tagged decay electron are considered. A Gaussian fit is considered in the range $[2.0, 2.4]\text{MeV}/\text{cm}$ and illustrated as the solid curve.

₁₈₀₈ The consistency between these muon distributions has been computed in two
₁₈₀₉ ways. Firstly, a Gaussian is fit to the peak of each distribution separately, whose
₁₈₁₀ mean is found to be $(2.272 \pm 0.003)\text{MeV}/\text{cm}$ and $(2.267 \pm 0.006)\text{MeV}/\text{cm}$ for SK-
₁₈₁₁ IV and SK-V respectively. The ratio of these is equal to 1.002 ± 0.003 . The means of
₁₈₁₂ the Gaussian fits are consistent with the expected stopping power of a minimum

ionising muon for a target material (water) with $Z/A \sim 0.5$ [181]. The second consistency check is performed by introducing a nuisance parameter, α , which modifies the SK-V distribution. The value of α which minimises the χ^2 value between the SK-IV and SK-V is determined by scanning across a range of values. This is repeated by applying the nuisance parameter as both a multiplicative factor and an additive shift. The χ^2 distributions for different values of α is illustrated in Figure 5.9. The values which minimise the χ^2 are found to be 0.0052 and 1.0024 for the additive and multiplicative implementations, respectively. No evidence of shifts larger than the 2.1% uncertainty on the energy scale systematic has been found in the reconstructed momentum distribution of SK-IV and SK-V.

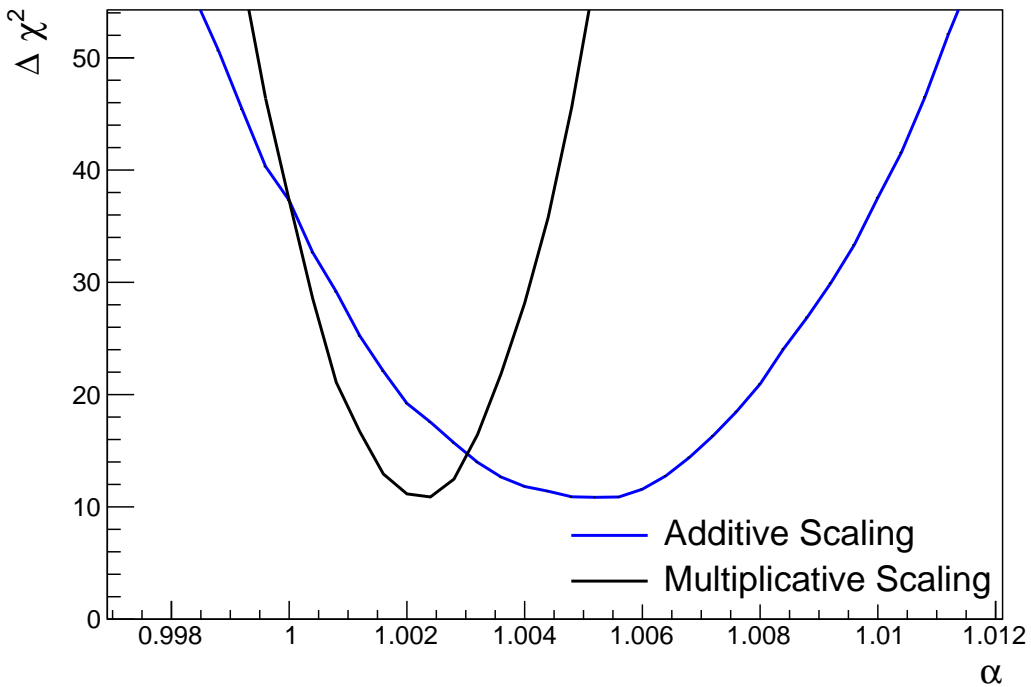


Figure 5.9: The χ^2 difference between the SK-IV and SK-V reconstructed muon momentum divided by range when the SK-V is modified by the scaling parameter α . Both additive (Blue) and multiplicative (Black) scaling factors have been considered. In practice, the additive scaling factor actually uses the value of $(\alpha - 1.0)$ but is illustrated like this so the results can be shown on the same axis range.

1823 5.3 Event Reduction at SK

1824 In normal data-taking operations, the SK detector observes many background
 1825 events alongside the beam and atmospheric neutrino signal events of physics
 1826 interest for this thesis. Cosmic ray muons and flasher events, which are the spon-
 1827 taneous discharge of a given PMT, contribute the largest amount of background
 1828 events in the energy range relevant to this thesis. Therefore the data recorded
 1829 is reduced with the aim of removing these background events. The reduction
 1830 process is detailed in [3, 57] and briefly summarised below.

1831 Atmospheric neutrino events observed in the SK detector are categorised
 1832 into three different types of samples: fully contained (FC), partially contained
 1833 (PC) and up-going muon (Up- μ), using PMT hit signatures in the inner and
 1834 outer detector (ID and OD, respectively). To identify FC neutrino events, it is
 1835 required that the neutrino interacts inside the fiducial volume of the ID and that
 1836 no significant OD activity is observed. For this analysis, an event is defined to be
 1837 in the fiducial volume provided the event vertex is at least 0.5m away from the
 1838 ID walls. PC events have the same ID requirements but can have a larger signal
 1839 present inside the OD. Typically, only high energy muons from ν_μ interactions can
 1840 penetrate the ID wall. The Up- μ sample contains events where muons are created
 1841 from neutrino interactions in the OD water or rock below the tank. They then
 1842 propagate upwards through the detector. Downward-going muons generated
 1843 from neutrino interactions above the tank are neglected because of the difficulty
 1844 in separating their signature from the cosmic muon shower background. The
 1845 sample categories are visually depicted in Figure 5.10.

1846 Based on the event characteristics, as defined by the `fitQun` event reconstruc-
 1847 tion software, the FC events are categorised by

- 1848 • **Visible Energy:** equal to the sum of the reconstructed kinetic energy of
 1849 particles above the Cerenkov threshold for all rings present in the event.
 1850 The purpose is to separate events into sub-GeV and multi-GeV categories.

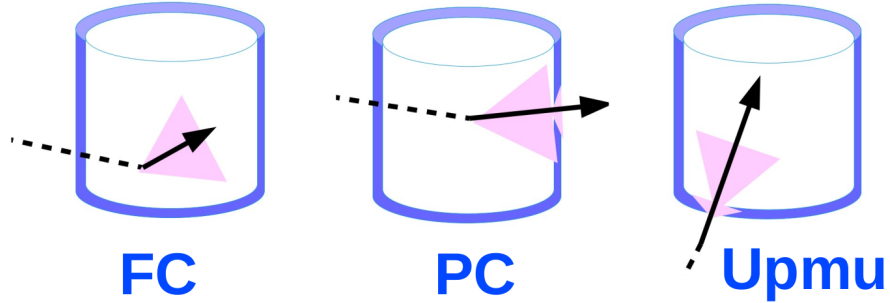


Figure 5.10: A depiction of the topology patterns for fully-contained (FC), partially-contained (PC), and up-going muon ($\text{Up-}\mu$) samples included in this analysis.

1851 • **Number of observed Cerenkov rings.** The purpose is to separate single-
 1852 ring and multi-ring events, where single-ring events predominantly consist
 1853 of quasi-elastic interactions and multi-ring events are typically resonant
 1854 pion production or deep inelastic scattering events.

1855 • **Particle identification parameter of the most energetic ring:** A value de-
 1856 termined from the maximum likelihood value based on `fitQun`'s electron,
 1857 muon, or pion hypothesis. The purpose is to separate electron-like and
 1858 muon-like events.

1859 • **Number of decay electrons:** The purpose is to separate quasi-elastic events
 1860 (which have one decay electron emitted from the muon decay) and resonant
 1861 pion production events (which have two decay electrons emitted from the
 1862 muon and pion).

1863 The PC and Up- μ categories are broken down into “through-going” and
 1864 “stopping” samples depending on whether the muon leaves the detector. This is
 1865 because the PC stopping events deposit the entire energy of the interaction into
 1866 the detector, resulting in better reconstruction. The energy of events that exit the
 1867 detector has to be estimated, with a typically worse resolution, which introduces
 1868 much larger systematic uncertainties. Through-going Up- μ samples are further
 1869 broken down by whether any hadronic showering was observed in the event
 1870 which typically indicates DIS interactions. The expected neutrino energy for the
 1871 different categories is given in Figure 5.11. FC sub-GeV and multi-GeV events

¹⁸⁷² peak around 0.7GeV and 3GeV respectively, with slightly different peak energies
¹⁸⁷³ for ν_e and ν_μ oscillation channels. PC and Up- μ are almost entirely comprised
¹⁸⁷⁴ of ν_μ events and peak around 7GeV and 100GeV, respectively.

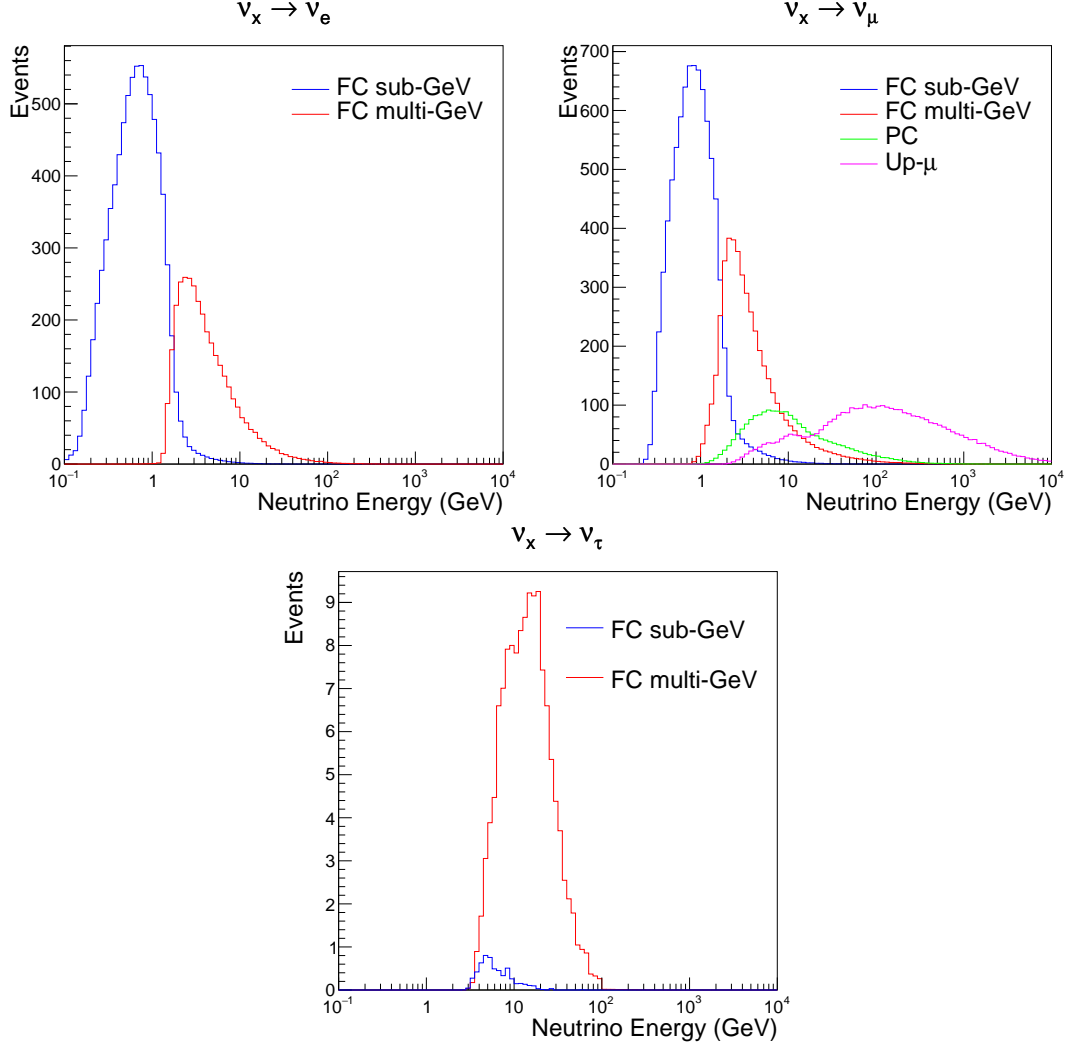


Figure 5.11: The predicted neutrino flux of the fully contained (FC) sub-GeV and multi-GeV, partially contained (PC), and upward-going muon (Up- μ) events. The prediction is broken down by the $\nu_x \rightarrow \nu_e$ prediction (top left), $\nu_x \rightarrow \nu_\mu$ prediction (top right) and $\nu_x \rightarrow \nu_\tau$ prediction (bottom). ν_x represents the flavours of neutrinos produced in the cosmic ray showers (electron and muon). Asimov A oscillation parameters are assumed (given in Table 2.2).

¹⁸⁷⁵ The first two steps in the FC reconstruction remove the majority of cosmic
¹⁸⁷⁶ ray muons by requiring a significant amount of ID activity compared to that
¹⁸⁷⁷ measured in the OD. Events that pass this cut are typically very high momentum
¹⁸⁷⁸ muons or events that leave very little activity in the OD. Consequently, a third

reduction step is then applied to select cosmic-ray muons that pass the initial reduction step. A purpose-built cosmic muon fitter is used to determine the entrance (or exit) position of the muon and a cut is applied to OD activity contained within 8m of this position. Flasher events are removed in the fourth reduction step which is based on the close proximity of PMT hits surrounding the PMT producing the flash. Events that pass all these reduction steps are reconstructed with the APFit algorithm. The fifth step of the reduction uses information from the more precise fitter to repeat the previous two steps with tighter cuts. Muons below the Cherenkov threshold can not generate optical photons in the ID but the associated decay electron can due to its lower mass. These are the types of events targeted in the fifth reduction step. The final cuts require the event vertex to be within the fiducial volume (0.5m from the wall although the nominal distance is 2.0m), visible energy $E_{vis} > 30\text{MeV}$ and fewer than 16 hits within the higher energy OD cluster. The culmination of the fully contained reduction results in 8.09 events/day in the nominal fiducial volume [84]. The uncertainty in the reconstruction is calculated by comparing Monte Carlo prediction to data. The largest discrepancy is found to be 1.3% in the fourth reduction step.

The PC and Up- μ events are processed through their own reduction processes detailed in [57]. Both of these samples are reconstructed with the APFit algorithm rather than `f1TQun`. This is because the efficiency of reconstructing events that leave the detector has not been sufficiently studied for reliable systematic uncertainties with `f1TQun`. The PC and Up- μ samples acquire events at approximately 0.66 and 1.44 events/day.

Beam neutrinos events undergo the same reduction steps as FC events and are then subject to further cuts [182]. The GPS system that links the timing between the beam facility and SK needs to be operating correctly and there should be no activity within the detector in the previous $100\mu\text{s}$ before the trigger. The events then need to triggered between $-2\mu\text{s}$ and $10\mu\text{s}$ of the expected spill timing.

1908 The beam neutrino samples are not split by visible energy since their energy
 1909 range is smaller than the atmospheric neutrino events. Following the T2K
 1910 analysis in [2], only single-ring beam neutrino events are considered. Similar to
 1911 atmospheric event selection, the number of decay electrons is used as a proxy for
 1912 distinguishing CCQE and CCRES events. The expected neutrino energy, broken
 1913 down by the number of decay electrons, is given in Figure 5.12.

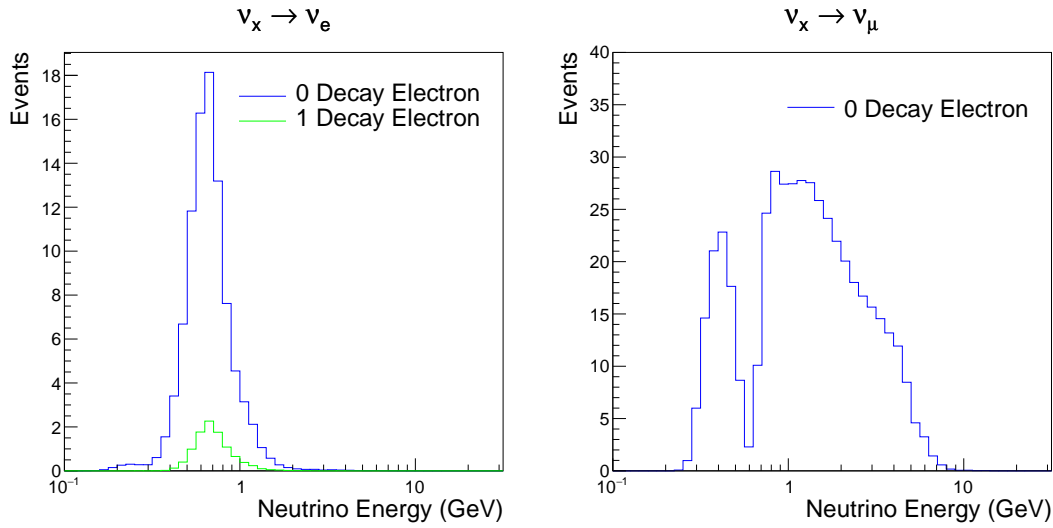


Figure 5.12: The predicted flux of beam neutrinos, as a function of neutrino energy. The predictions are broken down by the number of decay electrons associated with the particular events. Asimov A oscillation parameters are assumed (given in Table 2.2).

6

1914

1915

Sample Selections and Systematics

1916 The oscillation analysis presented within this thesis is built upon a simultaneous
1917 fit to atmospheric samples at SK, neutrino beam samples in the near detector,
1918 and beam samples at SK. This is the first simultaneous oscillation analysis of
1919 beam and atmospheric samples supported by the T2K and SK collaborations.
1920 Notably, the author of this thesis has been responsible for the building and
1921 developing the MaCh3 framework to support all sets of samples simultaneously.
1922 The definitions of the samples are documented in section 6.1, section 6.2, and
1923 section 6.3, respectively. The data collected and used within this analysis is
1924 detailed in Table 6.1. The near and far detector data corresponds to T2K runs
1925 2-9 and runs 1-10, respectively. The accumulated POT and beam power for runs
1926 1 – 10 are illustrated in Figure 6.1.

Data Type	Total
Near Detector FHC	1.15×10^{21} POT
Near Detector RHC	8.34×10^{20} POT
Far Detector FHC	1.97×10^{21} POT
Far Detector RHC	1.63×10^{21} POT
Atmospheric SK-IV	3244.4 days

Table 6.1: The amount of data collected in each detector used within this analysis. The data collected at the near and far detector, for both neutrino beam (FHC) and antineutrino beam (RHC), is measured as the number of protons on target (POT).

1927 The difference in POT recorded at the near and far detector is due to the
 1928 difference in downtime. The SK detector is very stable with almost 100% of
 1929 data recorded during beam operation. Due to various technical and operational
 1930 issues, the downtime of the near detector is significantly higher due to its more
 1931 complex design and operating requirements.

1932 The systematic parameters invoked within the flux, detector, and interaction
 1933 models used within this analysis are documented in section 6.4. The standard
 1934 configuration of the joint beam and atmospheric data fit utilises far detector sys-
 1935 tematics provided in the official inputs from the two experiments. Additionally,
 1936 a correlated detector model which fits the parameters used in sample selections
 1937 to data has been developed and documented in subsection 6.4.5.

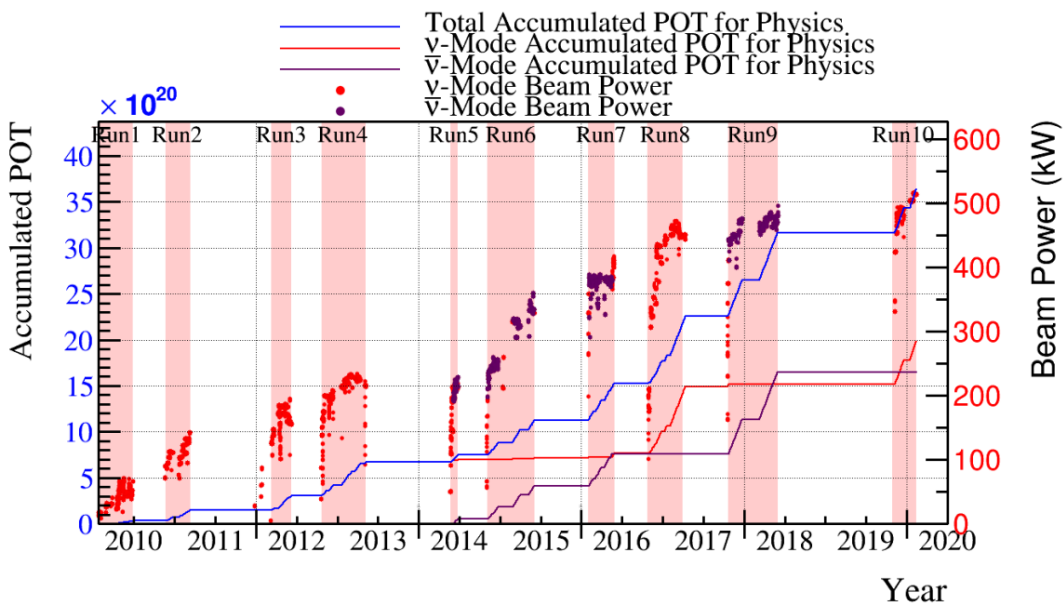


Figure 6.1: The accumulated beam data, measured as the number of protons on target (POT). The total data (blue) is given which comprises of the neutrino beam (red) and antineutrino (purple) components. The beam power for neutrino and antineutrino beams is given as the markers using the same colour scheme. The timescale runs from Run 1 which started in January 2010 until Run 10 which ended in February 2020. The ratio of accumulated data in neutrino and antineutrino beam is 54.7% : 45.3%.

1938 6.1 Atmospheric Samples

1939 The atmospheric event selection follows the official SK-IV analysis presented
1940 in [3] and is documented below. The Monte Carlo prediction used within this
1941 analysis corresponds to 500 years worth of neutrino events, which is scaled down
1942 to match the SK-IV livetime of 3244.4 days.

1943 The fully contained (FC), partially contained (PC), and upward going muon
1944 events ($\text{up-}\mu$) which pass the reduction cuts discussed in section 5.3 are further
1945 broken down into different samples based on reconstruction information. This
1946 section details the samples used within this oscillation analysis, alongside the
1947 chosen binning.

1948 FC events are first separated by the visible energy deposited within the
1949 detector. This is calculated as the sum of the reconstructed kinetic energy
1950 above the Cherenkov threshold for all rings present in the event. Events are
1951 separated by whether they were above or below $E_{\text{vis}} = 1.33\text{GeV}$. This separates
1952 “subGeV” and “multiGeV” events. Typically, lower energy events consist of
1953 charged current quasi-elastic (CCQE) interactions which are better understood
1954 and simpler to reconstruct resulting in smaller systematic uncertainties. Events
1955 are further separated by the number of rings associated with the event due to
1956 similar reasoning. As the oscillation probability is dependant upon the flavour
1957 of neutrino, electron and muon events are separated using a similar likelihood
1958 method to that discussed in section 5.2. To reduce computational resources
1959 required for the reconstruction, only electron and pion hypotheses are considered
1960 so this separation cut depends on the ratio of the electron to pion likelihoods,
1961 $\log(L_e/L_\pi)$. Finally, the number of decay electrons is used to classify events.
1962 Charged current resonant pion production (CCRES) interactions generate a final-
1963 state pion. This can decay, mostly likely through a muon, into a decay electron.
1964 Therefore any electron-like event with one decay electron or muon-like event
1965 with two decay electrons was most likely produced by a CCRES interaction.
1966 Consequently, the number of decay electrons can be used to distinguish CCQE

¹⁹⁶⁷ and CCRES interaction modes. Ultimately, FC subGeV events are separated
¹⁹⁶⁸ into the samples listed in Table 6.2.

Sample Name	Description
SubGeV- <i>e</i> like-0dcy	Single ring <i>e</i> -like events with zero decay electrons
SubGeV- <i>e</i> like-1dcy	Single ring <i>e</i> -like events with one or more decay electrons
SubGeV- <i>μ</i> like-0dcy	Single ring <i>μ</i> -like events with zero decay electrons
SubGeV- <i>μ</i> like-1dcy	Single ring <i>μ</i> -like events with one decay electrons
SubGeV- <i>μ</i> like-2dcy	Single ring <i>μ</i> -like events with two or more decay electrons
SubGeV- <i>π</i> 0like	Two <i>e</i> -like ring events with zero decay electrons and reconstructed π^0 mass $85 \leq m_{\pi^0} < 215$ MeV

Table 6.2: The fully contained subGeV samples, defined as events with visible energy $E_{vis} < 1.33$ GeV, used within this oscillation analysis.

¹⁹⁶⁹ In addition to the cuts discussed above, multiGeV samples also have addi-
¹⁹⁷⁰ tional cuts to separate samples which target neutrino and antineutrino events.
¹⁹⁷¹ As discussed in section 2.5, the matter resonance only occurs for neutrinos in the
¹⁹⁷² normal hierarchy and antineutrinos in the inverted mass hierarchy. Therefore,
¹⁹⁷³ having flavour-enriched samples aids in the determination of the mass hierarchy.
¹⁹⁷⁴ For a CCRES interaction,

$$\begin{aligned}
 \bar{\nu}_e + N &\rightarrow e^+ + N' + \pi^-, \\
 \nu_e + N &\rightarrow e^- + N' + \pi^+ \\
 &\quad \downarrow \mu^+ + \nu_\mu \\
 &\quad \downarrow e^+ + \nu_e + \bar{\nu}_\mu.
 \end{aligned} \tag{6.1}$$

¹⁹⁷⁵ The π^- emitted from a $\bar{\nu}_e$ interaction is more likely to be captured by an
¹⁹⁷⁶ oxygen nucleus than the π^+ from ν_e interactions [183]. These pions then decay,
¹⁹⁷⁷ mostly through muons, to electrons. Therefore the number of tagged decay
¹⁹⁷⁸ electrons associated with an event gives an indication of whether the interaction
¹⁹⁷⁹ was due to a neutrino or antineutrino: zero for $\bar{\nu}_e$ events, and one for ν_e events.
¹⁹⁸⁰ The ability to separate neutrino from antineutrino events is illustrated in Table 6.4,
¹⁹⁸¹ where the MultiGeV-*e*like-nue has 78% purity of CC neutrino interactions with
¹⁹⁸² only 7% antineutrino background, the rest consisting of NC backgrounds.

1983 The number of decay electrons discriminator works reasonably well for single-
 1984 ring events. However, this is not the case for multi-ring events. A multiGeV
 1985 multiring electron-like (MME) likelihood cut was introduced in [184, 185]. This
 1986 is a two-stage likelihood selection cut. Four observables are used in the first
 1987 likelihood cut to distinguish $CC\nu_e$ and $CC\bar{\nu}_e$ events from background:

- 1988 • The number of decay electrons
 1989 • The maximum distance between the vertex of the neutrino and the decay
 1990 electrons
 1991 • The energy deposited by the highest energy ring
 1992 • The particle identification of that highest energy ring

1993 Background events consist of $CC\nu_\mu$ and NC interactions. Typically, the
 1994 majority of the energy in these background events is carried by the hadronic
 1995 system. Additionally, muons tend to travel further than the pions from $CC\nu_e$
 1996 before decaying. Thus, the parameters used within the likelihood cut target these
 1997 typical background interaction kinematics.

Sample Name	Description
MultiGeV-elike-nue	Single ring e -like events with zero decay electrons
MultiGeV-elike-nuebar	Single ring e -like events with one or more decay electrons
MultiGeV-mulike	Single ring μ -like events
MultiRing-elike-nue	Two or more ring events with leading energy e -like ring and passed both MME and $\nu/\bar{\nu}$ separation cuts
MultiRing-elike-nuebar	Two or more ring events with leading energy e -like ring and passed MME and failed $\nu/\bar{\nu}$ separation cuts
MultiRing-mulike	Two or more ring events with leading energy μ -like ring and only requires $E_{vis} > 0.6\text{GeV}$
MultiRing-Other1	Two or more ring events with leading energy e -like ring and failed the MME likelihood cut

Table 6.3: The fully contained multiGeV samples used within this oscillation analysis. Both the sample name and description are given.

1998 Neutrino and antineutrino events are then separated by a second likelihood
 1999 method ($\nu/\bar{\nu}$ separation) detailed in [62]. This uses the number of decay electrons,

2000 the number of reconstructed rings, and the event’s transverse momentum. The
2001 last two parameters are used because higher-energy samples tend to have more
2002 pions produced above the Cherenkov threshold which results in more rings
2003 compared to an antineutrino interaction. Furthermore, the angular distribution
2004 also tends to be more forward peaked in antineutrino interactions as compared
2005 to neutrino interactions [3]. These FC multiGeV sample definitions are de-
2006 tailed in Table 6.3.

2007 The PC and up- μ samples are split by the amount of energy deposited within
2008 the outer detector, into “stopping” and “through-going” samples. If an event
2009 leaves the detector, the energy it takes with it has to be estimated which increases
2010 the systematic uncertainty compared to events entirely contained within the
2011 inner detector. This estimation is particularly poor at high energies, thus the
2012 up- μ through-going events are not binned in reconstructed momentum. The
2013 through-going up- μ are further separated by the presence of any electromagnetic
2014 showering in the event, as the assumption of non-showering muon does not give
2015 reliable reconstruction for these types of events [57]. In total, 13 FC, 2 PC, and
2016 3 up- μ atmospheric samples are included within this analysis.

2017 The atmospheric samples are binned in direct observables: reconstructed
2018 lepton momentum and direction, as given by Table 6.5. The distribution of
2019 the reconstructed lepton momentum (for samples that only have one bin in
2020 reconstructed zenith angle) and reconstructed direction for each atmospheric
2021 sample used within this analysis is illustrated in Figure 6.2.

2022 The reconstructed lepton momemtum, illustrated by interaction mode break-
2023 down, of some representative atmospheric samples is given in Figure 6.3. The
2024 equivalent distributions of all atmospheric samples used within this analy-
2025 sis can be found in [186]. The low energy samples tend to be dominated by
2026 the interaction mode they target (CCQE for SubGeV-elike-0dcy and CC1 π for
2027 SubGeV-elike-1dcy samples). The higher energy samples include much more
2028 CCOther interactions, especially at larger reconstructed lepton momentum.

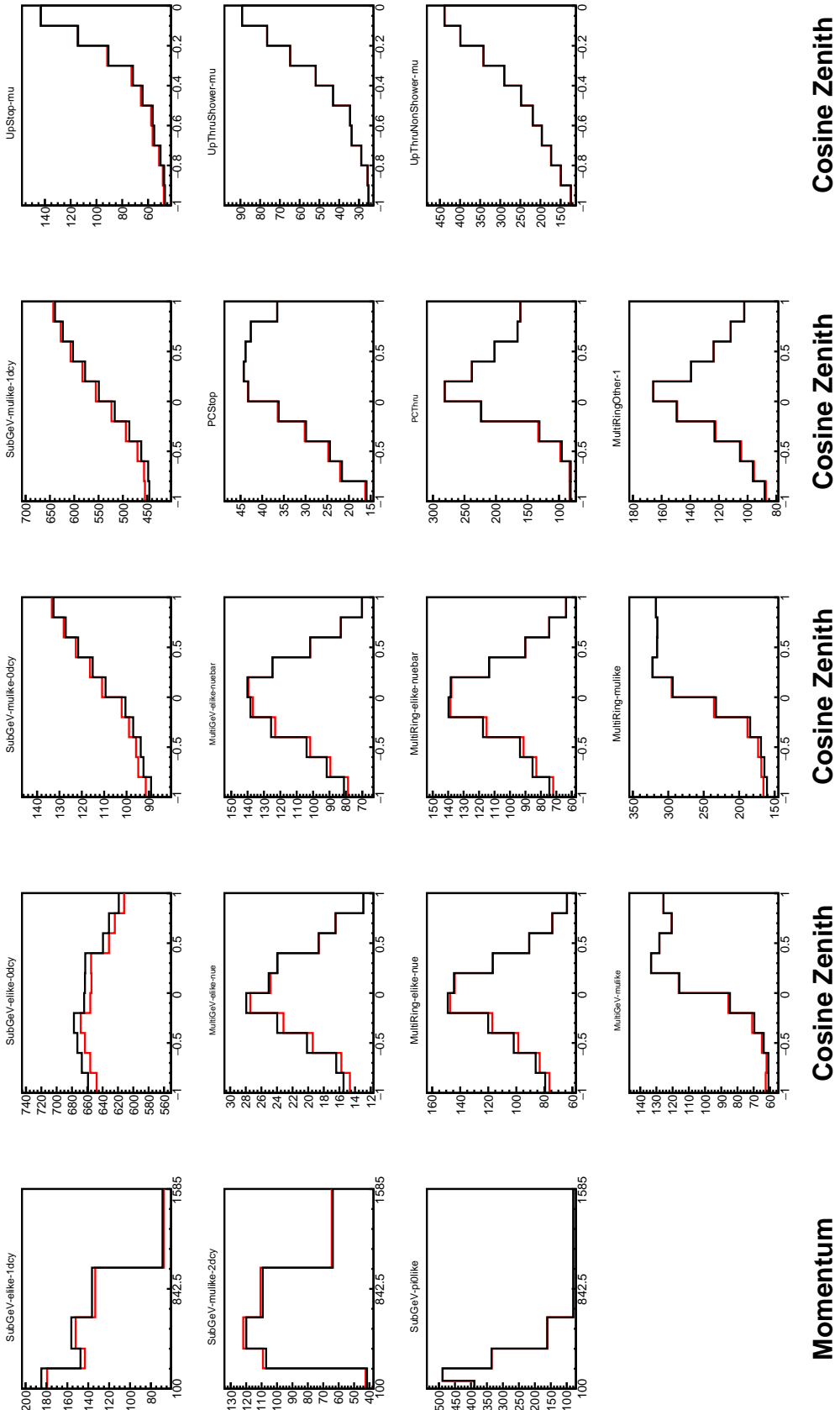


Figure 6.2: Comparison of the SK-IV atmospheric samples between predictions made with the CP-violating Asimov A (Black) and CP-conserving Asimov B (Red) oscillation parameter sets (given in Table 2.2). The subGeV samples CCRES and π^0 -like samples are given in their reconstructed lepton momentum. All other samples are presented in their reconstructed zenith angle projection.

Sample	$CC\nu_e$	$CC\bar{\nu}_e$	$CC(\nu_\mu + \bar{\nu}_\mu)$	$CC(\nu_\tau + \bar{\nu}_\tau)$	NC
SubGeV- <i>elike</i> -0dcy	72.17	23.3	0.724	0.033	3.77
SubGeV- <i>elike</i> -1dcy	86.81	1.773	7.002	0.062	4.351
SubGeV- <i>mulike</i> -0dcy	1.003	0.380	90.07	0.036	8.511
SubGeV- <i>mulike</i> -1dcy	0.023	0.	98.46	0.029	1.484
SubGeV- <i>mulike</i> -2dcy	0.012	0.	99.25	0.030	0.711
SubGeV- <i>pi0like</i>	6.923	2.368	0.928	0.011	89.77
MultiGeV- <i>elike</i> -nue	78.18	7.041	3.439	1.886	9.451
MultiGeV- <i>elike</i> -nuebar	56.68	37.81	0.174	0.614	4.718
MultiGeV- <i>mulike</i>	0.024	0.005	99.67	0.245	0.058
MultiRing- <i>elike</i> -nue	59.32	12.39	4.906	3.385	20
MultiRing- <i>elike</i> -nuebar	52.39	31.03	1.854	1.585	13.14
MultiRing- <i>mulike</i>	0.673	0.080	97.33	0.342	1.578
MultiRingOther-1	27.98	2.366	34.93	4.946	29.78
PCStop	8.216	3.118	84.45	0.	4.214
PCThrus	0.564	0.207	98.65	0.	0.576
UpStop-mu	0.829	0.370	98.51	0.	0.289
UpThruNonShower-mu	0.206	0.073	99.62	0.	0.103
UpThruShower-mu	0.128	0.054	99.69	0.	0.132

Table 6.4: The purity of each atmospheric sample used within this analysis, broken down by charged current (CC) and neutral current (NC) interactions and which neutrino flavour interacted within the detector. Each row sums to 100% by definition. Asimov A oscillation parameter sets are assumed (given in Table 2.2). Electron neutrino and antineutrino events are separated to illustrate the ability of the separation likelihood cuts used within the multiGeV and multiring sample selections.

Sample	$\cos(\theta_Z)$ Bins	Momentum Bin Edges ($\log_{10}(P)$ MeV)
SubGeV- <i>elike</i> -0dcy	10	2.0, 2.4, 2.6, 2.8, 3.0, 3.2
SubGeV- <i>elike</i> -1dcy	1	2.0, 2.4, 2.6, 2.8, 3.0, 3.2
SubGeV- <i>mulike</i> -0dcy	10	2.0, 2.4, 2.6, 2.8, 3.0, 3.2
SubGeV- <i>mulike</i> -1dcy	10	2.0, 2.4, 2.6, 2.8, 3.0, 3.2
SubGeV- <i>mulike</i> -2dcy	1	2.0, 2.4, 2.6, 2.8, 3.0, 3.2
SubGeV- <i>pi0like</i>	1	2.0, 2.2, 2.4, 2.6, 2.8, 3.2
MultiGeV- <i>elike</i> -nue	10	3.0, 3.4, 3.7, 4.0, 5.0
MultiGeV- <i>elike</i> -nuebar	10	3.0, 3.4, 3.7, 4.0, 5.0
MultiGeV- <i>mulike</i>	10	3.0, 3.4, 5.0
MultiRing- <i>elike</i> -nue	10	3.0, 3.4, 3.7, 5.0
MultiRing- <i>elike</i> -nuebar	10	3.0, 3.4, 3.7, 5.0
MultiRing- <i>mulike</i>	10	2.0, 3.124, 3.4, 3.7, 5.0
MultiRing- <i>Other1</i>	10	3.0, 3.4, 3.7, 4.0, 5.0
PC-Stop	10	2.0, 3.4, 5.0
PC-Through	10	2.0, 3.124, 3.4, 3.7, 5.0
Upmu-Stop	10	3.2, 3.4, 3.7, 8.0
Upmu-Through-Showering	10	2.0, 8.0
Upmu-Through-NonShowering	10	2.0, 8.0

Table 6.5: The reconstructed cosine zenith and lepton momentum binning assigned to the atmospheric samples. The “ $\cos(\theta_Z)$ Bins” column illustrates the number of bins uniformly distributed over the $-1.0 \leq \cos(\theta_Z) \leq 1.0$ region for fully and partially contained samples and $-1.0 \leq \cos(\theta_Z) \leq 0.0$ region for up- μ samples.

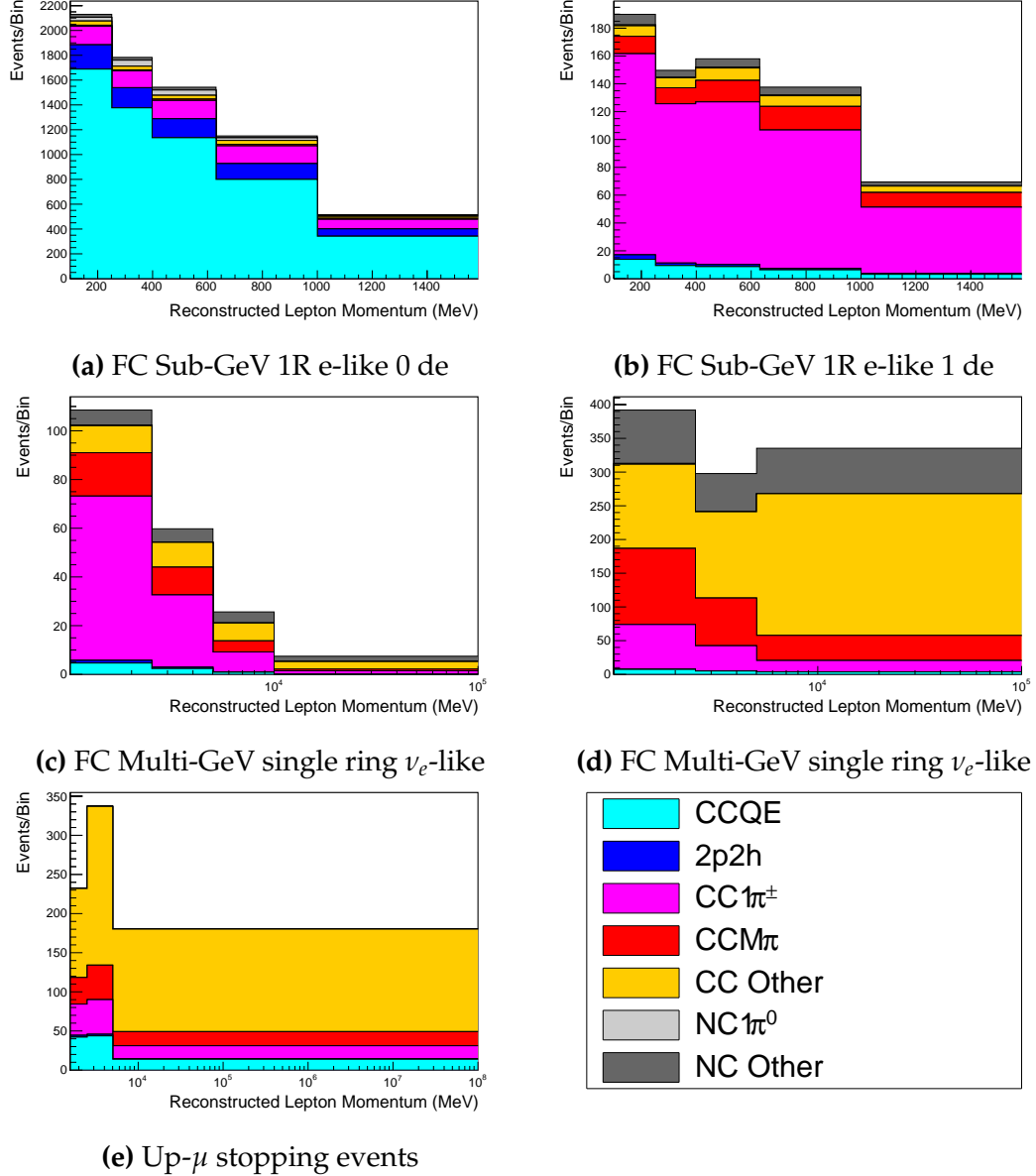


Figure 6.3: Breakdown by interaction mode of some representative atmospheric samples used within this analysis, illustrated as a function of reconstructed lepton momentum. The binning is provided in Table 6.5. Asimov A oscillation parameters are used to generate these plots. The interaction mode breakdown of all atmospheric samples used within this analysis can be found in [186].

2029 6.2 Near Detector Beam Samples

2030 The near detector sample selections are documented in detail within [187] and
2031 summarised below. Samples are selected based upon which of the two Fine
2032 Grained Detector (FGD) the vertex is reconstructed in as well as the operating
2033 mode of the beam: FHC or RHC. Wrong-sign neutrino background samples are
2034 considered in the RHC mode in order to add additional constraints on model
2035 parameters. Samples from the wrong-sign component of the FHC beam mode
2036 are not included as they are statistically insignificant compared to those samples
2037 already listed.

2038 The reconstruction algorithm uses a clustering algorithm to group hits within
2039 the TPC. It then adds information from the upstream FGD to form a track
2040 that passes through both sub-detectors. In FHC(RHC), the highest momentum
2041 negative(positive) curvature track is defined as the muon candidate. Before
2042 being assigned a sample, these candidate muon events must pass CC-inclusive
2043 cuts, as defined in [188]:

- 2044 • Event Timing: The DAQ must be operational and the event must occur
2045 within the expected beam time window consistent with the beam spill
- 2046 • TPC Requirement: The muon-candidate track path must intercept one or
2047 more TPCs
- 2048 • Fiducial volume: The event must originate from within the fiducial volume
2049 defined in [189]
- 2050 • Upstream Background: Remove events that have muon tracks that originate
2051 upstream of the FGDs by requiring no high-momentum tracks within
2052 150mm upstream of the candidate vertex. Additionally, events that occur
2053 within the downstream FGD are vetoed if a secondary track starts within
2054 the upstream FGD

- 2055 • Broken track removal: All candidates where the muon candidate is broken
2056 in two are removed

- 2057 • Muon PID: Measurements of dE/dx in a TPC are used to distinguish muon-
2058 like events, from electron-like or proton-like, using a likelihood cut

2059 In addition to these cuts, RHC neutrino events also have to undergo the
2060 following cuts to aid in the separation of neutrino and antineutrino [190]:

- 2061 • TPC Requirement: The track path must intercept TPC2
2062 • Positive Track: The highest momentum track must have a positive recon-
2063 structed charge
2064 • TPC1 Veto: Remove any events originating upstream of TPC1

2065 Once all CC-inclusive events have been determined, they are further split by
2066 pion multiplicity: CC0 π , CC1 π , and CCOther. Pions in the TPCs are selected by
2067 requiring a second track to be observed, which is separate from the muon track
2068 and is in the same beam spill window and sub-detector. The number of FGD
2069 pions is equal to the number of Michel electrons which were tagged within the
2070 same sub-detector and spill window. If this value is equal to zero, the number
2071 of FGD pions is equivalent to the number of pion-like tracks which have dE/dx
2072 measurements consistent with the pion hypothesis. The pion tracks from both
2073 FGD and TPC events are required to have a vertex consistent with that of the
2074 muon candidate. The Michel electron tagging is preferential as a delayed Michel
2075 is almost always a pion meaning this cut has a higher purity [188, 191], whereas a
2076 track in the FGD that is consistent with a pion could be another particle resulting
2077 in a lower purity. Michel electrons are neglected in the TPC as the pions very
2078 rarely stop due to the low density.

2079 CC0 π , CC1 π , and CCOther samples are defined with the following cuts:

- 2080 • ν_μ CC0 π Selection: No electrons in TPC and no charged pions or decay
2081 electrons within the TPC or FGD

- 2082 • ν_μ CC1 π **Selection:** Exactly one charged pion in either the TPC or FGD
- 2083 • ν_μ CCOther **Selection:** All events which are not classified into the above
2084 two selections

2085 Counting the three selections for each FGD in FHC and RHC running, includ-
2086 ing the wrong-sign background in RHC, 18 near detector samples are used within
2087 this analysis. These samples are binned in reconstructed lepton momentum
2088 (illustrated in Figure 6.4) and direction with respect to the beam. The binning
2089 is chosen such that each event has at least 20 Monte Carlo events in each bin
2090 [189]. This is to ensure that the bins are coarse enough to ensure the reduction
2091 of statistical errors, whilst also being fine enough to sample the high-resolution
2092 peak regions. The exact binning is detailed in [189].

2093 6.3 Far Detector Beam Samples

2094 The beam neutrino events which occur at the SK detector, which pass the
2095 reduction cuts detailed in section 5.3, are separated based on whether the beam
2096 was operating in FHC or RHC mode. The events are then separated into three
2097 samples: electron-like (1Re), muon-like (1R μ), and CC1 π^+ -like (1Re1de) which
2098 are observed as electron-like events with an associated decay electron [179].
2099 As discussed in section 6.1, positively charged pions emitted from neutrino
2100 interactions are more likely to produce decay electrons than negatively charged
2101 pions. Consequently, the CC1 π^+ -like sample is only selected when the beam is
2102 operating in FHC mode. Therefore, five beam samples measured at SK are
2103 used in this analysis.

2104 The fiducial volume definition for beam samples is slightly different from that
2105 used for the atmospheric samples. It uses both the distance to the closest wall
2106 (dWall) and the distance to the wall along the trajectory of the particle (toWall).
2107 This allows events that originate close to the wall but are facing into the tank to be
2108 included within the analysis, which would have otherwise been removed. These
2109 additional events are beneficial for a statistics-limited experiment. The exact

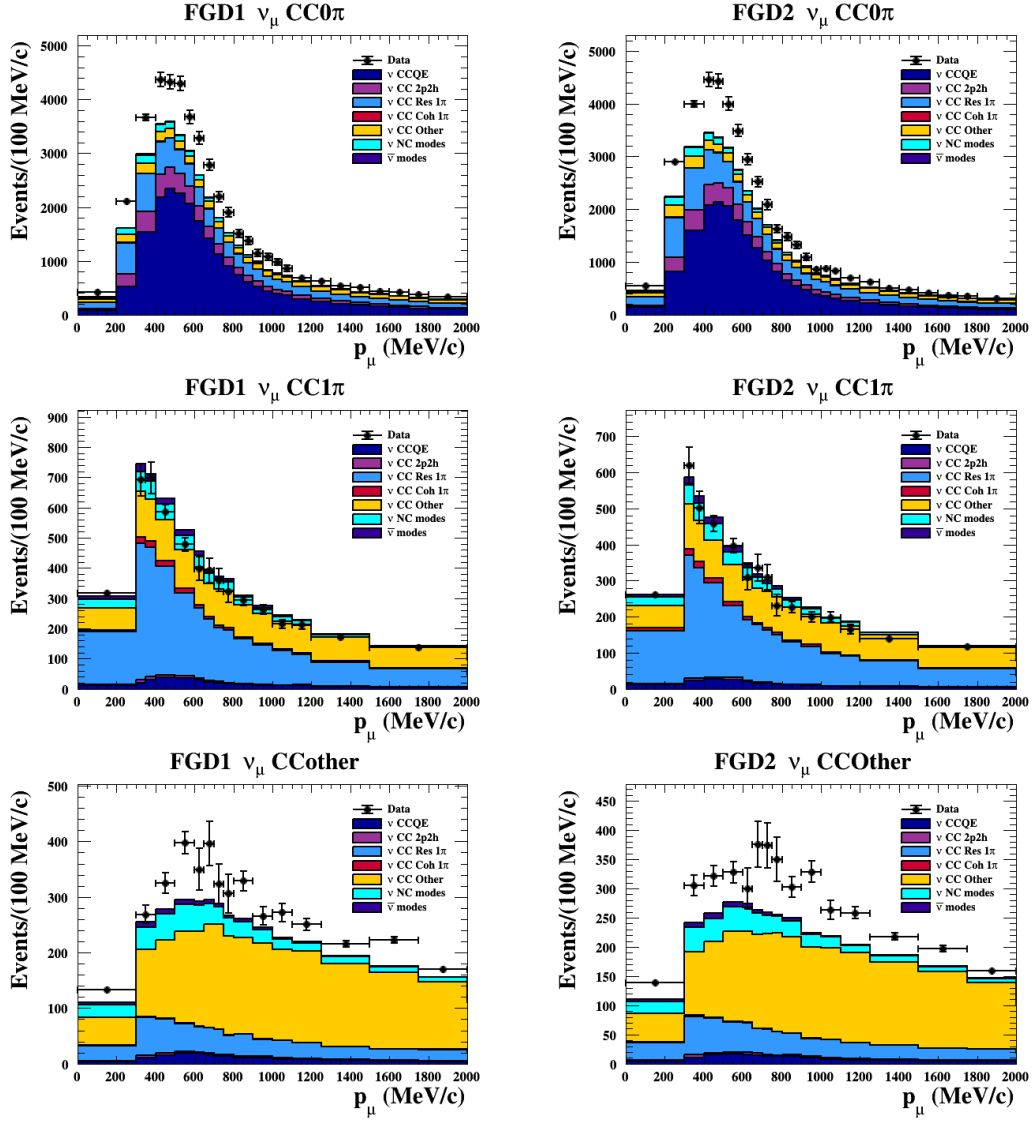


Figure 6.4: The nominal Monte Carlo predictions compared to data for the FGD1 and FGD2 samples in neutrino beam mode, broken down into the $CC\nu_\mu 0\pi$, $CC\nu_\mu 1\pi$ and $CC\nu_\mu$ Other categories. Figures taken from [187].

2110 cut values for both `dWall` and `tWall` are different for each of the three types of
 2111 sample and are optimised based on T2K sensitivity to δ_{CP} [177, 192]. They are:

2112 **1Re event selection** For an event to be classified as a 1Re-like, the event must sat-
 2113 isfy:

- 2114 • Fully-contained and have $dWall > 80\text{cm}$ and $tWall > 170\text{cm}$
- 2115 • Total of one ring which is reconstructed as electron-like with reconstructed

2116 momentum $P_e > 100\text{MeV}$

2117 • Zero decay electrons are associated with the event

2118 • Passes π^0 rejection cut discussed in section 5.2

2119 The zero decay electron cut removes non-CCQE interactions and the π^0
2120 rejection cut is designed to remove neutral current π^0 background events which
2121 can be easily reconstructed as 1Re-like events.

2122 The zero decay electron cut removes non-CCQE interactions and the π^0
2123 rejection cut is designed to remove neutral current π^0 background events which
2124 can be easily reconstructed as 1Re-like events.

2125 **CC1 π^+ event selection** This event selection is very similar to that of the 1Re
2126 sample. The only differences are that the dWall and toWall criteria are changed
2127 to $> 50\text{cm}$ and $> 270\text{cm}$, respectively, and exactly one decay electron is required
2128 from the π^+ decay.

2129 **1R μ event selection** A 1R μ -like event is determined by the following cuts:

2130 • Fully-contained and have $\text{dWall} > 50\text{cm}$ and $\text{toWall} > 250\text{cm}$

2131 • Total of one ring which is reconstructed as muon-like with reconstructed
2132 momentum $P_\mu > 200\text{MeV}$

2133 • Fewer than two decay electrons are associated with the event

2134 • Passes π^+ rejection cut discussed in section 5.2

2135 All of these samples are binned in reconstructed neutrino energy. This is
2136 possible under a particular interaction mode assumption, as the direction from
2137 the source is known extremely well. For the 1Re-like and 1R μ -like samples,

$$E_\nu^{rec} = \frac{(M_N - V_{nuc})E_l - m_l^2/2 + M_N V_{nuc} - V_{nuc}^2/2 + (M_P^2 + M_N^2)/2}{M_N - V_{nuc} - E_l + P_l \cos(\theta_{beam})}. \quad (6.2)$$

2138 Where M_N , M_P and m_l are the masses of the neutron, proton and outgoing
 2139 lepton, respectively. $V_{nuc} = 27\text{MeV}$ is the binding energy of the oxygen nucleus
 2140 [179], θ_{beam} is the angle between the beam and the direction of the outgoing
 2141 lepton, and E_l and P_l are the energy and momentum of that outgoing lepton.

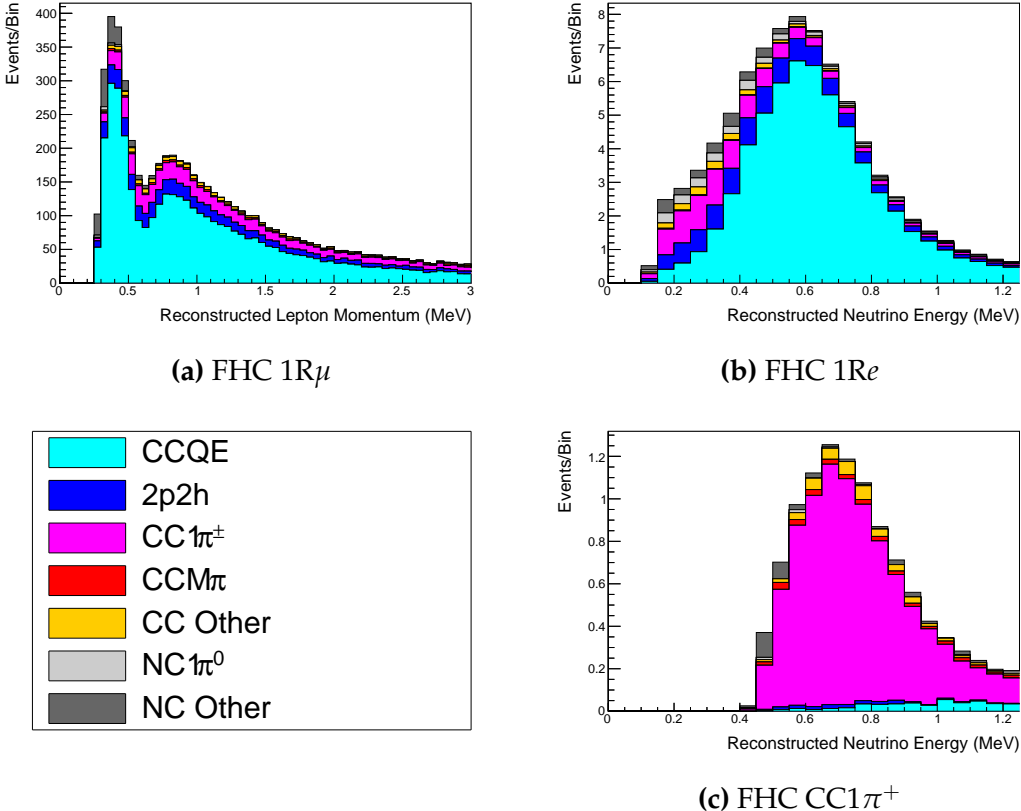


Figure 6.5: The reconstructed neutrino energy, as defined by Equation 6.2 and Equation 6.3, for the 1R μ -like, 1Re-like, and CC1 π^+ -like samples. The AsimovA oscillation parameters are assumed (given in Table 2.2). These samples are the FHC mode samples. For ease of viewing, the 1R μ sample only shows the $0 \leq E_\nu^{rec} < 3.0\text{GeV}$ but the binning extends to 30.0GeV .

2142 The reconstructed neutrino energy of the CC1 π^+ -like events also accounts
 2143 for the delta resonance produced within the interaction,

$$E_\nu^{rec} = \frac{2M_N E_l + M_{\Delta^{++}}^2 - M_N^2 - m_l^2}{2(M_N - E_l + P_l \cos(\theta_{beam}))}. \quad (6.3)$$

2144 Where $M_{\Delta^{++}}$ is the mass of the delta baryon. Binding energy effects are not
 2145 considered as a two-body process, with the delta baryon, is assumed. This follows
 2146 the T2K oscillation analysis presented in [2], although recent developments of

2147 the interaction model in the latest T2K oscillation analysis do include effects
2148 from binding energy in this calculation [193].

2149 The reconstructed neutrino energy for the FHC samples is illustrated in
2150 Figure 6.5. As expected, the $1R\mu$ -like and $1Re$ -like samples are heavily dominated
2151 by CCQE interactions, with smaller contributions from $2p2h$ meson exchange and
2152 resonant pion production interactions. The $CC1\pi^+$ -like sample predominantly
2153 consists of charged current resonant pion production interactions. The $1Re$ -like
2154 and $CC1\pi^+$ -like samples are also binned by the angle between the neutrino beam
2155 and the reconstructed lepton momentum. This is to aid in charged current and
2156 neutral current separation, as indicated in Figure 6.6. This is because the neutral
2157 current backgrounds are predominantly due to π^0 -decays, which decay into two
2158 γ rays. The opening angle of which (alongside the different final state kinematics)
2159 can produce a slightly broader angular distribution compared to the final state
2160 particles originating from charged current ν_e interactions.

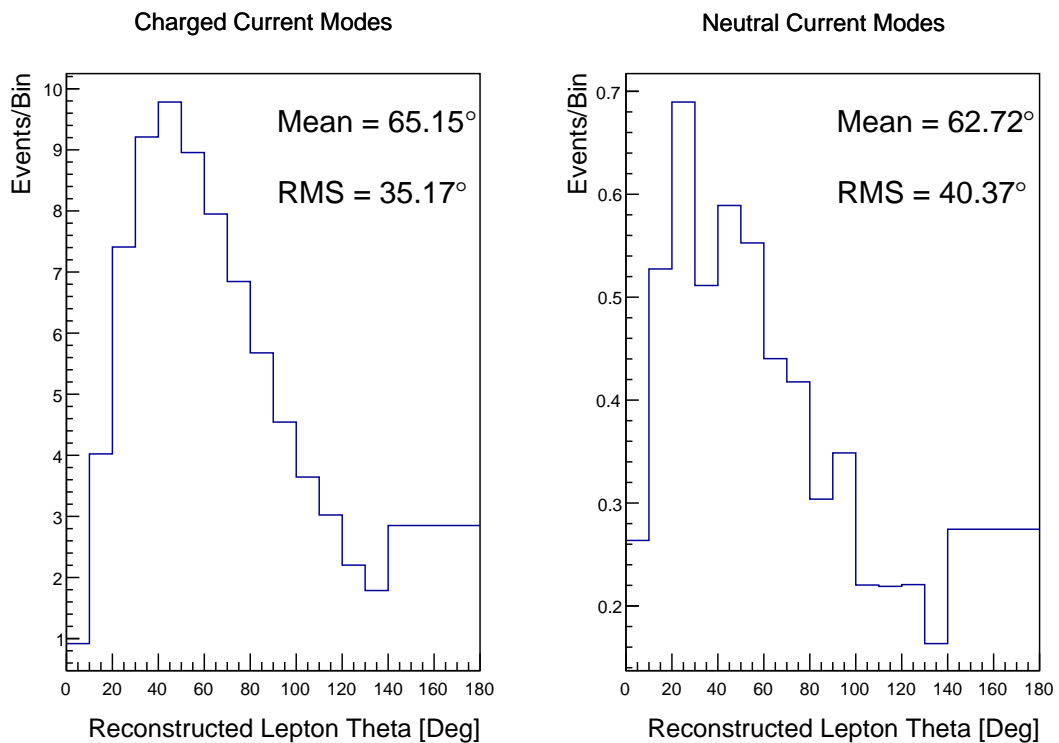


Figure 6.6: The distribution of the angle between the neutrino beam direction and the reconstructed final state lepton, for the FHC 1Re-like sample. The distribution is broken down by neutrino interaction mode into charged current (left) and neutral current (right) components. Asimov A oscillation parameter sets are assumed (given in Table 2.2). The RMS of the charged and neutral current plots are 35.17° and 40.37° , respectively.

2161 6.4 Systematic Uncertainties

2162 The systematic model parameters for this analysis are split into groups, or blocks,
2163 depending on their purpose. They consist of flux uncertainties, neutrino-matter
2164 interaction systematics, and detector efficiencies. There are also uncertainties on
2165 the oscillation parameters to which this analysis is not sensitive, namely Δm_{21}^2
2166 and $\sin^2(\theta_{12})$. These oscillation parameter uncertainties are taken from the 2020
2167 PDG measurements [76]. As described in chapter 4, each model parameter used
2168 within this analysis requires a prior uncertainty. This is provided via separate
2169 covariance matrices for each block. The covariance matrices can include prior
2170 correlations between parameters within a single block, but the separate treatment
2171 means prior correlations can not be included for parameters in different groups.
2172 Some parameters in these models have no reasonably motivated uncertainties
2173 and are assigned flat priors which do not modify the likelihood penalty. In
2174 practice, these flat prior parameters are actually assigned a Gaussian with a
2175 very large width to ensure the covariance matrix is positive definite. They are
2176 then checked at run time to determine if they contribute to the likelihood. The
2177 flux, neutrino interaction, and detector modeling simulations have already been
2178 discussed in section 5.1 and section 5.2. The uncertainties invoked within each
2179 of these models are described below.

2180 6.4.1 Beam Flux

2181 The neutrino beam flux systematics are based upon the uncertainty in the mod-
2182 eling of the components of the beam simulation. This includes the model of
2183 hadron productions and reinteractions, the shape, intensity, and alignment of
2184 the beam with respect to the target, and the uniformity of the magnetic field
2185 produced by the horn, alongside other effects. The uncertainty, as a function
2186 of neutrino energy, is illustrated in Figure 6.7 which includes a depiction of
2187 the total uncertainty as well as the contribution from individual components.
2188 The uncertainty around the peak of the energy distribution ($E_\nu \sim 0.6\text{GeV}$) is

2189 dominated by uncertainties in the beam profile and alignment. Outside of this
2190 region, uncertainties on hadron production dominate the error.

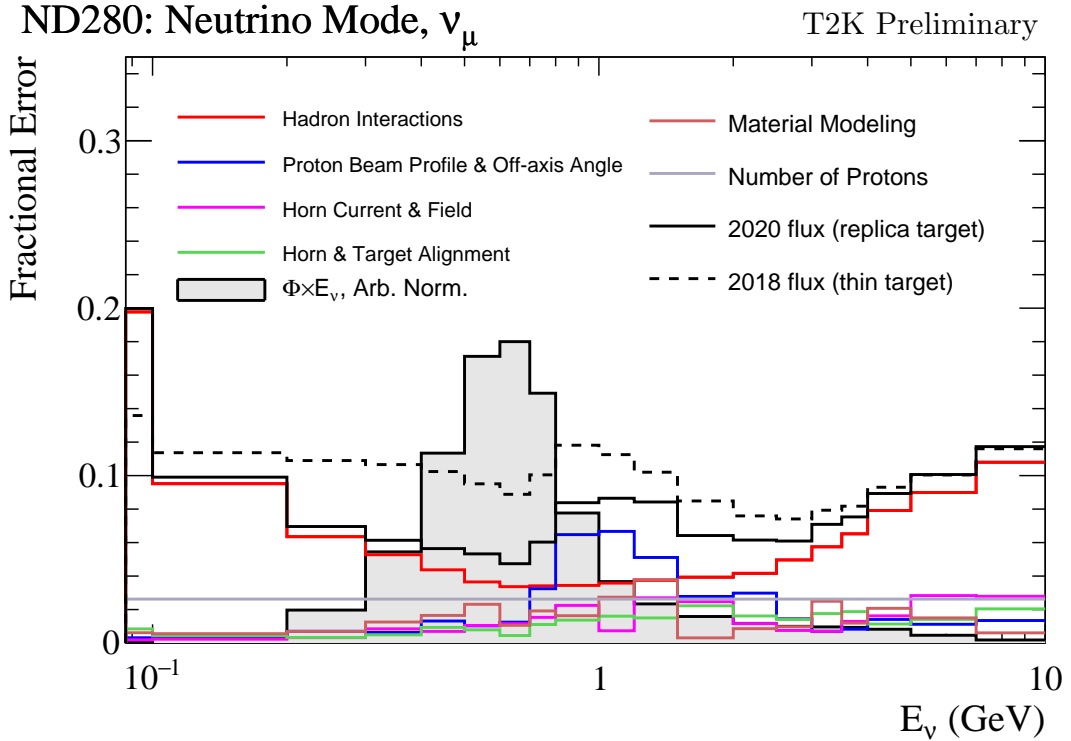


Figure 6.7: The total uncertainty evaluated on the near detector ν_μ flux prediction constrained by the replica-target data, illustrated as a function of neutrino energy. The solid(dashed) line indicates the uncertainty used within this analysis(the T2K 2018 analysis [194]). The solid histogram indicates the neutrino flux as a function of energy. Figure taken from [195].

2191 The beam flux uncertainties are described by one hundred parameters. They
2192 are split between the ND280 and SK detectors and binned by neutrino flavour:
2193 ν_μ , $\bar{\nu}_\mu$, ν_e and $\bar{\nu}_e$. The response is then broken down as a function of neutrino
2194 energy. The bin density in the neutrino energy is the same for the ν_μ in FHC
2195 and $\bar{\nu}_\mu$ in RHC beams, and narrows for neutrino energies close to the oscillation
2196 maximum of $E_\nu = 0.6\text{GeV}$. This binning is specified in Table 6.6. All of these
2197 systematic uncertainties are applied as normalisation parameters with Gaussian
2198 priors centered at 1.0 and error specified from a covariance matrix provided
2199 by the T2K beam group [195].

Neutrino Flavour	Sign	Neutrino Energy Bin Edges (GeV)
μ	Right	0., 0.4, 0.5, 0.6, 0.7, 1., 1.5, 2.5, 3.5, 5., 7., 30.
μ	Wrong	0., 0.7, 1., 1.5, 2.5, 30.
e	Right	0., 0.5, 0.7, 0.8, 1.5, 2.5, 4., 30.
e	Wrong	0., 2.5, 30.

Table 6.6: The neutrino energy binning for the different neutrino flavours. “Right” sign indicates neutrinos in the FHC beam and antineutrinos in the RHC beam. “Wrong” sign indicates antineutrinos in the FHC beam and neutrinos in the RHC beam. The binning of the detector response is identical for the FHC and RHC modes as well as at ND280 and SK.

2200 6.4.2 Atmospheric Flux

2201 The atmospheric neutrino flux is modeled by the HKKM model [53]. 16 systematic
 2202 uncertainties are applied to control the normalisation of each neutrino flavour,
 2203 energy, and direction. They are summarised below:

- 2204 • **Absolute Normalisation:** The overall normalisation of each neutrino flavour
 2205 is controlled by two independent systematic uncertainties, for $E_\nu < 1\text{GeV}$
 2206 and $E_\nu > 1\text{GeV}$, respectively. This is driven mostly by hadronic interaction
 2207 uncertainties for the production of pions and kaons [53]. The strength of
 2208 the response is dependent upon the neutrino energy. The uncertainty is
 2209 parameterized following Figure 11 in [53].
- 2210 • **Relative Normalisation:** Uncertainties on the ratio of $(\nu_\mu + \bar{\nu}_\mu) / (\nu_e + \bar{\nu}_e)$
 2211 are controlled by the difference between the HKKM model [53], FLUKA
 2212 [56] and Bartol models [52]. Three independent parameters are applied in
 2213 the energy ranges: $E_\nu < 1\text{GeV}$, $1\text{GeV} < E_\nu < 10\text{GeV}$, and $E_\nu > 10\text{GeV}$.
- 2214 • **$\nu/\bar{\nu}$ Normalisation:** The uncertainties in the π^+/π^- (and kaon equivalent)
 2215 production uncertainties in the flux of $\nu/\bar{\nu}$. The response is applied using
 2216 the same methodology as the relative normalisation parameters.
- 2217 • **Up/Down and Vertical/Horizontal Ratio:** Similar to the above two sys-
 2218 tematics, the difference between the HKKM, FLUKA, and Bartol model

2219 predictions, as a function of $\cos(\theta_Z)$, is used to control the normalisation of
 2220 events as a function of zenith angle.

- 2221 • **K/π Ratio:** Higher energy neutrinos ($E_\nu > 10\text{GeV}$) mostly originate in
 2222 kaon decay. Measurements of the ratio of K/π production [196] are used to
 2223 control the systematic uncertainty of the expected ratio of pion and kaon
 2224 production.
- 2225 • **Solar Activity:** As the 11-year solar cycle can affect the Earth's magnetic
 2226 field, the flux of primary cosmic rays varies across the same period. The
 2227 uncertainty is calculated by taking a ± 1 year variation, equating to a 10%
 2228 uncertainty for the SK-IV period.
- 2229 • **Atmospheric Density:** The height of the interaction of the primary cosmic
 2230 rays is dependent upon the atmospheric density. The HKKM assumes the
 2231 US standard 1976 [146] profile. This systematic controls the uncertainty in
 2232 that model.

2233 The total uncertainty is dominated by the absolute and relative normalisation
 2234 parameters. The effect of which is illustrated in Figure 6.8. Generally, the
 2235 uncertainty is large at low energy, reducing to $O(10\%)$ around the peak of the
 2236 flux distribution and then increasing once the neutrino energy exceeds 10GeV.

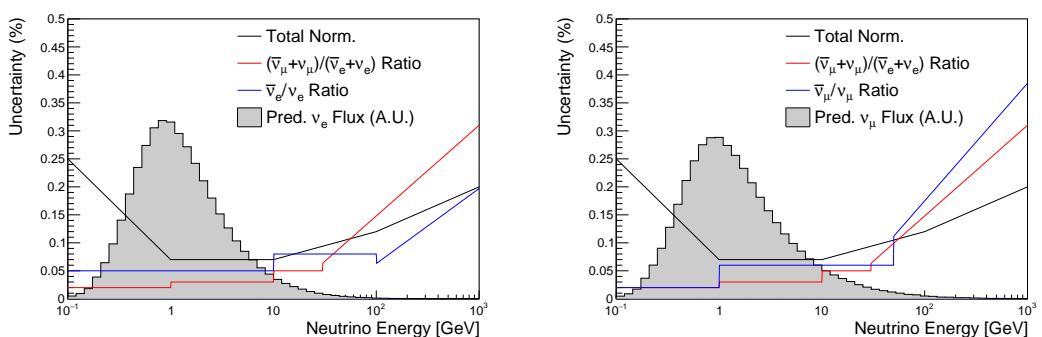


Figure 6.8: The uncertainty evaluated on the atmospheric ν_e (left) and ν_μ (right) flux predictions. The absolute normalisation and flavour ratio uncertainties are given. The solid histogram indicates the neutrino flux as a function of energy.

2237 Updates to the HKKM and Bartol models are underway [151] to use a similar
2238 tuning technique to that used in the beam flux predictions. After those updates,
2239 it may be possible to include correlations in the hadron production uncertainty
2240 systematics for beam and atmospheric flux predictions.

2241 6.4.3 Neutrino Interaction

2242 Neutrino interactions in the detectors are modeled by NEUT. The two indepen-
2243 dent oscillation analyses, T2K-only [197] and the SK-only [62], have developed
2244 separate interaction models. To maximise sensitivity out of this simultaneous
2245 beam and atmospheric analysis, a correlated interaction model has been defined
2246 in [186]. Where applicable, correlations allow the systematic uncertainties applied
2247 to the atmospheric samples to be constrained by near detector neutrino beam
2248 measurements. This can lead to stronger sensitivity to oscillation parameters
2249 as compared to an uncorrelated model.

2250 The low-energy T2K systematic model has a more sophisticated treatment
2251 of CCQE, 2p2h, and CCRES uncertainties, where extensive comparisons of
2252 this model have been performed to external data [197]. However, the model
2253 is not designed for high-energy atmospheric events, like those illustrated in
2254 Figure 5.11. Therefore the high energy systematic model from the SK-only
2255 analysis is implemented for the relevant multi-GeV, PC, and up- μ samples.
2256 The T2K CCQE model is more sophisticated so it has been implemented for
2257 all samples within this analysis, where separate low-energy and high-energy
2258 dials have been implemented. The low-energy dials are constrained by the near
2259 detector measurements and are uncorrelated to their high-energy counterparts.
2260 The author of this thesis was responsible for implementing and validating the
2261 combined cross-section model as documented in [186, 198].

2262 The high energy systematic model includes parameters developed from
2263 comparisons of Nieves and Rein-Seghal models which affect resonant pion
2264 producing interactions, comparisons of the GRV98 and CKMT models which
2265 control DIS interactions, and hadron multiplicity measurements which modulate

the normalisation of multi-pion producing events. The uncertainty on the ν_τ cross-section is particularly large and is controlled by a 25% normalisation uncertainty. These uncertainties are applied via normalisation or shape parameters. The former linearly scales the weight of all affected Monte-Carlo events, whereas the latter can increase or decrease a particular event's weight depending on its neutrino energy and mode of interaction. The response of the shape parameters is defined by third-order polynomial splines which return a weight for a particular neutrino energy. To reduce computational resources for the far detector fit, the response is binned by neutrino energy and sample binning: lepton momentum and cosine zenith binning for atmospheric splined responses and reconstructed neutrino energy and direction binning for beam samples. In total, 17 normalisation and 15 shape parameters are included in the high-energy model within this analysis.

Figure 6.9 indicates the predicted neutrino energy distribution for both beam and subGeV atmospheric samples. There is clearly significant overlap in neutrino energy between the subGeV atmospheric and beam samples, allowing similar kinematics in the final state particles. Figure 6.10 illustrates the fractional contribution of the different interaction modes per sample.

Comparing beam and atmospheric samples which target CCQE interactions (S.G. e-like 0de, S.G. μ -like [0,1]de, [FHC,RHC] 1R μ -like and [FHC,RHC] 1R e-like samples), there is a very similar contribution of CCQE, CC 2p2h, and CC1 π^\pm interactions. The samples which target CC1 π^\pm interactions, (S.G. e-like 0de, S.G. μ -like 2de and FHC 1R+1d.e e-like) also consist of very similar mode interactions.

As a consequence of the similarity in energy and mode contributions, correlating the systematic model between the beam and subGeV atmospheric samples ensures that this analysis attains the largest sensitivity to oscillation parameters while still ensuring neutrino interaction systematics are correctly accounted for. Due to its more sophisticated CCQE and 2p2h model, the T2K systematic model was chosen as the basis of the correlated model.

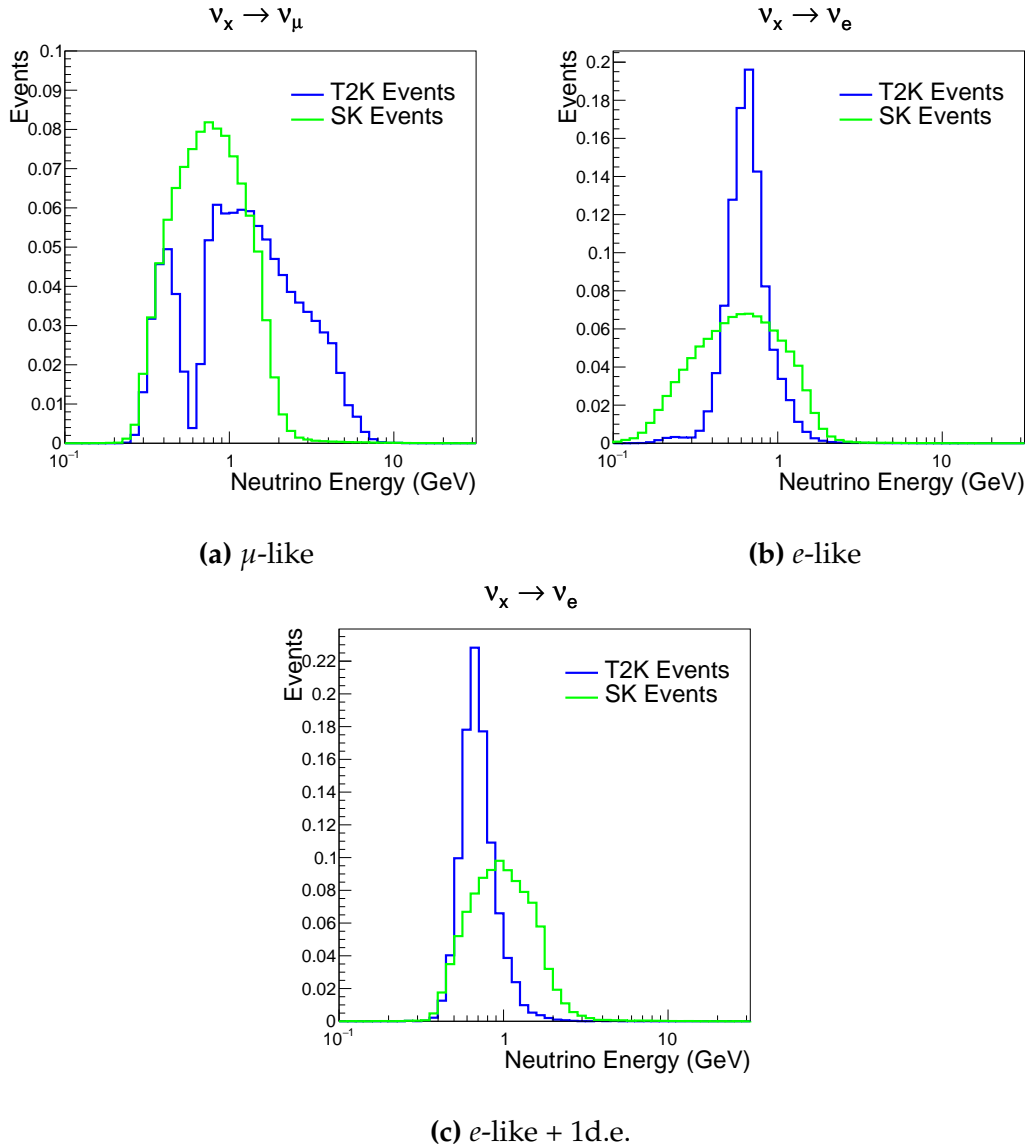


Figure 6.9: The predicted neutrino energy distribution for subGeV atmospheric and beam samples. FHC and RHC beam samples are summed together Asimov A oscillation parameters are assumed (given in Table 2.2). Beam and atmospheric samples with similar cuts are compared against one another.

2296 The T2K systematic model [197] is applied in a similar methodology to the
 2297 SK model parameters. It consists of 19 shape parameters and 24 normalisation
 2298 parameters. Four additional parameters, which model the uncertainty in the
 2299 binding energy, are applied in a way to shift the momentum of the lepton emitted
 2300 from a nucleus. This controls the uncertainty specified on the 27MeV binding
 2301 energy assumed within Equation 6.2. The majority of these parameters are

	CC QE	CC 2p2h	CC $1\pi^\pm$	CC $M\pi$	CC Other	NC $1\pi^0$	NC $1\pi^\pm$	NC $M\pi$	NC Coh.	NC Other
FHC 1R+1d.e. e-like	0.04	0.02	0.83	0.03	0.04	0.01	0.01	0.01	0.00	0.01
RHC 1R e-like	0.62	0.12	0.11	0.01	0.02	0.06	0.01	0.01	0.01	0.04
FHC 1R e-like	0.68	0.12	0.10	0.00	0.02	0.04	0.01	0.00	0.00	0.02
RHC 1R μ -like	0.62	0.13	0.17	0.02	0.03	0.00	0.02	0.00	0.00	0.00
FHC 1R μ -like	0.62	0.12	0.16	0.02	0.03	0.00	0.03	0.00	0.00	0.00
S.G. π^0 -like	0.05	0.01	0.02	0.00	0.01	0.68	0.06	0.07	0.06	0.04
S.G. μ -like 2de	0.04	0.01	0.80	0.10	0.04	0.00	0.00	0.00	0.00	0.00
S.G. μ -like 1de	0.72	0.11	0.12	0.01	0.02	0.00	0.01	0.00	0.00	0.00
S.G. μ -like 0de	0.68	0.11	0.10	0.01	0.02	0.01	0.05	0.01	0.00	0.02
S.G. e-like 1de	0.05	0.01	0.75	0.10	0.05	0.00	0.01	0.02	0.00	0.01
S.G. e-like 0de	0.73	0.11	0.10	0.01	0.02	0.02	0.00	0.00	0.00	0.00

Figure 6.10: The interaction mode contribution of each sample given as a fraction of the total event rate in that sample. Asimov A oscillation parameters are assumed (given in Table 2.2). The Charged Current (CC) modes are broken into quasi-elastic (QE), 2p2h, resonant charged pion production ($1\pi^\pm$), multi-pion production ($M\pi$), and other interaction categories. Neutral Current (NC) interaction modes are given in interaction mode categories: π^0 production, resonant charged pion production, multi-pion production, and others.

2302 assigned a Gaussian prior uncertainty. Those that have no reasonably motivated
 2303 uncertainty, or those which have not been fit to external data, are assigned a
 2304 flat prior which does not affect the penalty term.

2305 On top of the combination of the SK and T2K interaction models, several
 2306 other parameters have been specifically developed for the joint oscillation anal-
 2307 ysis. The majority of the atmospheric samples' δ_{CP} sensitivity comes from the
 2308 normalisation of subGeV electron-like events. These are modeled using a spectral
 2309 function to approximate the nuclear ground state. However, the near detector is
 2310 not able to constrain the model so an additional systematic is introduced which
 2311 models an alternative Continuous Random Phase Approximation (CRPA) nuclear
 2312 ground state. This dial approximates the event weights if a CRPA model had

been assumed rather than a spectral function. This dial only applies to ν_e and $\bar{\nu}_e$ as the near detector does not constraint ν_e cross-section measurements. It is applied as a shape parameter.

Further additions to the model have been introduced due to the inclusion of the subGeV π^0 atmospheric sample. This particularly targets charged current and neutral current π^0 producing interactions to help constrain the systematic uncertainties. Therefore, an uncertainty that affects neutral current resonant π^0 production is incorporated into this analysis. Comparisons of NEUT's NC resonant pion production predictions have been made to MiniBooNE [199] data and a consistent 16% to 21% underprediction is observed [186]. Consequently, a conservative 30% normalisation parameter is invoked.

Down-going events are mostly insensitive to oscillation parameters and can act similar to the near detector within an accelerator experiment (Details will be discussed in chapter 7). This region of phase space can act as a sideband and allows the cross-section model and near detector constraint to be studied. The distribution of events in this region is calculated using the technique outlined in subsection 4.3.4. The results are illustrated in Figure 6.11. For CCQE-targeting samples, the application of the near detector constraint is well within the statistical fluctuation of the down-going data. This means there is no significant tension is observed between the data and the Monte Carlo prediction after the near detector constraint is applied. This is not the case for samples with target CCRES interactions. The electron-like data is consistent with the constrained prediction at high reconstructed momenta but diverges at lower momentum, whereas the muon-like sample is under-predicted throughout the range of momenta. To combat this disagreement, an additional cross-section systematic dial, specifically designed to inflate the low pion momentum systematics was developed in [186]. This is a shape parameter implemented through a splined response.

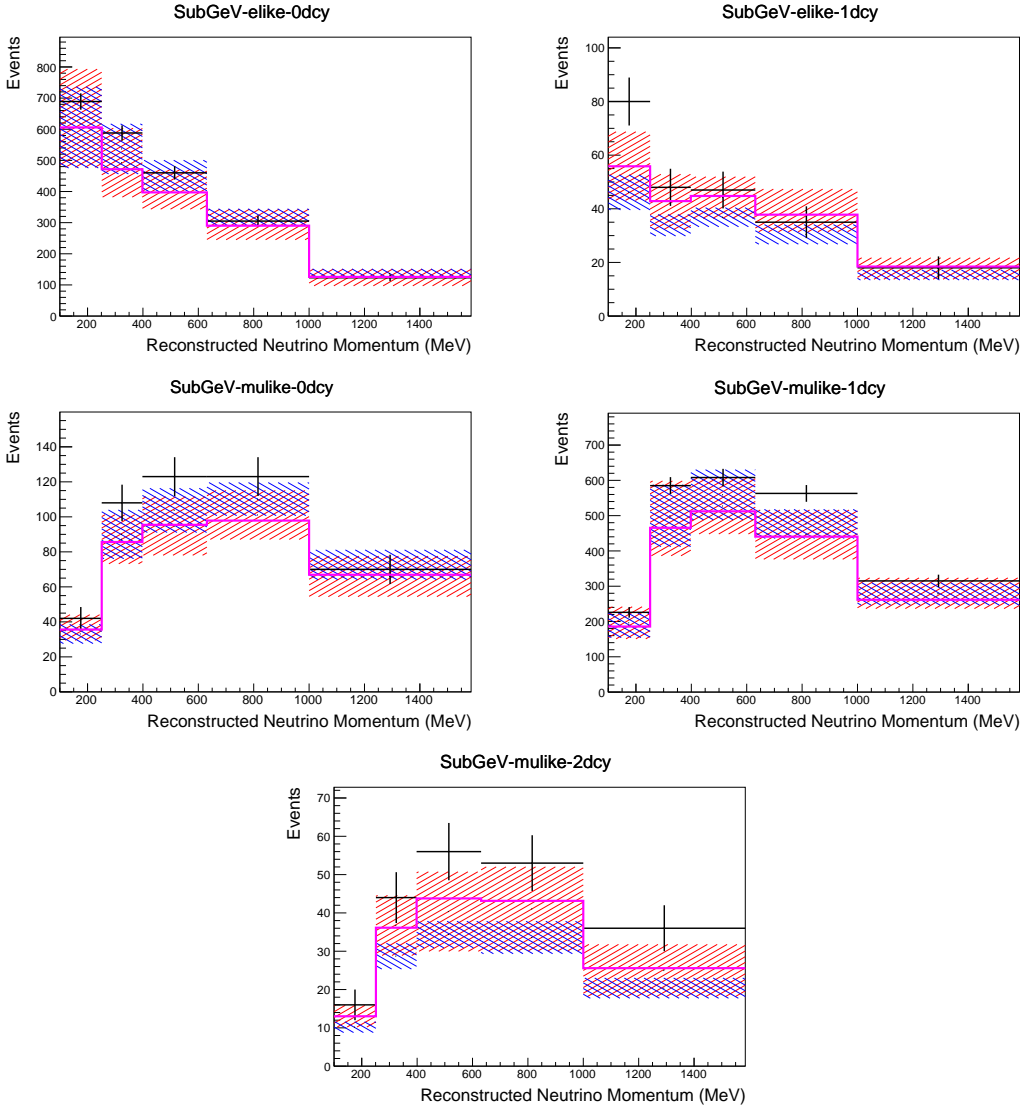


Figure 6.11: Down-going atmospheric subGeV single-ring samples comparing the mean and error of the pre-fit and post-fit Monte Carlo predictions in red and blue, respectively. The magenta histogram illustrates the Monte Carlo prediction using the generated dial values. The black points illustrate the down-going data with statistical errors given. The mean and errors of the Monte Carlo predictions are calculated by the techniques documented in subsection 4.3.4. The pre-fit spectrum is calculated by throwing the cross-section and atmospheric flux dial values from the pre-fit covariance matrix. The post-fit spectrum is calculated by sampling the cross-section dial values from an ND fit MCMC chain, whilst still throwing the atmospheric flux dials from the pre-fit covariance.

2340 6.4.4 Near Detector

2341 The systematics applied due to uncertainties arising from the response of the near
 2342 detector is documented in [126]. The response is described by 574 normalisation
 2343 parameters binned in the selected sample as well as momentum and angle,

2344 P_μ and $\cos(\theta_\mu)$, of the final-state muon. These are applied via a covariance
2345 matrix with each parameter being assigned a Gaussian prior from that covariance
2346 matrix. These normalisation parameters are built from underlying systematics,
2347 e.g. pion secondary interaction systematics, which are randomly thrown and
2348 the variation in each $P_\mu \times \cos(\theta_\mu)$ bin is determined. Two thousand throws are
2349 evaluated and a covariance matrix response is created. This allows significant
2350 correlations between FGD1 and FGD2 samples, as well as adjacent $P_\mu \times \cos(\theta_\mu)$
2351 bins. Statistical uncertainties are accounted for by including fluctuations of each
2352 event's weight from a Poisson distribution.

2353 Similar to the cross-section systematics, MaCh3 and BANFF are used to
2354 constrain the uncertainty of these systematics through independent validations.
2355 Each fitter generates a post-fit covariance matrix which is compared and passed
2356 to the far-detector oscillation analysis working group. As the analysis presented
2357 within this thesis uses the MaCh3 framework, a joint oscillation analysis fit of all
2358 three sets of samples and their respective systematics is performed.

2359 6.4.5 Far Detector

2360 Two configurations of the far detector systematic model implementation have
2361 been considered. Firstly, the far detector systematic uncertainties for beam and
2362 atmospheric samples are taken from their respective analysis inputs, denoted
2363 “official inputs” analysis, with no correlations assumed between the beam and at-
2364 mospheric samples. The beam- and atmospheric-specific inputs are documented
2365 in subsubsection 6.4.5.1 and subsubsection 6.4.5.2. Secondly, an alternative
2366 detector model has been developed which correlates the response of the SK
2367 detector systematics between the beam and atmospheric samples. Here, the
2368 distribution of parameters used for applying event cuts (e.g. electron-muon
2369 PID separation) is modified within the fit. It follows a similar methodology to
2370 the beam far detector systematics implementation but performs a joint fit of
2371 the beam and atmospheric data. This alternative implementation is detailed
2372 in subsubsection 6.4.5.3.

2373 **6.4.5.1 Beam Samples**

2374 There are 45 systematics which describe the response of the far detector to
2375 beam events [179], split into 44 normalisation parameters and one energy scale
2376 systematic. The energy scale systematic is applied as a multiplicative scaling
2377 of the reconstructed neutrino energy. It is estimated from data-to-Monte Carlo
2378 differences in the stopping muon sample in [62] and found to be 2.1%. The
2379 normalisation parameters are assigned a Gaussian error centered at one with
2380 width taken from a covariance matrix. A detailed breakdown of the generation
2381 of the covariance matrix is found in [192]. To build the covariance matrix, a fit
2382 is performed on atmospheric data which has been selected using beam sample
2383 selection cuts. These cuts use the variables, L^i , where the index i is detailed in
2384 Table 6.7. Each L^i is a smear, α , and shift, β parameter such that,

$$L_j^i \rightarrow \bar{L}_j^i = \alpha_j^i L + \beta_j^i. \quad (6.4)$$

2385 Where L_j^i (\bar{L}_j^i) correspond to nominal(varied) PID cut parameters given in
2386 Table 6.7. The shift and smear parameters are nuisance parameters with no prior
2387 constraints. They are binned by final-state topology, j , where the binning is given
2388 in Table 6.8. The final-state topology binning is because the detector will respond
2389 differently to events that have one or multiple rings. For example, the detector
2390 will be able to distinguish single-ring events better than two overlapping ring
2391 events, resulting in different systematic uncertainty for one-ring events compared
2392 to two-ring events. This approach is used to allow the cut parameter distributions
2393 to be modified within the fit, allowing for better data to Monte Carlo agreement.

Cut Variable	Parameter Name
0	<code>fitQun e/mu PID</code>
1	<code>fitQun e/pi0 PID</code>
2	<code>fitQun mu/pi PID</code>
3	<code>fitQun Ring-Counting Parameter</code>

Table 6.7: List of cut variables that are included within the shift/smear fit documented in [192].

Category	Description
1e	Only one electron above Cherenkov threshold in the final state
1 μ	Only one muon above Cherenkov threshold in the final state
1e+other	One electron and one or more other charged particles above Cherenkov threshold in the final state
1 μ +other	One muon and one or more other charged particles above Cherenkov threshold in the final state
1 π^0	Only one π^0 in the final state
1 π^\pm or 1p	Only one hadron (typically charged pion or proton) in the final state
Other	Any other final state

Table 6.8: Reconstructed event topology categories on which the SK detector systematics [192] are based.

2394 The mis-modeling of π^0 events is also considered. If one of the two rings
 2395 from a π^0 event is missed, this will be reconstructed as a CC ν_e -like event. This
 2396 is one of the largest systematics hindering the electron neutrino appearance
 2397 analyses. Consequently, additional systematics have been introduced to con-
 2398 strain the mis-modeling of π^0 events in SK, binned by reconstructed neutrino
 2399 energy. To evaluate this systematic uncertainty, a set of “hybrid- π^0 ” samples is
 2400 constructed. These events are built by overlaying one electron-like ring from
 2401 the SK atmospheric neutrino samples or decay electron ring from a stopping
 2402 cosmic ray muon with one simulated photon ring. Both rings are chosen so
 2403 that momenta and opening angle follow the decay kinematics of NC π^0 events
 2404 from the T2K-MC. Hybrid- π^0 Monte Carlo samples with both rings from the
 2405 SK Monte Carlo are produced to compare with the hybrid- π^0 data samples and
 2406 the difference in the fraction of events that pass the ν_e selection criteria is used
 2407 to assign the systematic errors. In order to investigate any data to Monte Carlo
 2408 differences that may originate from either the higher energy ring or lower energy
 2409 ring, two samples are built; a sample in which the electron constitutes the higher
 2410 energy ring from the π^0 decay (called the primary sample) and another one in
 2411 which it constitutes the lower energy ring (called the secondary sample). The
 2412 standard T2K ν_e fitQun event selection criteria are used to select events.

2413 Final contributions to the covariance matrix are determined by supplemen-
 2414 tary uncertainties obtained by comparing stopping muon data to Monte Carlo

prediction, as first introduced in section 5.2. The efficiency of tagging decay electrons is estimated by the stopping muon data to Monte Carlo differences by comparing the number of one decay electron events to the number of events with one or fewer decay electrons. Similarly, the rate at which fake decay electrons are reconstructed by `fiTQun` is estimated by comparing the number of two decay electron events to the number of events with one or two reconstructed decay electrons. The two sources of systematics are added in quadrature weighted by the number of events with one true decay electron yielding a 0.2% systematic uncertainty. A fiducial volume systematic of $\pm 2.5\text{cm}$ which corresponds to a 0.5% shift in the normalisation of events is also applied. Additional normalisation uncertainties based on neutrino flavour and interaction mode are also defined in [179, 200, 201].

Two additional sources of uncertainty are included: secondary and photoneuclear interactions. These are estimated by varying the underlying parameters are building a distribution of sample event rates. These contributions are then added in quadrature to the above covariance matrix. The final uncertainty on the SK detector systematics are provided in Figure 6.12.

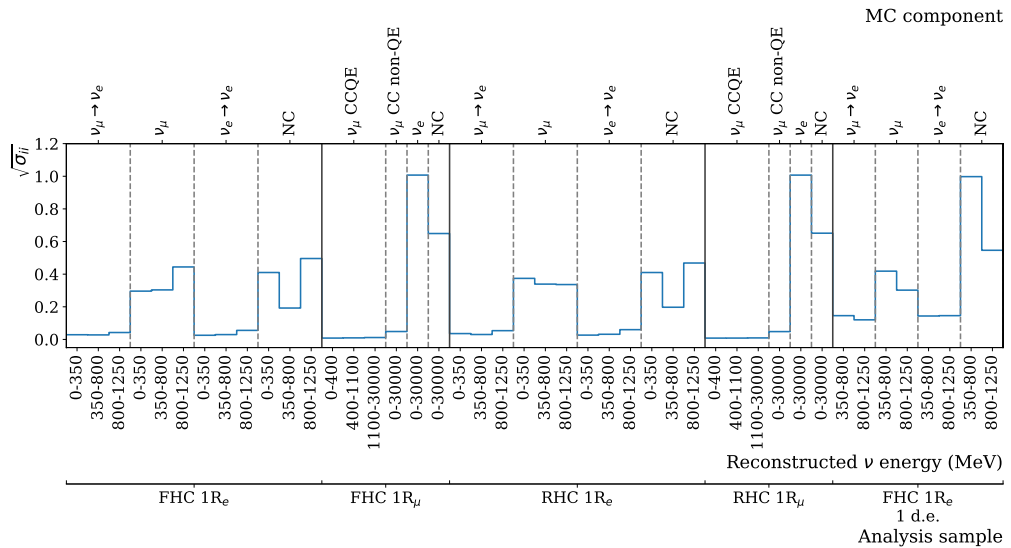


Figure 6.12: The fractional uncertainty on each of the 44 parameters describing the SK detector systematics (The energy scale systematic is neglected). The parameters are split by sample, oscillation channel, interaction mode and reconstructed neutrino energy.

2432 6.4.5.2 Atmospheric Samples

2433 The detector systematics for atmospheric samples, documented in [3], are split
2434 into two sub-groups: those which are related to particle identification and ring
2435 counting systematics, and those which are related to calibration, separation,
2436 and reduction uncertainties.

2437 The particle identification systematics consist of five parameters. The ring sep-
2438 aration systematic enforces an anti-correlated response between the single-ring
2439 and multi-ring samples. This is implemented as a fractional increase/decrease
2440 in the overall normalisation of each sample, depending on the distance to the
2441 nearest wall from an event's vertex. The coefficients of the normalisation are
2442 estimated prior to the fit and depend on the particular atmospheric sample. Two
2443 electron-muon separation systematics are included within this model which
2444 anti-correlates the response of the electron-like and muon-like samples: one for
2445 single-ring events and another for multi-ring events.

2446 The multi-ring electron-like separation likelihood, discussed in section 6.1,
2447 encodes the ability of the detector to separate neutrino from anti-neutrino events.
2448 Two normalisation parameters vary the relative normalisation of multi-ring ν_e
2449 and $\bar{\nu}_e$ samples whilst keeping a consistent overall event rate.

2450 There are 22 systematics related to calibration measurements, including effects
2451 from backgrounds, reduction, and showering effects. They are documented in
2452 [3] and are briefly summarised in Table 6.9. They are applied via normalisation
2453 parameters, with the separation systematics requiring the conservation of event
2454 rate across all samples.

2455 6.4.5.3 Correlated Detector Model

2456 A complete uncertainty model of the SK detector would be able to determine
2457 the systematic shift on the sample spectra for a variation of the underlying
2458 parameters, e.g. PMT angular acceptance. However, this is computationally
2459 intensive, requiring Monte Carlo predictions to be made for each plausible
2460 variation. Consequently, an effective parameter model has been utilised for

Index	Description
0	Partially contained reduction
1	Fully contained reduction
2	Separation of fully contained and partially contained events
3	Separation of stopping and through-going partially contained events in top of detector
4	Separation of stopping and through-going partially contained events in barrel of detector
5	Separation of stopping and through-going partially contained events in bottom of detector
6	Background due to cosmic rays
7	Background due to flasher events
8	Vertex systematic moving events into and out of fiducial volume
9	Upward going muon event reduction
10	Separation of stopping and through-going in upward going muon events
11	Energy systematic in upward going muon events
12	Reconstruction of the path length of upward going muon events
13	Separation of showering and non-showering upward going muon events
14	Background of stopping upward going muon events
15	Background of non-showering through-going upward going muon events
16	Background of showering through-going upward going muon events
17	Efficiency of tagging two rings from π^0 decay
18	Efficiency of decay electron tagging
19	Background from downgoing cosmic muons
20	Asymmetry of energy deposition in tank
21	Energy scale deposition

Table 6.9: Sources of systematic errors specified within the grouped into the “calibration” systematics model.

2461 a correlated detector model following from the T2K-only model implementation
 2462 documented in subsubsection 6.4.5.1. It correlates the detector systematics
 2463 between the far-detector beam and subGeV atmospheric samples due to their
 2464 similar energies and interaction types. As there are no equivalent beam samples,
 2465 the multi-GeV, multiring, PC, and Up- μ samples will be subject to the particle
 2466 identification systematics implementation as described in subsubsection 6.4.5.2
 2467 rather than using this correlated detector model. The calibration systematics also
 2468 described in the aforementioned chapter still apply to all atmospheric samples.
 2469 The correlated detector model utilises the same smear and shift parameters
 2470 documented in subsubsection 6.4.5.1, split by final state topology. Beyond this,

the shift and smear parameters are split by visible energy deposited within the detector, with binning specified in Table 6.10. This is because atmospheric events are categorised by subGeV and multi-GeV events based on visible energy, so this splitting is required when correlating the systematic model for beam and atmospheric events. Alongside the technical requirement, higher energy events will be better reconstructed due to fractionally less noise within the detector. As a result of the inclusion of visible energy binning, Equation 6.4 becomes

$$L_{jk}^i \rightarrow \bar{L}_{jk}^i = \alpha_{jk}^i L + \beta_{jk}^i, \quad (6.5)$$

where k is the visible energy bin.

Index	Range (MeV)
0	$30 \geq E_{vis} > 300$
1	$300 \geq E_{vis} > 700$
2	$700 \geq E_{vis} > 1330$
3	$E_{vis} \geq 1330$

Table 6.10: Visible energy binning for which the correlated SK detector systematics are based

The implementation of this systematic model takes the events reconstructed values of the cut parameters, modifies them by the particular shift and smear parameter for that event, and then re-applies event selection. This causes event migration, which is a new feature incorporated into the MaCh3 framework which is only achievable due to the event-by-event reweighting scheme.

Particular care has to be taken when varying the ring counting parameter. This is because the number of rings is a finite value (one-ring, two-ring, etc.) which can not be continuously varied through this shift and smear technique. Consequently a continuous ring counting parameter, RC_i , is calculated for the i^{th} event, following the definition in [178]: the preferred likelihoods from all considered one-ring (L_{1R}) and two-ring (L_{2R}) fits are determined. The difference

2490 is computed as $\Delta_{LLH} = \log(L_{1R}) - \log(L_{2R})$. The ring counting parameter is
 2491 then defined as

$$RC_i = \text{sgn}(\Delta_{LLH}) \times \sqrt{|\Delta_{LLH}|}, \quad (6.6)$$

2492 where $\text{sgn}(x) = x/|x|$. This ring counting parameter corresponds to an
 2493 intermediate likelihood value used within the `fitQun` algorithm to decide the
 2494 number of rings associated with a particular event. However, fake-ring merging
 2495 algorithms are applied after this likelihood value is used. Consequently, this
 2496 ring counting parameter does not always exactly correspond to the number of
 2497 reconstructed rings. This can be seen in Figure 6.13.

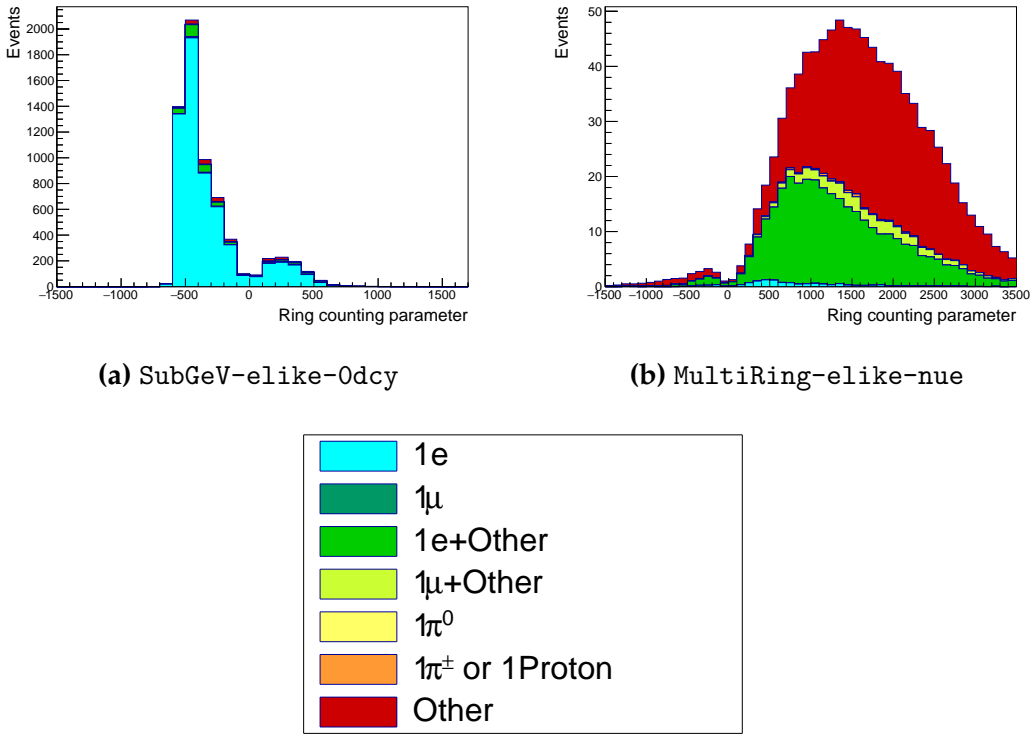


Figure 6.13: The ring counting parameter as defined in Equation 6.6 for the SubGeV-elike-0dcy and MultiRing-elike-nue samples.

2498 As the `fitQun` algorithm does not provide a likelihood value after the fake-
 2499 ring algorithms have been applied, the ring counting parameter distribution is
 2500 correlated to the final number of reconstructed rings through “maps”. These

2501 are two-dimensional distributions of the ring counting parameter and the final
 2502 number of reconstructed rings. An example is illustrated in Figure 6.14. In
 2503 principle, the `fitQun` reconstruction algorithm should be re-run after the variation
 2504 in the ring counting parameter. However, this is not computationally viable.
 2505 Therefore the “maps” are used as a reweighting template.

2506 The maps are split by final state topology and true neutrino flavour and
 2507 all `fitQun`-reconstructed Monte Carlo events are used to fill them. The maps
 2508 are row-normalised to represent the probability of X rings for a given RC_i
 2509 value. Prior to the oscillation fit, an event’s nominal weight is calculated as
 2510 $W^i(N_{Rings}^i, L_{jk}^i)$, where N_{Rings}^i is the reconstructed number of rings for the i^{th}
 2511 event and $W^i(x, y)$ is the bin content in map associated with the i^{th} event, where
 2512 x number of rings and y is ring counting parameter. Then during the fit, the
 2513 value of $R = W^i(N_{Rings}^i, \bar{L}_{jk}^i) / W^i(N_{Rings}^i, L_{jk}^i)$ is calculated as the event weight
 2514 for the i^{th} event. This is the only cut variable that uses a reweighting technique
 2515 rather than event migration.

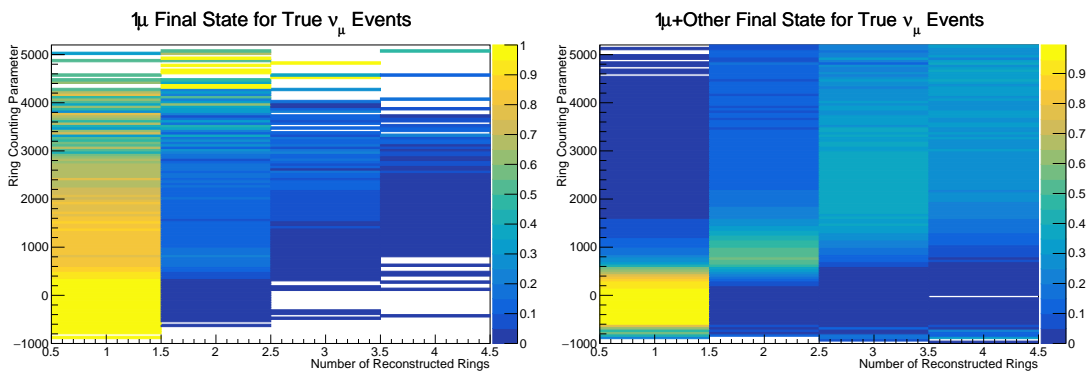


Figure 6.14: The ring counting parameter, defined in Equation 6.6, as a function of the number of reconstructed rings as found by the `fitQun` reconstruction algorithm. Left: true ν_μ events with only one muon above the Cherenkov threshold in the final state. Right: true ν_μ events with one muon and at least one other charged particle above the Cherenkov threshold in the final state.

2516 The π^0 systematics introduced in subsection 6.4.4 are applied via a covariance
 2517 matrix. This is not possible in the alternative model as no covariance matrix
 2518 is used. Thus, the implementation of the π^0 systematics has been modified.
 2519 The inputs from the hybrid π^0 sample are included via the use of “ χ^2 maps”,

which are two-dimensional histograms in α_{jk}^i and β_{jk}^i parameters over some range. Illustrative examples of the χ^2 maps are given in Figure 6.15. Due to their nature, the shift and smear parameters are typically very correlated. A map is produced for each cut parameter given in Table 6.7 and for each visible energy bin given in Table 6.10.

The maps are filled through the χ^2 comparison of the hybrid π^0 Monte Carlo and data in the particle identification parameters documented in Table 6.7. The Monte Carlo distribution is modified by the α_{jk}^i and β_{jk}^i scaling, whilst cross-section and flux nuisance parameters are thrown from their prior uncertainties. The χ^2 between the scaled Monte Carlo and data is calculated and the relevant point in the χ^2 map is filled.

The implementation within this alternative detector model is to add the bin contents of the maps, for the relevant values of the α_{jk}^i and β_{jk}^i parameters, to the likelihood penalty. Only $1\pi^0$ final state topology shift and smear parameters use this prior uncertainty.

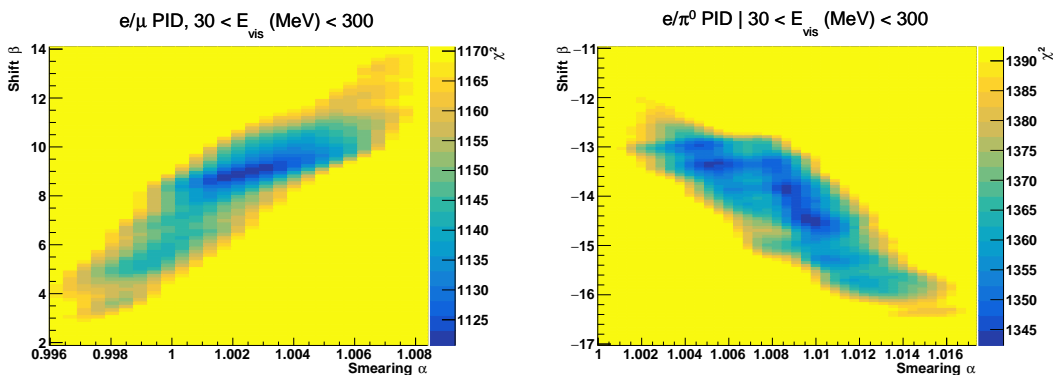


Figure 6.15: The χ^2 between the hybrid- π^0 Monte Carlo and data samples, as a function of smear (α) and shift (β) parameters, for events which have $1\pi^0$ final state topology. Left: Electron-muon separation PID parameter for events with $30 \leq E_{\text{vis}}(\text{MeV}) < 300$. Right: Electron- π^0 separation PID parameter for events with $30 \leq E_{\text{vis}}(\text{MeV}) < 300$.

Similarly, the implementation of the supplementary systematics documented in subsubsection 6.4.5.1 needs to be modified. A new framework [202] was built in tandem between the author of this thesis and the T2K-SK working group [179] so the additional parameters can be incorporated into the MaCh3 framework. These are applied as normalisation parameters, depending on the particular

2540 interaction mode, number of tagged decay electrons, and whether the primary
2541 particle generated Cherenkov light. They are assigned Gaussian uncertainties
2542 with widths described by a covariance matrix. Furthermore, the secondary
2543 interaction and photo-nuclear effects need to be accounted for in this detector
2544 model using a different implementation than that in subsubsection 6.4.5.1. This
2545 was done by including a shape parameter for each of the secondary interactions
2546 and the photo-nuclear systematic parameters.

2547 There are a total of 224 α_{jk}^i and β_{jk}^i parameters, of which 32 have prior
2548 constraints from the hybrid π^0 samples.

2549 One final complexity of this correlated detector model is that the two sets
2550 of samples, beam and subGeV atmospheric, use slightly different parameters
2551 to distinguish electron and muon-like events. The T2K samples use the value
2552 of $\log(L_e/L_\mu)$ whereas the atmospheric samples use the value of $\log(L_e/L_\pi)$,
2553 where L_X is the likelihood for hypothesis X. This is because the T2K fits use
2554 single-ring fiTQun fitting techniques, whereas multi-ring fits are applied to the
2555 atmospheric samples where only the electron and pion hypothesis are considered.
2556 The correlation between the two likelihood ratios is illustrated in Figure 6.16. As
2557 discussed in section 5.2, the pion hypothesis is a very good approximation of the
2558 muon hypothesis due to their similar mass. Consequently, using the same shift
2559 and smear parameters correlated between the beam and subGeV atmospheric
2560 samples is deemed a good approximation.

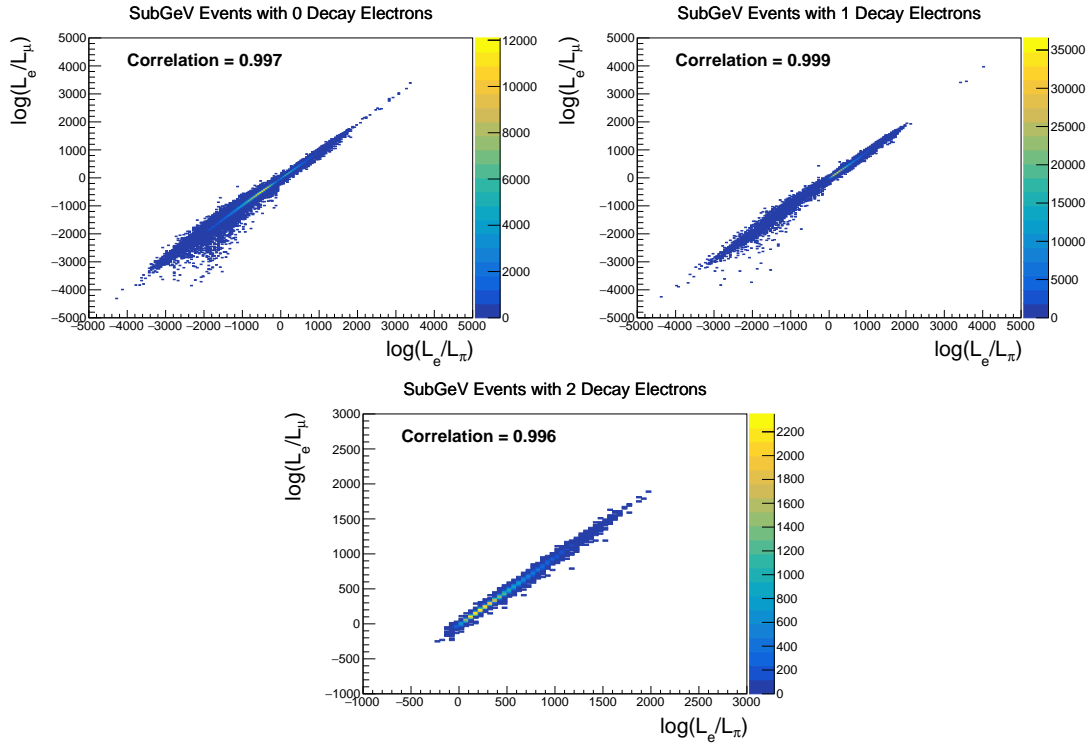


Figure 6.16: The distribution of $\log(L_e/L_\mu)$ compared to $\log(L_e/L_\pi)$ for subGeV events with zero (top left), one (top right) or two (bottom) decay electrons. The correlation in the distribution is calculated as 0.997, 0.999 and 0.996, respectively.

6.5 Likelihood Calculation

This analysis performs a joint oscillation parameter fit of the ND280 beam samples, the T2K far detector beam samples, and the SK atmospheric samples introduced in this chapter.

Once the Monte Carlo predictions of each beam and atmospheric sample have been built, a likelihood needs to be constructed. This is done by comparing the binned Monte Carlo prediction to binned data. The Monte Carlo prediction is calculated at a particular point, $\vec{\theta}$, in the model parameter space such that $N_i^{MC} = N_i^{MC}(\vec{\theta})$, where N_i represents the bin content of the i^{th} bin. The data and Monte Carlo spectra are represented by N_i^D and N_i^{MC} , respectively. The bin contents for the beam near detector, beam far detector and atmospheric samples are denoted with *ND*, *FD*, and *Atm*, respectively. Taking the FHC1Rmu far detector sample as an example, the binning index runs over all the reconstructed neutrino

2574 energy bins. The likelihood calculation between the data and the Monte Carlo
2575 prediction for a particular bin follows a Poisson distribution, where the data
2576 is treated as a fluctuation of the simulation.

2577 The data can consist of either real data or an ‘Asimov’ Monte Carlo prediction,
2578 which is typically used for sensitivity studies and denoted ‘Asimov data’. The
2579 process for building Asimov data is as follows. The Monte Carlo prediction is
2580 reweighted using a particular set of oscillation parameters (potentially those
2581 listed in Table 2.2) and systematic parameter tune. The resulting spectra for each
2582 sample is then defined to be the Asimov data for that sample. Whilst this results
2583 in unphysical non-integer data predictions, it eliminates statistical fluctuations
2584 from the data. Therefore, the results of a fit to Asimov data should not include any
2585 biases from statistical fluctuations. Furthermore, these results should produce
2586 posterior probability distributions consistent with the parameters which were
2587 used to make the data prediction. That is to say, the fit results should return the
2588 known parameters. Any biases seen would be attributed to correlations between
2589 each oscillation parameter and correlations between oscillation and systematic
2590 parameters. Consequently, Asimov fit results present the maximum precision
2591 at which the oscillation parameters could be measured to.

2592 Following the T2K analysis presented in [2], the likelihood contribution for
2593 the near detector samples also includes a Monte Carlo statistical uncertainty
2594 term, derived from the Barlow and Beeston statistical treatment [203, 204]. It
2595 includes a contribution to the likelihood that treats the generated Monte Carlo
2596 prediction as a statistical fluctuation of the actual true simulation assuming an
2597 infinite amount of statistics had been created. The technical implementation of
2598 this additional likelihood term is documented in [187] and briefly summarised
2599 as follows. The term is defined as,

$$\frac{(\beta_i - 1)^2}{2\sigma_{\beta_i}^2}, \quad (6.7)$$

2600 where β_i represents a scaling parameter for the i^{th} bin that relates the bin
2601 content for the amount of Monte Carlo actually generated N_i^{MC} to the bin content

2602 if an infinite amount of Monte Carlo statistics had been generated $N_{i,true}^{MC}$, such
 2603 that $N_{i,true}^{MC} = \beta_i \times N_i^{MC}$. In the case where a sufficient amount of Monte Carlo
 2604 statistics had been generated, $\beta_i = 1$. An analytical solution for β_i is given in
 2605 [187]. Additionally, $\sigma_{\beta_i} = \sqrt{\sum_i w_i^2 / N_i^{MC}}$ where $\sqrt{\sum_i w_i^2}$ represents the sum of
 2606 the square of the weights of the Monte Carlo events which fall into bin i .

2607 An additional contribution to the likelihood comes from the variation of
 2608 the systematic model parameters. For those parameters with well-motivated
 2609 uncertainty estimates, a covariance matrix, V , describes the prior knowledge of
 2610 each parameter as well as any correlations between the parameters. Due to a
 2611 technical implementation, a single covariance matrix describes each “block” of
 2612 model parameters, e.g. beam flux systematics. The covariance matrix associated
 2613 with the k^{th} block is denoted V^k . There are seven individual blocks of system-
 2614 atics ($N_b = 7$): oscillation parameters, beam flux systematics, atmospheric flux
 2615 systematics, neutrino interaction systematics, near detector systematics, beam
 2616 far detector systematics, and atmospheric far detector systematics. The number
 2617 of parameters in the k^{th} block is defined as $n(k)$.

2618 The equation for the likelihood \mathcal{L} includes all the terms discussed above,

$$\begin{aligned}
 -\ln(\mathcal{L}) = & \\
 & \sum_i^{\text{NDbins}} N_i^{\text{ND},MC}(\vec{\theta}) - N_i^{\text{ND},D} + N_i^{\text{ND},D} \times \ln \left[N_i^{\text{ND},D} / N_i^{\text{ND},MC}(\vec{\theta}) \right] + \frac{(\beta_i - 1)^2}{2\sigma_{\beta_i}^2} \\
 & + \sum_i^{\text{FDbins}} N_i^{\text{FD},MC}(\vec{\theta}) - N_i^{\text{FD},D} + N_i^{\text{FD},D} \times \ln \left[N_i^{\text{FD},D} / N_i^{\text{FD},MC}(\vec{\theta}) \right] \\
 & + \sum_i^{\text{Atmbins}} N_i^{\text{Atm},MC}(\vec{\theta}) - N_i^{\text{Atm},D} + N_i^{\text{Atm},D} \times \ln \left[N_i^{\text{Atm},D} / N_i^{\text{Atm},MC}(\vec{\theta}) \right] \\
 & + \frac{1}{2} \sum_k^{\text{N}_b} \sum_i^{n(k)} \sum_j^{n(k)} (\vec{\theta}^k)_i (V^k)_{ij}^{-1} (\vec{\theta}^k)_j.
 \end{aligned} \tag{6.8}$$

2619 The negative log-likelihood value is determined at each step of the MCMC
 2620 to build the posterior distribution defined in chapter 4. This value is minimised
 2621 when the Monte Carlo prediction tends towards the data spectrum.

7

2622

2623

Oscillation Probability Calculation

2624 It is important to understand how and where the sensitivity to the oscillation parameters comes from for both atmospheric and beam samples. An
2625 overview of how these samples respond to changes in δ_{CP} , Δm_{32}^2 , and $\sin^2(\theta_{23})$
2626 is given in section 2.5. This section also explains the additional complexities
2627 involved when performing an atmospheric neutrino analysis as compared to
2628 a beam-only analysis.

2630 Without additional techniques, atmospheric sub-GeV upward-going neutrinos ($E_\nu < 1.33\text{GeV}, \cos(\theta_Z) < 0.$) can artificially inflate the sensitivity to $\delta_{CP,zaza}$
2631 due to the quickly varying oscillation probability in this region. Therefore, a
2632 “sub-sampling” approach has been developed to reduce these biases ensuring
2633 accurate and reliable sensitivity measurements. This technique ensures that small-
2634 scale unresolvable features of the oscillation probability have been averaged over
2635 whilst the large-scale features in the oscillation probability are unaffected. The
2636 documentation and validation of this technique are found in section 7.1. The
2637 oscillation probability calculation is computationally intensive due to the large
2638 number of matrix multiplications needed. Consequently, the CUDAProb3 imple-
2639 mentation choice made within the fitting framework, as detailed in section 7.2,
2640 ensures that the analysis can be done in a timely manner.

Whilst the beam neutrinos are assumed to propagate through a constant density slab of material, the density variations through the Earth result in more complex oscillation patterns for atmospheric neutrinos. Furthermore, the uncertainty in the electron density can modify the oscillation probability for the denser core layers of the Earth. The model of the Earth used within this analysis is detailed in section 7.3. This includes information about the official SK-only methodology as well as improvements that have been made to remove some of the approximations used in that analysis. Another complexity of atmospheric neutrino oscillation studies is that the height of production in the atmosphere is not known on an event-by-event basis. An analytical averaging technique that approximates the uncertainty of the oscillation probability has been followed, with the author of this thesis being responsible for the implementation and validation. This implementation of an external technique is described in section 7.4.

7.1 Treatment of Fast Oscillations

As shown in Figure 7.1, atmospheric neutrino oscillations have a significantly more complex structure for upgoing neutrinos with energy below 1GeV. This is because the L/E dependence of the oscillation probability in this region induces rapid variations for small changes in L or E . As discussed in section 2.5, this is also the region in which atmospheric neutrinos have sensitivity to δ_{CP} . In practice, the direction of the neutrino is inferred from the direction of the final state particles traveling in the detector. The correlation between these two directions can be particularly weak for low-energy neutrino interactions. This creates a distinct difference from the beam neutrinos where the position of the source is very precisely known.

As a consequence of the unresolvable structure, an event rate consistent with the averaged oscillation probability is observed in the subGeV upgoing region. This creates a computational problem: A significantly large amount of Monte Carlo statistics would be required to accurately predict the number of events if Monte Carlo averaging was the only technique used. This section describes

2671 the ‘sub-sampling’ approach developed for this analysis and compares it to the
2672 methodology used within the SK-only analysis.

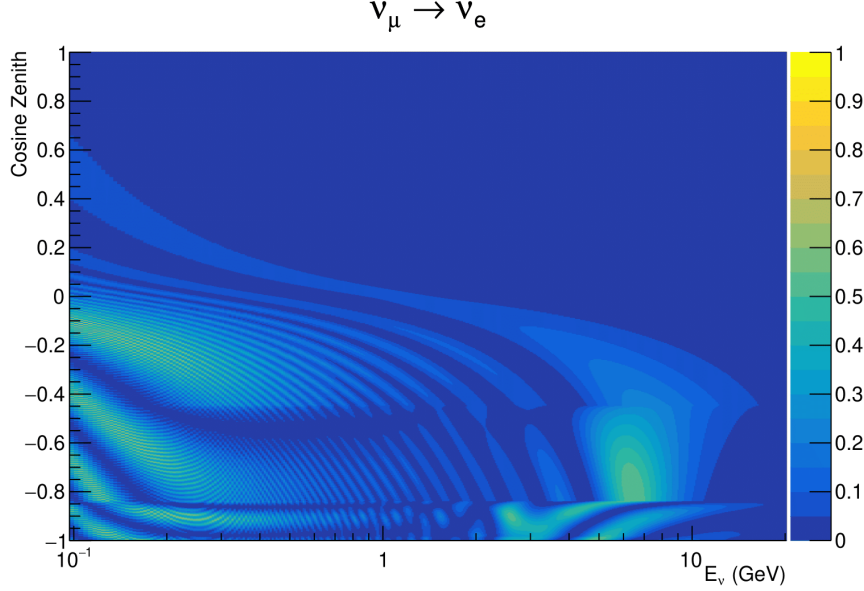


Figure 7.1: The oscillation probability $P(\nu_\mu \rightarrow \nu_e)$, given as a function of neutrino energy and zenith angle, which highlights an example of the “fast” oscillations in the sub-GeV upgoing region.

2673 The official SK-only analysis uses the osc3++ oscillation parameter fitter
2674 [79]. To perform the fast oscillation averaging, it uses a ‘nearest-neighbour’
2675 technique. For a given Monte Carlo neutrino event, the nearest twenty Monte
2676 Carlo neighbours in reconstructed lepton momentum and zenith angle are
2677 found and a distribution of their neutrino energies is built. The RMS, σ , of
2678 this distribution is then used to compute an average oscillation probability for
2679 the given neutrino Monte Carlo event.

2680 For the i^{th} event, the oscillation weight is calculated as

$$W_i = \frac{1}{5}P(E_i, \bar{L}_i) + \frac{1}{5}\sum_{\beta=-1, -0.5, 0.5, 1} P(E_i + \beta\sigma_i, L_\beta), \quad (7.1)$$

2681 where $P(E, L)$ is the oscillation probability calculation for neutrino energy E
2682 and path length L and the two path lengths, \bar{L}_i and L_β are described below. All
2683 of the oscillation probability calculations are performed with a fixed zenith angle
2684 such that the same density profile is used. The uncertainty in the production

height is controlled by using an “average” production height, \bar{L}_i , which represents the average path length computed using twenty production heights taken from the Honda flux model’s prediction [55]. These inputs are provided in 5% intervals of the cumulative distribution function. The value of \bar{L}_i is calculated as:

$$\bar{L}_i = \frac{1}{20} \sum_{j=1}^{20} \sqrt{(R_E + h_j)^2 - R_E^2 (1 - \cos^2 \theta_i)} - R_E \cos \theta_i. \quad (7.2)$$

Where R_E is the Earth’s radius and θ_i is the zenith angle of the i^{th} event. The production heights h_j represent the $(j \times 5)^{th}$ percentile of the cumulative distribution function. L_β values (where the values of β are given in Equation 7.1) are similarly calculated but instead use different combinations of four production heights,

$$\begin{aligned} L_{-1.0} &= \frac{1}{4} L(45, 50, 55, 60), \\ L_{-0.5} &= \frac{1}{4} L(35, 40, 65, 70), \\ L_{+0.5} &= \frac{1}{4} L(25, 30, 75, 68), \\ L_{+1.0} &= \frac{1}{4} L(15, 20, 85, 89). \end{aligned} \quad (7.3)$$

Where $L(i, j, k, l)$ represents the sum of the path lengths with fixed zenith angle and production heights corresponding to the i^{th} , j^{th} , k^{th} and l^{th} percentile of the cumulative distribution function. The values that are taken as β (and values for L_β) are chosen to smooth the oscillation contours in Δm_{32}^2 without incurring loss of sensitivity [205].

This averaging technique works because of the inference between the zenith angle and the reconstructed direction of final state particles in the detector. For low-energy neutrinos, where the resolution of the true neutrino direction is poor, σ_i will be large, resulting in significant averaging effects. Contrary to this, the inferred direction of high-energy neutrinos will be much closer to the true value, meaning that σ_i will be smaller, culminating in small averaging effects.

In practice, these calculations are performed prior to the fit as only oscillation parameters at fixed points are considered. The MCMC technique used in this thesis requires oscillation probabilities to be evaluated at arbitrary parameter values, not known *a priori*. Calculating the five oscillation probabilities per event required by the SK technique is computationally infeasible, so a different averaging technique is used. However, the concept of the averaging technique can be taken from it.

To perform a similar averaging as the SK analysis, a sub-sampling approach using binned oscillograms has been devised. A coarsely binned oscillogram is defined in $\cos(\theta_Z)$ and E_ν . For a given set of oscillation parameters, a single oscillation probability will be assigned to each coarse bin. This value will then apply to all Monte Carlo events which fall into that bin. To assign these oscillation probabilities, the probability is calculated at $N \times N$ points on a grid within a particular bin. This ensemble of oscillation probabilities is averaged to define the coarse bin's oscillation probability, assuming a flat prior in E_ν and $\cos(\theta_Z)$ within the bin. Figure 7.2 illustrates the $N = 2$ example where the assigned value to a coarse bin is the average of the four fine bins which fall in that coarse bin. Whilst the coarse bin edges do not have to be linear on either axis, the sub-division of the fine bins is linear within the range of a coarse bin.

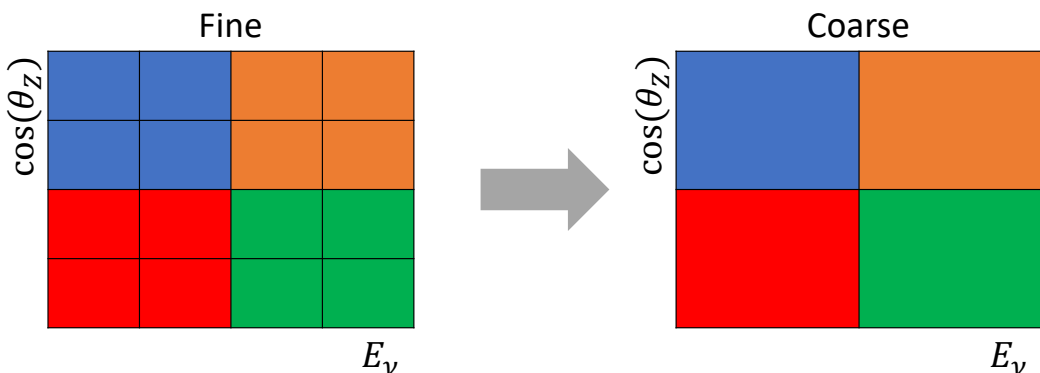


Figure 7.2: Illustration of the averaging procedure for $N = 2$. The oscillation probabilities calculated on the finer left binning are averaged to obtain the oscillation probabilities in the coarser right binning. These averaged oscillation probabilities with the coarser binning are then applied to each event during the fit.

2724 The coarse binning is defined with 67×52 bins in true neutrino energy \times
 2725 cosine zenith. It is picked to be identical to that provided in [205]. In general, the
 2726 binning is logarithmically spaced in neutrino energy but has some hand-picked
 2727 bin edges around the matter resonance to smoothly increased the bin density.
 2728 This is to avoid smearing this region which can be well sampled by the Monte
 2729 Carlo. The cosine zenith binning is approximately linearly spaced across the
 2730 allowable range but the values of layer transitions are hit precisely: -0.8376 (core-
 2731 mantle) and -0.4464 (mantle/transition zone). Bins are spread further apart for
 2732 downgoing events as this is a region unaffected by the fast oscillation wavelengths
 2733 and reduces the total number of calculations required to perform the calculation.

2734 The choice of N is justified based on two studies. Firstly, the variation of event
 2735 rates of each sample is studied as a function of N . For a given set of oscillation
 2736 parameters thrown from the PDG prior constraints (detailed in Table 2.1), the
 2737 oscillation probabilities are calculated using a given value of N . Each sample
 2738 is re-weighted and the event rate is stored. The value of N is scanned from
 2739 1, which corresponds to no averaging, to 19, which corresponds to the largest
 2740 computationally viable subdivision binning. The event rate of each sample at
 2741 large N is expected to converge to a stationary value due to the fine binning fully
 2742 sampling the small-scale structure. Figure 7.3 illustrates this behaviour for the
 2743 SubGeV_elike_0dcy sample for 9 different throws of the oscillation parameters.

2744 Denoting the event rate for one sample for a given throw t at each N by λ_t^N ,
 2745 the average over all considered N values ($\bar{\lambda}_t = \frac{1}{24} \sum_{N=1}^{24} \lambda_t^N$) is computed. The
 2746 variance in the event rate at each N is then calculated as

$$\text{Var}[\lambda^N] = \frac{1}{N_{\text{throws}}} \sum_{t=1}^{N_{\text{throws}}} \left(\lambda_t^N - \bar{\lambda}_t \right)^2 - \left[\frac{1}{N_{\text{throws}}} \sum_{t=1}^{N_{\text{throws}}} \left(\lambda_t^N - \bar{\lambda}_t \right) \right]^2. \quad (7.4)$$

2747 In practice, the following procedure is undertaken. For a particular throw,
 2748 the difference between the event rate at a particular choice of N and the mean
 2749 of the distribution is calculated. This is illustrated in Figure 7.4. This value
 2750 is then calculated for all the 2000 throws, generating a distribution of $\lambda_t^N - \bar{\lambda}_t$.

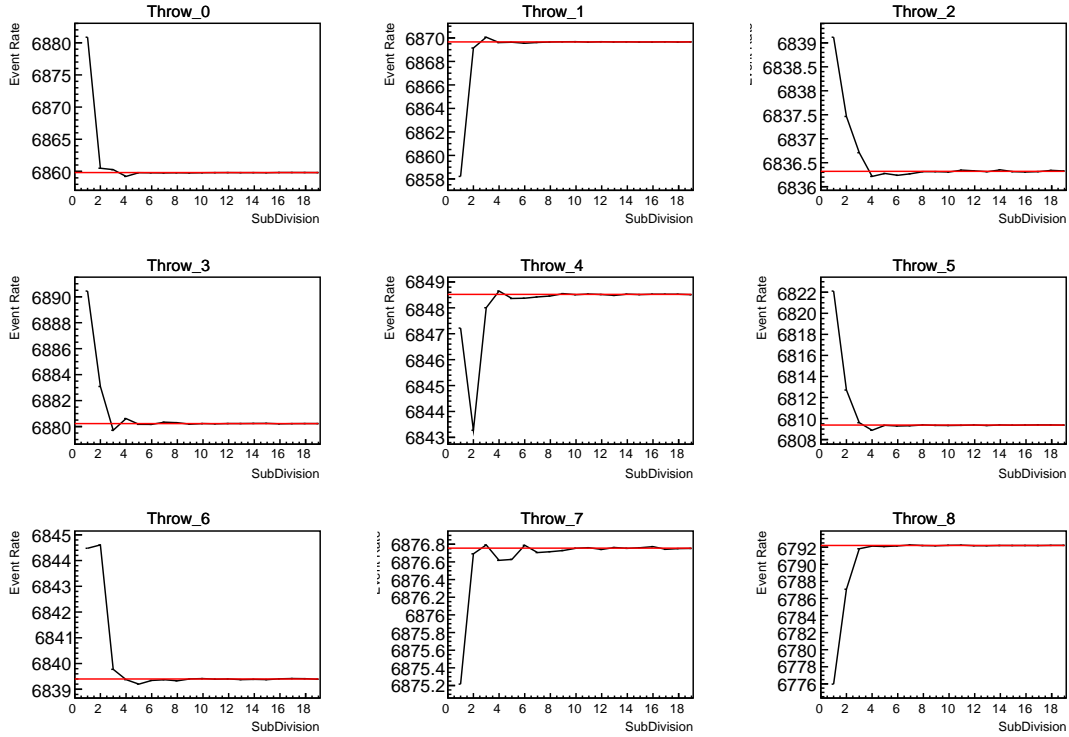


Figure 7.3: Event rate of the SubGeV_elike_0dcy sample as a function of the number of sub-divisions per coarse bin. Each subplot represents the event rate of the sample at a different oscillation parameter set thrown from the PDG priors detailed in Table 2.1. The red line in each subplot represents the mean of the event rate over the different values of sub-divisions for that particular oscillation parameter throw.

2751 This is repeated for each of the values of N considered within this study. The
 2752 distributions of this value, for $N = \{1, 5\}$, are given in Figure 7.5. As expected,
 2753 the distribution gets narrower and tends towards zero for the higher values of N .

2754 The aim of the study is to find the lowest value of N such that this variance
 2755 is below 0.001. This utilises the width of the distributions given in Figure 7.5.
 2756 This is the typical threshold used by T2K fitters to validate systematic imple-
 2757 mentation so has been set as the same criteria. The results of this study for
 2758 each atmospheric sample used within this thesis are illustrated in Figure 7.6 for
 2759 2000 throws of the oscillation parameters. As can be seen, the variance is below
 2760 the threshold at $N = 10$, and is driven primarily by the SubGeV_mulike_1dcy
 2761 and SubGeV_elike_0dcy samples.

2762 The second study to determine the value of N is as follows. The likelihood
 2763 for each sample is computed against an Asimov data set created with Asimov A

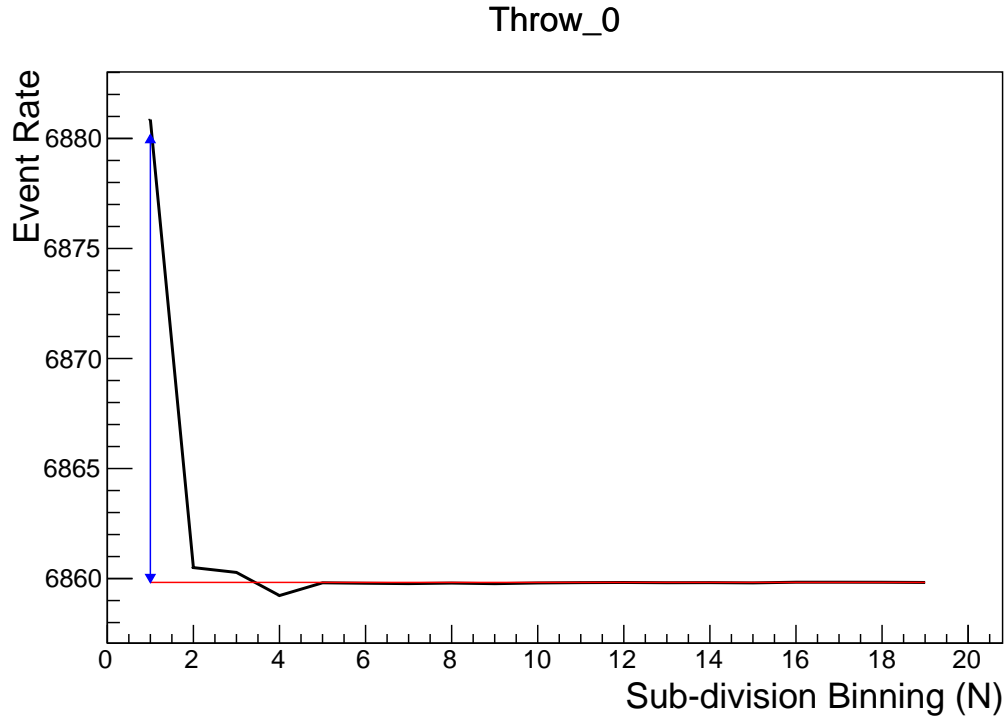


Figure 7.4: Event rate of the SubGeV_elike_0dcy sample, for a particular oscillation parameter throw, as a function of the number of sub-divisions, N , per coarse bin. The difference between the mean event rate (red), $\bar{\lambda}$, and the event rate at $N = 1$, $\lambda^{N=1}$ is defined as $\lambda^N - \bar{\lambda}$ and illustrated by the blue arrow.

2764 oscillation parameters (Table 2.2). Following Equation 7.4, the variance of the log-
2765 likelihood over all considered N is computed. The results are shown in Figure 7.7.

2766 A choice of $N = 10$ sub-divisions per coarse bin has a variance in both
2767 event rate and log-likelihood residuals less than the required threshold of 0.001.
2768 The largest value of the likelihood variance is of order 10^{-7} , corresponding to
2769 an error on the log-likelihood of about 3×10^{-4} which is small enough to be
2770 negligible for the oscillation analysis.

2771 Figure 7.8 illustrates the effect of the smearing using $N = 10$. The fast oscilla-
2772 tions in the sub-GeV upgoing region have been replaced with a normalisation
2773 effect whilst the large matter resonance structure remains.

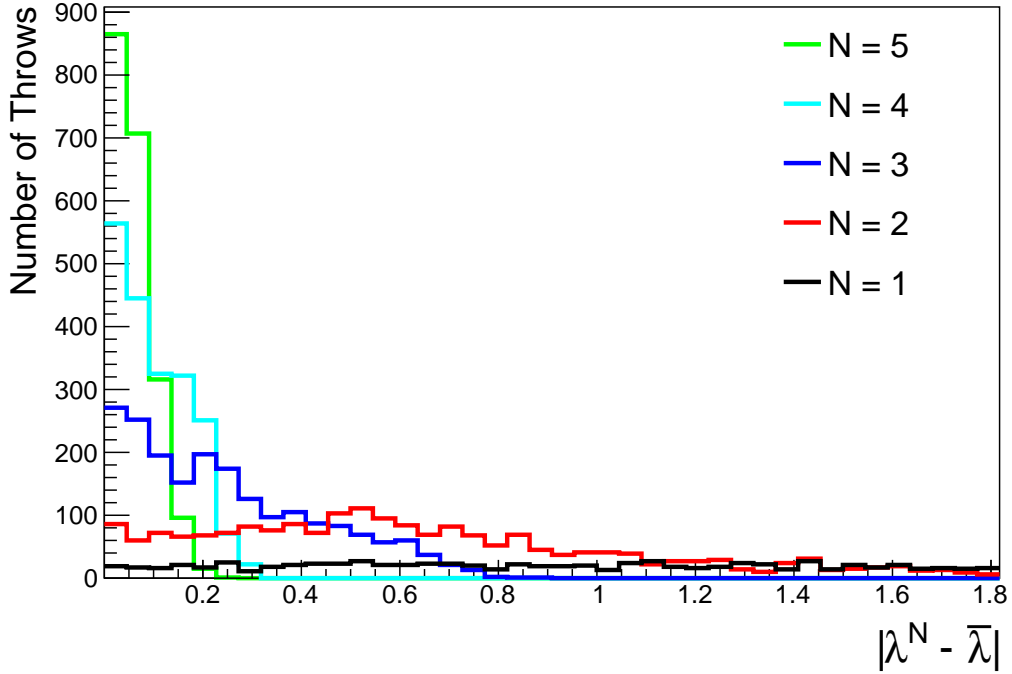


Figure 7.5: The distribution of $\lambda^N - \bar{\lambda}$ for various values of N . As expected, the distribution gets narrower for larger values of N .

2774 7.2 Calculation Engine

2775 As previously discussed in section 7.1, the calculation of oscillation probabilities
 2776 is performed at run-time. Consequently, the time per calculation is crucial for fit
 2777 performance. The initial fitting framework used for this analysis was developed
 2778 with ProbGPU [206]. This is a GPU-only implementation of the prob3 engine
 2779 [207]. It is primarily designed for neutrino propagation in a beam experiment
 2780 (single layer of constant density) with the atmospheric propagation code not
 2781 being used prior to the analysis in this thesis.

2782 Another engine, CUDAProb3 [208], has been interfaced with the fitting frame-
 2783 work used in this analysis. This interfacing was done by the author of this
 2784 thesis. It has been specifically optimised for atmospheric neutrino oscillation
 2785 calculation so does not contain the code to replace the beam oscillation calculation.
 2786 The engine utilises object-orientated techniques as compared to the functional
 2787 implementation of ProbGPU. This allows the energy and cosine zenith arrays to

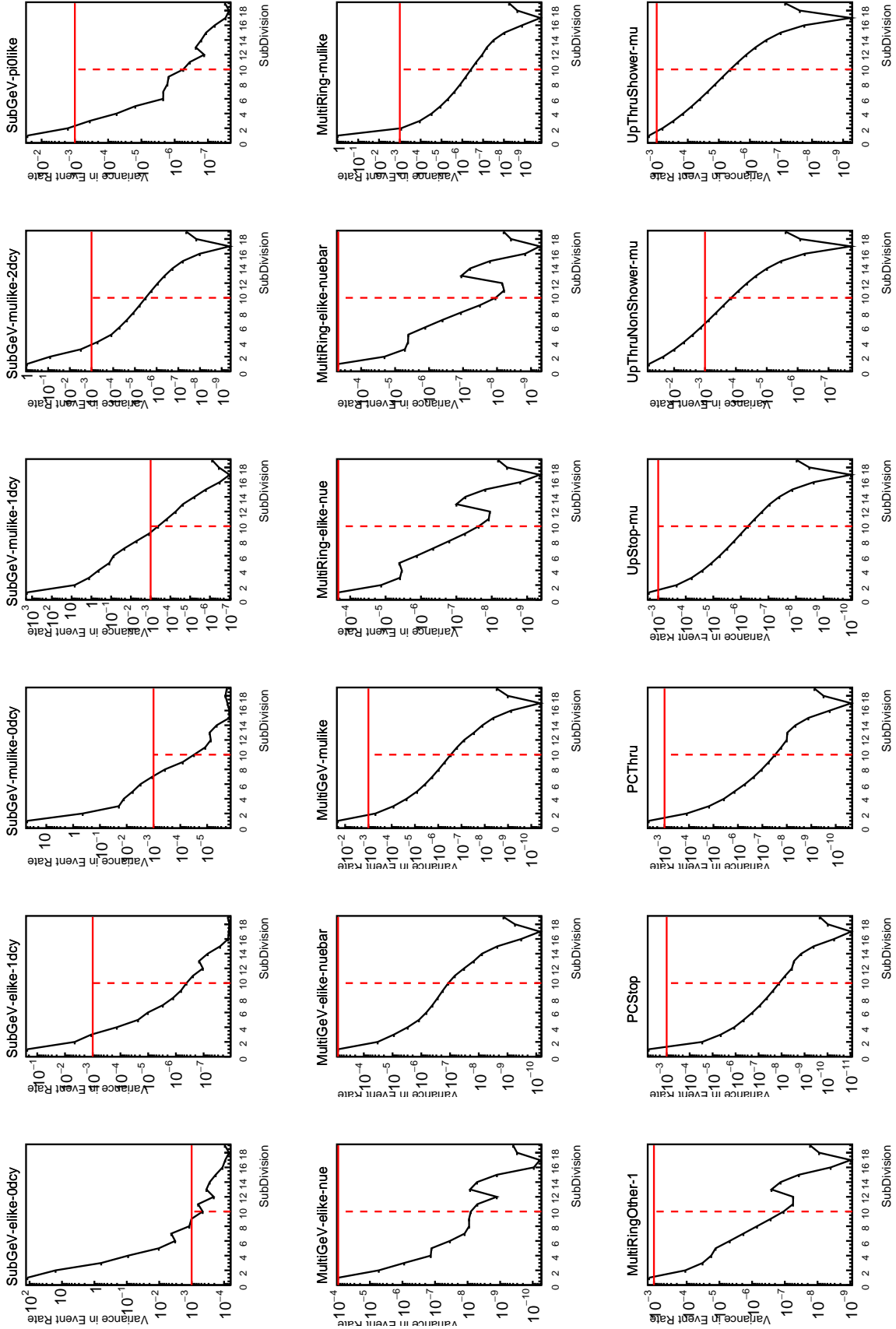


Figure 7.6: Variance of event rate for each atmospheric sample as a function of the number of sub-divisions per coarse bin. The solid red line indicates the 0.1% threshold and the dashed red line indicates the variance at a sub-division $N = 10$.

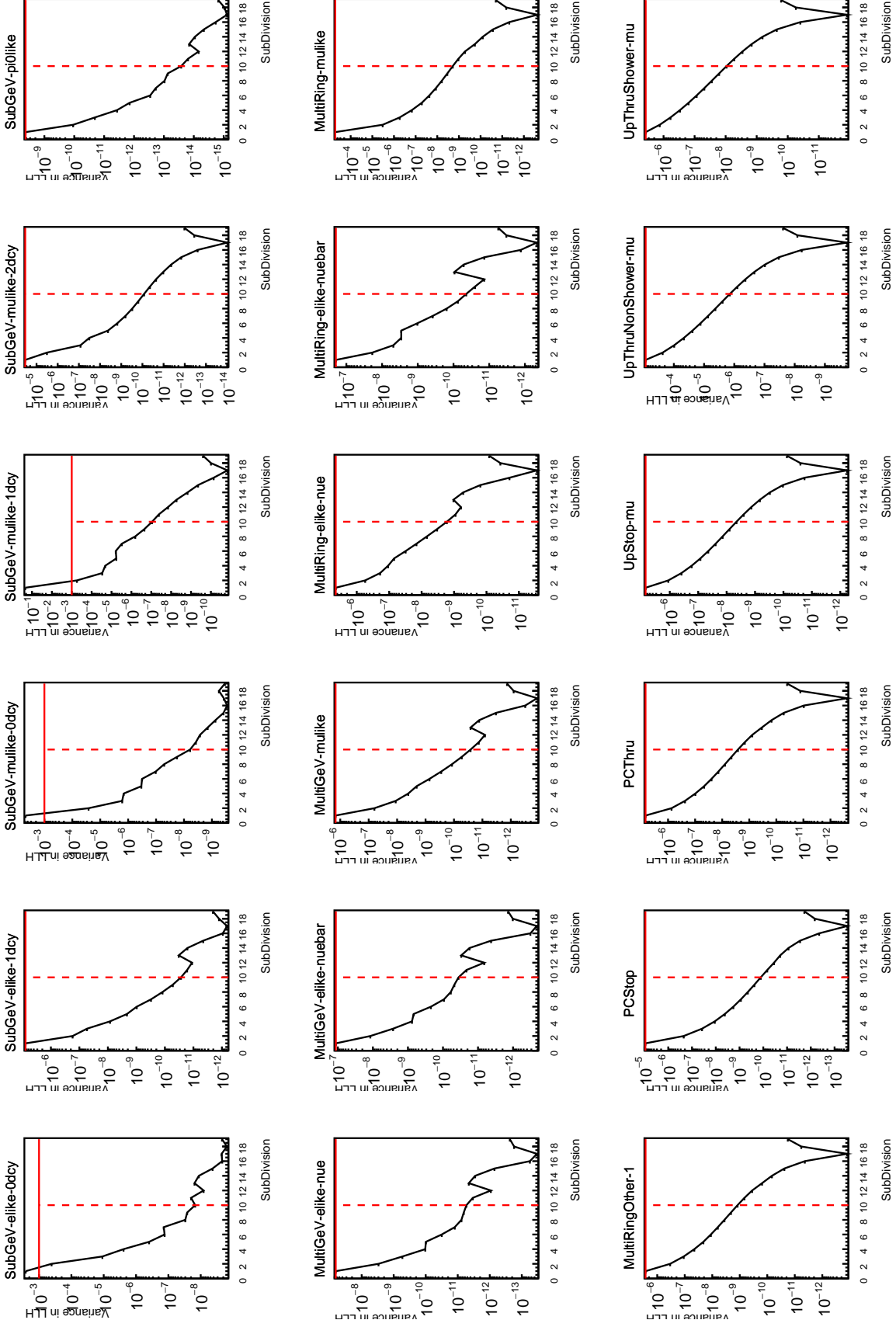


Figure 7.7: Variance of sample likelihood, when compared to 'Asimov data' set at Asimov A, for each atmospheric sample as a function of the number of sub-divisions per coarse bin. The solid red line indicates the 0.1% threshold and the dashed red line is a graphical indication of the variance at a sub-division $N = 10$.

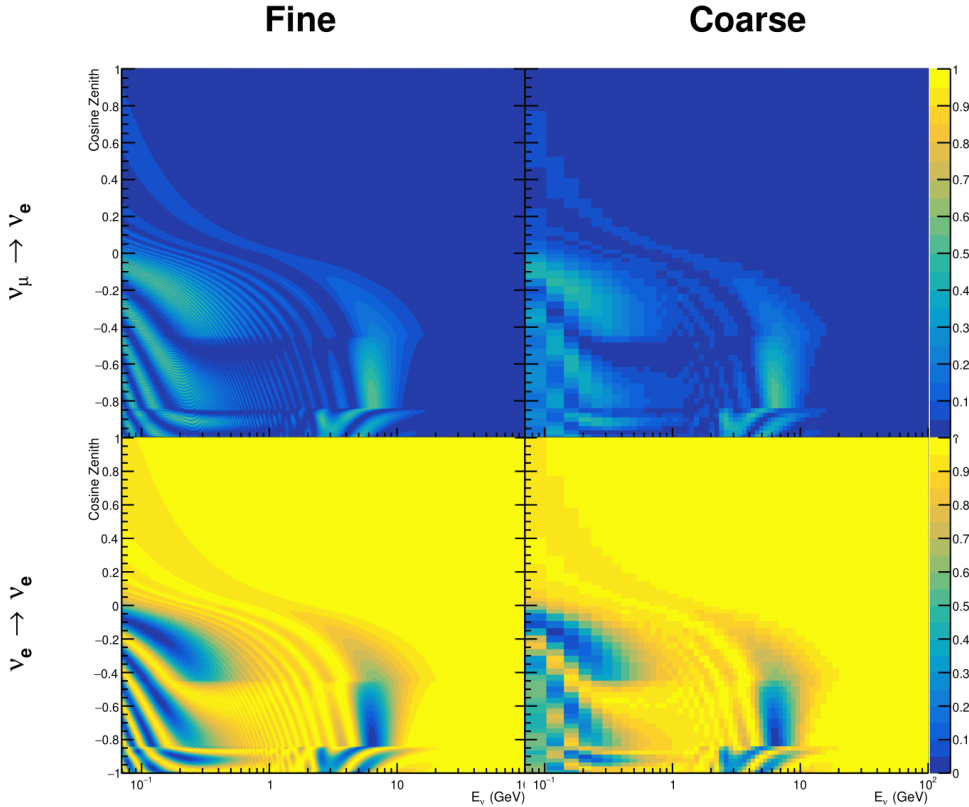


Figure 7.8: The oscillation probability, $P(\nu_\mu \rightarrow \nu_e)$ (top row) and $P(\nu_e \rightarrow \nu_e)$ (bottom row), given as a function of neutrino energy and zenith angle. The left column gives the “fine” binning used to calculate the oscillation probabilities and the right column illustrates the “coarse” binning used to reweight the Monte Carlo events. The fine binning choice is given with $N = 10$, which was determined to be below the threshold from Figure 7.6 and Figure 7.7.

2788 be kept on GPU memory, rather than having to load these arrays onto GPU
 2789 memory for each calculation. Reducing the memory transfer between CPU and
 2790 GPU significantly reduces the time required for calculation. This can be seen
 2791 in Figure 7.9, where the GPU implementation of CUDAProb3 is approximately
 2792 three times faster than the ProbGPU engine.

2793 Another significant advantage of CUDAProb3 is that it contains a CPU multi-
 2794 threaded implementation which is not possible with the ProbGPU or prob3 engines.
 2795 This eliminates the requirement for GPU resources when submitting jobs to batch
 2796 systems. As illustrated in Figure 7.9, the calculation speed depends on the number

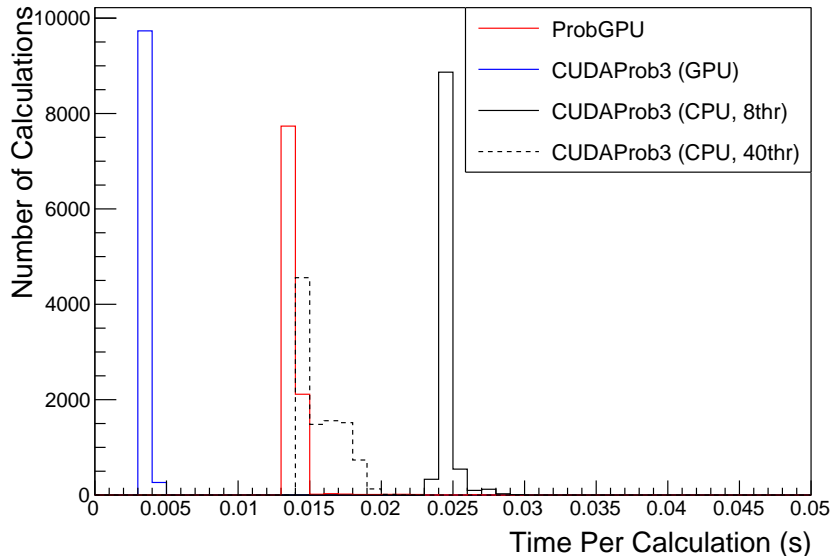


Figure 7.9: The calculation time taken to both calculate the oscillation probabilities and fill the “coarse” oscillograms, following the technique given in section 7.1, for the CUDAProb3 and ProbGPU (Red) calculation engines. CUDAProb3 has both a GPU (Blue) and CPU (Black) implementation, where the CPU implementation is multi-threaded. Therefore, 8-threads (solid) and 40-threads (dashed) configurations have been tested. Prob3, which is a CPU single-thread implementation has a mean step time of 1.142s.

of available threads. Using 8 threads (which is typical of the batch systems being used) is approximately twice as slow as the ProbGPU engine implementation, but would allow the fitting framework to be run on many more resources. This fact is utilised for any SK-only fits but GPU resources are required for any fits which include beam samples due to the ProbGPU requirement. Based on the benefits shown by the implementation in this section, efforts are being placed into including linear propagation for beam neutrino propagation into the engine [209].

7.3 Matter Density Profile

For an experiment observing neutrinos propagating through the Earth, a model of the Earth’s density profile is required. The model used within this analysis is based on the Preliminary Reference Earth Model (PREM) [80], as illustrated in Figure 2.8. Table 2.3 documents the density and radii of the layers used within the constant density approximation used by the SK-only analysis [79]. The

density measurements provided in the PREM model are provided in terms of mass density, whereas neutrino oscillations are sensitive to the electron number density. This value can be computed as the product of the chemical composition, or the Z/A value, and the mass density of each layer. Currently, the only way to measure the chemical composition value for layers close to the Earth's core is through neutrino oscillations. The chemical composition of the upper layers of the Earth's Mantle and the Transition zone is well known due to it being predominantly pyrolite which has a chemical composition value of 0.496 [210]. The chemical composition dial for the core layers is set to a value of 0.468, as calculated in [211]. As this value is less well known, it is assigned a Gaussian error with a standard deviation equivalent to the difference in chemical composition in core and mantle layers. Figure 7.10 illustrates the effect of moving from the $Z/A = 0.5$ method which is used in the official SK-only analysis to these more precise values.

The beam oscillation probability in this thesis uses a baseline of 295km, density 2.6g/cm^3 , and chemical composition 0.5 as is done by the official T2K-only analysis [212].

For a neutrino with given $E_\nu, \cos(\theta_Z)$, the oscillation probability calculation engine must be passed a list of the matter regions that the neutrino traversed, with the path length and fixed density in each region. However, a neutrino passing through the earth experiences a range of radii, and thus a range of densities, in each region. In the SK-only analysis, the earth density model used is piecewise-constant, thereby ignoring this effect. For this thesis, the density values for the calculation engine are found by averaging the earth density along the neutrino's path in each layer,

$$\langle \rho \rangle_i = \frac{1}{t_{i+1} - t_i} \int_{t_i}^{t_{i+1}} \rho(t) dt, \quad (7.5)$$

where t_i are the intersection points between each layer and t is the path length of the trajectory across the layer. This leads to an improved approximation. For this averaging, the simplification of the PREM model developed in [213] is

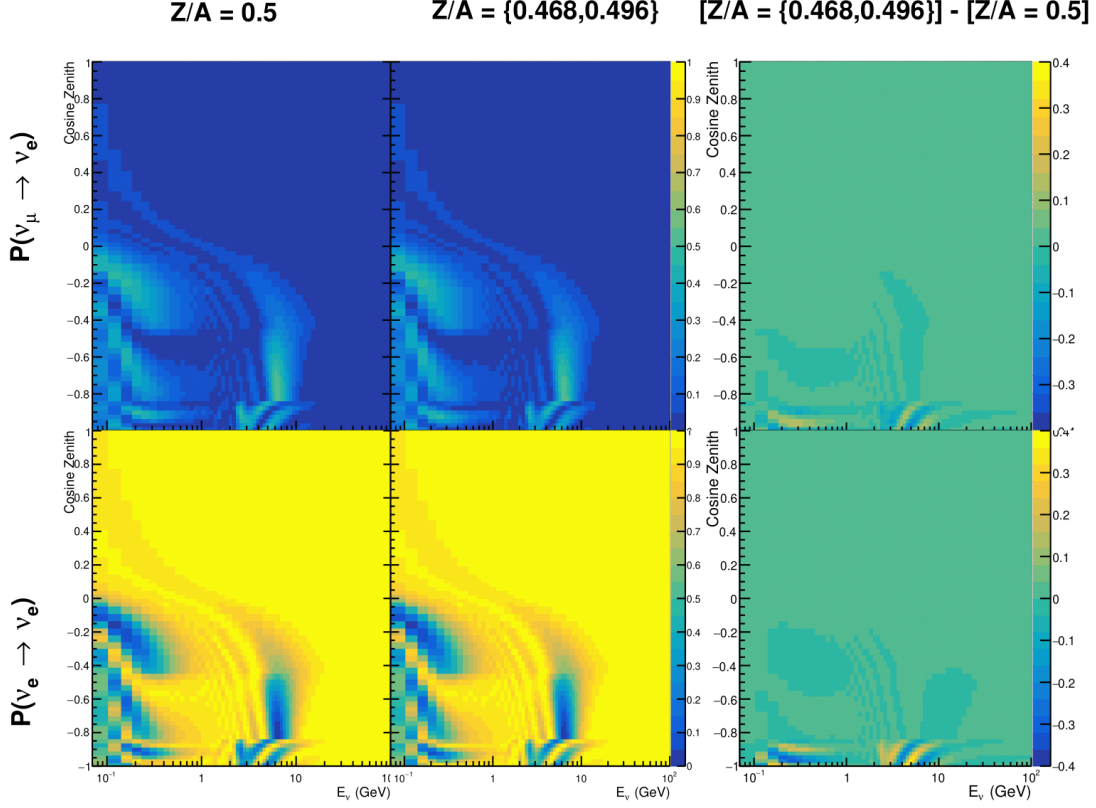


Figure 7.10: The oscillation probability, $P(\nu_\mu \rightarrow \nu_e)$ (top row) and $P(\nu_e \rightarrow \nu_e)$ (bottom row), given as a function of neutrino energy and zenith angle. The left column gives probabilities where the constant $Z/A = 0.5$ approximation which is used in the official SK-only analysis. The middle column gives the probabilities where $Z/A = [0.468, 0.498]$ values are used, as given in Table 2.3. The right column illustrates the difference in oscillation probability between the two different techniques.

used. The layers of the prem model are combined into four to reduce calculation time, with a quadratic fit to each section. This fit was not performed by the author of the thesis and is documented in [205]. The coefficients of the quadratic fit to each layer are given in Table 7.1 with the final distribution illustrated in Figure 7.11. The quadratic approximation is clearly much closer to the PREM model as compared to the constant density approximation.

The effect of using the quadratic density per $\cos(\theta_Z)$ model is highlighted in Figure 7.12. The slight discontinuity in the oscillation probability around $\cos(\theta_Z) \sim -0.45$ in the fixed density model, which is due to the transition to

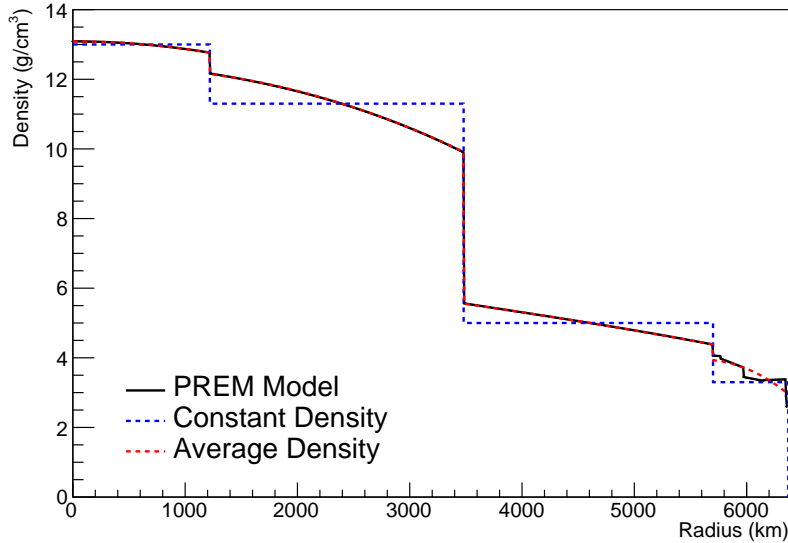


Figure 7.11: The density of the Earth given as a function of the radius, as given by the PREM model (Black), the constant density four-layer approximation (Blue), as used in the official SK-only analysis, and the quadratic approximation of the PREM model (Red).

Layer	Outer Radius [km]	Density [g/cm ³]
Inner Core	1220	$13.09 - 8.84x^2$
Outer Core	3480	$12.31 + 1.09x - 10.02x^2$
Lower Mantle	5701	$6.78 - 1.56x - 1.25x^2$
Transition Zone	6371	$-50.42 + 123.33x - 69.95x^2$

Table 7.1: The quadratic polynomial fits to the PREM model for four assumed layers of the PREM model. The fit to calculate the coefficients is given in [205], where $x = R / R_{\text{Earth}}$.

mantle layer boundary, has been reduced. This is expected as the difference in the density across this boundary is significantly smaller in the quadratic density model as compared to the constant density model. Whilst the difference in density across the other layer transitions is reduced, there is still a significant difference. This means the discontinuities in the oscillation probabilities remain but are significantly reduced. However, as the quadratic density approximation matches the PREM model well in this region, these discontinuities are due to the Earth model rather than an artifact of the oscillation calculation.

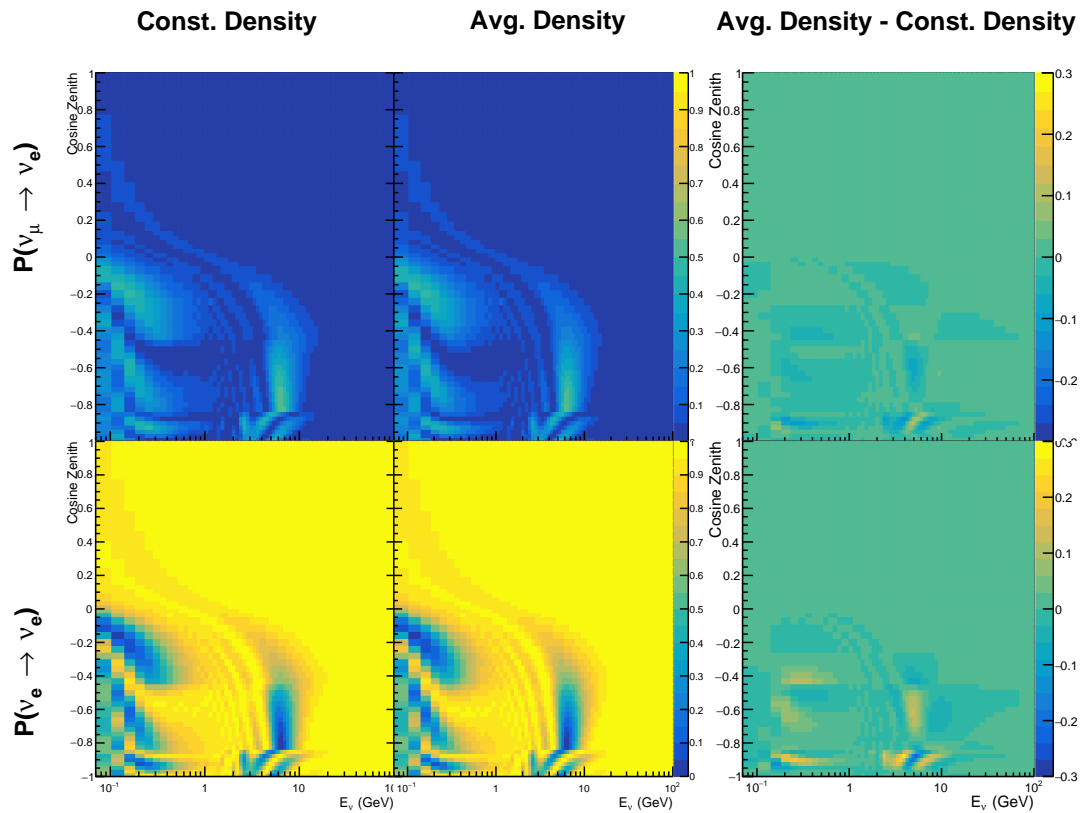


Figure 7.12: The oscillation probability, $P(\nu_\mu \rightarrow \nu_e)$ (top row) and $P(\nu_e \rightarrow \nu_e)$ (bottom row), given as a function of neutrino energy and zenith angle. The left column gives probabilities where the four-layer constant density approximation is used. The middle column gives the probabilities where the density is integrated over the trajectory, using the quadratic PREM approximation, for each $\cos(\theta_Z)$ is used. The right column illustrates the difference in oscillation probability between the two different techniques.

2855 7.4 Production Height Averaging

2856 As discussed in section 2.5, the height at which the cosmic ray flux interacts
2857 in the atmosphere is not known on an event-by-event basis. The production
2858 height can vary from the Earth’s surface to $\sim 50\text{km}$ above that. The SK-only
2859 analysis methodology (described in section 7.1) for including the uncertainty
2860 on the production height is to include variations from the Honda model when
2861 pre-calculating the oscillation probabilities prior to the fit. This technique is not
2862 possible for this analysis which uses continuous oscillation parameters that can
2863 not be known prior to the fit. Consequently, an analytical averaging technique
2864 was developed in [205]. The author of this thesis was not responsible for the
2865 derivation of the technique but has performed the implementation and validation
2866 of the technique for this analysis alone.

2867 Using the 20 production heights per Monte Carlo neutrino event, provided
2868 as 5% percentiles from the Honda flux model, a production height distribution
2869 $p_j(h|E_\nu, \cos \theta_Z)$ is built for each neutrino flavour $j = \nu_e, \bar{\nu}_e, \nu_\mu, \bar{\nu}_\mu$. In practice, a
2870 histogram is filled with 20 evenly spaced bins in production height h between
2871 0 and 50km. The neutrino energy and cosine zenith binning of the histogram
2872 are the same as that provided in section 7.1. The average production height,
2873 $\bar{h} = \int dh \frac{1}{4} \sum_j p_j(h|E_\nu, \cos(\theta_Z))$, is calculated. This assumes a linear average over
2874 the four flavours of neutrino which are considered to be generated in cosmic
2875 ray showers. The production height binning of this histogram is then translated
2876 into $\delta t(h) = t(\bar{h}) - t(h)$, where $t(x)$ is the distance travelled along the trajectory
2877 in the atmosphere from some production height, x .

2878 For the i^{th} traversed layer, the transition amplitude, $D_i(t_{i+1}, t_i)$, is computed.
2879 The time-ordered product of these is then used as the overall transition amplitude
2880 via

$$A(t_{n+1}, t_0) = D_n(t_{n+1}, t_n) \dots D_1(t_2, t_1) D_0(t_1, t_0), \quad (7.6)$$

2881 where,

$$\begin{aligned} D_n(t_{n+1}, t_n) &= \exp[-iH_n(t_{n+1} - t_n)] \\ &= \sum_{k=1}^3 C_k \exp[ia_k(t_{n+1} - t_n)] \end{aligned} \quad (7.7)$$

2882 is expressed as a diagonalised time-dependent solution to the Schrodinger
 2883 equation. The 0th layer is the propagation through the atmosphere and is the
 2884 only term that depends on the production height. Using the substitution $t_0 =$
 2885 $t(\bar{h}) - \delta t(h)$, it can be shown that

$$D_0(t_1, t_0) = D_0(t_1, \bar{h})D_0(\delta t). \quad (7.8)$$

2886 Thus Equation 7.6 becomes

$$\begin{aligned} A(t_{n+1}, t_0) &= D_n(t_{n+1}, t_n) \dots D_1(t_2, t_1) D_0(t_1, \bar{h}) D(\delta t) \\ &= A(t_{n+1}, \bar{h}) \sum_{k=1}^3 C_k \exp[ia_k \delta t], \\ &= \sum_{k=1}^3 B_k \exp[ia_k \delta t]. \end{aligned} \quad (7.9)$$

2887 The oscillation probability averaged over production height is then calculated
 2888 as

$$\begin{aligned} \bar{P}(\nu_j \rightarrow \nu_i) &= \int d(\delta t) p_j(\delta t | E_\nu, \cos \theta_Z) P(\nu_j \rightarrow \nu_i) \\ &= \int d(\delta t) p_j(\delta t | E_\nu, \cos \theta_Z) A(t_{n+1}, t_0) A^*(t_{n+1}, t_0) \\ &= \sum_{km} (B_k)_{ij} (B_m)_{ij}^* \int d(\delta t) p_j(\delta t | E_\nu, \cos \theta_Z) \exp[i(a_k - a_m) \delta t]. \end{aligned} \quad (7.10)$$

2889 It is important to note that the exact value of \bar{h} used does not matter as the
 2890 values of δt would change to compensate for any modification to the value of \bar{h} .

2891 In practice, implementation in CUDAProb3 [208] is relatively straightforward
 2892 as the majority of these terms are already calculated in the standard oscillation
 2893 calculation. Figure 7.13 illustrates the results of the production height averaging.

2894 As expected, the main effect is observed in the low-energy downward-going
 2895 and horizontal-going events. Upward-going events have to travel the radius
 2896 of the Earth, $R_E = 6371\text{km}$, where the production height uncertainty is a small
 2897 fraction of the total path length.

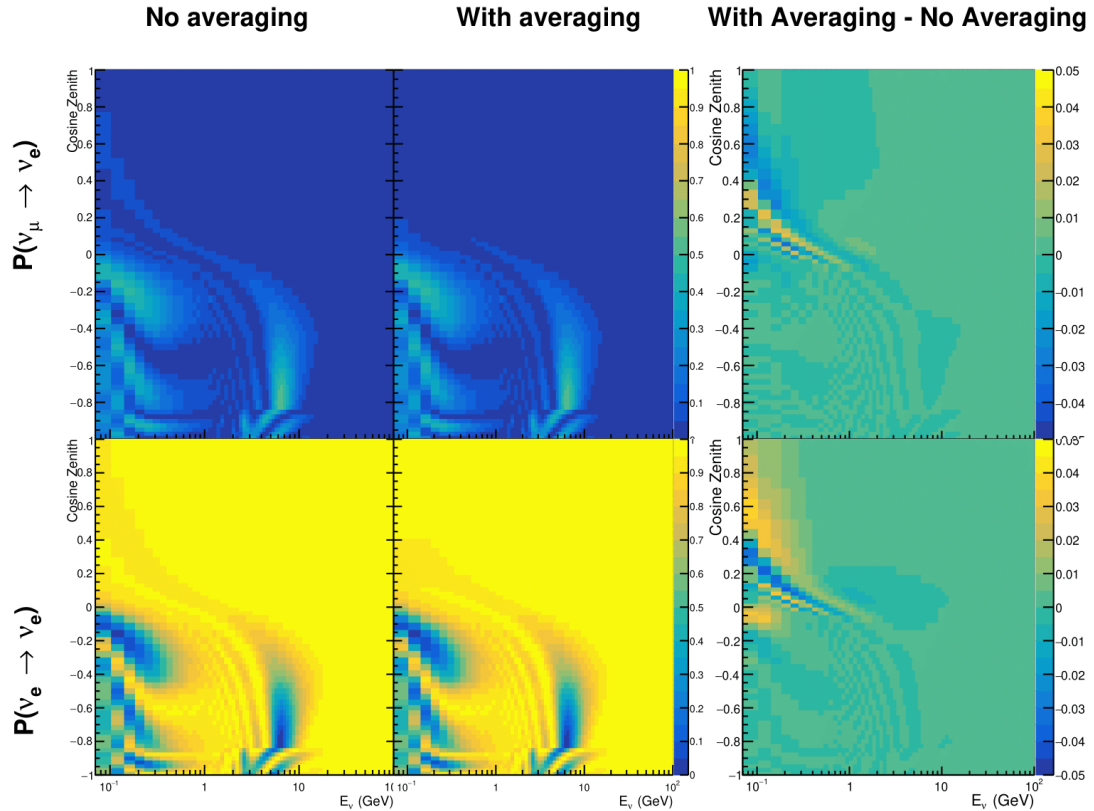


Figure 7.13: The oscillation probability, $P(\nu_\mu \rightarrow \nu_e)$ (top row) and $P(\nu_e \rightarrow \nu_e)$ (bottom row), given as a function of neutrino energy and zenith angle. The left column gives probabilities where a fixed production height of 25km is used. The middle column gives the probabilities where the production height is analytically averaged. The right column illustrates the difference in oscillation probability between the two different techniques.

8

2898

2899

Oscillation Analysis

2900 Using the samples and systematics defined in chapter 6, this chapter documents
2901 a simultaneous beam and atmospheric oscillation analysis from the T2K and SK
2902 experiments. The MaCh3 Bayesian MCMC framework introduced in chapter 4
2903 is used for all studies performed within this thesis.

2904 The MaCh3 framework has been validated through many tests. The code
2905 that handles the beam far detector samples was developed by the author and
2906 validated by comparison to the 2020 T2K analysis [2]. The sample event rates and
2907 likelihood evaluations of beam samples generated by the framework used within
2908 this thesis were compared to those from the T2K analysis by the author of this
2909 thesis. Variations of the sample predictions were compared at $\pm 1\sigma$ and $\pm 3\sigma$ and
2910 good agreement was found in all cases. A similar study, led by Dr. C. Wret was
2911 used to validate the near detector portion of the code [198]. The implementation
2912 of the atmospheric samples within MaCh3 was completed and cross-checked by
2913 the author of this thesis against the P-Theta framework (introduced in section 3.2).
2914 Both fitters are provided with the same inputs and can therefore cross-validate
2915 each other. These validations compared the event rate and likelihood calculation.
2916 Documentation of all the above validations can be found in [198]. These stringent
2917 validations ensure that the code is doing as intended.

2918 8.1 Monte Carlo Prediction

- 2919 Using the three sets of dial values (generated, pre-fit, and post-fit tunes) defined
 2920 in subsection 6.4.3, the predicted event rates for each sample are given in Table 8.1.
 2921 The oscillated and un-oscillated event rates are calculated for each tune.

Sample	Total Predicted Events					
	Generated		Pre-fit		Post-fit	
	Osc	UnOsc	Osc	UnOsc	Osc	UnOsc
SubGeV- <i>elike</i> -0dcy	7121.0	7102.6	6556.8	6540.0	7035.2	7015.7
SubGeV- <i>elike</i> -1dcy	704.8	725.5	693.8	712.8	565.7	586.0
SubGeV- <i>mulike</i> -0dcy	1176.5	1737.2	1078.6	1588.1	1182.7	1757.1
SubGeV- <i>mulike</i> -1dcy	5850.7	8978.1	5351.7	8205.1	5867.0	9009.9
SubGeV- <i>mulike</i> -2dcy	446.9	655.2	441.6	647.7	345.9	505.6
SubGeV- <i>pi0like</i>	1438.8	1445.4	1454.9	1461.1	1131.1	1136.2
MultiGeV- <i>elike</i> -nue	201.4	195.6	201.1	195.3	202.6	196.7
MultiGeV- <i>elike</i> -nuebar	1141.5	1118.3	1060.7	1039.5	1118.5	1095.7
MultiGeV- <i>mulike</i>	1036.7	1435.8	963.1	1334.1	1015.2	1405.9
MultiRing- <i>elike</i> -nue	1025.1	982.2	1026.8	984.3	1029.8	986.4
MultiRing- <i>elike</i> -nuebar	1014.8	984.5	991.0	962.0	1008.9	978.5
MultiRing- <i>mulike</i>	2510.0	3474.4	2475.6	3425.8	2514.6	3480.4
MultiRingOther-1	1204.5	1279.1	1205.8	1280.3	1207.4	1281.0
PCStop	349.2	459.2	338.4	444.7	346.8	456.1
PCThrus	1692.8	2192.5	1661.5	2149.8	1689.2	2187.8
UpStop-mu	751.2	1295.0	739.7	1271.6	750.4	1293.0
UpThruNonShower-mu	2584.4	3031.6	2577.9	3019.4	2586.8	3034.0
UpThruShower-mu	473.0	488.6	473.2	488.7	473.8	489.4
FHC1Rmu	328.0	1409.2	301.1	1274.7	345.1	1568.0
RHC1Rmu	133.0	432.3	122.7	396.2	135.0	443.9
FHC1Re	84.6	19.2	77.4	18.2	93.7	19.7
RHC1Re	15.7	6.4	14.6	6.1	15.9	6.3
FHC1Re1de	10.5	3.2	10.3	3.1	8.8	2.9

Table 8.1: The Monte Carlo predicted event rate of each far detector sample used within this analysis. Three model parameter tunes are considered, as defined in subsection 6.4.3. Un-oscillated and oscillated predictions are given, where the oscillated predictions assume Asimov A oscillation parameters provided in Table 2.2.

- 2922 Generally, the samples that target CCQE interaction modes observe a decrease
 2923 in prediction when comparing the generated values with the pre-fit dial values.
 2924 This is in accordance with the Monte Carlo being produced at $M_A^{QE} = 1.21\text{GeV}$
 2925 [157] whilst the pre-fit dial value is set to $M_A^{QE} = 1.03\text{GeV}$ as suggested by [197].

Furthermore, the predicted event rates of samples that target CCRES interaction modes are significantly reduced when considering the post-BANFF fit. This follows the observations in subsection 6.4.3. The strength of the accelerator neutrino experiment can be seen in the remarkable difference between the oscillated and unoscillated predictions in the FHC1Rmu and RHC1Rmu samples. There is a very clear decrease in the expected event rate between the oscillated and un-oscillated predictions which is not as obvious as in the atmospheric samples. This is due to the fact that the beam energy is tuned to the maximum disappearance probability, which is not the case for the naturally generated atmospheric neutrinos.

8.2 Likelihood Scans

Using the definition of the likelihood presented in section 6.5, the contribution of each sample to the likelihood from a variation of a particular parameter can be studied. This process identifies which samples drive the determination of the oscillation parameters in the joint fit. Figure 8.1 presents the variation of all the samples (beam and atmospheric) at the far detector to the oscillation parameters of interest: δ_{CP} , $\sin^2(\theta_{13})$, $\sin^2(\theta_{23})$, and Δm_{32}^2 . These plots are colloquially called ‘likelihood scans’ (or ‘log-likelihood scans’). The process of making these plots is as follows. An Asimov data set is built using the AsimovA oscillation parameters and pre-fit systematic tune. The Monte Carlo is then reweighted using the value of the oscillation parameter at each point on the x-axis of the scan. The likelihood is then calculated between the Asimov data and Monte Carlo prediction and plotted.

Due to the caveat of fixed systematic parameters and the correlations between oscillation parameters being ignored when creating these likelihood scans, the value of $\chi^2 = 1$ (or $-2 \times \ln(\text{Likelihood}) = 1$) does not equate to the typical 1σ sensitivity. However, it does give an indication of which samples respond most strongly to variations in a particular oscillation parameter. The point at

2954 which the likelihood tends to zero illustrates the value of the parameter used
 2955 to build the Asimov data prediction.

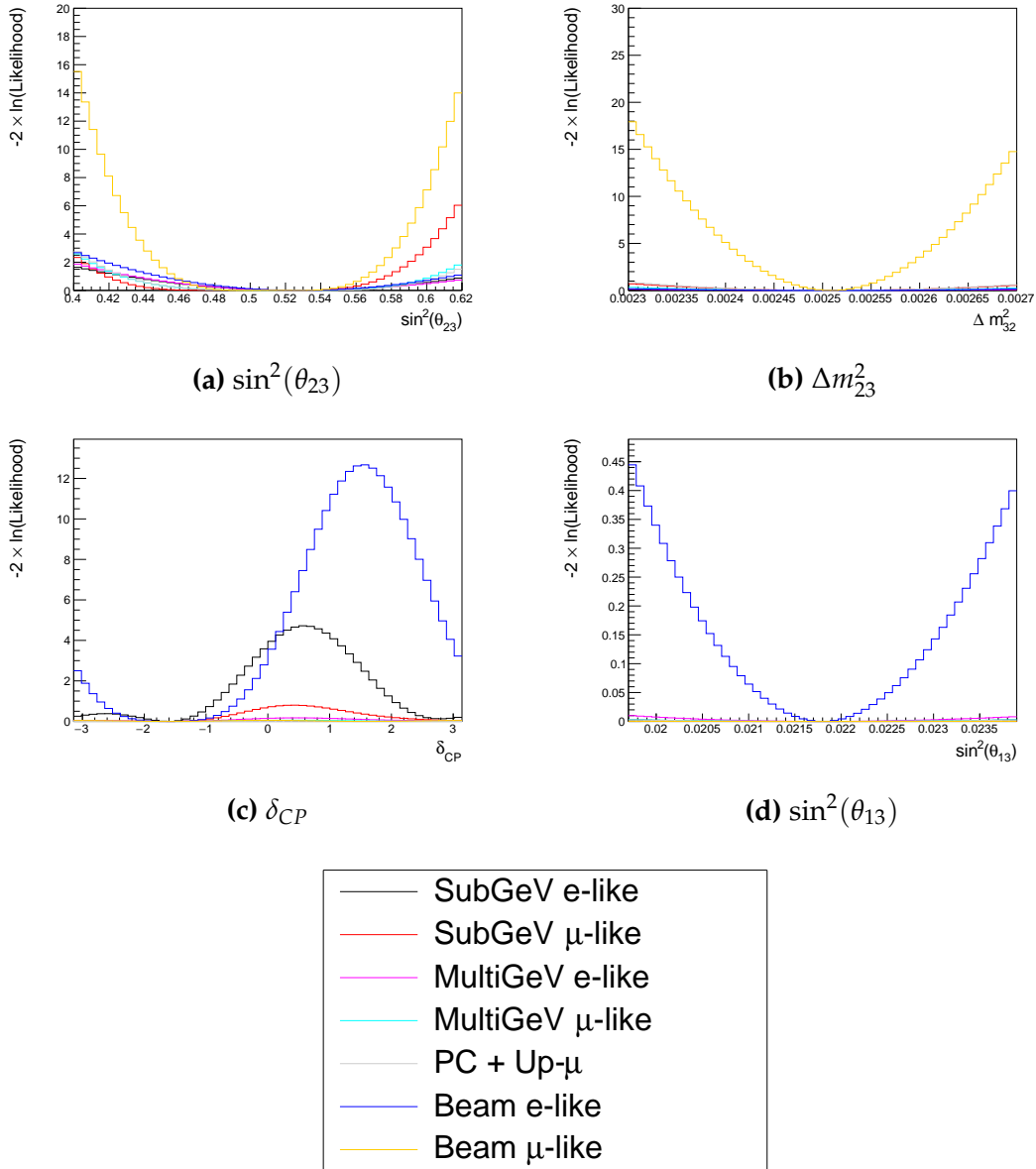


Figure 8.1: The response of the likelihood, as defined in section 6.5, illustrating the response of the samples to a variation of an oscillation parameter.

2956 The sensitivity to $\sin^2(\theta_{23})$ is mostly dominated by the beam muon-like
 2957 samples. The response of an individual atmospheric sample is small but non-
 2958 negligible such that the summed response over all atmospheric samples becomes
 2959 comparable to that of the muon-like beam samples. Consequently, the sensitivity

of the joint fit to $\sin^2(\theta_{23})$ would be expected to be greater than the beam-only analysis. The only sample that responds to the $\sin^2(\theta_{13})$ oscillation parameter is the electron-like beam sample. Consequently, no increase in sensitivity beyond that of the T2K-only analysis would be expected from the joint fit. Regardless, the sensitivity of the beam sample is significantly weaker than the external reactor constraint so prior knowledge will dominate any sensitivity to $\sin^2(\theta_{13})$ which is included within this thesis. The Δm_{21}^2 and $\sin^2(\theta_{12})$ parameters are not considered as there is simply no sensitivity in any sample considered within this analysis. The response to Δm_{32}^2 is completely dominated by the beam muon-like samples. This is because the beam neutrino energy is specifically tuned to match the maximal disappearance probability. Despite this, improvements to the $|\Delta m_{32}^2|$ sensitivity may be expected due to additional mass hierarchy determination added by the atmospheric samples.

Two-dimensional scans of the appearance ($\sin^2(\theta_{13}) - \delta_{CP}$) and disappearance ($\sin^2(\theta_{23}) - \Delta m_{32}^2$) parameters are illustrated in Figure 8.2 and Figure 8.3, respectively. The caveat of fixed systematic parameters and correlations between other oscillation parameters being neglected still apply.

The appearance log-likelihood scans show the distinct difference in how the beam and atmospheric samples respond. The beam samples have an approximately constant width of the 2σ and 3σ contours, throughout all ranges of δ_{CP} . Whereas, the response of the atmospheric samples to $\sin^2(\theta_{13})$ is very strongly correlated to the value of δ_{CP} . At higher values of $\sin^2(\theta_{13})$, two lobes appear around $\delta_{CP} \sim -\pi/2$ and $\delta_{CP} \sim 2.4$. Consequently, this difference allows some of the degeneracy in a beam-only fit to be broken. Comparing the beam-only and joint fit likelihood scans, the 2σ continuous contour in δ_{CP} for beam samples becomes closed when the atmospheric samples are added. This may result in a stronger sensitivity to δ_{CP} . Similarly, the width of the 3σ contours also becomes dependent upon the value of δ_{CP} . Furthermore, atmospheric samples have little sensitivity to $\sin^2(\theta_{13})$ on their own, as evidenced in Figure 8.1, but may improve sensitivity to the parameter when combined within the simultaneous

2990 fit. It is important to remember that these likelihood scans are not sensitivity
2991 measurements as the systematic parameters are fixed and the correlation between
2992 oscillation parameters is neglected. However, they are a very encouraging result
2993 for the joint fit.

2994 The disappearance log-likelihood scans in $\sin^2(\theta_{23}) - \Delta m_{32}^2$ space (Figure 8.3)
2995 show the expected behaviour when considering the one-dimensional scans
2996 already discussed. The uncertainty on the width of $|\Delta m_{32}^2|$ is mostly driven by the
2997 beam samples. However, the width of this contour in the inverted mass region
2998 ($\Delta m_{32}^2 < 0$) is significantly reduced due to the ability of the atmospheric samples
2999 to select the correct (normal) mass hierarchy. The width of the uncertainty
3000 in $\sin^2(\theta_{23})$ is also reduced compared to the beam-only sensitivities, with a
3001 further decrease in the inverted hierarchy region due to the better mass hierarchy
3002 determination.

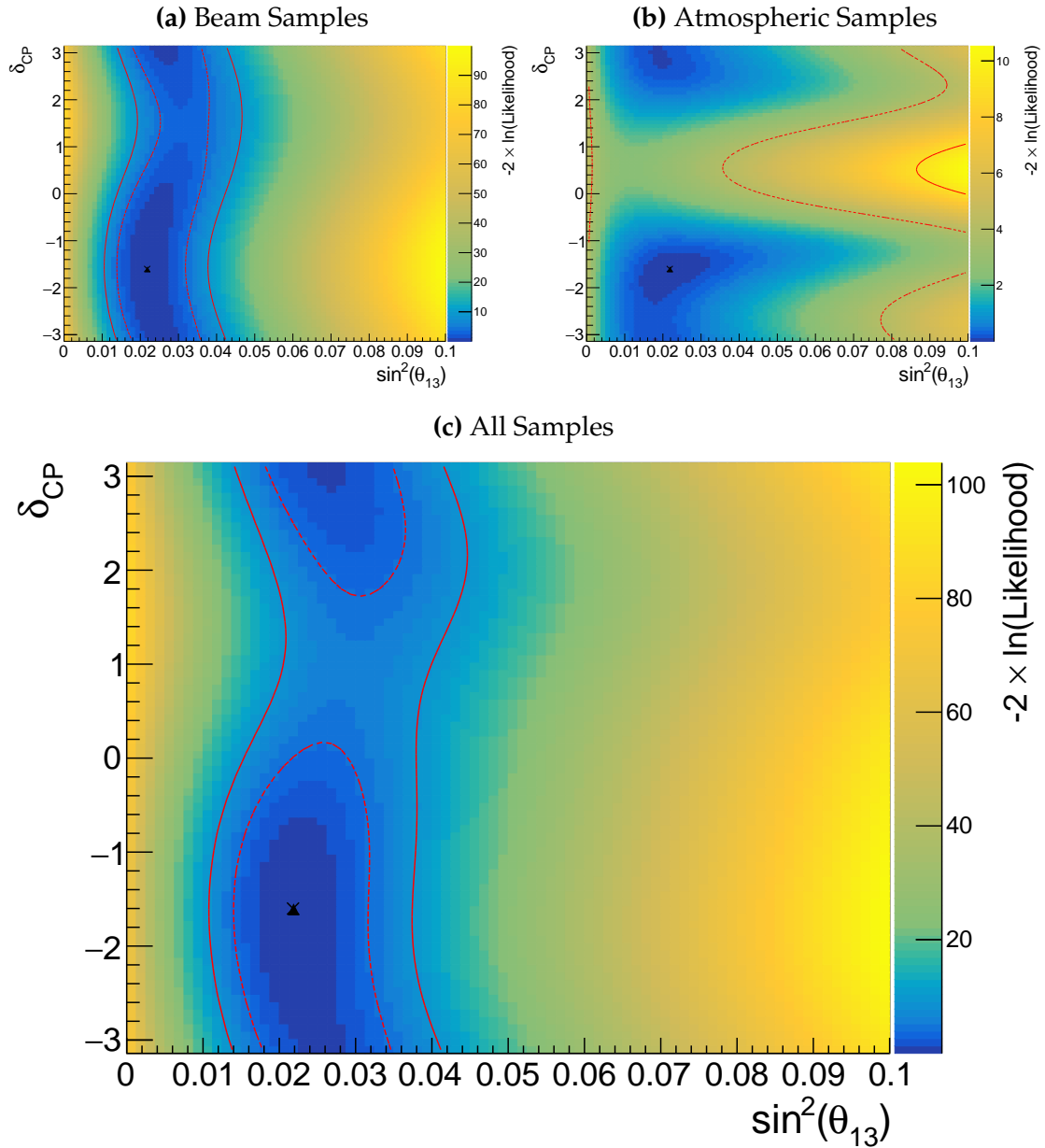


Figure 8.2: Two-dimensional log-likelihood scan of the appearance ($\sin^2(\theta_{13})-\delta_{CP}$) parameters showing the response of the beam samples (top left), atmospheric samples (top right) and the summed response (bottom). The Asimov A oscillation parameters, defined in Table 2.2, are known to be the true point (Black Cross). The position of the smallest log-likelihood is highlighted with the triangle. Prior uncertainty terms of the oscillation parameters are neglected. The two(three) sigma contour levels are illustrated with the dashed(solid) red line.

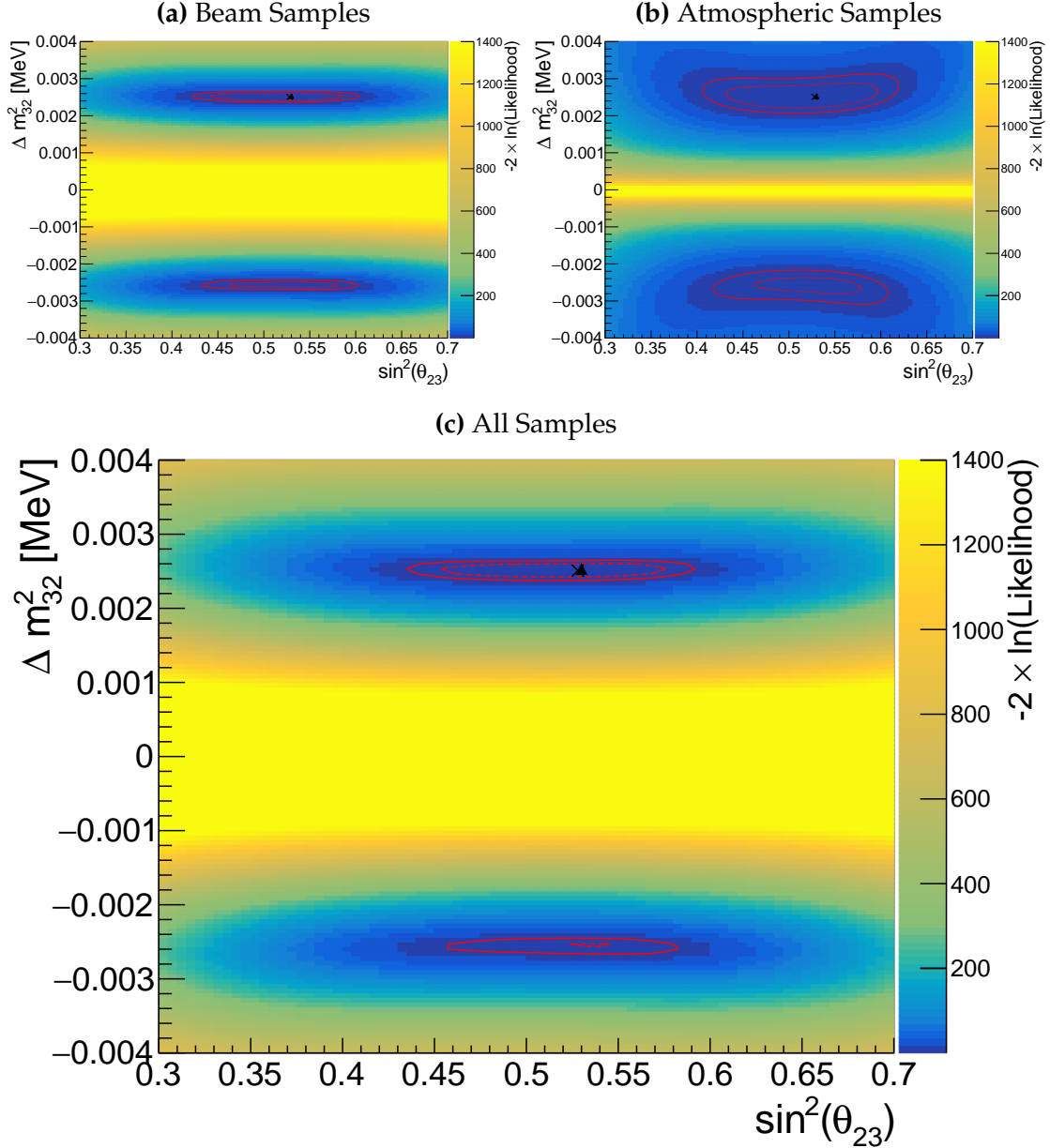


Figure 8.3: Two-dimensional log-likelihood scan of the disappearance ($\sin^2(\theta_{23}) - \Delta m_{32}^2$) parameters showing the response of the beam samples (top left), atmospheric samples (top right) and the summed response (bottom). The Asimov A oscillation parameters, defined in Table 2.2, are known to be the true point (Black Cross). The position of the smallest log-likelihood is highlighted with the triangle. Prior uncertainty terms of the oscillation parameters are neglected. The two(three) sigma contour levels are illustrated with the dashed(solid) red line.

The likelihood scans illustrated thus far only consider the sensitivity of this analysis for a fixed set of true oscillation parameters, namely Asimov A defined in Table 2.2. Whilst computationally infeasible to run many fits at different parameter sets, it is possible to calculate the likelihood response to different Asimov data sets. Figure 8.4 and Figure 8.5 illustrate how the sensitivity changes for differing true values of δ_{CP} and $\sin^2(\theta_{23})$, respectively. For both of these plots, the other oscillation parameters are fixed at their Asimov A values. Consequently, the caveat of fixed systematic parameters and correlations between other oscillation parameters being neglected still applies.

To explain how these plots are made, consider Figure 8.4. This plot is built by considering multiple one-dimensional log-likelihood scans, each creating an Asimov data set with the value of δ_{CP} taken from the x-axis. The likelihood to this particular Asimov data set is calculated after reweighting the Monte Carlo prediction to each value of δ_{CP} on the y-axis.

Figure 8.4 illustrates the sensitivity to δ_{CP} . To interpret this plot, larger contours result in more phase space being excluded from the 1σ region. The 1σ intervals contain regions where the beam and atmospheric samples have discontinuous contours. For example, for the x-axis value of $\delta_{CP} = 0$, the beam samples sensitivity would include two discontinuous regions excluded from the 1σ interval: $\delta_{CP} \sim 0$ and $\delta_{CP} \sim \pi$. This behaviour is also seen in atmospheric samples response but at a value of $\delta_{CP} \sim -1$. This difference allows the joint fit to have increased sensitivity to these regions. Consequently, the difference between the beam-only and joint beam-atmospheric fit should be studied using multiple Asimov data sets.

Despite the increased sensitivity at 1σ , the 2σ intervals from the joint fit are more similar to the two independent sensitivities and the off-diagonal degeneracies mostly remain. This indicates that the joint fit has the strength to aid parameter determination but can not entirely break the degeneracies in δ_{CP} at higher confidence levels.

Figure 8.5 illustrates a similar analysis as above, although the value of $\sin^2(\theta_{23})$ is varied and δ_{CP} is fixed to the Asimov A parameter value. Due to the beam parameters and baseline being tuned to specifically target this oscillation parameter, the average sensitivity of the beam samples is stronger than the atmospheric samples. However, the degeneracy around maximal mixing ($\sin^2(\theta_{23}) = 0.5$) is significantly more peaked in the beam samples compared to the atmospheric samples. This means that a value of $\sin^2(\theta_{23}) \sim 0.56$ would be contained within the 1σ confidence interval for a true value of $\sin^2(\theta_{23}) \sim 0.46$ if using the beam-only analysis, whereas it would be excluded in the joint analysis.

This behaviour is strengthened when considering the 2σ intervals, to the point where two distinct discontinuous regions of the 2σ intervals exist around the Asimov point $\sin^2(\theta_{23}) \sim 0.41, 0.6$. Given the caveat of only considering likelihood scans, the joint analysis would mostly eliminate the discontinuous intervals in these regions. This means that the joint fit could feasibly have an increased preference for the correct octant hypothesis.

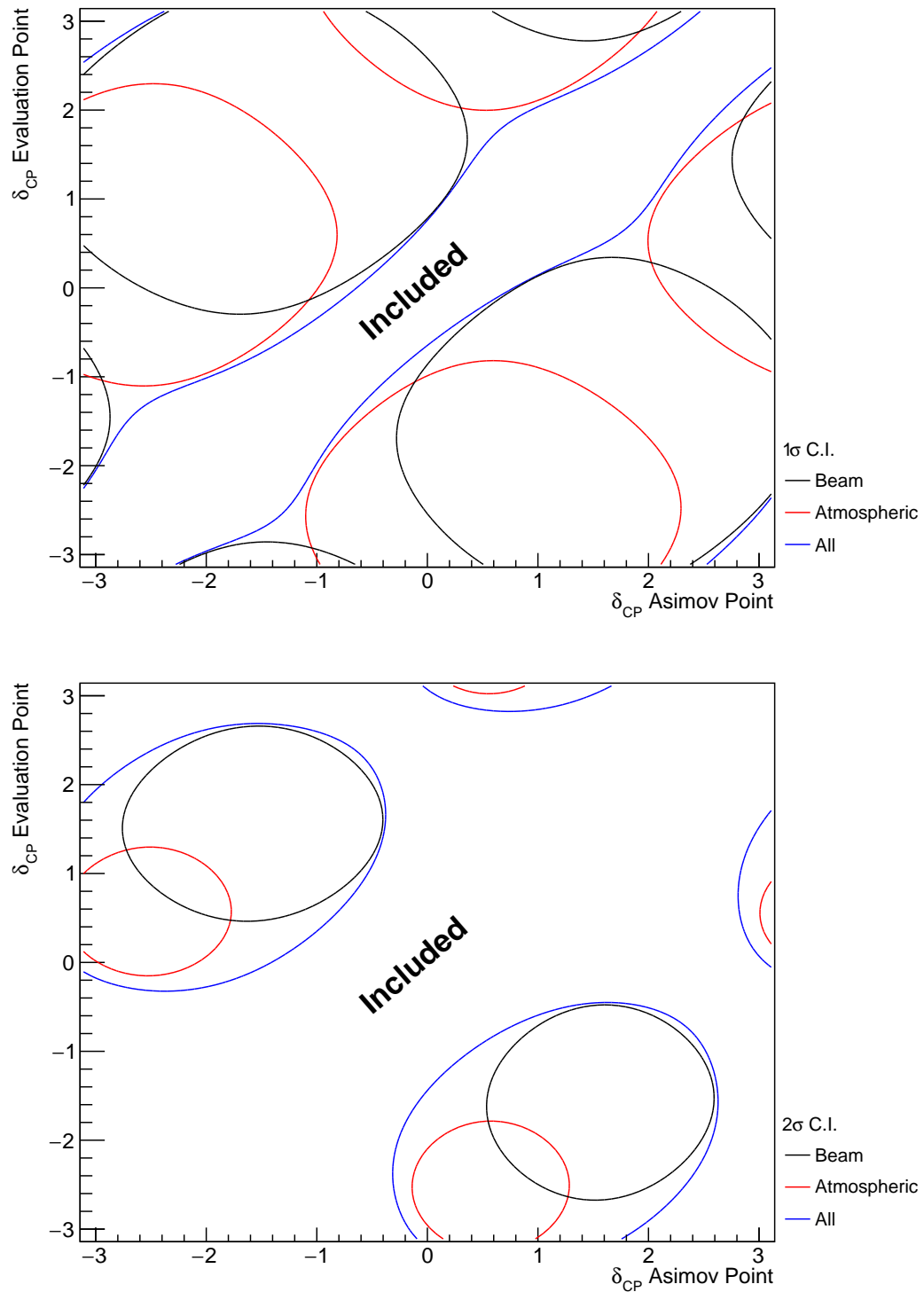


Figure 8.4: A series of one-dimensional likelihood scans over δ_{CP} , where an Asimov data set is built for each value of δ_{CP} on the x-axis and the likelihood is evaluated for each value of δ_{CP} on the y-axis. The diagonal represents the minimum log-likelihood and defines the region included within the 1σ (Top) and 2σ (Bottom) confidence intervals. The beam (black) and atmospheric (red) samples are individually plotted and the joint fit (blue) is the sum of the two.

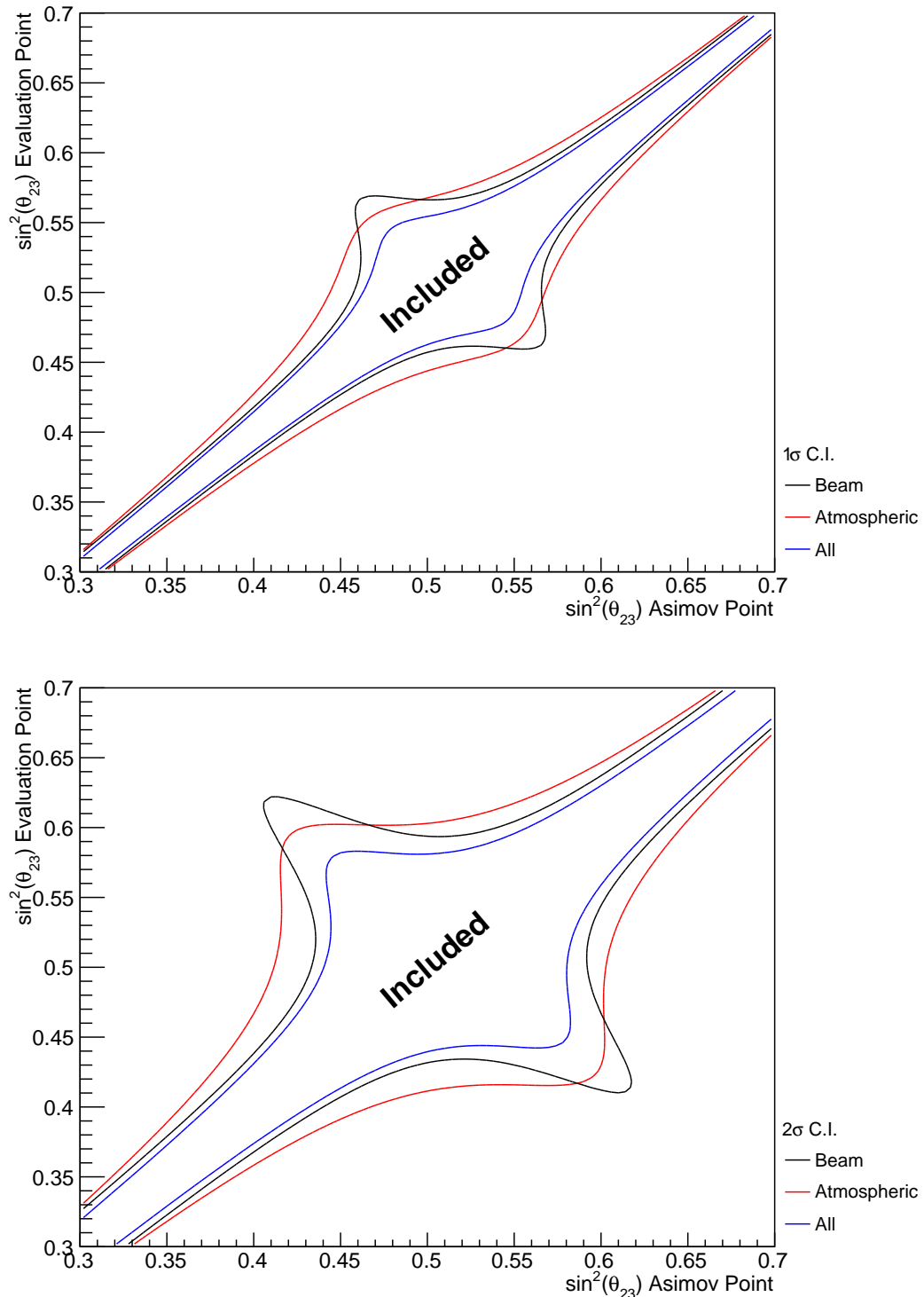


Figure 8.5: A series of one-dimensional likelihood scans over $\sin^2(\theta_{23})$, where an Asimov data set is built for each value of $\sin^2(\theta_{23})$ on the x-axis and the likelihood is evaluated for each value of $\sin^2(\theta_{23})$ on the y-axis. The diagonal represents the minimum log-likelihood and defines the region included within the 1σ (Top) and 2σ (Bottom) confidence intervals. The beam (black) and atmospheric (red) samples are individually plotted and the joint fit (blue) is the sum of the two.

Alongside oscillation parameters (Figure 8.1), the sensitivity to systematic parameters can also be studied for the joint fit. As some of these parameters are correlated between the beam and atmospheric events, the response of the atmospheric samples can modify the constraint. This means the systematics can have additional constraints than they would from a beam-only analysis. Therefore, the response from the beam and the atmospheric samples to various systematic parameters has been compared in Figure 8.6. The Asimov data set has been created using the AsimovA oscillation parameter and the pre-fit systematic tune. For example, the systematic parameter controlling the effective axial mass coupling in CCQE interactions, M_A^{QE} , is clearly dominated by the ND constraint. An example where the response of the atmospheric sample is approximately similar to the near detector constraint is the 2p2h CtoO normalisation systematic. This systematic models the scaling of the 2p2h interaction cross-section on a carbon target to an oxygen target. There are also systematics that have no near detector constraint. For example, the systematic parameters which describe the normalisation of the NC1Gamma and NCOther interaction modes. The atmospheric and beam samples can have similar sensitivity to these systematics due to their similar composition in energy and interaction mode. As an example of how the atmospheric samples can help constrain systematic parameters used within the T2K-only analysis, these NC background events in beam electron-like samples will be more constrained with the additional sensitivity of atmospheric samples. This would be expected to reduce the overall uncertainty of the beam electron-like event rates in the joint analysis compared to the beam-only studies. This could modify the sensitivity of the beam samples due to the more constrained background events.

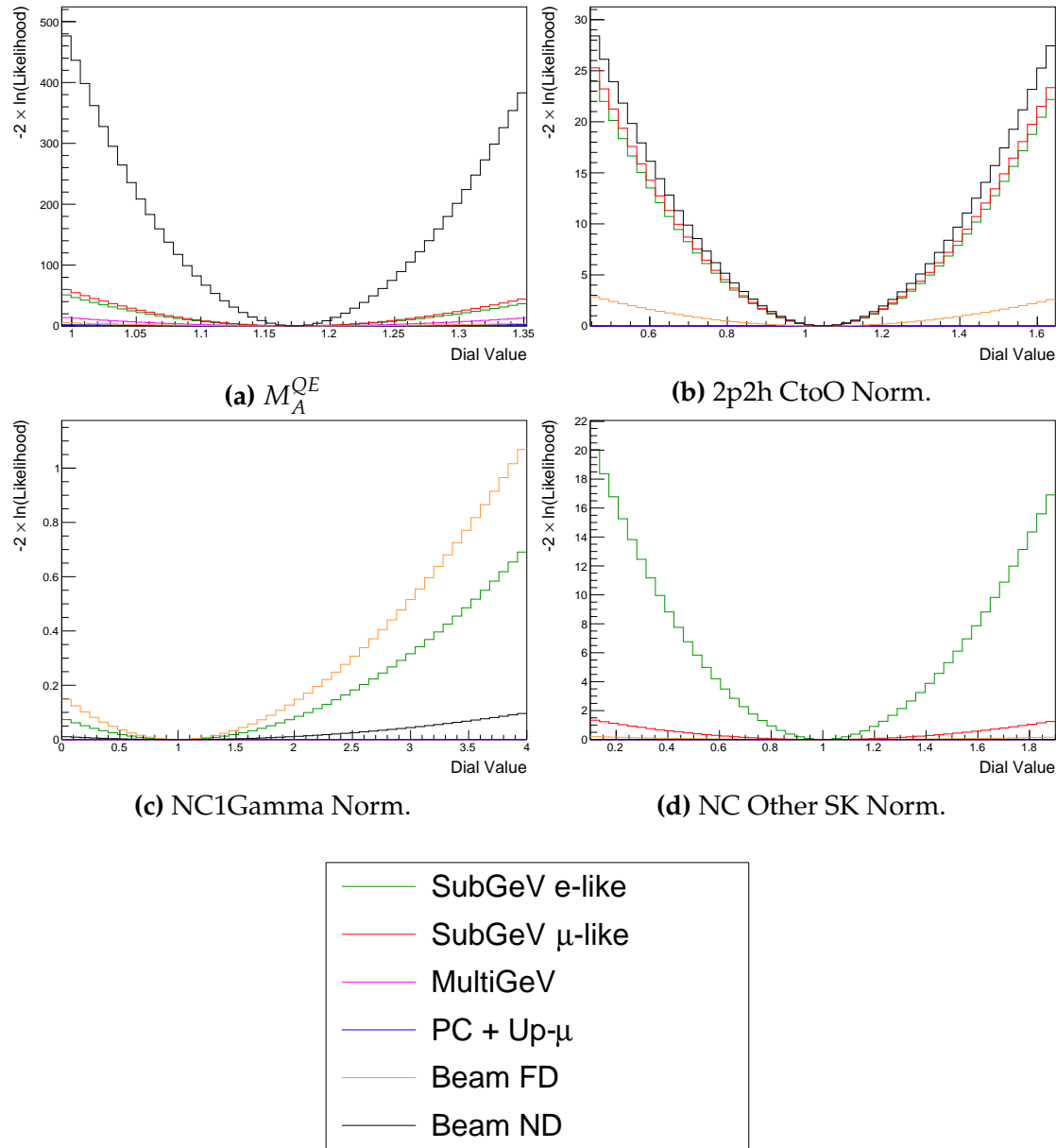


Figure 8.6: The response of the likelihood, as defined in section 8.2, illustrating the response of the samples to the various cross-section systematic parameters.

3072 8.3 Sensitivity Studies

3073 The sensitivities of the joint T2K and SK oscillation analysis are presented in
3074 the form of Asimov fits. These fits consider beam samples from the near and
3075 far detector alongside atmospheric samples at SK. This technique builds an
3076 Asimov data set (following section 6.5) using the AsimovA oscillation parameters
3077 and post-BANFF systematic tune, which is then fit. This technique eliminates
3078 statistical fluctuations from the data, therefore, providing the maximum sen-
3079 sitivity of the analysis.

3080 In practice, the Asimov fits presented within this analysis are modified from
3081 the above definition. An Asimov prediction of both beam and atmospheric far
3082 detector samples is fit whilst the true data is used for near detector samples. The
3083 Asimov predictions at the far detector are built using the post-BANFF tune (as
3084 discussed in section 3.2). These modifications mean that the results are equivalent
3085 to performing a far detector Asimov fit using inputs from the BANFF data fit.
3086 Consequently, this allows the results to be cross-checked with the results from
3087 the P-Theta analysis. The comparison has been performed and is documented in
3088 [214]. No significant discrepancies were found between the fitters.

3089 This section proceeds with the following studies. Firstly, the sensitivity
3090 of the atmospheric samples using the correlated detector model is detailed in
3091 subsection 8.3.1. This includes studying the choice of applying the 2020 PDG
3092 reactor constraint [76] to the atmospheric samples, which is documented in
3093 subsection 8.3.2. Additionally, the effect of applying the near-detector constraints
3094 onto the atmospheric samples is discussed in subsection 8.3.3. The main result is
3095 the sensitivity of the simultaneous beam and atmospheric fit. The sensitivities,
3096 both with and without the application of the reactor constraint, are presented
3097 in subsection 8.3.4 and subsection 8.3.5, respectively. To indicate the benefit
3098 of the joint analysis, the sensitivities are compared to the 2020 T2K beam-only
3099 sensitivities [2, 215] in subsection 8.3.6 and subsection 8.3.7. The T2K analysis
3100 is used as a reference as it uses the same samples and a similar systematic

model. As shown in section 8.2, the response of the beam and atmospheric samples change depending upon the true set of oscillation parameters assumed. Therefore, subsection 8.3.8 documents the sensitivities at an alternative oscillation parameter set. These results have been presented at the Neutrino 2022 conference on behalf of the T2K and SK collaborations [4].

8.3.1 Atmospheric-Only Sensitivity Without Reactor Constraint

This section presents the results of an Asimov fit using samples from the near detector and only atmospheric samples from the far detector. The results are presented as one-dimensional or two-dimensional histograms which have been marginalised over all other parameters using the technique outlined in subsection 4.3.1. Each histogram displays the posterior probability density and illustrates the credible intervals, calculated using the technique in subsection 4.3.2. For this fit, a flat prior is used for $\sin^2(\theta_{13})$ meaning that the reactor constraint is not applied. The Asimov data is generated assuming the AsimovA oscillation parameter set defined in Table 2.2 and the post-BANFF systematic parameter tune.

Figure 8.7 illustrates the posterior probability density for δ_{CP} , marginalised over both hierarchies. The fit favours the known oscillation parameter ($\delta_{CP} = -1.601$) although the posterior probability is very flat through the range of $-\pi < \delta_{CP} < -1$ and $2 < \delta_{CP} < \pi$. There is also a region around $\delta_{CP} \sim 0.4$ which is disfavoured at 2σ . This indicates that the SK samples can rule out some parts of the CP conserving parameter space reasonably well, near $\delta_{CP} \sim 0.4$, when the true value of $\delta_{CP} \sim -\pi/2$.

The posterior probability density in Δm_{32}^2 is given in Figure 8.8. This distribution includes steps in both the normal hierarchy (NH, $\Delta m_{32}^2 > 0$) and the inverse hierarchy (IH, $\Delta m_{32}^2 < 0$). The highest posterior probability density is found within the NH 1σ credible interval, which agrees with the known oscillation parameter value, $2.509 \times 10^{-3}\text{eV}^2$. However, all of the credible intervals span both of the hierarchy hypotheses.

Without Reactor Constraint, Both Hierarchies

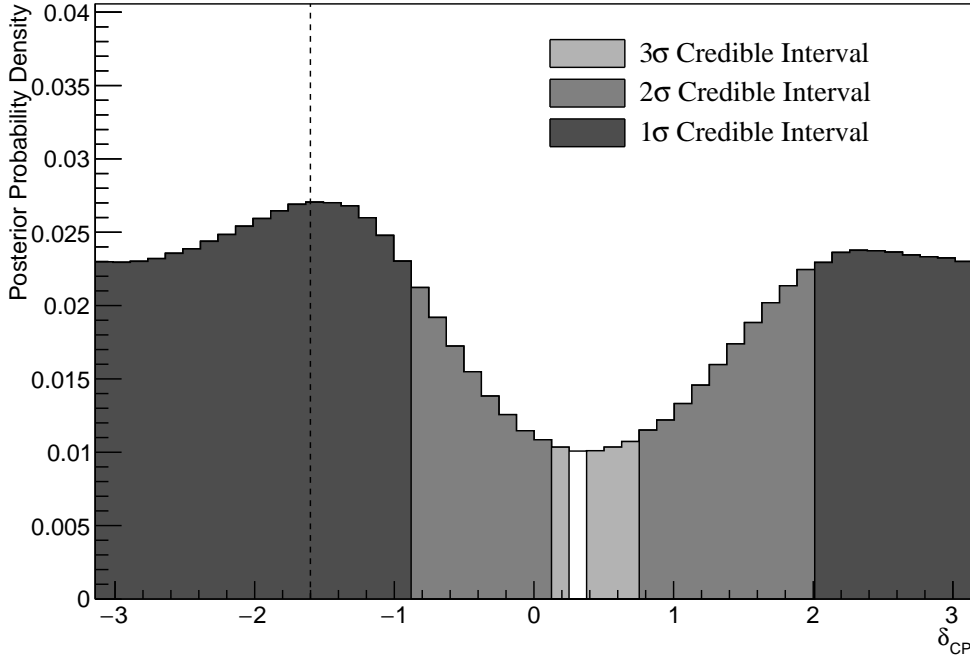


Figure 8.7: The one-dimensional posterior probability density distribution in δ_{CP} , marginalised over both hierarchies, from the SK atmospheric-only fit. The reactor constraint is not applied. The vertical dashed line represents the known value of δ_{CP} .

	LO ($\sin^2 \theta_{23} < 0.5$)	UO ($\sin^2 \theta_{23} > 0.5$)	Sum
NH ($\Delta m_{32}^2 > 0$)	0.17	0.40	0.58
IH ($\Delta m_{32}^2 < 0$)	0.13	0.29	0.42
Sum	0.31	0.69	1.00

Table 8.2: The distribution of steps in an SK atmospheric-only fit, presented as the fraction of steps in the upper (UO) and lower (LO) octants and the normal (NH) and inverted (IH) hierarchies. The reactor constraint is not applied. The Bayes factors are calculated as $B(\text{NH}/\text{IH}) = 1.37$ and $B(\text{UO}/\text{LO}) = 2.24$.

Following the discussion in subsection 4.3.3, the Bayes factor for hierarchy preference can be calculated by determining the fraction of steps that fall into the NH and the IH regions, as an equal prior is placed on both hypotheses. A similar calculation can be performed by calculating the fraction of steps which fall in the lower octant (LO, $\sin^2 \theta_{23} < 0.5$) or upper octant (UO, $\sin^2 \theta_{23} > 0.5$). The fraction of steps, broken down by hierarchy and octant, are given in Table 8.2. The Bayes factor for preferred hierarchy hypothesis is $B(\text{NH}/\text{IH}) = 1.37$. Jeffrey's

Without Reactor Constraint, Both Hierarchies

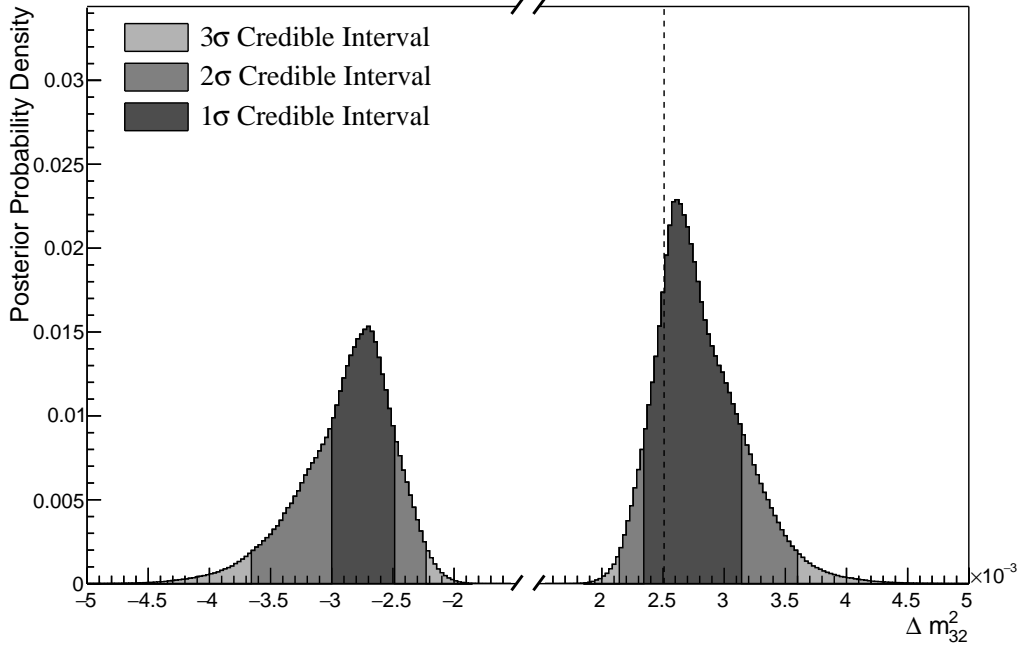


Figure 8.8: The one-dimensional posterior probability density distribution in Δm_{32}^2 , marginalised over both hierarchies, from the SK atmospheric-only fit. The reactor constraint is not applied. The vertical dashed line represents the known value of Δm_{32}^2 .

scale, given in Table 4.1, states this value of the Bayes factor indicates a weak preference for the normal hierarchy hypothesis. The Bayes factor for choice of octant is $B(\text{UO}/\text{LO}) = 2.24$. This is also classified as a weak preference for the UO. Both of these show that the fit is returning the correct choice of hypotheses (NH and UO) for the known Asimov A oscillation parameters defined in Table 2.2.

The 1 σ credible intervals, broken down by hierarchy, and position in parameter space of the highest posterior probability density is given in Table 8.3. These are taken from the one-dimensional projections of the oscillation parameters, marginalised over all other parameters within the fit. As the distribution is binned, the highest posterior density is presented as the center of the bin with the highest posterior density with an error equal to the bin width. For the known Asimov value of $\delta_{CP} = -1.601$, the 1 σ credible interval rules out a region between $\delta_{CP} = -0.88$ and $\delta_{CP} = 1.96$, when marginalising over both hierarchies. The position of the highest posterior density is $\delta_{CP} = -1.57 \pm 0.07$ which is clearly

Parameter	Interval	HPD
δ_{CP} , (BH)	$[-\pi, -0.88], [2.01, \pi]$	-1.57 ± 0.07
δ_{CP} , (NH)	$[-\pi, -0.88], [1.88, \pi]$	-1.57 ± 0.07
δ_{CP} , (IH)	$[-\pi, -0.88], [2.01, \pi]$	-1.57 ± 0.07
Δm_{32}^2 (BH) [$\times 10^{-3}\text{eV}^2$]	$[-3.00, -2.49], [2.34, 3.14]$	2.61 ± 0.02
Δm_{32}^2 (NH) [$\times 10^{-3}\text{eV}^2$]	$[2.41, 3.04]$	2.59 ± 0.03
Δm_{32}^2 (IH) [$\times 10^{-3}\text{eV}^2$]	$[-3.11, -2.41]$	-2.73 ± 0.03
$\sin^2(\theta_{23})$ (BH)	$[0.476, 0.584]$	0.542 ± 0.006
$\sin^2(\theta_{23})$ (NH)	$[0.488, 0.596]$	0.554 ± 0.006
$\sin^2(\theta_{23})$ (IH)	$[0.476, 0.584]$	0.542 ± 0.006

Table 8.3: The position of the highest posterior probability density (HPD) and width of the 1σ credible interval for the SK atmospheric-only fit. The reactor constraint is not applied. The values are presented by which hierarchy hypothesis is assumed: marginalised over both hierarchies (BH), normal hierarchy only (NH), and inverted hierarchy only (IH).

3150 compatible with the known oscillation parameter value.

3151 The sensitivity of the atmospheric samples to $\sin^2(\theta_{13})$ is presented in Fig-
 3152 ure 8.9. The likelihood scans presented in Figure 8.1 suggest that the sensitivity
 3153 to $\sin^2(\theta_{13})$ will be small. This behaviour is also seen in the fit results, where the
 3154 width of the 1σ credible intervals span the region of $\sin^2(\theta_{13}) = [0.008, 0.08]$. This
 3155 is more than an order of magnitude worse than the constraint from reactor
 3156 experiments [76].

3157 As previously discussed, the correlations between oscillation parameters are
 3158 also important to understand how the atmospheric samples respond. Figure 8.10
 3159 illustrates the two dimensional $\sin^2(\theta_{13})-\delta_{CP}$ sensitivity, marginalised over all
 3160 other parameters. The shape of the 1σ credible interval shows that the constrain-
 3161 ing power of the fit on δ_{CP} is dependent upon the value of $\sin^2(\theta_{13})$. Furthermore,
 3162 they show a strong resemblance to the likelihood scans illustrated in Figure 8.2.
 3163 Whilst the atmospheric samples do not strongly constrain the value of $\sin^2(\theta_{13})$,
 3164 the value of $\sin^2(\theta_{13})$ does impact the atmospheric samples' sensitivity to δ_{CP} .

Without Reactor Constraint, Both Hierarchies

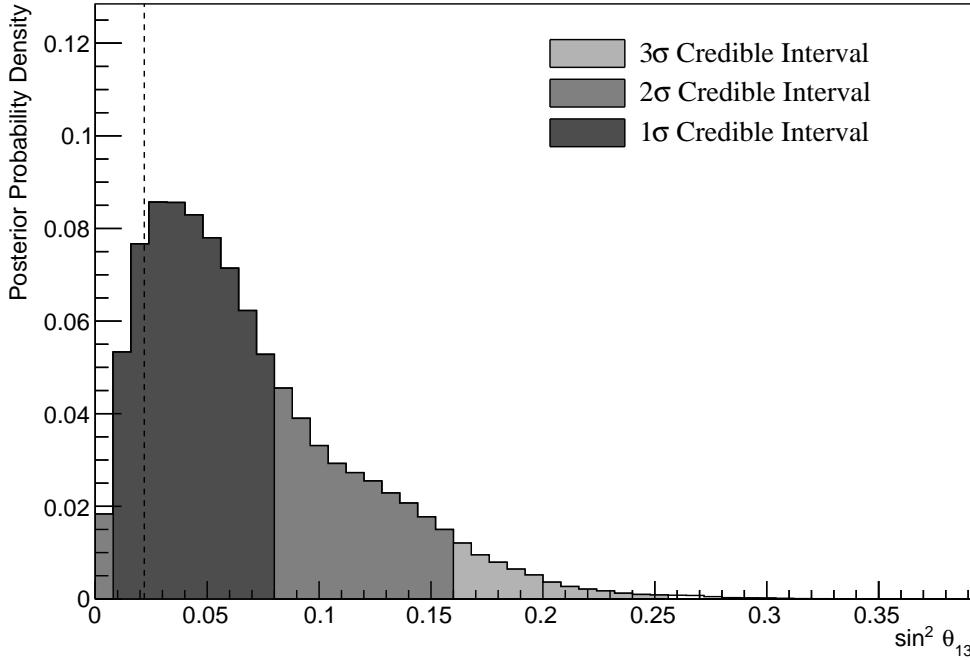


Figure 8.9: The one-dimensional posterior probability density distribution in $\sin^2(\theta_{13})$, marginalised over both hierarchies, from the SK atmospheric-only fit. The reactor constraint is not applied. The vertical dashed line represents the known value of $\sin^2(\theta_{13})$.

3165 The $\sin^2(\theta_{23}) - \Delta m_{32}^2$ disappearance contours are illustrated in Figure 8.11. As
 3166 expected, the area contained in the inverted hierarchy 1σ credible interval is
 3167 slightly smaller than that in the normal hierarchy. This follows from the Bayes
 3168 factor showing a weak preference for NH meaning that more of the steps will exist
 3169 in the $\Delta m_{32}^2 > 0$ region. The known oscillation parameters of $\sin^2(\theta_{23}) = 0.528$
 3170 and $\Delta m_{32}^2 = 2.509 \times 10^{-3} \text{ eV}^2$ are contained within the 1σ credible interval.

3171 Figure 8.12 illustrates the two-dimensional projections for each permutation of
 3172 oscillation parameters which this analysis is sensitive to: δ_{CP} , $\sin^2(\theta_{13})$, $\sin^2(\theta_{23})$,
 3173 and Δm_{32}^2 . The purpose of this plot is to illustrate the correlations between
 3174 the oscillation parameters. The contours are calculated whilst marginalising
 3175 over both hierarchies, however, only the NH is illustrated when plotting the
 3176 Δm_{32}^2 parameter. As expected the correlations play a significant role in these
 3177 sensitivity measurements, especially the choice of the $\sin^2(\theta_{13})$ constraint. Most
 3178 notably, the application of reactor constraint would be expected to alter both the

Without Reactor Constraint, Both Hierarchies

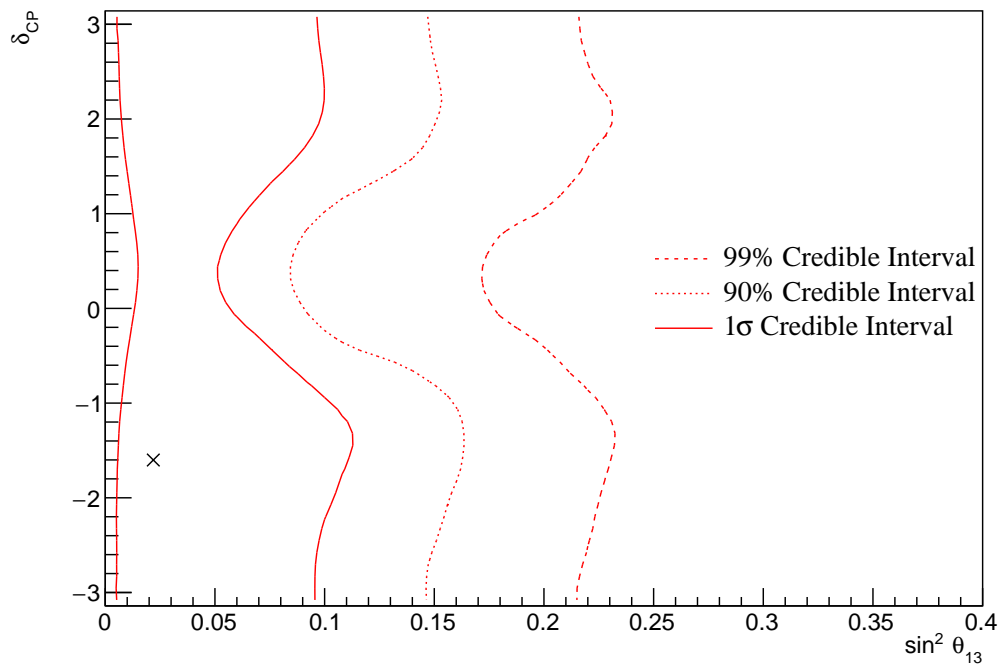


Figure 8.10: The two-dimensional posterior probability density distribution in δ_{CP} – $\sin^2(\theta_{13})$, marginalised over both hierarchies, from the SK atmospheric-only fit. The reactor constraint is not applied. The marker represents the known value of δ_{CP} – $\sin^2(\theta_{13})$.

³¹⁷⁹ width and position of the Δm_{32}^2 intervals due to the strong correlation between
³¹⁸⁰ the parameters.

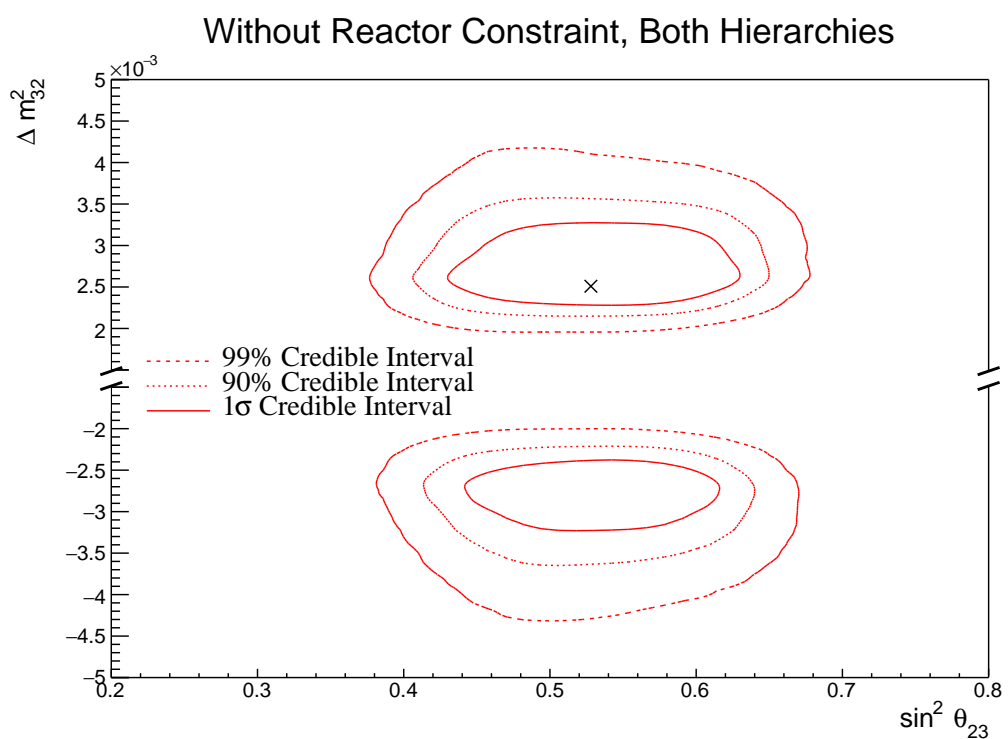


Figure 8.11: The two-dimensional posterior probability density distribution in $\Delta m_{32}^2 - \sin^2(\theta_{23})$, marginalised over both hierarchies, from the SK atmospheric-only fit. The reactor constraint is not applied. The marker represents the known value of $\Delta m_{32}^2 - \sin^2(\theta_{23})$.

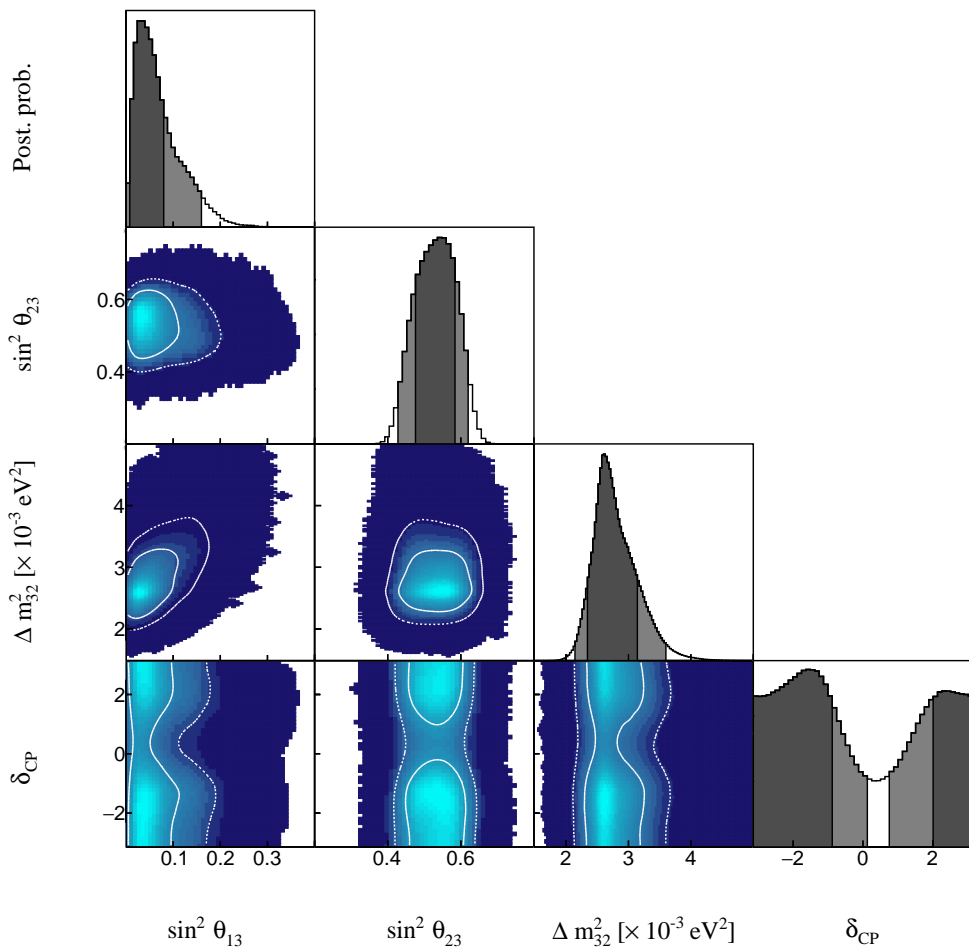


Figure 8.12: The posterior probability density distribution from the SK atmospheric-only fit. The reactor constraint is not applied. The distribution is given for each two-dimensional permutation of the oscillation parameters of interest. The one-dimensional distribution of each parameter is also given.

3181 8.3.2 Atmospheric-Only Sensitivity With Reactor Constraint

3182 The results in subsection 8.3.1 discuss the atmospheric sensitivity when the reactor
 3183 constraint is not applied. The correlations illustrated in Figure 8.12 indicate that
 3184 the marginalisation effects could contribute to differing sensitivities when the
 3185 external reactor constraint is applied. Using the technique discussed in subsec-
 3186 tion 4.1.1, the posterior distribution of the fit in subsection 8.3.1 can be reweighted
 3187 to include the reactor constraint of $\sin^2(\theta_{13}) = (2.18 \pm 0.08) \times 10^{-2}$ [76].

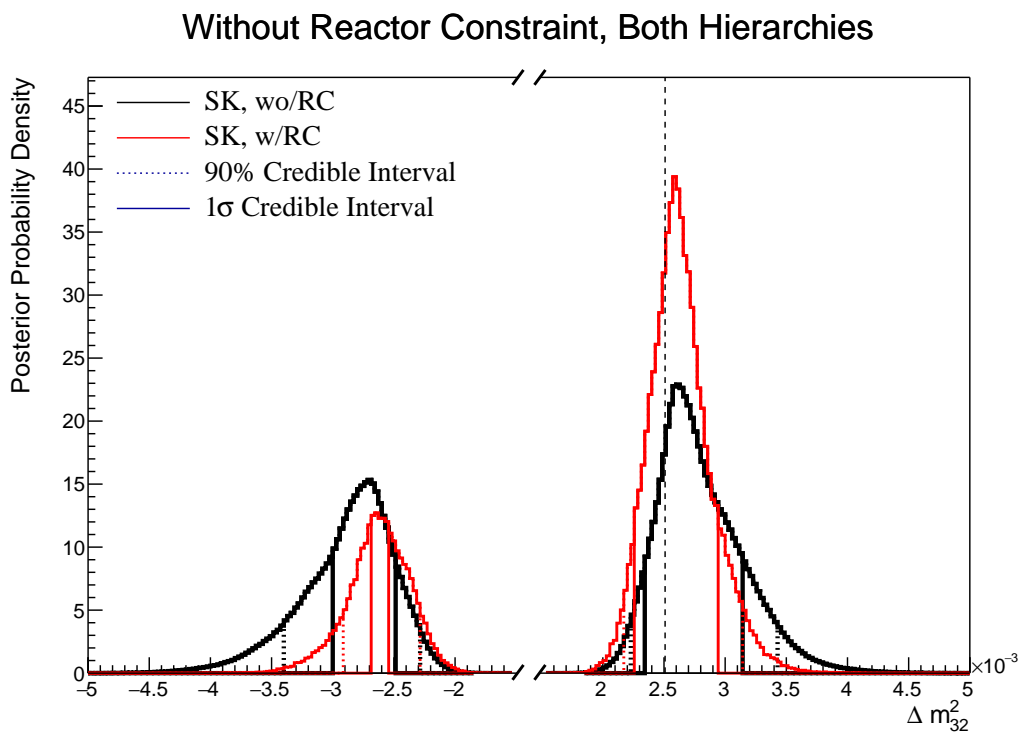


Figure 8.13: The one-dimensional posterior probability density distribution in Δm_{32}^2 compared between the SK atmospheric-only fit (Black) and the SK atmospheric fit with the reactor constraint applied (Red). The distributions are marginalised over both hierarchies. The vertical dashed line represents the known value of Δm_{32}^2 .

3188 The reactor constraint increases the sensitivity of the atmospheric samples to
 3189 Δm_{32}^2 as illustrated in Figure 8.13. The 1σ credible interval in Δm_{32}^2 is determined
 3190 to be $[-2.69, -2.54] \times 10^{-3} \text{ eV}^2$ and $[2.25, 2.94] \times 10^{-3} \text{ eV}^2$. The width of the IH
 3191 credible interval is reduced by $\sim 70\%$ when the reactor constraint is applied. Due
 3192 to the marginalisation effects observed in Figure 8.12, the favoured region of Δm_{32}^2
 3193 moves closer to zero for both hierarchies. A clear explanation of this behaviour is

³¹⁹⁴ illustrated in Figure 8.14, which shows the posterior distribution in the Δm_{32}^2 –
³¹⁹⁵ $\sin^2(\theta_{13})$ parameters. The correlation between Δm_{32}^2 and $\sin^2(\theta_{13})$ is such that
³¹⁹⁶ lower values of $\sin^2(\theta_{13})$ tend towards lower values of $|\Delta m_{32}^2|$. Therefore the
³¹⁹⁷ application of the reactor constraint moves the posterior distribution towards
³¹⁹⁸ the known oscillation parameter.

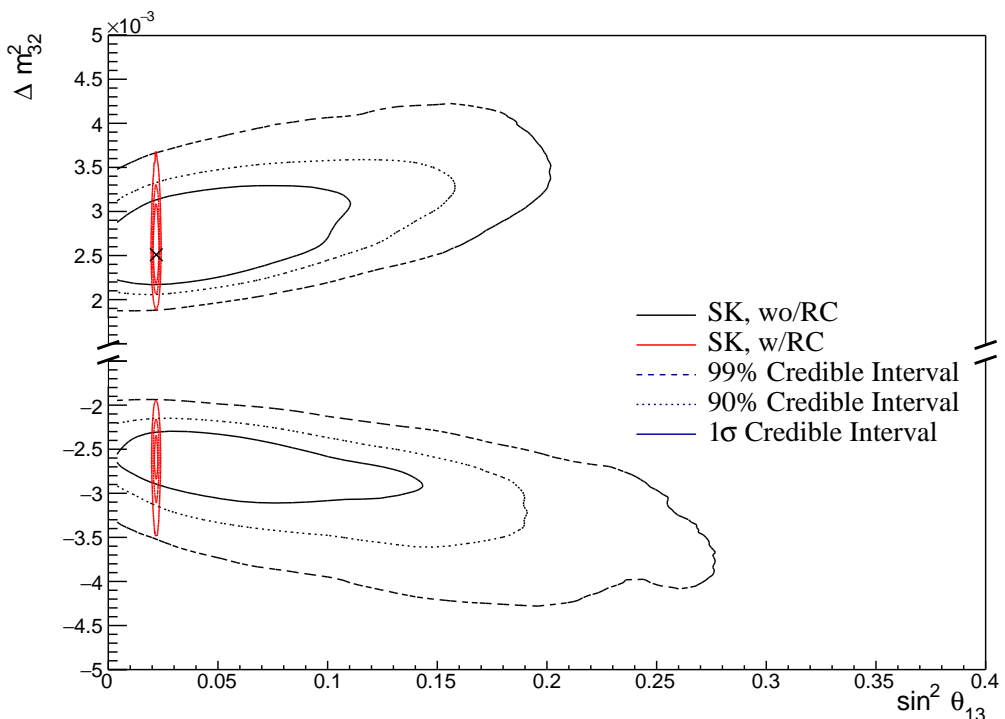


Figure 8.14: The two-dimensional posterior probability density distribution in $\Delta m_{32}^2 - \sin^2(\theta_{13})$ compared between the SK atmospheric-only fit (Black) and the SK atmospheric fit with the reactor constraint (Red). The distributions are marginalised over both hierarchies. The marker represents the known value of $\Delta m_{32}^2 - \sin^2(\theta_{13})$.

	LO ($\sin^2 \theta_{23} < 0.5$)	UO ($\sin^2 \theta_{23} > 0.5$)	Sum
NH ($\Delta m_{32}^2 > 0$)	0.21	0.53	0.74
IH ($\Delta m_{32}^2 < 0$)	0.08	0.18	0.26
Sum	0.29	0.71	1.00

Table 8.4: The distribution of steps in an SK atmospheric with reactor constraint fit, presented as the fraction of steps in the upper (UO) and lower (LO) octants and the normal (NH) and inverted (IH) hierarchies. The Bayes factors are calculated as $B(\text{NH}/\text{IH}) = 2.85$ and $B(\text{UO}/\text{LO}) = 2.39$.

3199 Table 8.4 presents the fraction of steps in each hierarchy and octant model
3200 for the fit after the reactor constraint has been applied. The reactor constraint
3201 significantly increases the NH preference, increasing the Bayes factor from
3202 $B(\text{NH}/\text{IH}) = 1.37$ to $B(\text{NH}/\text{IH}) = 2.85$ when the reactor constraint is applied.
3203 This is still defined as a weak preference for the NH hypothesis according to
3204 Jeffrey's scale, however, it is a stronger preference than when the constraint is
3205 not applied. The preference for the correct octant model is also slightly increased
3206 by the application of the reactor constraint.

3207 8.3.3 Impact of Near Detector Constraints for Atmospheric Sam- 3208 ples

3209 The choice of applying the near detector constraints to the low-energy atmo-
3210 spheric samples was introduced in subsection 6.4.3. This subsection illustrates the
3211 effect of removing the ND constraint on the sensitivity of the atmospheric samples
3212 to the oscillation parameters. To do this, the fit presented in subsection 8.3.1 has
3213 been compared to another fit where the constraints from the near detector have
3214 not been included. This is the only case where the near detector constraints are
3215 neglected throughout this chapter. For both fits, the Asimov data was generated
3216 assuming the ‘AsimovA’ oscillation parameter set defined in Table 2.2 and the
3217 post-BANFF systematic parameter tune.

3218 The change in sensitivity on δ_{CP} is given in Figure 8.15. The reactor constraint
3219 is not applied in either of the fits within this comparison. The fit which includes
3220 the near detector constraint is slightly more peaked at the known oscillation
3221 parameter value. The width of the 1σ credible intervals are approximately the
3222 same (identical to within a bin width) and the same conclusion holds for the
3223 higher credible intervals. The change in sensitivity to other oscillation parameters
3224 has been studied and no significant discrepancies were found. This shows that
3225 the exact choice of constraint does not significantly affect the physics conclusions
3226 one would make from this analysis.

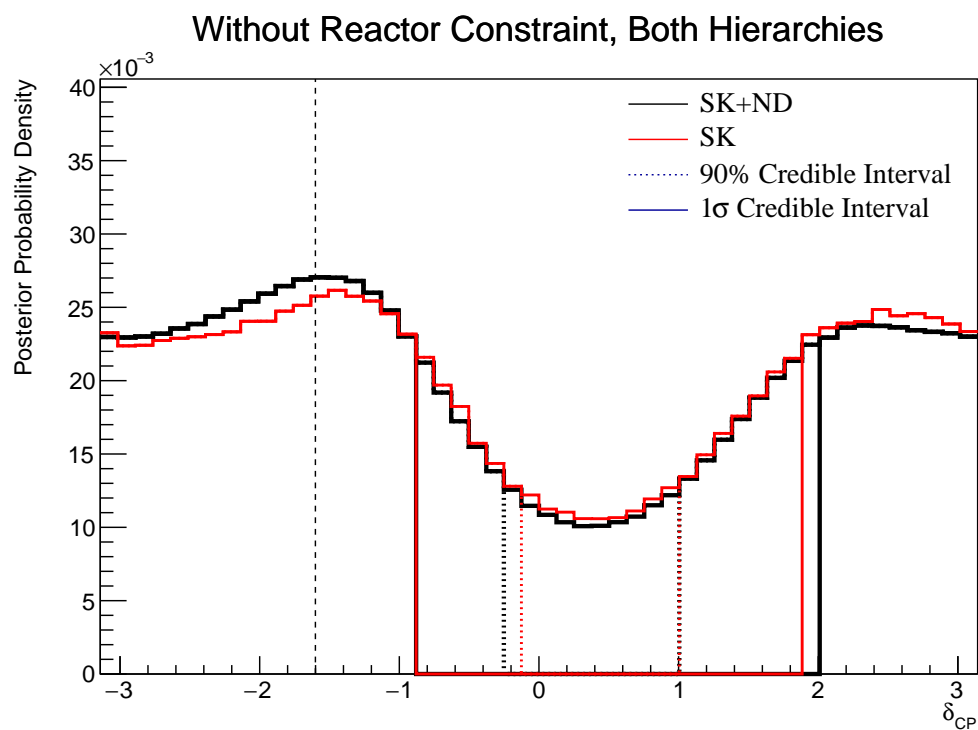


Figure 8.15: The one-dimensional posterior probability density distribution in δ_{CP} compared between the SK atmospheric-only fit where the near detector constraint is (Black) and is not (Red) applied. The distributions are marginalised over both hierarchies. The reactor constraint is not applied in either fit. The vertical dashed line represents the known value of δ_{CP} .

3227 8.3.4 Atmospheric and Beam Sensitivity without Reactor Con- 3228 straint

3229 This section presents the sensitivities of the simultaneous beam and atmospheric
 3230 analysis where the reactor constraint is not applied. Similar to the previous
 3231 studies, the Asimov data is built assuming the post-BANFF systematic tune and
 3232 Asimov A oscillation parameters defined in Table 2.2. This fit uses all 18 near
 3233 detector beam samples, 5 far detector beam samples, and 18 atmospheric samples.

Without Reactor Constraint, Both Hierarchies

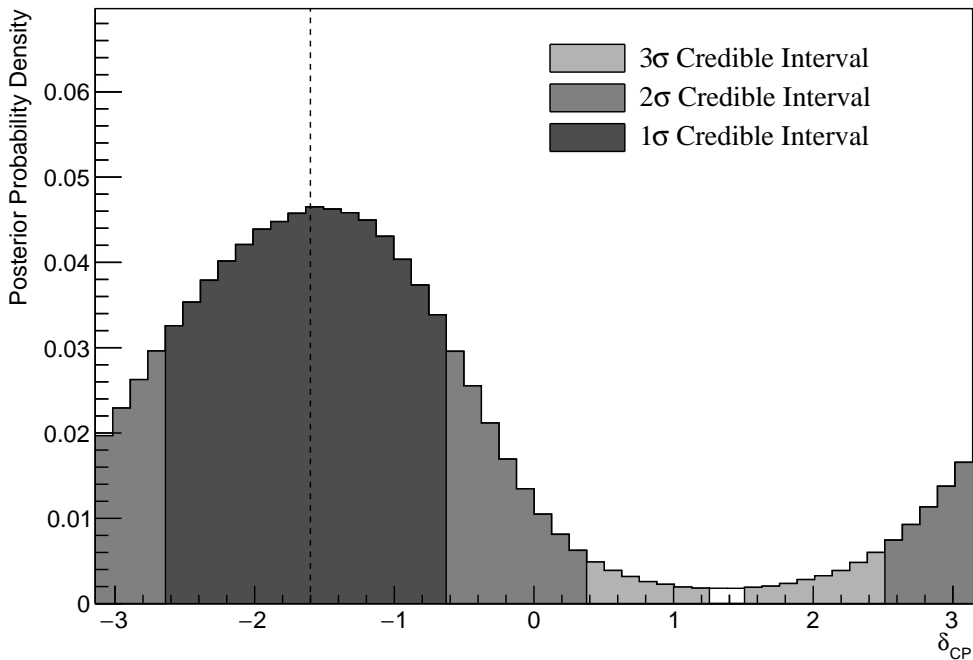


Figure 8.16: The one-dimensional posterior probability density distribution in δ_{CP} , marginalised over both hierarchies, from the joint beam-atmospheric fit. The reactor constraint is not applied. The vertical dashed line represents the known value of δ_{CP} .

3234 The sensitivity to δ_{CP} , marginalised over both hierarchies, is given in Fig-
 3235 ure 8.16. The credible intervals and highest posterior distribution for each
 3236 oscillation parameter is given in Table 8.5. The highest posterior probability
 3237 density is $\delta_{CP} = -1.57 \pm 0.07$ and is compatible with the known value of
 3238 $\delta_{CP} = -1.601$. The CP-conserving values of $\delta_{CP} = 0, \pm\pi$ are disfavoured at
 3239 1 σ credible interval. There is also a region around $\delta_{CP} = 1.4$ which is disfavoured
 3240 at more than 3 σ . Whilst these conclusions can only be made at this particular

3241 Asimov point, it does show that if the true value of δ_{CP} were CP-violating,
3242 this joint analysis would be able to disfavour CP conserving values at over 1σ
3243 without any external constraints.

Parameter	Interval	HPD
δ_{CP} , (BH)	$[-2.64, -0.63]$	-1.57 ± 0.07
δ_{CP} , (NH)	$[-2.76, -0.63]$	-1.45 ± 0.07
δ_{CP} , (IH)	$[-2.39, -0.88]$	-1.57 ± 0.07
Δm_{32}^2 (BH) [$\times 10^{-3}\text{eV}^2$]	[2.45, 2.58]	2.51 ± 0.01
Δm_{32}^2 (NH) [$\times 10^{-3}\text{eV}^2$]	[2.47, 2.56]	2.51 ± 0.01
Δm_{32}^2 (IH) [$\times 10^{-3}\text{eV}^2$]	$[-2.60, -2.51]$	-2.55 ± 0.01
$\sin^2(\theta_{23})$ (BH)	[0.480, 0.545]	0.518 ± 0.003
$\sin^2(\theta_{23})$ (NH)	[0.480, 0.545]	0.508 ± 0.003
$\sin^2(\theta_{23})$ (IH)	[0.480, 0.545]	0.513 ± 0.003

Table 8.5: The position of the highest posterior probability density (HPD) and width of the 1σ credible interval for the joint beam-atmospheric fit. The reactor constraint is not applied. The values are presented by which hierarchy hypothesis is assumed: marginalised over both hierarchies (BH), normal hierarchy only (NH), and inverted hierarchy only (IH).

3244 The sensitivity to Δm_{32}^2 is illustrated in Figure 8.17. Notably, the 1σ credible
3245 interval is entirely contained within the NH region, as further evidenced by
3246 Table 8.5. This illustrates good sensitivity to the mass hierarchy as it is correctly
3247 selecting the correct hypothesis. This is reflected in the 1σ credible intervals being
3248 approximately the same when they are constructed considering both hierarchies
3249 and when considering only the NH region. The NH distribution favours this
3250 region surrounding the known Asimov point, $\Delta m_{32}^2 = 2.509 \times 10^{-3}\text{eV}^2$, where
3251 the highest posterior probability density is at $\Delta m_{32}^2 = (2.51 \pm 0.01) \times 10^{-3}\text{eV}^2$.

3252 The fraction of steps in each of the mass hierarchy regions and octants of
3253 $\sin^2(\theta_{23})$ is given in Table 8.6. The Bayes factors are determined to be $B(\text{NH}/\text{IH}) =$
3254 3.67 and $B(\text{UO}/\text{LO}) = 1.74$. Jeffrey's scale states that this value of the mass
3255 hierarchy Bayes factor illustrates substantial evidence for the NH hypothesis.

This corresponds to the correct hypothesis given the known oscillation parameters and is a stronger statement than the atmospheric-only analysis can provide. It is important to note that this substantial preference requires no external constraints. The Bayes factor for octant determination represents a weak preference for the upper octant, therefore, selecting the correct octant hypothesis.

	LO ($\sin^2 \theta_{23} < 0.5$)	UO ($\sin^2 \theta_{23} > 0.5$)	Sum
NH ($\Delta m_{32}^2 > 0$)	0.29	0.50	0.79
IH ($\Delta m_{32}^2 < 0$)	0.08	0.13	0.21
Sum	0.37	0.63	1.00

Table 8.6: The distribution of steps in a joint beam-atmospheric fit, presented as the fraction of steps in the upper (UO) and lower (LO) octants and the normal (NH) and inverted (IH) hierarchies. The reactor constraint is not applied. The Bayes factors are calculated as $B(\text{NH}/\text{IH}) = 3.67$ and $B(\text{UO}/\text{LO}) = 1.74$.

Without Reactor Constraint, Both Hierarchies

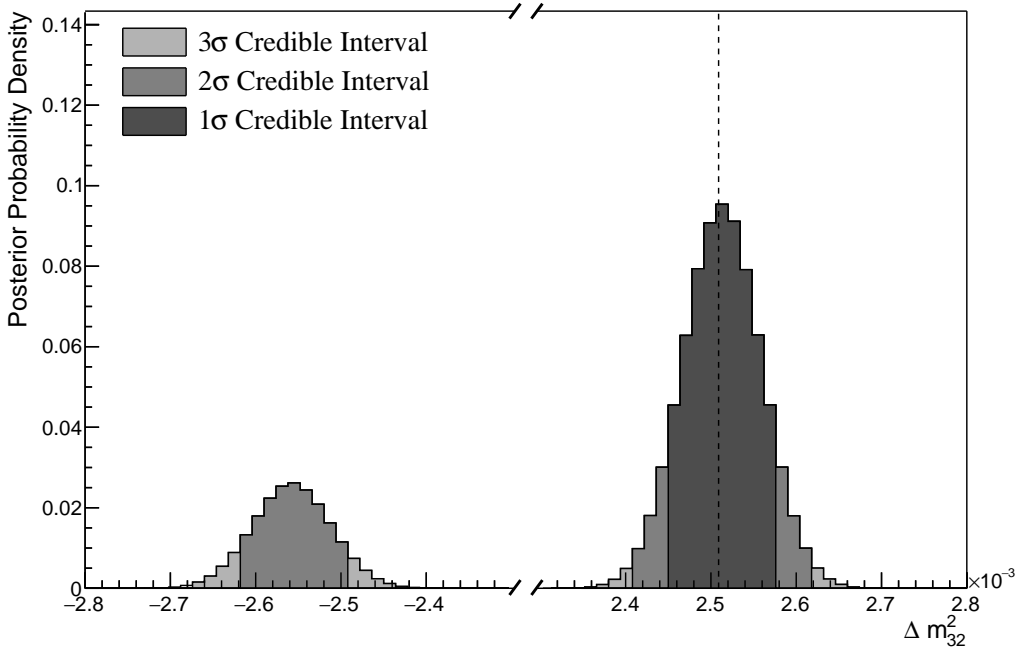


Figure 8.17: The one-dimensional posterior probability density distribution in Δm_{32}^2 , marginalised over both hierarchies, from the joint beam-atmospheric fit. The reactor constraint is not applied. The vertical dashed line represents the known value of Δm_{32}^2 .

The sensitivity to $\sin^2(\theta_{23})$ is presented in Figure 8.18. There is a clear

3262 preference for the upper octant but the peak of the distribution is relatively
 3263 flat. It peaks at $\sin^2(\theta_{23}) = 0.509 \pm 0.003$ which is in the region of the known
 3264 value of $\sin^2(\theta_{23}) = 0.528$. The difference in the highest posterior distribution
 3265 and the width of the credible interval is relatively unchanged when consid-
 3266 ering different hierarchy hypotheses showing no strong correlation between
 3267 $\sin^2(\theta_{23})$ and $|\Delta m_{32}^2|$.

Without Reactor Constraint, Both Hierarchies

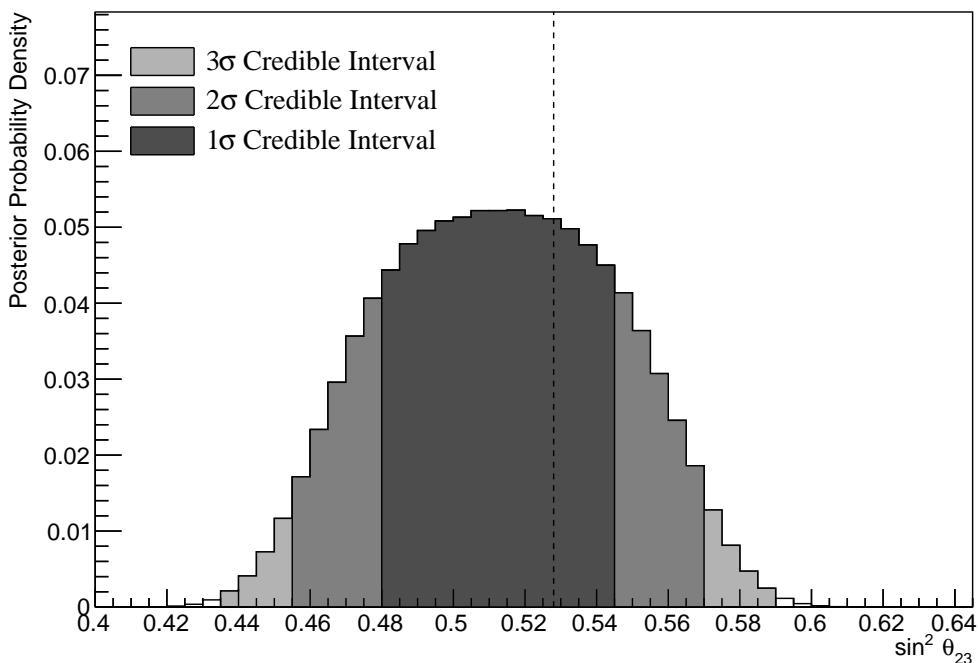


Figure 8.18: The one-dimensional posterior probability density distribution in $\sin^2(\theta_{23})$, marginalised over both hierarchies, from the joint beam-atmospheric fit. The reactor constraint is not applied. The vertical dashed line represents the known value of $\sin^2(\theta_{23})$.

3268 The sensitivity presented as a function of the appearance parameters ($\sin^2(\theta_{13}) - \delta_{CP}$)
 3269 is given in Figure 8.19. As expected, the contours follow the likelihood shape
 3270 given in Figure 8.2, where the 2σ credible intervals have a closed contour exclu-
 3271 sing the region around $\delta_{CP} \sim 1.2$. The width of the 3σ credible interval in $\sin^2(\theta_{13})$
 3272 is dependent upon the value of δ_{CP} . Close to the Asimov point, $\delta_{CP} = -1.601$, the
 3273 width of the 3σ credible interval approximately spans $\sin^2(\theta_{13}) = [0.013, 0.04]$.
 3274 This is reduced to a region of $\sin^2(\theta_{13}) = [0.023, 0.042]$ at the most disfavoured
 3275 value of δ_{CP} . The 1σ credible interval is consistent with the known oscillation

parameter. Application of the reactor constraint would be expected to decrease the width of the 1σ credible intervals in δ_{CP} due to the triangular shape of the posterior probability.

The sensitivity in terms of the disappearance parameters, $\sin^2(\theta_{23}) - \Delta m_{32}^2$, is given in Figure 8.20. The area contained within the IH contours is significantly smaller than the area within the NH contours. The IH credible intervals are also notably tighter in the $\sin^2(\theta_{23})$ dimension. No significant correlation is observed between $\sin^2(\theta_{23})$ and $|\Delta m_{32}^2|$.

Without Reactor Constraint, Both Hierarchies

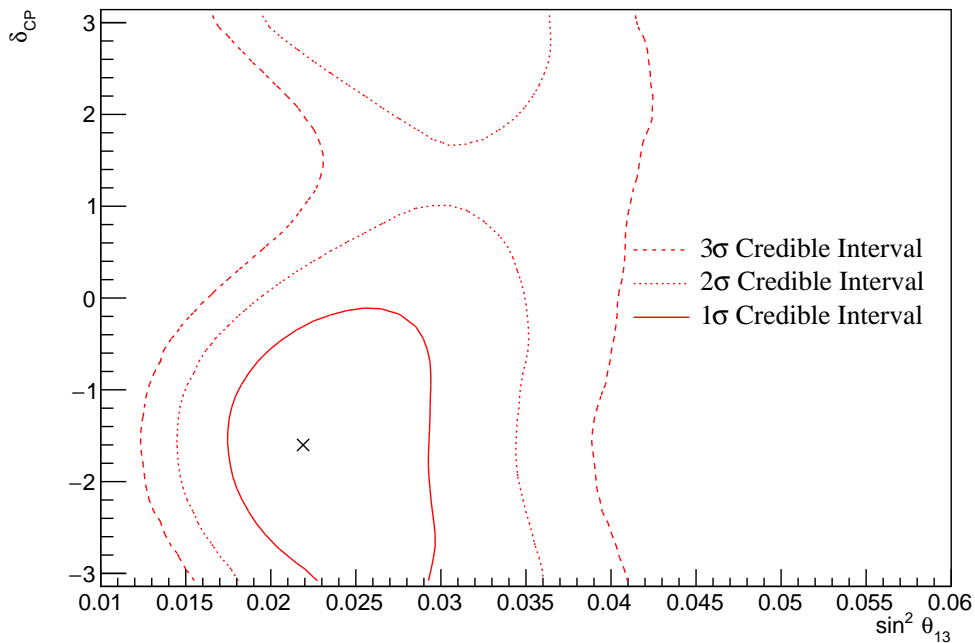


Figure 8.19: The two-dimensional posterior probability density distribution in $\delta_{CP}-\sin^2(\theta_{13})$, marginalised over both hierarchies, from the joint beam-atmospheric fit. The reactor constraint is not applied. The marker represents the known value of $\delta_{CP}-\sin^2(\theta_{13})$.

The two-dimensional posterior distribution for each permutation of the oscillation parameters of interest is given in Figure 8.21. The most notable observation is that the $\sin^2(\theta_{13})$ and $\sin^2(\theta_{23})$ are anti-correlated. If the value of $\sin^2(\theta_{13})$ was constrained closer to the known oscillation parameter value, the preferred value of $\sin^2(\theta_{23})$ would increase. This would move the highest posterior probability

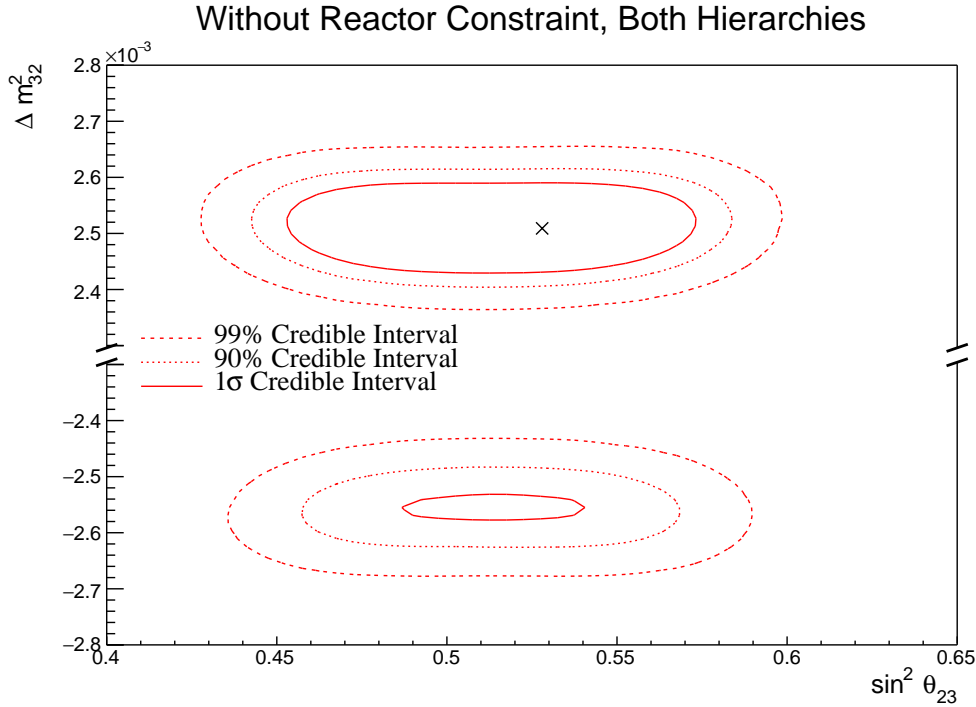


Figure 8.20: The two-dimensional posterior probability density distribution in $\Delta m_{32}^2 - \sin^2(\theta_{23})$, marginalised over both hierarchies, from the joint beam-atmospheric fit. The reactor constraint is not applied. The marker represents the known value of $\Delta m_{32}^2 - \sin^2(\theta_{23})$.

closer in line with the known value and could lead to an increase in the preference for the UO hypothesis.

Furthermore, the δ_{CP} and $|\Delta m_{32}^2|$ oscillation parameters are anti-correlated, such that higher values of $|\Delta m_{32}^2|$ prefer lower values of δ_{CP} . Whilst this is an interesting result on its own, the width of the Δm_{32}^2 contours also depend on $\sin^2(\theta_{13})$. This introduces another correlation effect that could modify the sensitivity to δ_{CP} once the reactor constraint is applied.

The correlation between $\sin^2(\theta_{13})$ and Δm_{32}^2 can be seen in Figure 8.22. A much larger fraction of the posterior distribution is contained in the NH for lower values of $\sin^2(\theta_{13})$. Consequently, the application of the reactor constraint would be expected to significantly increase the preference for NH.

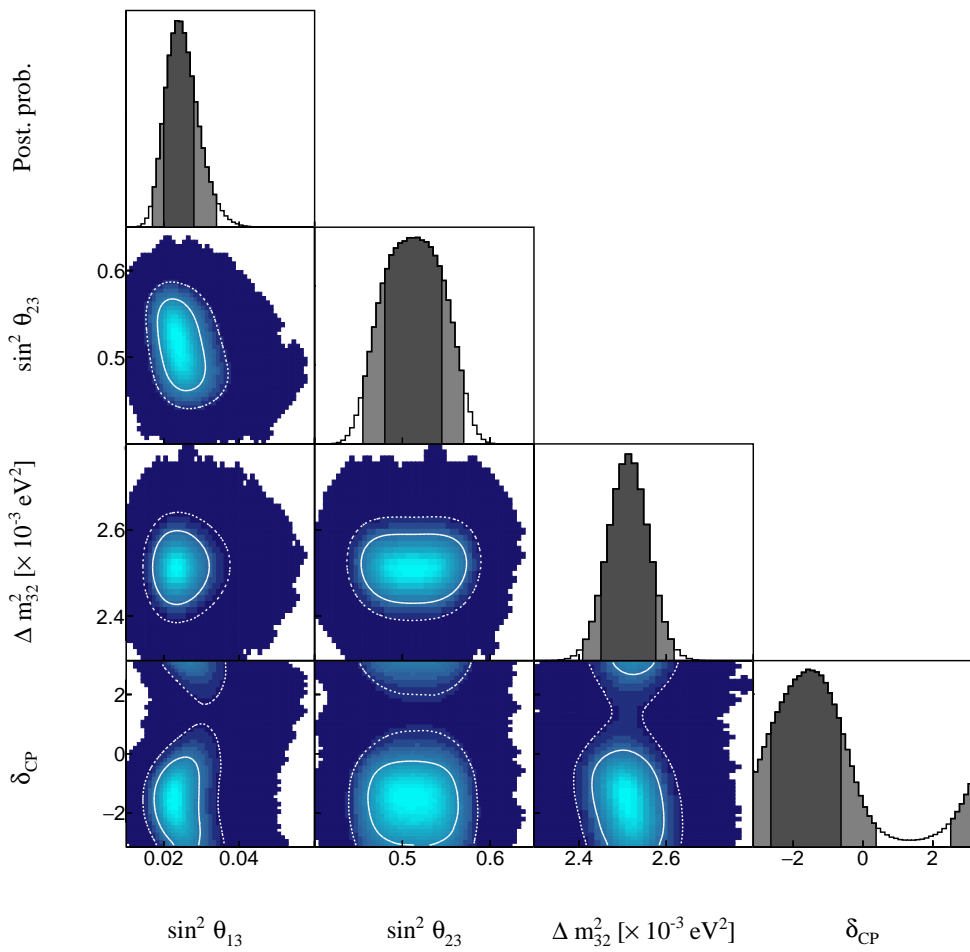


Figure 8.21: The posterior probability density distribution from the joint beam-atmospheric fit. The reactor constraint is not applied. The distribution is given for each two-dimensional permutation of the oscillation parameters of interest. The one-dimensional distribution of each parameter is also given.

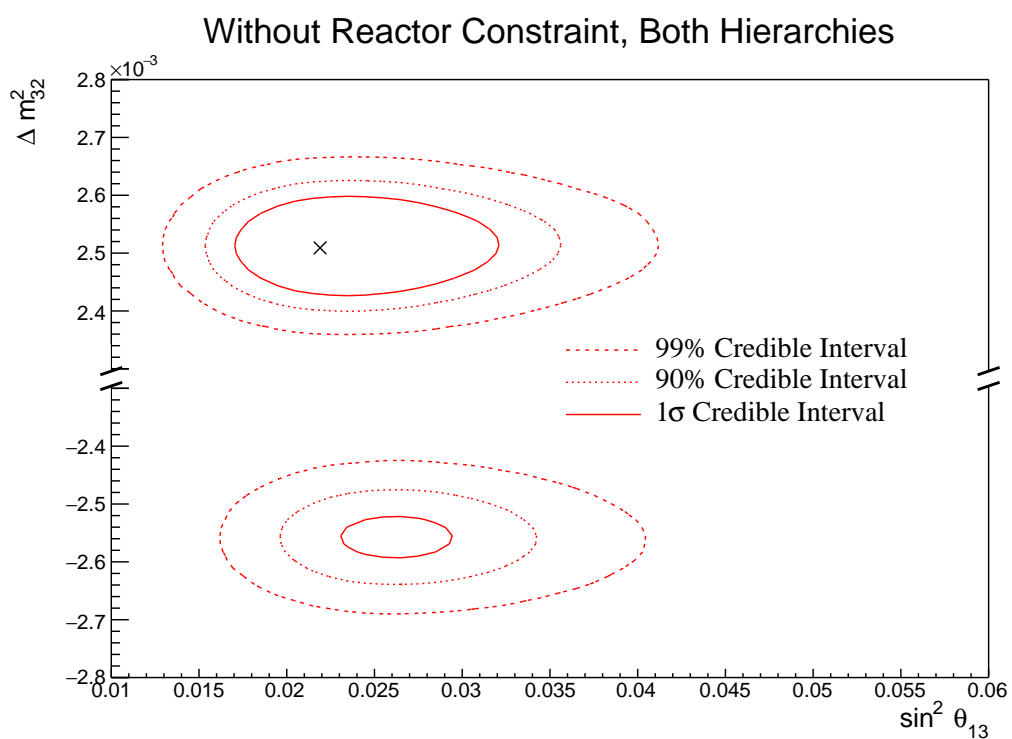


Figure 8.22: The two-dimensional posterior probability density distribution in $\Delta m_{32}^2 - \sin^2(\theta_{13})$, marginalised over both hierarchies, from the joint beam-atmospheric fit. The reactor constraint is not applied. The marker represents the known value of $\Delta m_{32}^2 - \sin^2(\theta_{13})$.

3300 8.3.5 Atmospheric and Beam Sensitivity with Reactor Constraint

3301 This section presents the sensitivities of the joint beam-atmospheric fit when
 3302 the reactor constraint is applied to $\sin^2(\theta_{13})$. As with the previous studies, the
 3303 Asimov data is made using the AsimovA oscillation parameter set defined in
 3304 Table 2.2 and the post-BANFF systematic parameter tune.

3305 **With Reactor Constraint, Both Hierarchies**

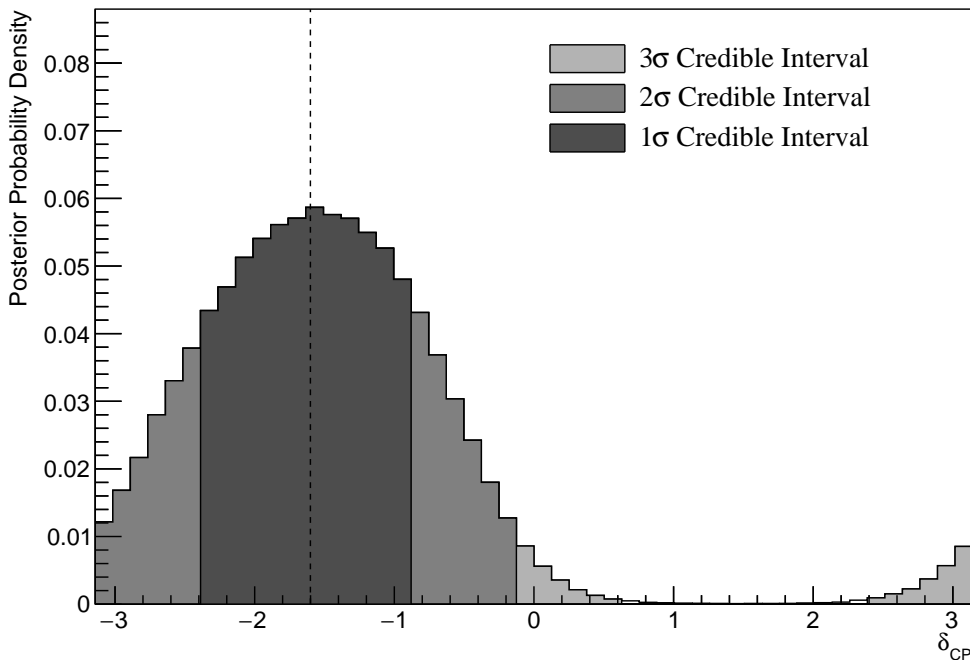


Figure 8.23: The one-dimensional posterior probability density distribution in δ_{CP} , marginalised over both hierarchies, from the joint beam-atmospheric fit where the reactor constraint is applied. The vertical dashed line represents the known value of δ_{CP} .

3305 Figure 8.23 illustrates the sensitivity to δ_{CP} , marginalised over both hierarchies.
 3306 The CP-conserving value of $\delta_{CP} = 0$ is disfavoured at 2σ whilst the value of $\delta_{CP} =$
 3307 $\pm\pi$ is very close to being disfavoured at 2σ . Furthermore, the 3σ credible interval
 3308 excludes the region of $\delta_{CP} = [0.63, 2.39]$, thus clearly disfavouring the region of
 3309 $\delta_{CP} = \pi/2$ at more than 3σ for this particular set of known oscillation parameters.
 3310 The width of the 1σ credible intervals and the position of the highest posterior
 3311 probability density is given in Table 8.7. The highest posterior probability density
 3312 in δ_{CP} is calculated as $\delta_{CP} = -1.57 \pm 0.07$ showing no significant biases in the
 3313 determination of the known oscillation parameters.

3314 The effect of applying the reactor constraint for δ_{CP} in the joint beam-atmospheric
 3315 fit is presented in Figure 8.24. The reactor constraint significantly improves the
 3316 ability of the fit to select the known parameter value. This behaviour is evidenced
 3317 by the tightening of the 1σ and 90% credible intervals and the disfavoured region,
 3318 centered at $\delta_{CP} \sim \pi/2$, becoming wider when the reactor constraint is applied.
 3319 This follows from the correlations shown in Figure 8.19, where a lower value
 3320 of $\sin^2(\theta_{13})$ results in tighter constraints on δ_{CP} .

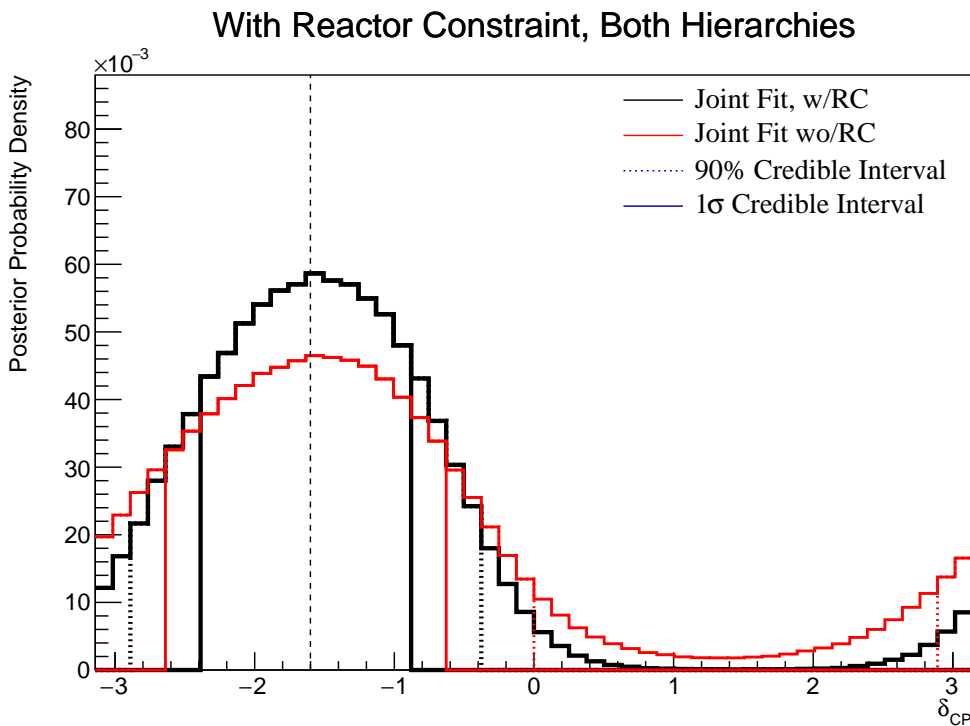


Figure 8.24: The one-dimensional posterior probability density distribution in δ_{CP} compared between the joint beam-atmospheric fit (Red) and the joint beam-atmospheric fit with the reactor constraint (Black). The distributions are marginalised over both hierarchies. The vertical dashed line represents the known value of δ_{CP} .

3321 The sensitivity to $\sin^2(\theta_{23})$, marginalised over both hierarchies, is given in
 3322 Figure 8.25. The highest posterior probability density is located at $\sin^2(\theta_{23}) =$
 3323 0.528 ± 0.03 which agrees with the known value of $\sin^2(\theta_{23}) = 0.528$. The
 3324 distribution clearly favours the UO with almost the entirety of the 1σ credible
 3325 interval being contained in that region. Figure 8.26 highlights the sensitivity
 3326 of the joint fit both with and without the reactor constraint. The fit where the

Parameter	Interval	HPD
δ_{CP} , (BH)	[-2.39, -0.88]	-1.57 ± 0.07
δ_{CP} , (NH)	[-2.39, -0.75]	-1.57 ± 0.07
δ_{CP} , (IH)	[-2.14, -1.01]	-1.57 ± 0.07
Δm_{32}^2 (BH) [$\times 10^{-3}\text{eV}^2$]	[2.45, 2.56]	2.51 ± 0.01
Δm_{32}^2 (NH) [$\times 10^{-3}\text{eV}^2$]	[2.47, 2.56]	2.51 ± 0.01
Δm_{32}^2 (IH) [$\times 10^{-3}\text{eV}^2$]	[-2.60, -2.51]	-2.55 ± 0.01
$\sin^2(\theta_{23})$ (BH)	[0.490, 0.555]	0.528 ± 0.03
$\sin^2(\theta_{23})$ (NH)	[0.490, 0.555]	0.528 ± 0.03
$\sin^2(\theta_{23})$ (IH)	[0.500, 0.560]	0.538 ± 0.03

Table 8.7: The position of the highest posterior probability density (HPD) and width of the 1σ credible interval for the joint beam-atmospheric fit where the reactor constraint is applied. The values are presented by which hierarchy hypothesis is assumed: marginalised over both hierarchies (BH), normal hierarchy only (NH), and inverted hierarchy only (IH).

reactor constraint is applied selects the known value much better. This is a result of the marginalisation effects between the $\sin^2(\theta_{13})$ and $\sin^2(\theta_{23})$ parameters, as observed in Figure 8.21.

The fraction of steps from the joint fit, after the reactor constraint is applied, is given in Table 8.8 and split by the two hierarchy and two octant hypotheses. The reactor constraint significantly reduces the fraction of steps that are contained within the IH-LO region from 0.08 to 0.03, whilst significantly increasing the fraction of steps within the NH-UO region from 0.50 to 0.62. The application of the reactor constraint increases the Bayes factor from $B(\text{NH}/\text{IH}) = 3.67$ to $B(\text{NH}/\text{IH}) = 6.47$. There is a very clear preference for the NH, with the Jeffreys scale stating a substantial preference for both fits. The Bayes factor for UO preference is calculated as $B(\text{UO}/\text{LO}) = 2.64$. Whilst still a weak preference, this is certainly a stronger statement than the sensitivity when the reactor constraint is not applied.

The sensitivity of the joint beam-atmospheric fit to Δm_{32}^2 , with the reactor constraint applied, is presented in Figure 8.27. The 1σ credible interval is

With Reactor Constraint, Both Hierarchies

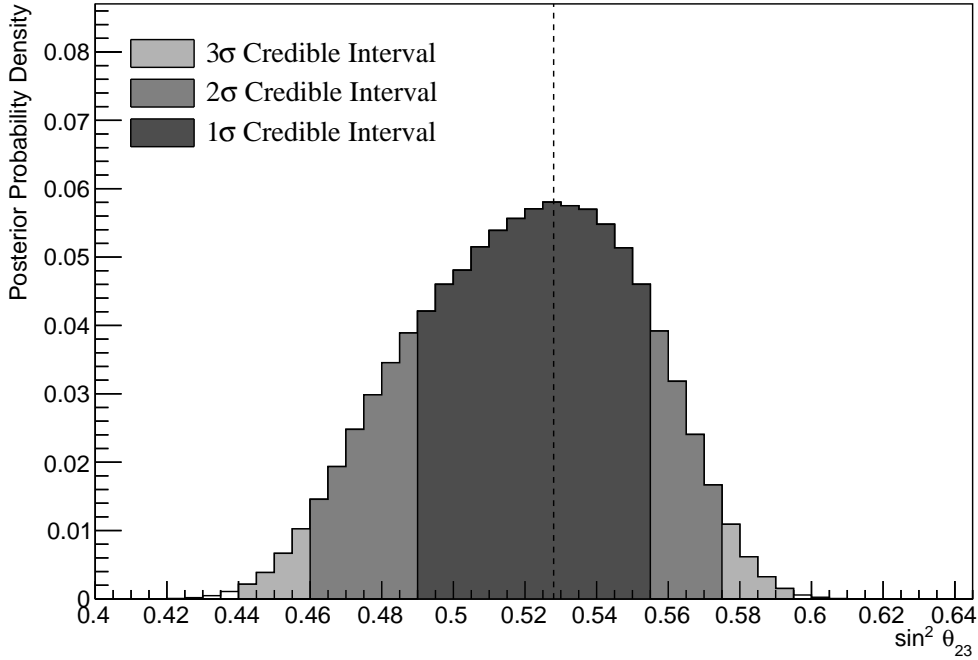


Figure 8.25: The one-dimensional posterior probability density distribution in $\sin^2(\theta_{23})$, marginalised over both hierarchies, from the joint beam-atmospheric fit where the reactor constraint is applied. The vertical dashed line represents the known value of $\sin^2(\theta_{23})$.

	LO ($\sin^2 \theta_{23} < 0.5$)	UO ($\sin^2 \theta_{23} > 0.5$)	Sum
NH ($\Delta m_{32}^2 > 0$)	0.24	0.62	0.87
IH ($\Delta m_{32}^2 < 0$)	0.03	0.10	0.13
Sum	0.27	0.73	1.00

Table 8.8: The distribution of steps in a joint beam-atmospheric with the reactor constraint fit applied, presented as the fraction of steps in the upper (UO) and lower (LO) octants and the normal (NH) and inverted (IH) hierarchies. The Bayes factors are calculated as $B(\text{NH}/\text{IH}) = 6.47$ and $B(\text{UO}/\text{LO}) = 2.64$.

3343 entirely contained within the NH region and the position of the highest posterior
 3344 probability density is given as $(2.49 \pm 0.01) \times 10^{-3} \text{ eV}^2$. This illustrates no bias
 3345 between the fit results and the known oscillation parameters. The application
 3346 of the reactor constraint does not significantly move the position or width of
 3347 the credible intervals.

3348 The sensitivity to the appearance parameters ($\sin^2(\theta_{13}) - \delta_{CP}$) is given in Fig-
 3349 ure 8.28. The distribution is mostly uncorrelated between the two parameters and

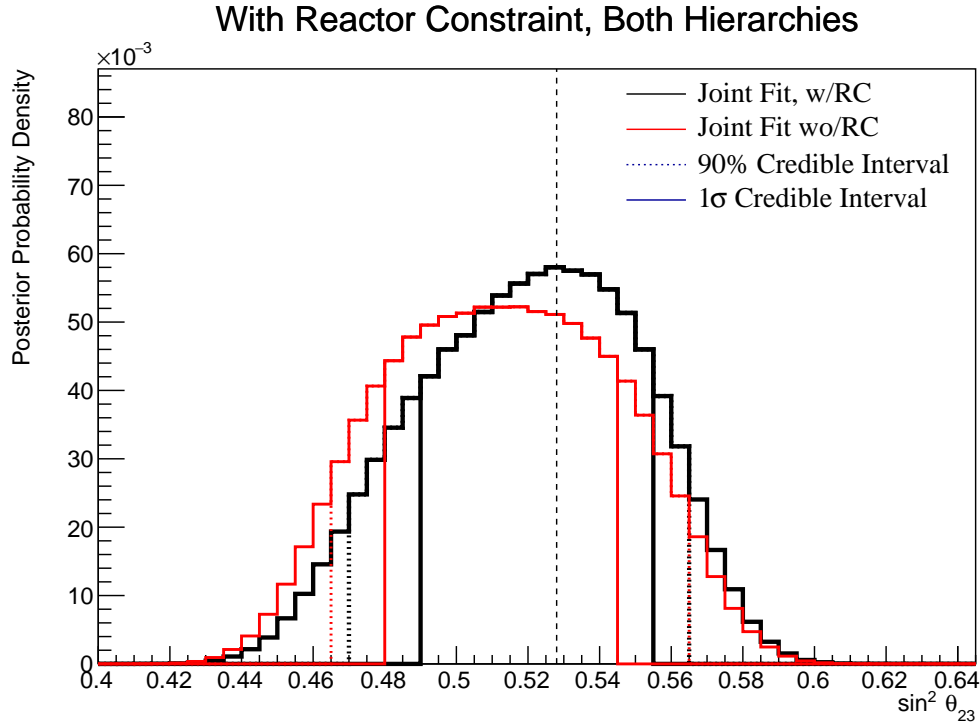


Figure 8.26: The one-dimensional posterior probability density distribution in $\sin^2(\theta_{23})$ compared between the joint beam-atmospheric fit (Red) and the joint beam-atmospheric fit with the reactor constraint (Black). The distributions are marginalised over both hierarchies. The vertical dashed line represents the known value of $\sin^2(\theta_{23})$.

is centered at the known oscillation parameters. The 1σ credible interval excludes
 $\delta_{CP} = 0$ and $\delta_{CP} = \pm\pi$. Furthermore, the 3σ credible intervals exclude the
region of $\delta_{CP} = \pi/2$.

The sensitivity to the disappearance parameters ($\sin^2(\theta_{23}) - \Delta m_{32}^2$) is illustrated
in Figure 8.29. The 1σ credible interval is entirely contained within the NH
region reflecting the same results as the one-dimensional marginalised results in
Figure 8.27. Both the NH and IH regions favour the UO, with a visually similar
preference in both hierarchies. The width of the 1σ contour, in Δm_{32}^2 , does not
significantly depend upon the value or octant of $\sin^2(\theta_{23})$. This shows that there
are no strong correlations between these two parameters.

Figure 8.30 illustrates the posterior distribution for each permutation of
two oscillation parameters of interest. The application of the reactor constraint
significantly reduces the correlations previously seen in Figure 8.21.

With Reactor Constraint, Both Hierarchies

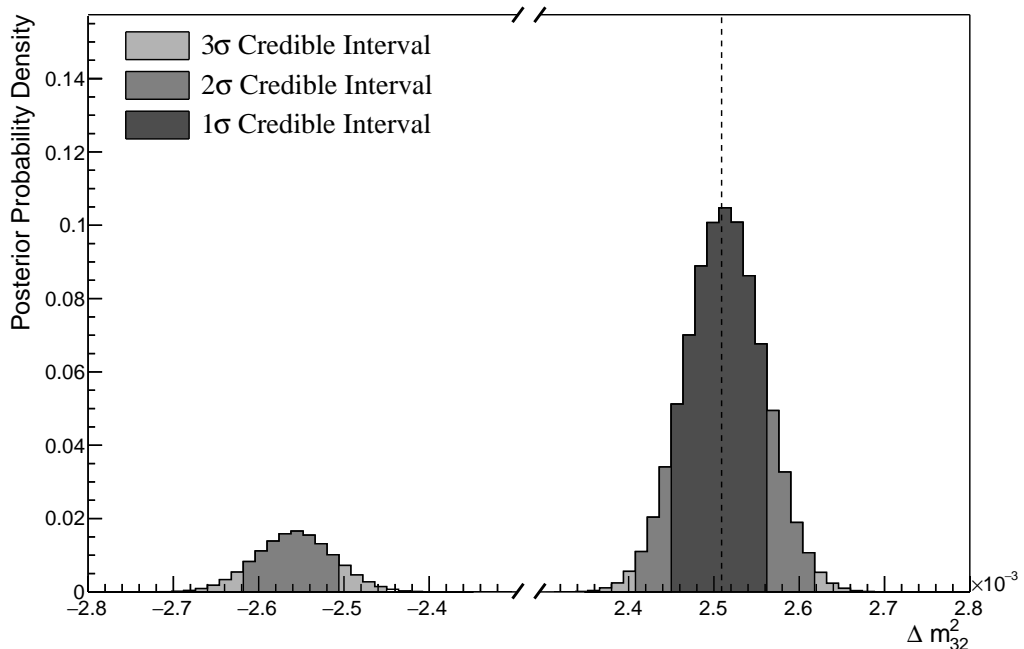


Figure 8.27: The one-dimensional posterior probability density distribution in Δm_{32}^2 from the joint beam-atmospheric fit where the reactor constraint is applied. The vertical dashed line represents the known value of Δm_{32}^2 .

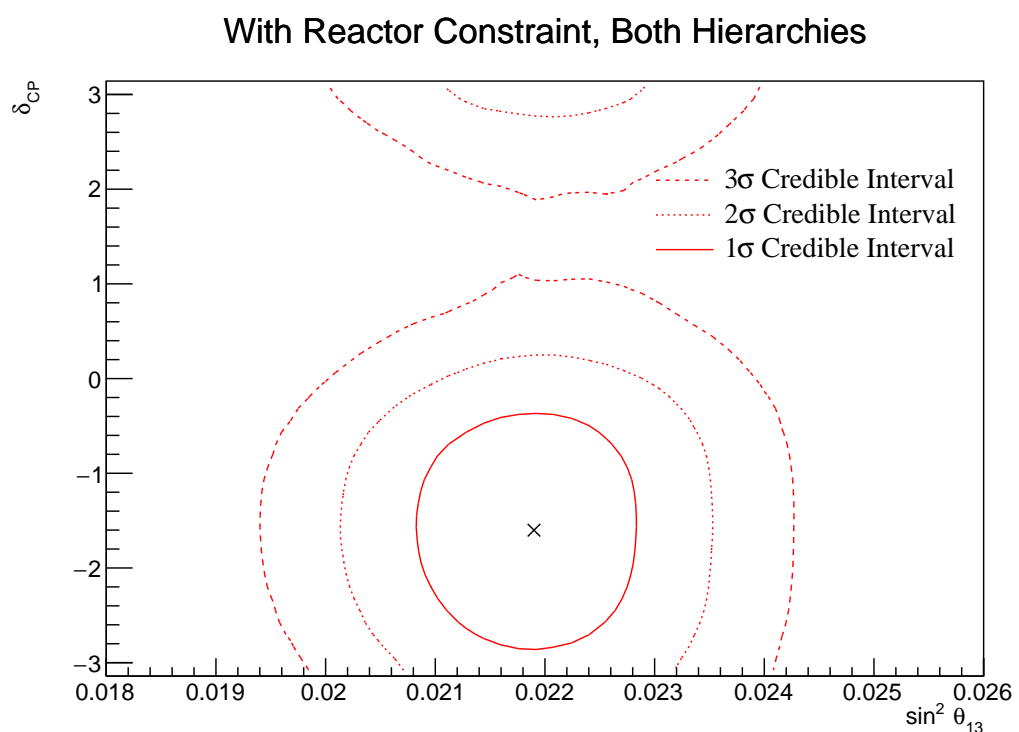


Figure 8.28: The two-dimensional posterior probability density distribution in $\delta_{CP} - \sin^2(\theta_{13})$, marginalised over both hierarchies, from the joint beam-atmospheric fit where the reactor constraint is applied. The marker represents the known value of $\delta_{CP} - \sin^2(\theta_{13})$.

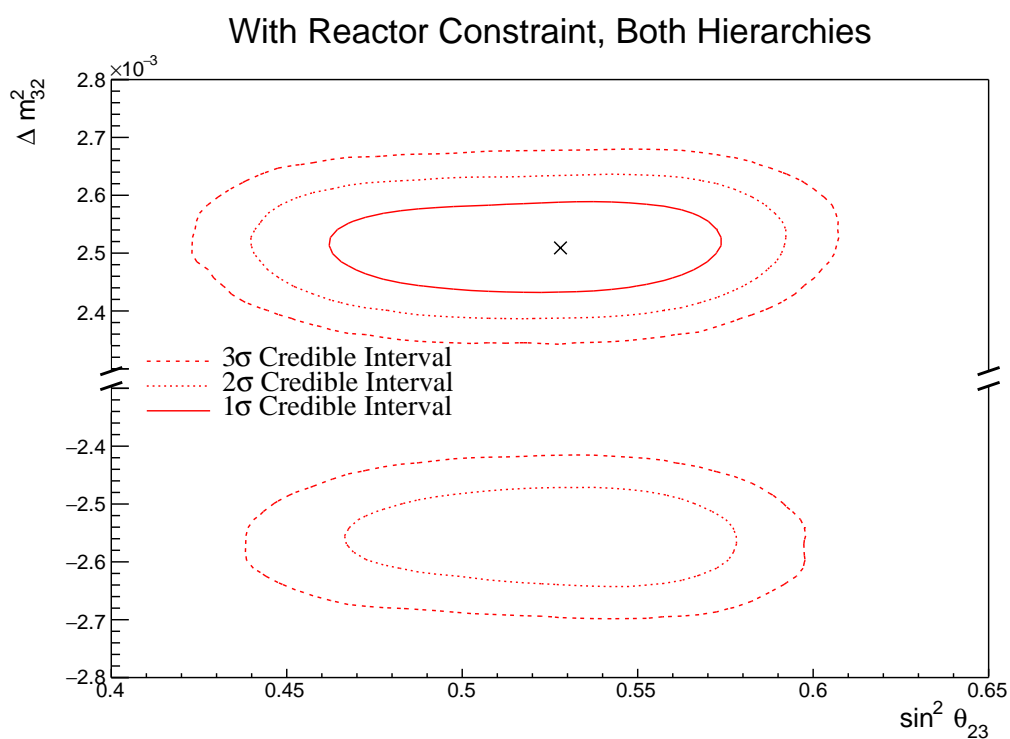


Figure 8.29: The two-dimensional posterior probability density distribution in $\Delta m_{32}^2 - \sin^2(\theta_{23})$, marginalised over both hierarchies, from the joint beam-atmospheric fit where the reactor constraint is applied. The marker represents the known value of $\Delta m_{32}^2 - \sin^2(\theta_{23})$.

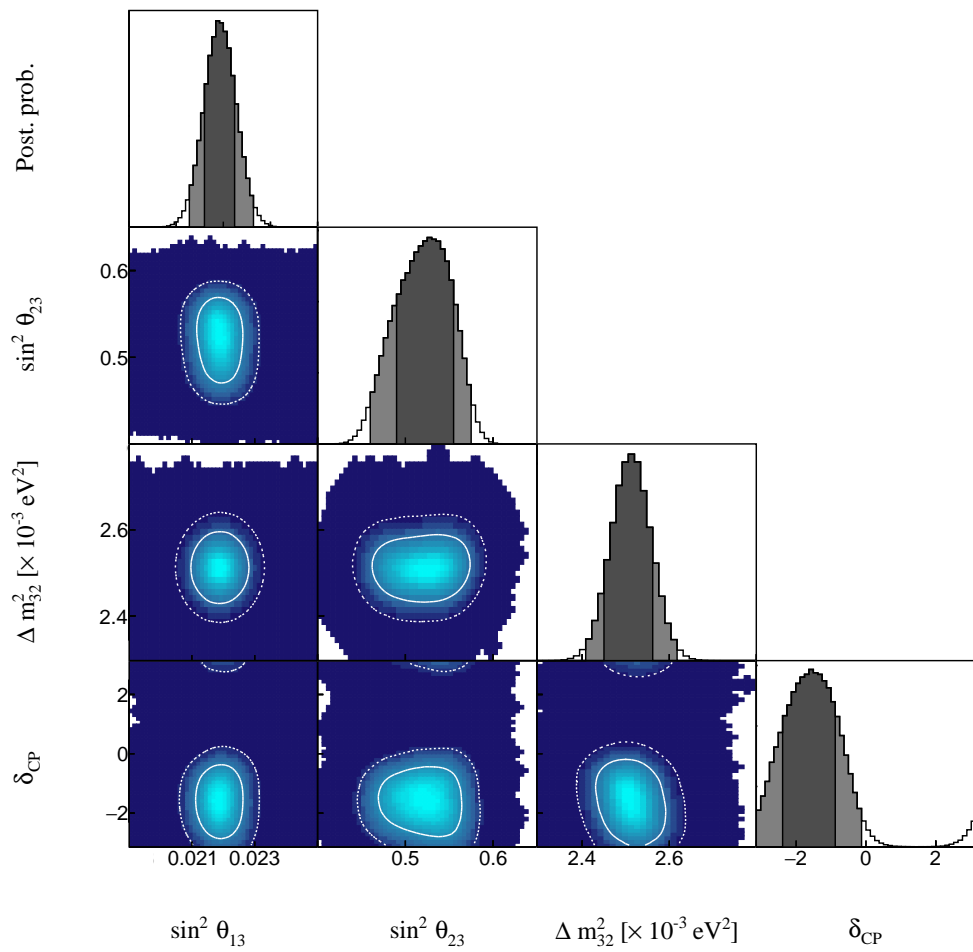


Figure 8.30: The posterior probability density distribution from the joint beam-atmospheric fit where the reactor constraint is applied. The distribution is given for each two-dimensional permutation of the oscillation parameters of interest. The one-dimensional distribution of each parameter is also given.

3363 8.3.6 Comparison to Latest T2K Sensitivities without Reactor 3364 Constraint

3365 The benefits of the joint beam-atmospheric analysis can be determined by compar-
 3366 ing the sensitivities to the beam-only analysis presented in [2, 215]. This section
 3367 presents those comparisons for sensitivities built using the Asimov A oscillation
 3368 parameters defined in Table 2.2 and the post-BANFF systematic tune. The reactor
 3369 constraint is not applied within either of the fits used in these comparisons.

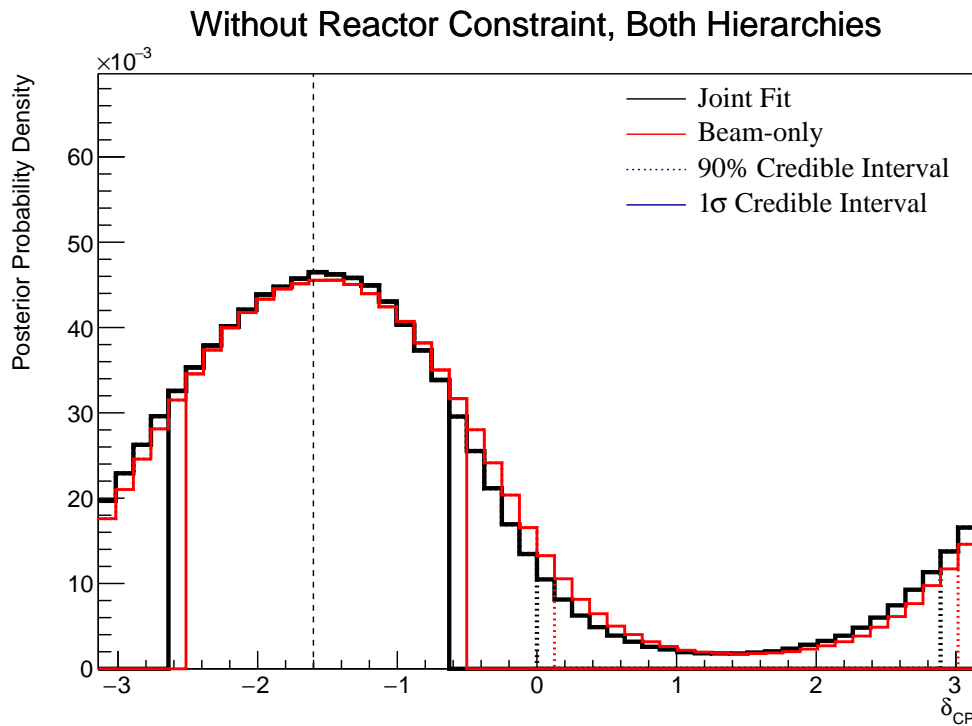


Figure 8.31: The one-dimensional posterior probability density distribution in δ_{CP} compared between the joint beam-atmospheric fit (Black) and the latest T2K sensitivities (Red) [2, 215]. The reactor constraint is not applied in either fit. The distributions are marginalised over both hierarchies. The vertical dashed line represents the known value of δ_{CP} .

3370 The sensitivity, marginalised over both hierarchies, to δ_{CP} from the joint beam-
 3371 atmospheric and beam-only fits is presented in Figure 8.31. As expected from the
 3372 likelihood scans (Figure 8.4), the sensitivity to δ_{CP} is not significantly increased.
 3373 This is because the known oscillation parameter value lies at the position where
 3374 the beam samples dominate the sensitivity compared to the SK samples.

3375 The sensitivity to Δm_{32}^2 is compared between the joint beam-atmospheric fit
 3376 and beam-only fit in Figure 8.32. The 1σ credible interval of the joint beam-
 3377 atmospheric fit is entirely contained within the NH region. This shows the
 3378 significant increase in the ability of the fit to determine the correct mass hierarchy,
 3379 compared to the beam-only analysis. This is further evidenced by the fact that the
 3380 90% credible intervals from the joint fit are also tighter in the IH region compared
 3381 to the beam-only analysis. The Bayes factor for mass hierarchy determination
 3382 for the beam-only and joint beam-atmospheric fits are $B(\text{NH}/\text{IH}) = 1.91$ and
 3383 $B(\text{NH}/\text{IH}) = 3.67$, respectively. According to Jeffrey's scale, the beam-only
 3384 analysis represents a weak preference for the NH hypothesis whereas the joint fit
 3385 returns a substantial preference for the NH hypothesis. Notably, this conclusion
 3386 does not require any external constraints and clearly illustrates the benefit of
 3387 the joint analysis.

Without Reactor Constraint, Both Hierarchies

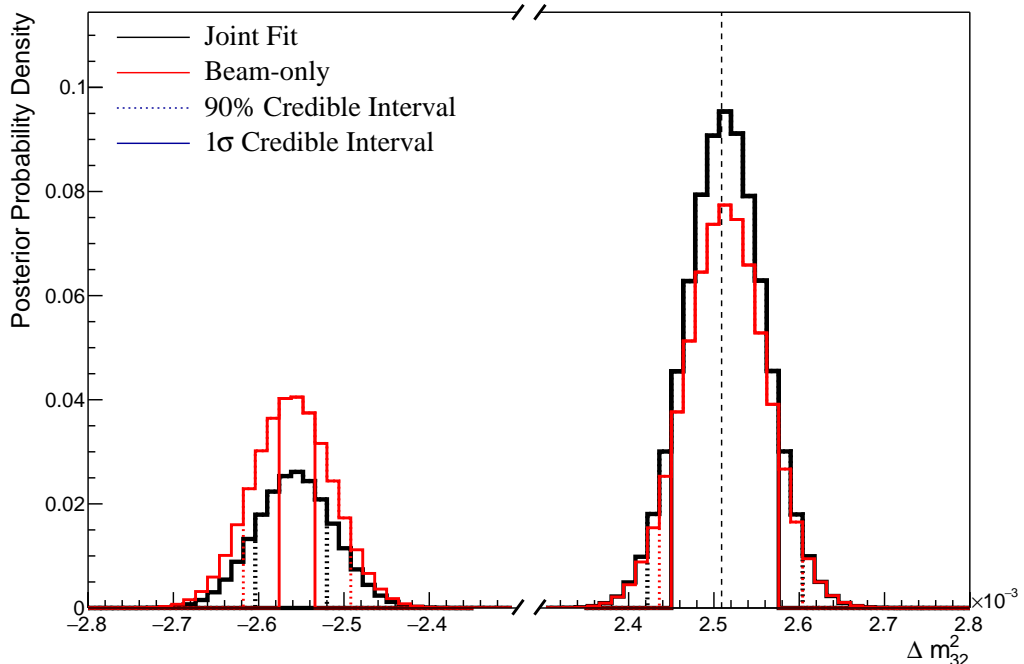


Figure 8.32: The one-dimensional posterior probability density distribution in Δm_{32}^2 compared between the joint beam-atmospheric fit (Black) and the latest T2K sensitivities (Red) [2, 215]. The reactor constraint is not applied in either fit. The vertical dashed line represents the known value of Δm_{32}^2 .

3388 The sensitivity to $\sin^2(\theta_{23})$, marginalised over both hierarchies, for both the
 3389 beam-only and joint beam-atmospheric analysis are presented in Figure 8.33. The
 3390 peak of the posterior distribution from the joint analysis is more aligned with the
 3391 known value of $\sin^2(\theta_{23}) = 0.528$ compared to the beam-only analysis. The Bayes
 3392 factors for the beam-only and joint beam-atmospheric fit are $B(\text{UO}/\text{LO}) = 1.56$
 3393 and $B(\text{UO}/\text{LO}) = 1.74$, respectively. Therefore, the joint beam-atmospheric fit
 3394 does prefer the UO more strongly than the beam-only analysis, albeit slightly.

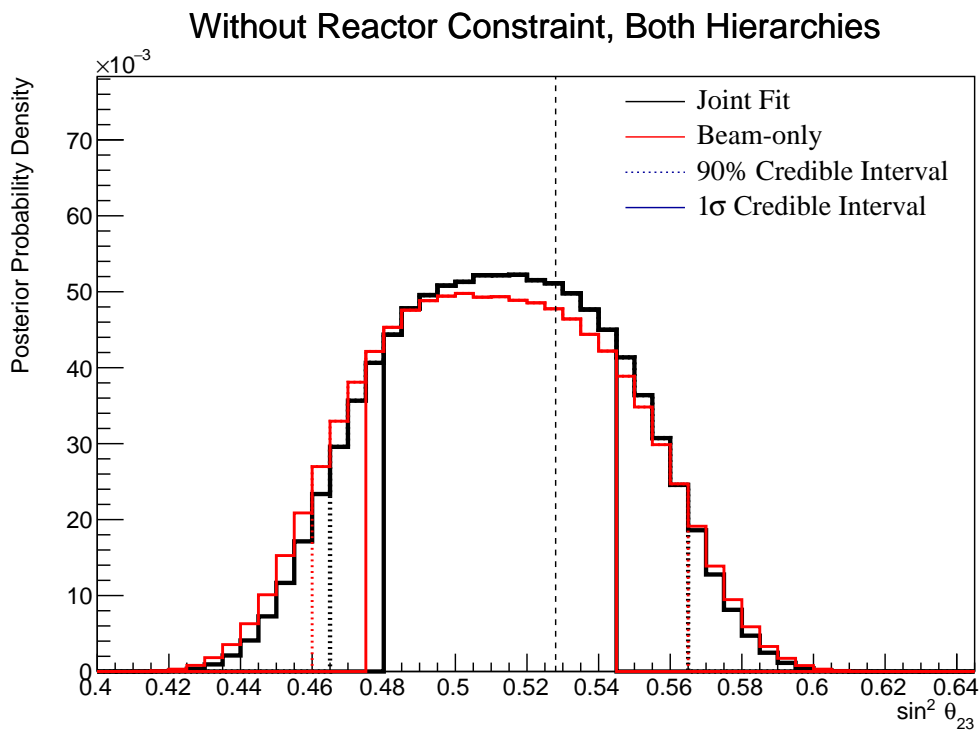


Figure 8.33: The one-dimensional posterior probability density distribution in $\sin^2(\theta_{23})$ compared between the joint beam-atmospheric fit (Black) and the latest T2K sensitivities (Red) [2, 215]. The reactor constraint is not applied in either fit. The distributions are marginalised over both hierarchies. The vertical dashed line represents the known value of $\sin^2(\theta_{23})$.

3395 Whilst the beam-only and joint beam-atmospheric fits have similar sensi-
 3396 tivity to δ_{CP} and $\sin^2(\theta_{23})$ when projected in one-dimension, the benefit of the
 3397 joint analysis becomes more obvious when the sensitivities are presented in
 3398 two-dimensions. The sensitivity of the two fits to the appearance parameters
 3399 ($\delta_{CP} - \sin^2(\theta_{13})$) is illustrated in Figure 8.34. The width of the 99% joint fit credible
 3400 interval in $\sin^2(\theta_{13})$ is squeezed in the region of $\delta_{CP} \sim 0$ compared to the

beam-only analysis. This is the same behaviour that is seen in the appearance likelihood scans presented in Figure 8.2. The 1σ and 90% also exhibit slightly tighter constraints on δ_{CP} . This is most prevalent in the region of $\delta_{CP} \sim 0$ and $\sin^2(\theta_{13}) \sim 0.03$. Whilst the atmospheric samples do not have significant sensitivity to $\sin^2(\theta_{13})$ (as shown in Figure 8.1), they aid in breaking the degeneracy between the oscillation parameters allowing for tighter constraints.

The sensitivity to the disappearance parameters $\sin^2(\theta_{23}) - \Delta m_{32}^2$ is presented in Figure 8.35 for both the beam-only and joint beam-atmospheric fits. Whilst the one-dimensional sensitivity comparisons considered so far show the improvements of the joint fit, the two-dimensional projection really shows the benefit of adding the atmospheric samples to the beam samples. The area contained within the IH credible intervals is drastically reduced in the joint fit. This follows from the better determination of the mass hierarchy seen in the Bayes factor comparisons. Even in the NH region, the widths of the credible intervals in $\sin^2(\theta_{23})$ decreases, albeit to a smaller extent.

The comparison in sensitivity to $\delta_{CP} - \Delta m_{32}^2$ is illustrated in Figure 8.36. The contours from the joint beam-atmospheric fit are much smaller in the IH region as compared to the beam-only analysis. This culminates in a region around $\delta_{CP} \sim \pi/2$ in the H region which is excluded at 3σ . This behaviour is not present within the beam-only analysis. Consistent with the previous observations, the area contained within the IH credible intervals is significantly reduced in comparison to the beam-only analysis.

The sensitivity to Δm_{32}^2 , as a function of $\sin^2(\theta_{13})$, is presented in Figure 8.37. Similar to previous observations, the Δm_{32}^2 contours within IH region of the joint fit are much smaller than the beam-only analysis. Notably, the joint fit IH 1σ credible intervals exclude the region around the reactor constraint. This suggests that the application of the reactor constraint would further increase the preference for NH in the joint fit compared to its effect on the beam-only analysis.

The beam-only and joint beam-atmospheric fits have a slightly different contour shape between the $\sin^2(\theta_{13})$ and $\sin^2(\theta_{23})$ parameters, as illustrated

Without Reactor Constraint, Both Hierarchies

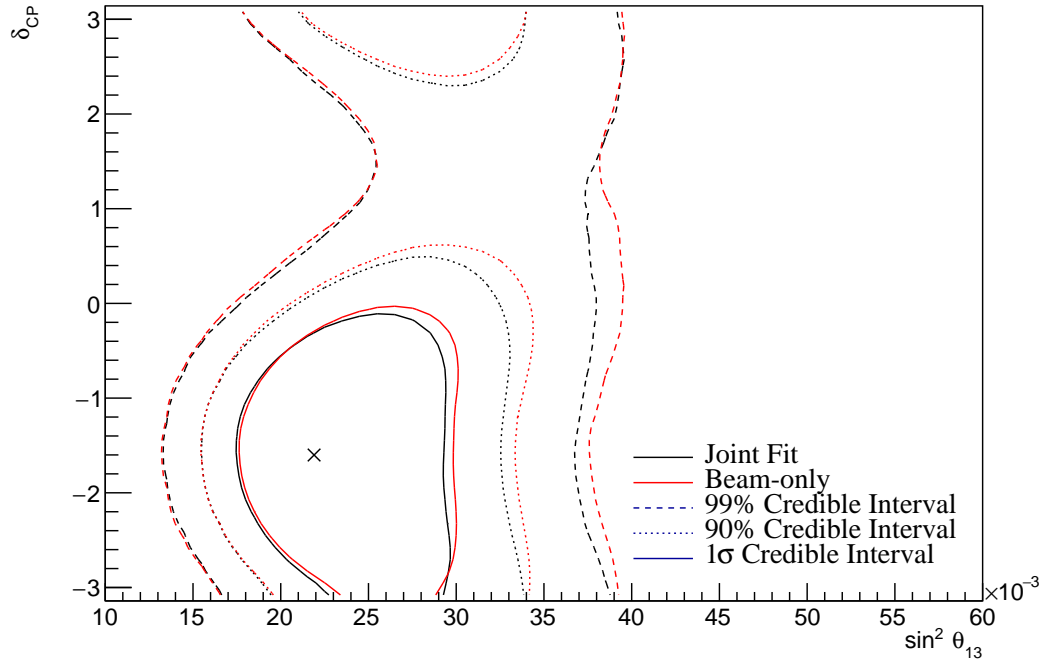


Figure 8.34: The two-dimensional posterior probability density distribution in $\delta_{CP} - \sin^2(\theta_{13})$ compared between the joint beam-atmospheric fit (Black) and the latest T2K sensitivities (Red) [2, 215]. The reactor constraint is not applied in either fit. The distributions are marginalised over both hierarchies. The marker represents the known value of $\delta_{CP} - \sin^2(\theta_{13})$.

³⁴³¹ by Figure 8.38. The joint analysis disfavours the wrong octant hypothesis more
³⁴³² strongly in the region of high $\sin^2(\theta_{13})$. This change in correlation means that the
³⁴³³ application of the reactor constraint could affect the two analyses differently.

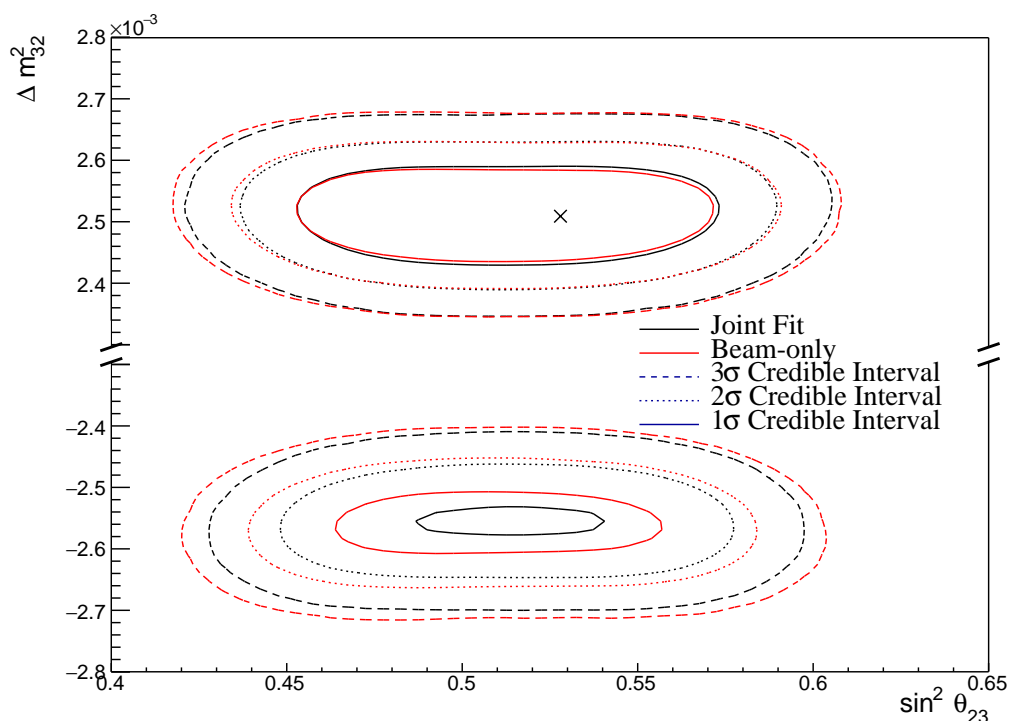


Figure 8.35: The two-dimensional posterior probability density distribution in $\Delta m_{32}^2 - \sin^2(\theta_{23})$ compared between the joint beam-atmospheric fit (Black) and the latest T2K sensitivities (Red) [2, 215]. The reactor constraint is not applied in either fit. The marker represents the known value of $\Delta m_{32}^2 - \sin^2(\theta_{23})$.

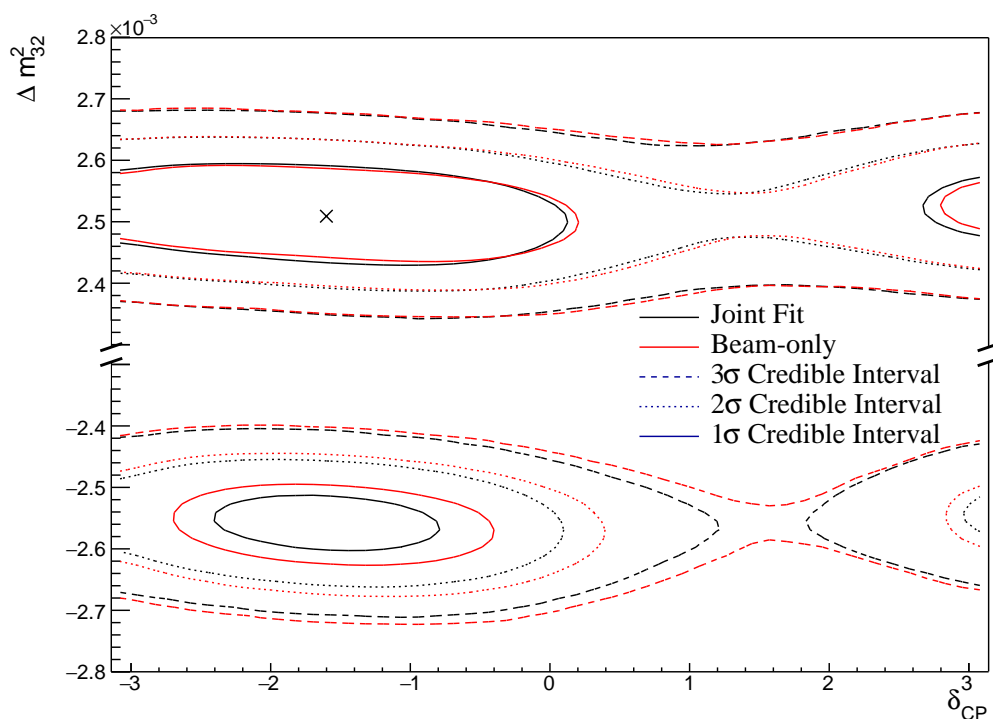


Figure 8.36: The two-dimensional posterior probability density distribution in $\Delta m_{32}^2 - \Delta_{CP}$ compared between the joint beam-atmospheric fit (Black) and the latest T2K sensitivities (Red) [2, 215]. The reactor constraint is not applied in either fit. The marker represents the known value of $\Delta m_{32}^2 - \Delta_{CP}$.

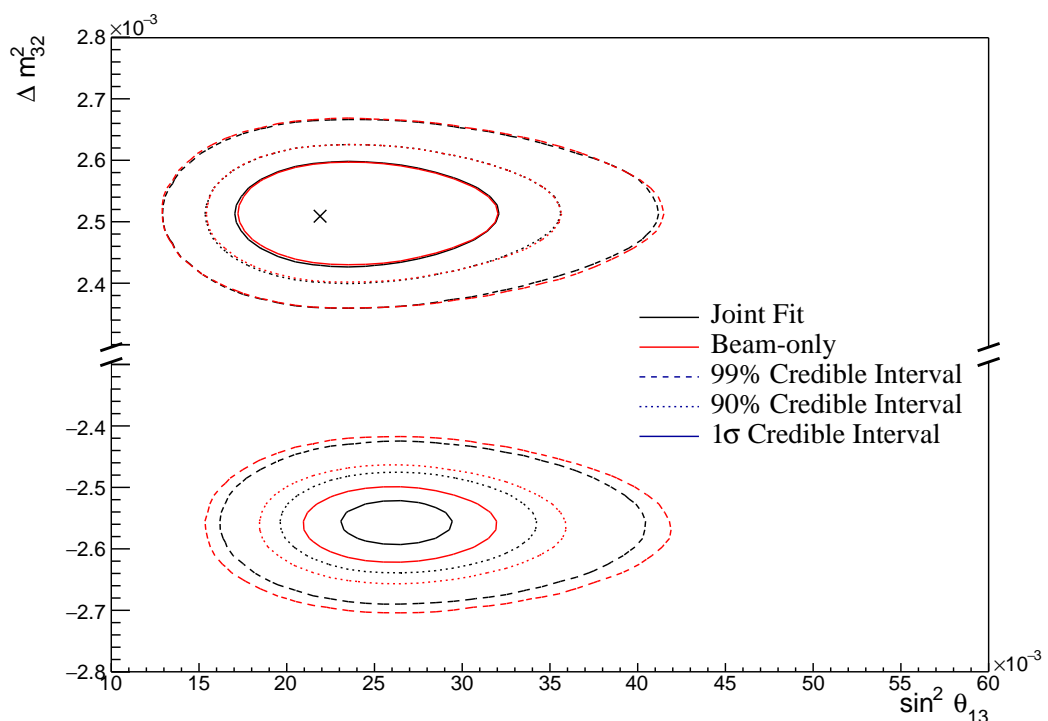


Figure 8.37: The two-dimensional posterior probability density distribution in $\Delta m_{32}^2 - \sin^2(\theta_{23})$ compared between the joint beam-atmospheric fit (Black) and the latest T2K sensitivities (Red) [2, 215]. The reactor constraint is not applied in either fit. The marker represents the known value of $\Delta m_{32}^2 - \sin^2(\theta_{23})$.

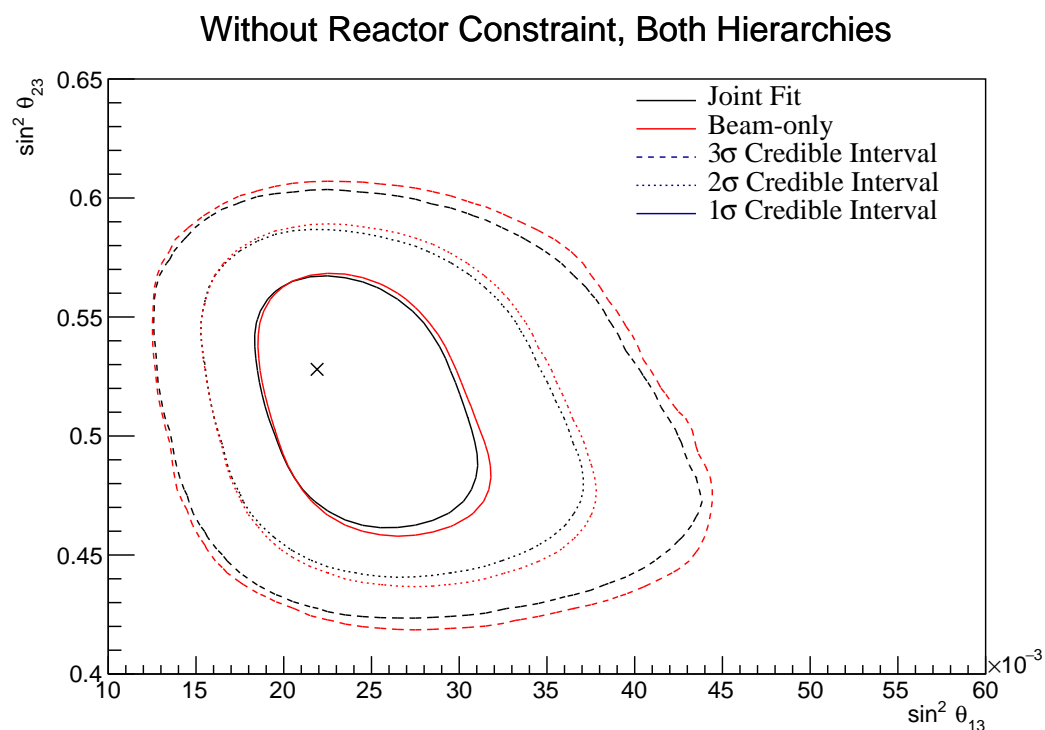


Figure 8.38: The two-dimensional posterior probability density distribution in $\sin^2(\theta_{23}) - \sin^2(\theta_{13})$ compared between the joint beam-atmospheric fit (Black) and the latest T2K sensitivities (Red) [2, 215]. The reactor constraint is not applied in either fit. The distributions are marginalised over both hierarchies. The marker represents the known value of $\sin^2(\theta_{23}) - \sin^2(\theta_{13})$.

3434 8.3.7 Comparison to Latest T2K Sensitivities with Reactor Con- 3435 straint

3436 This section illustrates the comparison between the joint beam-atmospheric and
 3437 beam-only fits when the reactor constraint is applied. As shown in Figure 8.37,
 3438 the application of the reactor constraint is expected to significantly increase
 3439 the joint fit's preference for the NH hypothesis, compared to the beam-only
 3440 analysis. Figure 8.39 illustrates the sensitivities of the two fits to the disappearance
 3441 parameters ($\sin^2(\theta_{23}) - \Delta m_{32}^2$). This plot further illustrates the benefit of the joint
 3442 beam-atmospheric analysis. The 1σ credible interval in the IH region is entirely
 3443 removed in the joint analysis but not for the beam-only analysis.

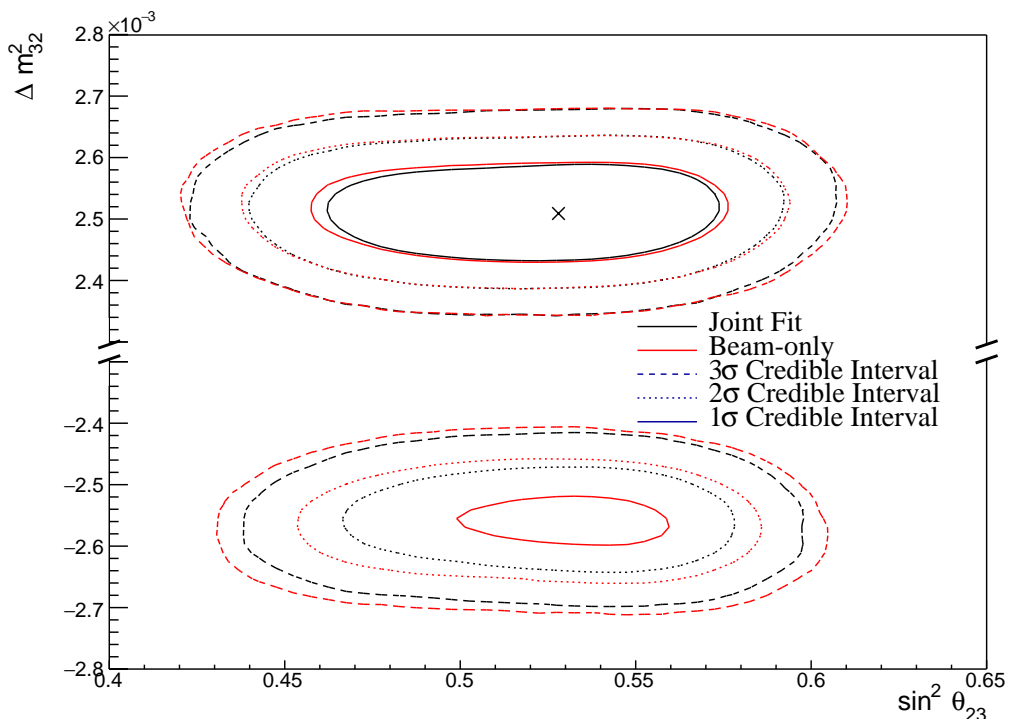


Figure 8.39: The two-dimensional posterior probability density distribution in $\Delta m_{32}^2 - \sin^2(\theta_{23})$ compared between the joint beam-atmospheric fit (Black) and the latest T2K sensitivities (Red) [2, 215]. The reactor constraint is applied in both fits. The marker represents the known value of $\Delta m_{32}^2 - \sin^2(\theta_{23})$.

3444 The credible intervals of the joint fit are also tighter in the $\sin^2(\theta_{23})$ dimension
 3445 than the beam-only analysis in both mass hierarchy regions. This shows that
 3446 beyond the ability of the joint fit to prefer the NH more strongly than the beam-

only analysis, the precision to which it can measure $\sin^2(\theta_{23})$ is also improved. The Bayes factor for NH preference is calculated as $B(\text{NH}/\text{IH}) = 6.47$ and $B(\text{NH}/\text{IH}) = 3.09$ for the joint beam-atmospheric and beam-only analysis, respectively. This important conclusion illustrates that the joint beam-atmospheric analysis can provide a substantial preference for the NH hypothesis whilst the beam-only analysis can not.

The Bayes factors for UO preference which are $B(\text{UO}/\text{LO}) = 2.86$ and $B(\text{UO}/\text{LO}) = 2.47$ for the joint beam-atmospheric and beam-only analysis, respectively. Both of these represent a mild preference for the UO but a stronger preference is observed in the joint analysis.

The sensitivity of the beam-only and joint beam-atmospheric analyses, to the appearance parameters ($\delta_{CP} - \sin^2(\theta_{13})$), are compared in Figure 8.40. These results are marginalised over both hierarchies. For this particular set of known oscillation parameters (AsimovA defined in Table 2.2), the beam-only analysis dominates the sensitivity. The joint fit does slightly increase the sensitivity to δ_{CP} but it does not change any conclusions that would be made. As expected, the prior knowledge dominates any sensitivity either fit would have on $\sin^2(\theta_{13})$.

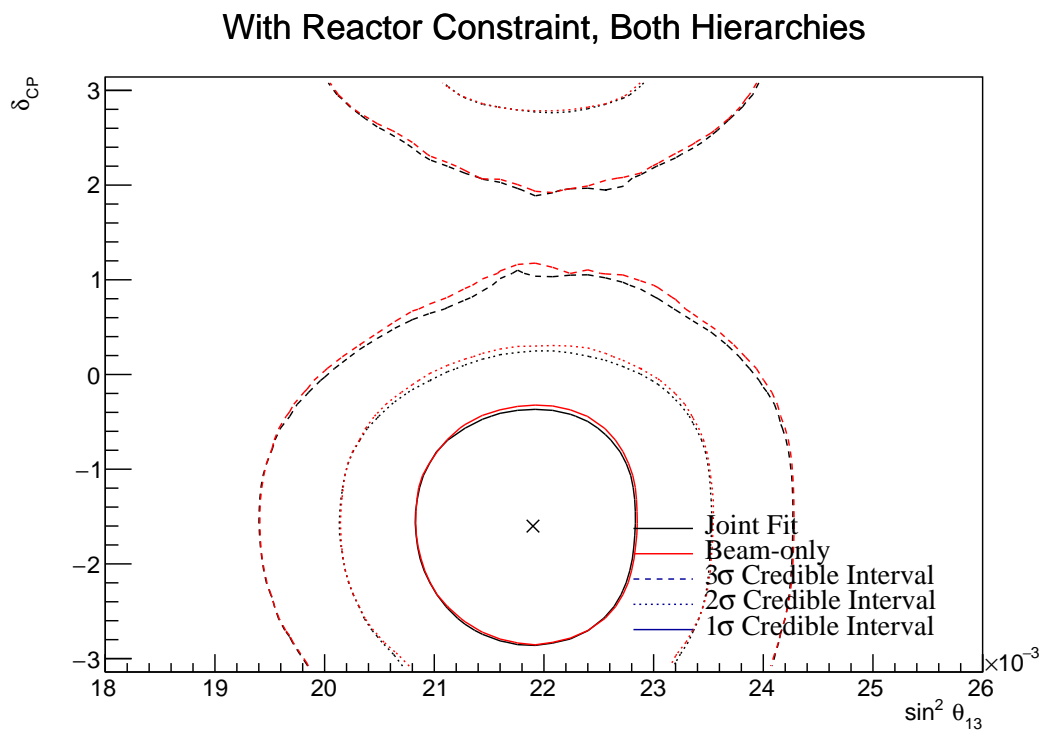


Figure 8.40: The two-dimensional posterior probability density distribution in δ_{CP} – $\sin^2(\theta_{13})$ compared between the joint beam-atmospheric fit (Black) and the latest T2K sensitivities (Red) [2, 215]. The reactor constraint is applied in both fits. The distributions are marginalised over both hierarchies. The marker represents the known value of δ_{CP} – $\sin^2(\theta_{13})$.

3464 8.3.8 Alternate Asimov Parameter Set

3465 Figure 8.4 and Figure 8.5 show that the choice of the parameter set at which the
 3466 Asimov data is made can affect the conclusion. ‘AsimovA’ oscillation parameters
 3467 are defined at a region of δ_{CP} which is preferred by the T2K experiment. This
 3468 explains why the addition of the atmospheric samples does not significantly in-
 3469 crease the sensitivity to δ_{CP} , as illustrated in subsection 8.3.6 and subsection 8.3.7.
 3470 This section presents the sensitivities when ‘AsimovB’ oscillation parameters,
 3471 as defined in Table 2.2, are assumed (alongside the post-BANFF tune) when
 3472 building the Asimov data.

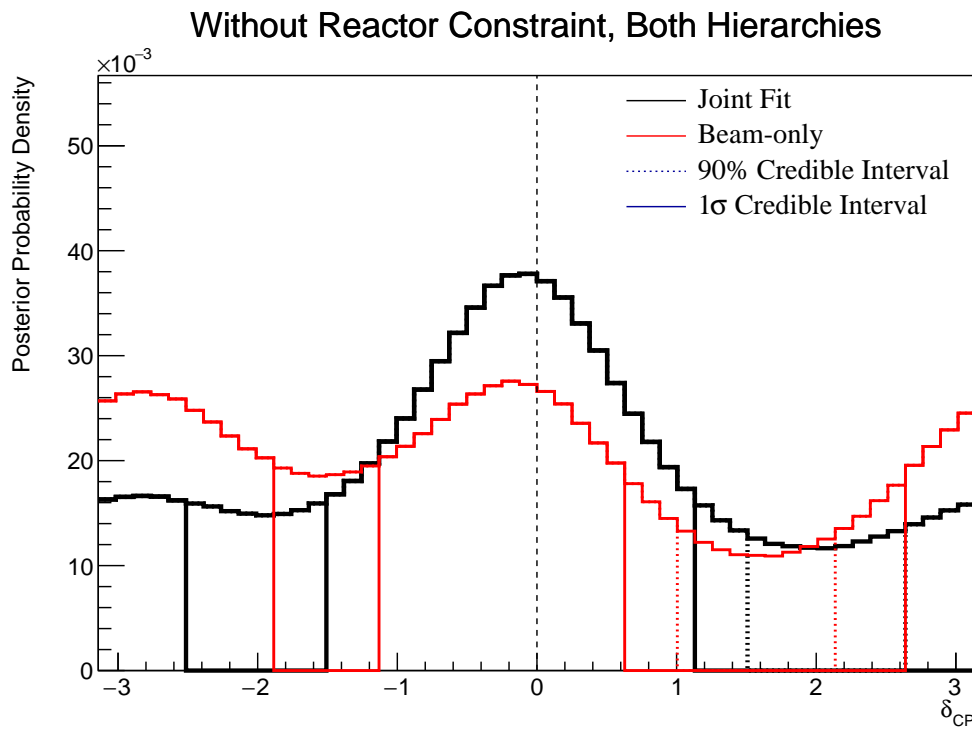


Figure 8.41: The one-dimensional posterior probability density distribution in δ_{CP} compared between the joint beam-atmospheric fit (Black) and the latest T2K sensitivities (Red) [2, 215]. The reactor constraint is not applied in either fit. The distributions are marginalised over both hierarchies. The vertical dashed line represents the known value of δ_{CP} .

3473 The sensitivity to δ_{CP} for the joint beam-atmospheric fit is presented in
 3474 Figure 8.41. The results are compared to those from the beam-only analysis
 3475 in [2, 215]. The reactor constraint is not applied in either of the fits. The

shape of the posterior distribution from the joint analysis is more peaked at the known oscillation parameter value compared to the beam-only analysis, which has approximately the same posterior probability density at $\delta_{CP} = 0$ and $\delta_{CP} = \pm\pi$. This shows the ability of the joint analysis to better determine the correct phase of δ_{CP} if the true value were CP-conserving. The 1σ credible intervals and the position of the highest posterior probability density are given in Table 8.9. The highest posterior density for the joint beam-atmospheric analysis is $\delta_{CP} = -0.06 \pm 0.06$ which is consistent with the known value.

Parameter	Interval	HPD
δ_{CP} , (BH)	$[-\pi, -2.51], [-1.51, 1.13]$	-0.06 ± 0.06
δ_{CP} , (NH)	$[-1.13, 1.63]$	0.06 ± 0.06
δ_{CP} , (IH)	$[-3.02, -1.88], [-1.76, 0.13]$	-0.44 ± 0.06
Δm_{32}^2 (BH) [$\times 10^{-3}\text{eV}^2$]	$[-2.60, -2.52], [2.46, 2.56]$	2.51 ± 0.01
Δm_{32}^2 (NH) [$\times 10^{-3}\text{eV}^2$]	$[2.47, 2.56]$	2.52 ± 0.01
Δm_{32}^2 (IH) [$\times 10^{-3}\text{eV}^2$]	$[-2.61, -2.52]$	-2.57 ± 0.01
$\sin^2(\theta_{23})$ (BH)	$[0.430, 0.480], [0.545, 0.585]$	0.453 ± 0.003
$\sin^2(\theta_{23})$ (NH)	$[0.430, 0.485], [0.550, 0.580]$	0.453 ± 0.003
$\sin^2(\theta_{23})$ (IH)	$[0.435, 0.480], [0.540, 0.585]$	0.568 ± 0.003

Table 8.9: The position of the highest posterior probability density (HPD) and width of the 1σ credible interval for the joint beam-atmospheric fit. The reactor constraint is not applied. The values are presented by which hierarchy hypothesis is assumed: marginalised over both hierarchies (BH), normal hierarchy only (NH) and inverted hierarchy only (IH).

Naively, if just the 1σ credible interval were considered without observing the shape of the distribution, it would appear that the joint analysis would have a worse sensitivity to δ_{CP} due to the larger interval around $\delta_{CP} = 0$. The 1σ credible interval for the beam-only analysis is given as the range $\delta_{CP} = [-\pi, -1.88], [-1.13, 0.63]$ and $[2.64, \pi]$ which contains 56% of all values of δ_{CP} . Whereas, the joint beam-atmospheric analysis contains 52% of all δ_{CP} values within the 1σ credible interval. Therefore, if the area within the 1σ credible

3491 interval were to be compared between the two fits, the joint analysis would
3492 be shown to have better precision.

3493 This apparent contradiction stems from the methodology in which the credible
3494 interval is calculated. The technique used in this analysis (documented in
3495 subsection 4.3.2) fills the credible interval by selecting bins in order of probability
3496 density until 68% of the posterior density is contained. If instead, the credible
3497 interval were calculated by expanding around the highest posterior probability,
3498 the benefits of the joint fit would be more obvious. In the case where the shape
3499 of the posterior was uni-modal, these two techniques would be equivalent to
3500 statistical fluctuations.

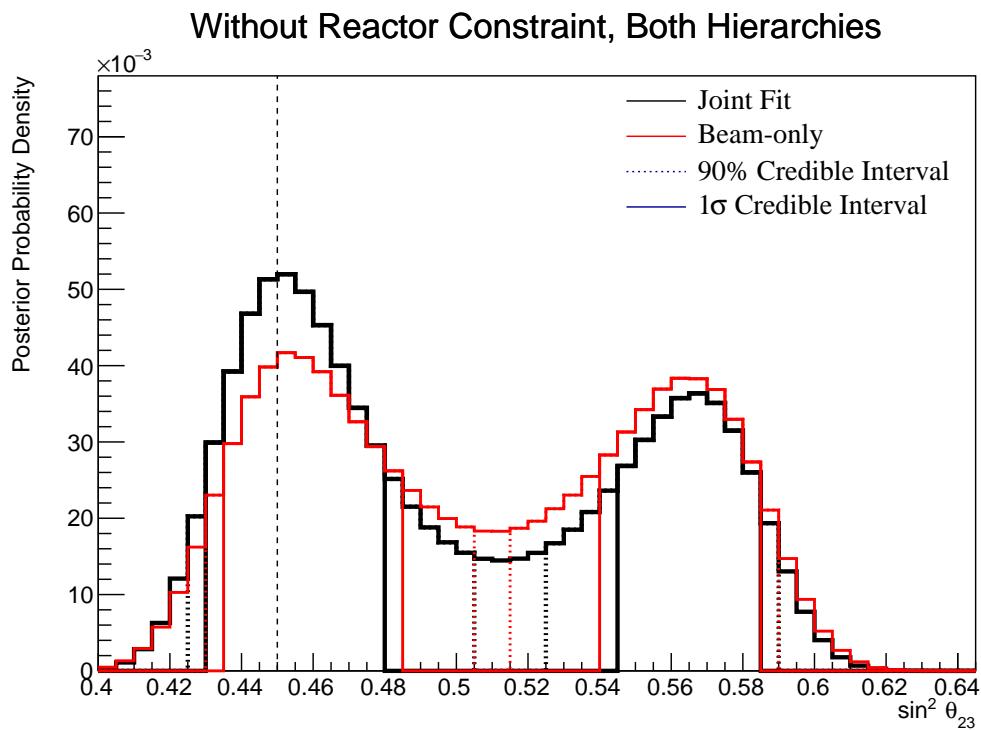


Figure 8.42: The one-dimensional posterior probability density distribution in $\sin^2(\theta_{23})$ compared between the joint beam-atmospheric fit (Black) and the latest T2K sensitivities (Red) [2, 215]. The reactor constraint is not applied in either fit. The distributions are marginalised over both hierarchies. The vertical dashed line represents the known value of $\sin^2(\theta_{23})$.

3501 The sensitivity of the joint beam-atmospheric fit to $\sin^2(\theta_{23})$ is presented in
3502 Figure 8.42. The sensitivity is compared to that of the beam-only analysis in [2,
3503 215]. The reactor constraint is not applied in either of the fits being compared.

3504 The joint beam-atmospheric fit has a much larger probability density in the region
 3505 surrounding the known oscillation parameter, $\sin^2(\theta_{23}) = 0.45$. This shows the
 3506 better octant determination of the joint analysis compared to the beam-only fit.
 3507 The ratio of the posterior density at the peak of the lower octant to the peak of
 3508 the upper octant from the joint fit is 1.43 compared to 1.09 from the beam-only
 3509 analysis. The area contained within the 1σ credible interval for the joint analysis
 3510 is $\sin^2(\theta_{23}) = [0.430, 0.480]$ and $\sin^2(\theta_{23}) = [0.545, 0.585]$, whereas the beam-
 3511 only analysis includes $\sin^2(\theta_{23}) = [0.435, 0.485]$ and $\sin^2(\theta_{23}) = [0.540, 0.585]$.
 3512 This corresponds to a $\sim 5\%$ (binning dependent) increase in precision from
 3513 the joint analysis.

	LO ($\sin^2 \theta_{23} < 0.5$)	UO ($\sin^2 \theta_{23} > 0.5$)	Sum
NH ($\Delta m_{32}^2 > 0$)	0.35	0.24	0.59
IH ($\Delta m_{32}^2 < 0$)	0.19	0.22	0.41
Sum	0.54	0.46	1.00

Table 8.10: The distribution of steps in a joint beam-atmospheric fit, presented as the fraction of steps in the upper (UO) and lower (LO) octants and the normal (NH) and inverted (IH) hierarchies. The reactor constraint is not applied. The Bayes factors are calculated as $B(\text{NH}/\text{IH}) = 1.43$ and $B(\text{LO}/\text{UO}) = 1.19$.

3514 The distribution of steps, split by hierarchy and octant hypothesis, is presented
 3515 in Table 8.10. The Bayes factor for hierarchy and octant determination are
 3516 $B(\text{NH}/\text{IH}) = 1.43$ and $B(\text{LO}/\text{UO}) = 1.19$, respectively. These values compare
 3517 to $B(\text{NH}/\text{IH}) = 1.08$ and $B(\text{LO}/\text{UO}) = 0.91$ from the beam-only analysis. This
 3518 evidences the joint analysis's ability to select the correct octant and hierarchy
 3519 hypothesis. Comparisons to the AsimovA Bayes factors presented in Table 8.6
 3520 show how the preferences for the correct octant and hierarchy depend on the
 3521 true value of δ_{CP} and $\sin^2(\theta_{23})$.

3522 The sensitivity of the beam-only and joint beam-atmospheric analysis to
 3523 Δm_{32}^2 is given in Figure 8.43. The joint analysis has a stronger preference for the
 3524 correct hierarchy (NH) which is shown by the higher Bayes factor compared
 3525 to the beam-only analysis. This is further evidenced by the width of the 90%

Without Reactor Constraint, Both Hierarchies

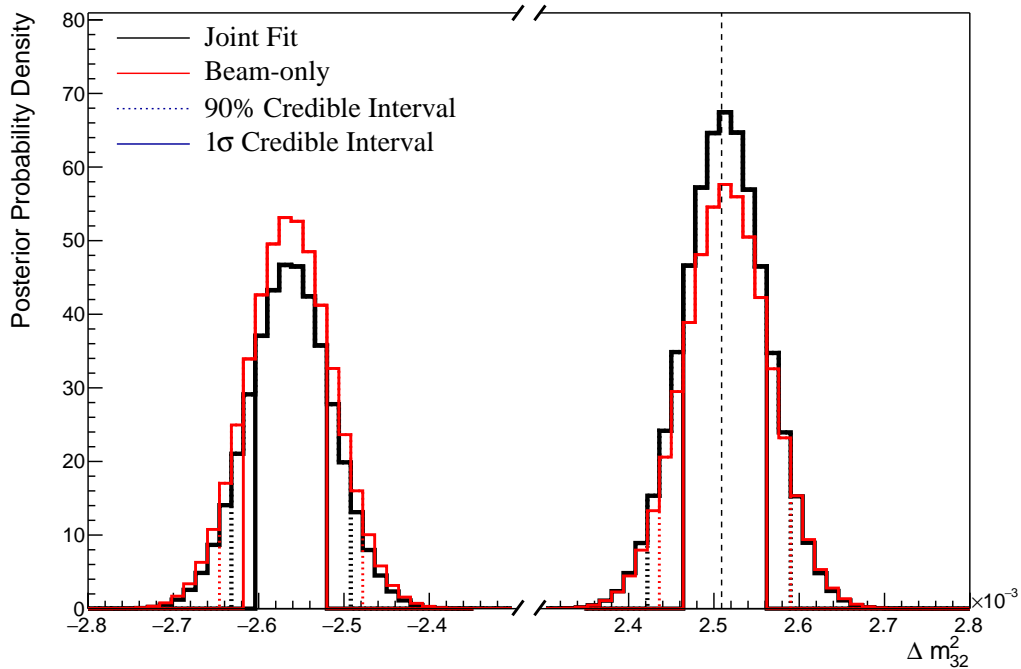


Figure 8.43: The one-dimensional posterior probability density distribution in Δm_{32}^2 compared between the joint beam-atmospheric fit (Black) and the latest T2K sensitivities (Red) [2, 215]. The reactor constraint is not applied in either fit. The vertical dashed line represents the known value of Δm_{32}^2 .

credible interval in the IH region being tighter in the joint analysis compared to the beam-only analysis.

3528 8.3.9 Effect of Systematics

3529 The effect of systematics on each sample used in this analysis is calculated using
3530 the posterior predictive method documented in subsection 4.3.4. The distribution
3531 of each sample’s spectrum has been generated by sampling 2000 steps from the
3532 posterior distribution of the joint beam-atmospheric fit. This technique reweights
3533 the Monte Carlo prediction using the systematic values given by a particular
3534 step, stores the sample spectra, and repeats for the desired number of steps.
3535 The oscillation parameters are always fixed at Asimov A values to only study
3536 the effect of systematic parameters.

3537 Figure 8.44 illustrates the distribution for the SubGeV-*elike*-0dcy atmospheric
3538 sample. The fit being sampled is detailed in subsection 8.3.4. The distribution
3539 closely resembles the Asimov data spectrum. This would be expected from
3540 an Asimov fit where the Monte Carlo is fit to itself but gives more credibility
3541 to the results of the fit.

3542 The total event rate for each sample from each of the sampled steps is
3543 calculated and the fractional uncertainty, $\Delta N_i / N_i$ where N_i is the event rate of the
3544 i^{th} sample, is calculated. These values are presented in Table 8.11. In general, the
3545 impact of the systematics has a $\sim 3\%$ uncertainty on the event rate of atmospheric
3546 samples, where CC1 π -targeting samples have slightly larger uncertainties than
3547 the CCQE-like samples. The fractional uncertainties on the beam samples are
3548 compared to those from the beam-only analysis presented in [2, 215]. The
3549 uncertainties on the one-ring muon samples are mostly unchanged, whereas
3550 the uncertainties on the one-ring electron samples are different. As discussed in
3551 section 8.2, the atmospheric samples should be able to add constraints on the NC
3552 background events present in the FHC1Re and RHC1Re samples. The uncertainty
3553 reduction seen in those samples is due to those additional constraints. The reason
3554 why the FHC1Re1de has a higher uncertainty in this analysis is due to the addition
3555 of the ad-hoc systematic introduced for CC1 π interactions (see subsection 6.4.3).

3556 Beyond the impact of the uncertainty on each sample’s event rate, the post-fit
3557 constraint on each systematic parameter should be checked. Figure 8.45 illustrates

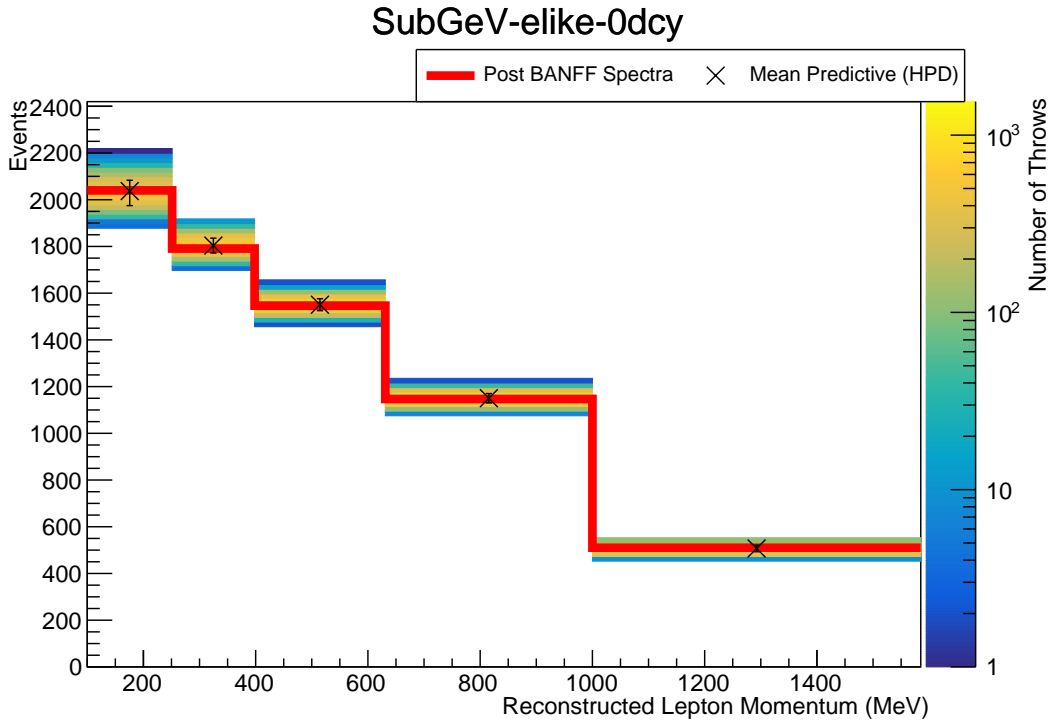


Figure 8.44: Result of the posterior predictive method for the SubGeV_elike_0dcy sample after sampling 2000 steps from the joint beam-atmospheric chain detailed in subsection 8.3.4 (Coloured histogram). The mean and uncertainty is presented for each bin. The Asimov data prediction (denoted ‘Post BANFF Spectra’, Red) assumes the post-BANFF tune and Asimov A oscillation parameters.

the central value and uncertainty on a select group of interaction systematics, for both the joint beam-atmospheric (from subsection 8.3.4) and the beam-only analysis. From the discussion in section 8.2, the uncertainty on systematics which are strongly constrained by the near detector should not significantly change when adding the atmospheric analysis. This behaviour is evidenced by the fact that the ratio of constraints between the two fits are very similar (within a few %) for almost all systematics. The only systematic which is more constrained in the joint beam-atmospheric analysis is the *NCOtherSK* normalisation parameter, which has a $O(10\%)$ tighter constraint. As expected, the atmospheric samples have been able to constrain this systematic which leads to the reduction in uncertainty for the beam electron-like samples.

Sample	Percentage Uncertainty (%)	
	Joint Analysis	Beam-only Analysis
SubGeV-elike-0dcy	2.53	-
SubGeV-elike-1dcy	3.28	-
SubGeV-mulike-0dcy	2.62	-
SubGeV-mulike-1dcy	2.23	-
SubGeV-mulike-2dcy	3.96	-
SubGeV-pi0like	2.84	-
MultiGeV-elike-nue	5.14	-
MultiGeV-elike-nuebar	2.79	-
MultiGeV-mulike	2.99	-
MultiRing-elike-nue	2.94	-
MultiRing-elike-nuebar	2.83	-
MultiRing-mulike	2.89	-
MultiRingOther-1	2.70	-
PCStop	3.22	-
PCThru	2.99	-
UpStop-mu	2.95	-
UpThruNonShower-mu	2.70	-
UpThruShower-mu	3.19	-
FHC1Rmu	2.49	2.33
RHC1Rmu	2.89	2.93
FHC1Re	4.12	4.57
RHC1Re	5.15	5.65
FHC1Re1de	13.38	11.51

Table 8.11: The percentage uncertainty, $\Delta N / N$, as calculated from sampling 2000 throws from a joint beam-atmospheric chain. The same values for the beam samples are provided from the beam-only analysis [2, 215]. These uncertainties consider all systematic parameters to be sampled from the fit whilst the oscillation parameters are fixed at the Asimov A oscillation set.

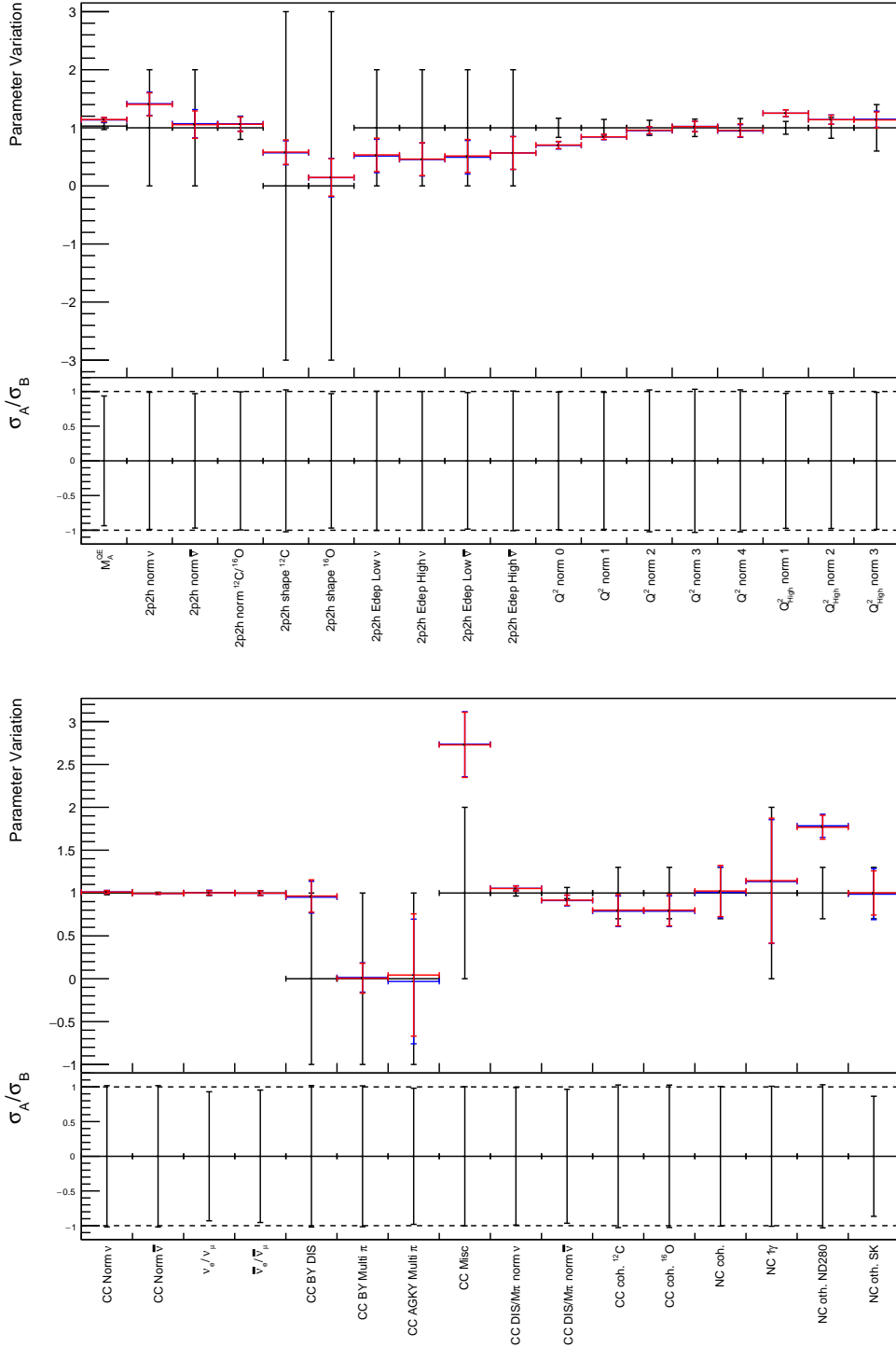


Figure 8.45: Central values and 1σ uncertainties for a select group of interaction systematics. The constraints from the prior uncertainty (Black), joint atmospheric-beam fit given in subsection 8.3.4 (Red) and beam-only analysis [2, 215] (Blue) are presented. The top part of each plot presents the parameter variation and the bottom part represents the ratio of the uncertainty between the joint beam-atmospheric and beam-only fits, where a value below 1.0 means the joint fit has a tighter constraint than the beam-only analysis.

3569 8.4 Summary of Sensitivity Studies

3570 The sensitivities to each oscillation parameter from the joint beam-atmospheric
 3571 and beam-only fits, which use the Asimov A oscillation parameter set, are
 3572 summarised in Table 8.12. As the posterior distribution to δ_{CP} is cyclical, only
 3573 the position of the highest posterior density (HPD) is given. The uncertainty
 3574 corresponds to the width of the bin in which the HPD is located. Furthermore,
 3575 the Δm_{32}^2 reported values only consider the NH credible interval region as the
 3576 full discussion can be found in the previous section.

Fit	δ_{CP} (HPD)	$\Delta m_{32}^2 [\times 10^{-3} \text{eV}^2]$	$\sin^2(\theta_{23})$	$\sin^2(\theta_{13}) [\times 10^{-2}]$
Asimov A	-1.601	2.509	0.528	2.19
Beam	-1.45 ± 0.06	$2.51^{+0.07}_{-0.06}$	$0.501^{+0.044}_{-0.026}$	$2.45^{+0.45}_{-0.35}$
Beam w/RC	-1.57 ± 0.06	$2.51^{+0.08}_{-0.06}$	$0.533^{+0.022}_{-0.043}$	$2.19^{+0.06}_{-0.07}$
Joint	-1.57 ± 0.06	$2.51^{+0.07}_{-0.06}$	$0.518^{+0.027}_{-0.038}$	$2.35^{+0.45}_{-0.35}$
Joint w/RC	-1.57 ± 0.06	$2.51^{+0.05}_{-0.06}$	$0.528^{+0.027}_{-0.038}$	$2.18^{+0.07}_{-0.06}$

Table 8.12: A comparison of the sensitivity to each oscillation parameter of interest, from the beam-only [2, 215] and joint atmospheric-beam fits discussed within this thesis. The results are illustrated both with and without the reactor constraint (RC). The best-fit values are taken from the highest posterior density (HPD) and the error comes from the width of the one-dimensional 1σ credible intervals. As the posterior distribution in δ_{CP} is cyclical, the highest posterior distribution is given instead.

3577 The Bayes factors from the beam-only and joint atmospheric-beam analyses
 3578 are presented in Table 8.13. The strength of each preference, from Jeffrey's
 3579 scale (Table 4.1), is also given.

3580 To summarise this information, the joint fit prefers a tighter 1σ credible
 3581 interval in $\sin^2(\theta_{23})$ along with a stronger Bayes factor for preferring the correct
 3582 octant hypothesis. The increase in sensitivity to $|\Delta m_{32}^2|$ between the two fits is
 3583 negligible but the joint analysis substantially prefers the correct mass hierarchy
 3584 hypothesis. It does not require any external constraints on $\sin^2(\theta_{13})$ to make
 3585 this statement. The joint analysis also produces a value of $\sin^2(\theta_{13})$ closer to the
 3586 known value compared to the beam-only analysis. When the reactor constraint is

Fit	$B(\text{NH}/\text{IH})$		$B(\text{UO}/\text{LO})$	
	Value	Strength	Value	Strength
Asimov A				
Beam	1.91	Weak	1.56	Weak
Beam w/RC	3.09	Weak	2.47	Weak
Joint	3.67	Substantial	1.74	Weak
Joint w/RC	6.47	Substantial	2.64	Weak
Asimov B				
Beam	1.08	Weak	0.91	Weak
Beam w/RC	0.98	Weak	1.15	Weak
Joint	1.43	Weak	1.19	Weak
Joint w/RC	1.36	Weak	1.52	Weak

Table 8.13: A comparison of the Bayes factors for mass hierarchy and $\sin^2(\theta_{23})$ octant hypotheses, from the beam-only [2, 215] and joint atmospheric-beam fits discussed within this thesis. The results are illustrated both with and without the reactor constraint (RC). The strength of the preference for the normal mass hierarchy and upper octants are provided by Jeffrey's scale Table 8.13.

3587 applied, the preference for both the NH and UO hypotheses increases but does
 3588 not change the statement which would be made.

3589 The fits from the Asimov B comparisons (subsection 8.3.9) show the improved
 3590 ability for the joint analysis to more precisely select the true value of δ_{CP} if it were
 3591 CP-conserving, compared to the beam-only analysis. This is evidenced by the
 3592 area contained within the 1σ credible interval decreasing by $\sim 4\%$. Furthermore,
 3593 the joint fit is able to better determine the octant of $\sin^2(\theta_{23})$ when the true
 3594 value is moved further away from the boundary as evidenced by the larger
 3595 Bayes factor. There is also a $\sim 5\%$ reduction of area contained within the 1σ
 3596 credible interval in $\sin^2(\theta_{23})$.

9

3597

3598

Conclusions and Outlook

3599 This thesis has presented the sensitivities of a joint beam and atmospheric neu-
3600 trino oscillation analysis from the Tokai-to-Kamioka (T2K) and Super-Kamiokande
3601 (SK) experiments combining the two independent analyses presented by the
3602 collaborations [2, 3]. This study uses 3244.4 days of SK livetime and $1.97 \times$
3603 $10^{21}(1.63 \times 10^{21})$ POT recorded at the far detector in the neutrino(antineutrino)
3604 beam operating mode. The ND280 near detector is used within this analysis to
3605 constrain the beam flux and cross-section systematics. It uses 1.15×10^{21} POT and
3606 8.34×10^{20} POT in the neutrino and antineutrino running modes, respectively.

3607 This analysis uses a Bayesian Markov Chain Monte Carlo fitting technique
3608 implemented within the MaCh3 framework. This analysis has significantly devel-
3609 oped the fitting framework, both in terms of technical features and performance.
3610 This includes supporting new samples, systematics, and oscillation channels.
3611 These developments have become the foundation of the fitter's expansion into
3612 other neutrino oscillation experiments. Beyond these improvements, a novel
3613 technique for calculating the atmospheric neutrino oscillation probabilities has
3614 been developed. This calculation uses a sub-sampling linear-averaging approach
3615 to ensure that the sensitivities being calculated are not biased due to insufficient
3616 Monte Carlo statistics in a region of rapidly varying probability. It illustrates a

3617 computationally feasible method of reliably calculating oscillation probabilities
3618 that can be utilised within any fitting framework.

3619 The sensitivity of the joint beam-atmospheric analysis is presented in Table 9.1,
3620 and compared to the beam-only analysis [2]. The sensitivities are evaluated
3621 using a set of known oscillation parameter values close to the results from a
3622 previous T2K analysis [78] (denoted AsimovA in Table 9.1). The joint analysis
3623 has a stronger sensitivity to $\sin^2(\theta_{23})$, as evidenced by the tighter 1σ credible
3624 intervals when the constraints from reactor experiments are not applied. The
3625 joint fit's sensitivity to δ_{CP} is marginally stronger than beam-only analysis. Whilst
3626 the sensitivity to $|\Delta m_{32}^2|$ is mostly unchanged between the two analyses, the
3627 sensitivity to select the correct hierarchy is significantly improved. This follows
3628 from a substantial preference for the normal hierarchy hypothesis presented
3629 within the joint analysis, as classified by Jeffrey's scale [134]. This is notable as
3630 the beam-only analysis cannot make this statement, either with or without the
3631 application of the reactor constraint. The joint fit's preference for the correct
3632 hierarchy increases once the reactor constraint is applied. The preference for
3633 selecting the correct octant of $\sin^2(\theta_{23})$ is classified as weak by Jeffrey's scale but
3634 is still stronger than the statement made by the beam-only analysis.

3635 The sensitivities of the beam-only and joint atmospheric-beam fit have also
3636 been compared at a set of known oscillation parameters which are CP-conserving
3637 and in the lower octant of $\sin^2(\theta_{23})$. The joint analysis has a $\sim 5\%$ improved abil-
3638 ity to select the known values more precisely compared to the beam-only analysis.

3639 Whilst this analysis provides the first sensitivities of a joint beam and atmo-
3640 spheric analysis, there are more improvements that could be made. Since this
3641 analysis began, the T2K collaboration has released an updated oscillation analysis
3642 with additional near and far detector samples alongside a more sophisticated
3643 interaction model [4]. The overall change in oscillation parameter measurement
3644 observed by T2K is relatively minor but the stronger constraints on the systemat-
3645 ics could impact this joint analysis to a larger extent. Further developments could
3646 consider the effect of correlating the beam and atmospheric flux uncertainties

Fit	δ_{CP} (HPD)	Δm_{32}^2 [$\times 10^{-3}$ eV 2]	$\sin^2(\theta_{23})$	$B(\text{NH/IH})$	$B(\text{UO/LO})$
Asimov A	-1.601	2.509	0.528	NH	UO
Beam	$-1.45^{+0.06}_{-0.06}$	$2.51^{+0.07}_{-0.06}$	$0.501^{+0.044}_{-0.026}$	1.91	1.56
Beam w/RC	$-1.57^{+0.06}_{-0.06}$	$2.51^{+0.08}_{-0.06}$	$0.533^{+0.022}_{-0.043}$	3.09	2.47
Joint	$-1.57^{+0.06}_{-0.06}$	$2.51^{+0.07}_{-0.06}$	$0.518^{+0.027}_{-0.038}$	3.67	1.74
Joint w/RC	$-1.57^{+0.06}_{-0.06}$	$2.51^{+0.05}_{-0.06}$	$0.528^{+0.027}_{-0.038}$	6.47	2.64

Table 9.1: A comparison of the sensitivity to each oscillation parameter of interest, from the beam-only [2, 215] and joint atmospheric-beam fits discussed within this thesis. The results are illustrated both with and without the reactor constraint (RC). The best-fit values are taken from the highest posterior density (HPD) and the error comes from the width of the one-dimensional 1σ credible intervals. As the posterior distribution in δ_{CP} is cyclical, the highest posterior distribution is given instead. The Bayes factors are provided for the mass hierarchy preference: normal hierarchy (NH) and inverse hierarchy (IH), and $\sin^2(\theta_{23})$ octant preference: upper octant (UO) and lower octant (LO).

3647 relating to hadron production, where updates of the Bartol and Honda models
3648 may allow this to be studied [151].

3649 Beyond these model improvements, more data is available than what is
3650 assumed for this analysis. The T2K experiment has accumulated an additional
3651 1.78×10^{20} POT in neutrino mode. Similarly, there are several early SK periods
3652 that have not been considered within this analysis as the reconstruction software
3653 used in this analysis has not been validated for those periods. SK will also
3654 continue to accumulate statistics with Gadolinium doping. Developments in the
3655 atmospheric sample selections may also benefit from the Gadolinium dopants as
3656 neutron capture will aid in neutrino/antineutrino separation leading to better
3657 mass hierarchy sensitivity. This would require including interaction systematics
3658 for neutron capture of Gadolinium which has already started [216].

3659 This analysis shows the increased sensitivity to oscillation parameters from
3660 the combination of beam and atmospheric samples. It has developed the MaCh3
3661 fitting framework and has laid the foundations of the fitter's expansion into other
3662 neutrino oscillation experiments. The sensitivities presented in this thesis, and
3663 the techniques that were used to generate them, are significant to the future of

³⁶⁶⁴ neutrino oscillation physics which will likely perform similar analyses. As such,
³⁶⁶⁵ they have been presented by the T2K and SK collaborations at the Neutrino 2022
³⁶⁶⁶ conference [4]. Moving towards the next generation of neutrino experiments,
³⁶⁶⁷ this analysis has the potential to become the basis of the oscillation analysis
³⁶⁶⁸ for the future Hyper-Kamiokande experiment which aims to make conclusive
³⁶⁶⁹ statements about CP-violation in the neutrino sector.

Bibliography

- [1] Andrei D Sakharov. "Violation of CP invariance, C asymmetry, and baryon asymmetry of the universe". In: *Soviet Physics Uspekhi* 34.5 (May 1991), pp. 392–393. URL: <https://doi.org/10.1070/pu1991v034n05abeh002497>.
- [2] P. Dunne. "Latest Neutrino Oscillation Results from T2K". In: *Neutrino 2020* (2020). URL: <https://zenodo.org/record/3959557>.
- [3] M. Jiang et al. "Atmospheric neutrino oscillation analysis with improved event reconstruction in Super-Kamiokande IV". en. In: *Prog. Theor. Exp. Phys.* 2019.5 (May 2019).
- [4] C. Bronner. "Accelerator Neutrino I Recent results from T2K". In: *Neutrino 2022* (2022). URL: <https://zenodo.org/record/6683821>.
- [5] J. Chadwick. "Intensitätsverteilung im magnetischen Spectrum der β -Strahlen von radium B + C". In: *Verhandl. Dtsc. Phys. Ges.* 16 (1914), p. 383. URL: <http://cds.cern.ch/record/262756>.
- [6] C. D. Ellis and W. A. Wooster. "The average energy of disintegration of radium E". en. In: *Proc. R. Soc. Lond. A Math. Phys. Sci.* 117.776 (Dec. 1927), pp. 109–123.
- [7] W. Pauli. "Dear radioactive ladies and gentlemen". In: *Phys. Today* 31N9 (1978), p. 27.
- [8] E. Fermi. "An attempt of a theory of beta radiation. 1." In: *Z. Phys.* 88 (1934), pp. 161–177.
- [9] F. Reines and C. L. Cowan. "Detection of the Free Neutrino". In: *Phys. Rev.* 92 (3 1953), pp. 830–831. URL: <https://link.aps.org/doi/10.1103/PhysRev.92.830>.
- [10] C. L. Cowan et al. "Detection of the Free Neutrino: a Confirmation". In: *Science* 124.3212 (1956), pp. 103–104. URL: <http://science.sciencemag.org/content/124/3212/103>.
- [11] G. Danby et al. "Observation of High-Energy Neutrino Reactions and the Existence of Two Kinds of Neutrinos". In: *Phys. Rev. Lett.* 9 (1 1962), pp. 36–44. URL: <https://link.aps.org/doi/10.1103/PhysRevLett.9.36>.
- [12] K. Kodama et al. "Observation of tau neutrino interactions". In: *Physics Letters B* 504.3 (2001), pp. 218 –224. URL: <http://www.sciencedirect.com/science/article/pii/S0370269301003070>.
- [13] A. Aguilar-Arevalo et al. "Evidence for neutrino oscillations from the observation of anti-neutrino(electron) appearance in a anti-neutrino(muon) beam". In: *Phys. Rev.* D64 (2001), p. 112007. arXiv: [hep-ex/0104049 \[hep-ex\]](https://arxiv.org/abs/hep-ex/0104049).

- 3705 [14] A. A. Aguilar-Arevalo et al. "Improved Search for $\bar{\nu}_\mu \rightarrow \bar{\nu}_e$ Oscillations in the
3706 MiniBooNE Experiment". In: *Phys. Rev. Lett.* 110 (16 2013), p. 161801. URL:
3707 <https://link.aps.org/doi/10.1103/PhysRevLett.110.161801>.
- 3708 [15] Planck Collaboration. "Planck 2018 results. VI. Cosmological parameters". In: *aap*
3709 641 (Sept. 2020).
- 3710 [16] J. A. Bagger et al. "Precision electroweak measurements on the Z resonance". In: *Physics Reports* 427.5 (2006), pp. 257–454. URL:
3711 <http://www.sciencedirect.com/science/article/pii/S0370157305005119>.
- 3713 [17] B. Pontecorvo. "Neutrino Experiments and the Problem of Conservation of
3714 Leptonic Charge". In: *Sov. Phys. JETP* 26 (1968). [Zh. Eksp. Teor.
3715 Fiz.53,1717(1967)], pp. 984–988.
- 3716 [18] B. Pontecorvo. "Inverse beta processes and nonconservation of lepton charge". In:
3717 *Sov. Phys. JETP* 7 (1958). [Zh. Eksp. Teor. Fiz.34,247(1957)], pp. 172–173.
- 3718 [19] M. Kobayashi and T. Maskawa. "CP-Violation in the Renormalizable Theory of
3719 Weak Interaction". In: *Progress of Theoretical Physics* 49.2 (1973), pp. 652–657. URL:
3720 <http://dx.doi.org/10.1143/PTP.49.652>.
- 3721 [20] N. Cabibbo. "Unitary Symmetry and Leptonic Decays". In: *Phys. Rev. Lett.* 10 (12
3722 1963), pp. 531–533. URL:
3723 <https://link.aps.org/doi/10.1103/PhysRevLett.10.531>.
- 3724 [21] A. Maio et al. "Search for Majorana neutrinos with the SNO+ detector at
3725 SNOLAB". In: *Journal of Physics: Conference Series* 587 (2015), p. 012030. URL:
3726 <https://doi.org/10.1088/1742-6596/587/1/012030>.
- 3727 [22] A. Y. Smirnov. "The MSW effect and Solar Neutrinos". In: *ArXiv* (2003). URL:
3728 <https://arxiv.org/abs/hep-ph/0305106>.
- 3729 [23] S. P. Mikheyev and A. Y. Smirnov. "Resonance enhancement of oscillations in
3730 matter and solar neutrino spectroscopy". In: *Soviet Journal of Nuclear Physics* 42 (6
3731 1985), pp. 913–917.
- 3732 [24] L. Wolfenstein. "Neutrino oscillations in matter". In: *Phys. Rev. D* 17 (9 1978),
3733 pp. 2369–2374. URL: <https://link.aps.org/doi/10.1103/PhysRevD.17.2369>.
- 3734 [25] V. D. Barger et al. "Matter Effects on Three-Neutrino Oscillations". In: *Phys. Rev.*
3735 *D* 22 (1980), p. 2718.
- 3736 [26] Y. Ashie et al. "Evidence for an Oscillatory Signature in Atmospheric Neutrino
3737 Oscillations". In: *Phys. Rev. Lett.* 93 (10 2004), p. 101801. URL:
3738 <https://link.aps.org/doi/10.1103/PhysRevLett.93.101801>.
- 3739 [27] Q. R. Ahmad et al. "Direct Evidence for Neutrino Flavor Transformation from
3740 Neutral-Current Interactions in the Sudbury Neutrino Observatory". In: *Phys.*
3741 *Rev. Lett.* 89 (1 2002), p. 011301. URL:
3742 <https://link.aps.org/doi/10.1103/PhysRevLett.89.011301>.
- 3743 [28] Nobel Prize. *2015 Nobel prize in Physics as listed by Nobelprize.org*.
3744 https://www.nobelprize.org/nobel_prizes/physics/laureates/2015/.
3745 Accessed: 22-06-2022.
- 3746 [29] J. A. Formaggio and G. P. Zeller. "From eV to EeV: Neutrino Cross Sections
3747 Across Energy Scales". In: *Rev. Mod. Phys.* 84 (2012), pp. 1307–1341. arXiv:
3748 1305.7513 [hep-ex].

- 3749 [30] A. Oralbaev, M. Skorokhvatov, and O. Titov. "The inverse beta decay: a study of
3750 cross section". In: *Journal of Physics: Conference Series* 675.1 (2016), p. 012003. URL:
3751 <https://doi.org/10.1088/1742-6596/675/1/012003>.
- 3752 [31] A. Bellerive. "Review of solar neutrino experiments". en. In: *Int. J. Mod. Phys. A*
3753 19.08 (Mar. 2004), pp. 1167–1179.
- 3754 [32] R. Davis, D. S. Harmer, and K. C. Hoffman. "Search for Neutrinos from the Sun".
3755 In: *Phys. Rev. Lett.* 20 (21 1968), pp. 1205–1209. URL:
3756 <https://link.aps.org/doi/10.1103/PhysRevLett.20.1205>.
- 3757 [33] N. Vinyoles et al. "A new generation of standard solar models". In: *Astrophys. J.*
3758 835.2 (Jan. 2017), p. 202.
- 3759 [34] V. Gribov and B. Pontecorvo. "Neutrino astronomy and lepton charge". en. In:
3760 *Phys. Lett. B* 28.7 (Jan. 1969), pp. 493–496.
- 3761 [35] K. S. Hirata et al. "Observation of ${}^8\text{B}$ solar neutrinos in the Kamiokande-II
3762 detector". In: *Phys. Rev. Lett.* 63 (1 1989), pp. 16–19. URL:
3763 <https://link.aps.org/doi/10.1103/PhysRevLett.63.16>.
- 3764 [36] W. Hampel et al. "GALLEX solar neutrino observations: results for GALLEX IV".
3765 en. In: *Phys. Lett. B* 447.1-2 (Feb. 1999), pp. 127–133.
- 3766 [37] J. N. Abdurashitov et al. "Measurement of the solar neutrino capture rate with
3767 gallium metal". In: *Phys. Rev. C* 60 (5 1999), p. 055801. URL:
3768 <https://link.aps.org/doi/10.1103/PhysRevC.60.055801>.
- 3769 [38] Borexino Collaboration. "Comprehensive measurement of pp-chain solar
3770 neutrinos". en. In: *Nature* 562.7728 (Oct. 2018), pp. 505–510.
- 3771 [39] B. Aharmim et al. "A search for neutrinos from the SolarhepReaction and the
3772 diffuse supernova neutrino background with the Sudbury neutrino observatory".
3773 en. In: *Astrophys. J.* 653.2 (Dec. 2006), pp. 1545–1551.
- 3774 [40] Borexino Collaboration. "Experimental evidence of neutrinos produced in the
3775 CNO fusion cycle in the Sun". In: *Nature* 587.7835 (2020), pp. 577–582. URL:
3776 <https://doi.org/10.1038%2Fs41586-020-2934-0>.
- 3777 [41] K. Abe et al. "T2K neutrino flux prediction". In: *Phys. Rev. D* 87 (1 2013),
3778 p. 012001. URL: <https://link.aps.org/doi/10.1103/PhysRevD.87.012001>.
- 3779 [42] D. G. Michael et al. "Observation of Muon Neutrino Disappearance with the
3780 MINOS Detectors in the NuMI Neutrino Beam". In: *Phys. Rev. Lett.* 97 (19 2006),
3781 p. 191801. URL:
3782 <https://link.aps.org/doi/10.1103/PhysRevLett.97.191801>.
- 3783 [43] M. H. Ahn et al. "Measurement of neutrino oscillation by the K2K experiment".
3784 In: *Phys. Rev. D* 74 (7 2006), p. 072003. eprint:
3785 <https://link.aps.org/doi/10.1103/PhysRevD.74.072003>.
- 3786 [44] M. A. Acero et al. "First measurement of neutrino oscillation parameters using
3787 neutrinos and antineutrinos by NOvA". In: *Phys. Rev. Lett.* 123 (15 2019),
3788 p. 151803. URL:
3789 <https://link.aps.org/doi/10.1103/PhysRevLett.123.151803>.
- 3790 [45] K. Abe et al. "The T2K experiment". In: *Nuclear Instruments and Methods in Physics*
3791 *Research Section A* 659.1 (2011), pp. 106 –135. eprint:
3792 <http://www.sciencedirect.com/science/article/pii/S0168900211011910>.

- 3793 [46] B. Abi et al. "Long-baseline neutrino oscillation physics potential of the DUNE
3794 experiment". en. In: *Eur. Phys. J. C Part. Fields* 80.10 (Oct. 2020).
- 3795 [47] Hyper-Kamiokande Proto-Collaboration. "Physics potential of a long-baseline
3796 neutrino oscillation experiment using a J-PARC neutrino beam and
3797 Hyper-Kamiokande". In: *Prog. Theor. Exp. Phys.* 2015.5 (May 2015), pp. 53C02–0.
- 3798 [48] C. Blanco, D. Hooper, and P. Machado. "Constraining sterile neutrino
3799 interpretations of the LSND and MiniBooNE anomalies with coherent neutrino
3800 scattering experiments". In: *Phys. Rev. D* 101.7 (2020). URL:
3801 <https://doi.org/10.1103%2Fphysrevd.101.075051>.
- 3802 [49] MicroBooNE Collaboration. "Search for an Excess of Electron Neutrino
3803 Interactions in MicroBooNE Using Multiple Final State Topologies". In: *arXiv*
3804 (2021). URL: <https://arxiv.org/abs/2110.14054>.
- 3805 [50] B. Armbruster et al. "Upper limits for neutrino oscillations $\bar{\nu}_\mu \rightarrow \bar{\nu}_e$ from muon
3806 decay at rest". In: *Phys. Rev. D* 65 (11 2002), p. 112001. URL:
3807 <https://link.aps.org/doi/10.1103/PhysRevD.65.112001>.
- 3808 [51] T. K. Gaisser and M. Honda. "Flux of Atmospheric Neutrinos". In: *Annual Review
3809 of Nuclear and Particle Science* 52.1 (2002), pp. 153–199. URL:
3810 <https://doi.org/10.1146%2Fannurev.nucl.52.050102.090645>.
- 3811 [52] G. D. Barr et al. "Three-dimensional calculation of atmospheric neutrinos". In:
3812 *Phys. Rev. D* 70.2 (2004). URL: <https://doi.org/10.1103/physrevd.70.023006>.
- 3813 [53] M. Honda et al. "Calculation of atmospheric neutrino flux using the interaction
3814 model calibrated with atmospheric muon data". In: *Phys. Rev. D* 75.4 (2007). URL:
3815 <https://doi.org/10.1103/physrevd.75.043006>.
- 3816 [54] M. Honda et al. "New calculation of the atmospheric neutrino flux in a
3817 three-dimensional scheme". In: *Phys. Rev. D* 70 (4 2004), p. 043008. URL:
3818 <https://link.aps.org/doi/10.1103/PhysRevD.70.043008>.
- 3819 [55] M. Honda et al. "Improvement of low energy atmospheric neutrino flux
3820 calculation using the JAM nuclear interaction model". In: *Phys. Rev. D* 83 (12
3821 2011), p. 123001. URL:
3822 <https://link.aps.org/doi/10.1103/PhysRevD.83.123001>.
- 3823 [56] A. Fassò et al. *FLUKA: Status and Prospects for Hadronic Applications*. Ed. by
3824 Andreas Kling et al. Berlin, Heidelberg: Springer Berlin Heidelberg, 2001,
3825 pp. 955–960.
- 3826 [57] Y. Ashie et al. "Measurement of atmospheric neutrino oscillation parameters by
3827 Super-Kamiokande I". In: *Phys. Rev. D* 71.11 (2005). URL:
3828 <https://doi.org/10.1103/physrevd.71.112005>.
- 3829 [58] F. Reines et al. "Evidence for high-energy cosmic-ray neutrino interactions". In:
3830 *Phys. Rev. Lett.* 15.9 (Aug. 1965), pp. 429–433.
- 3831 [59] D. Casper et al. "Measurement of atmospheric neutrino composition with the
3832 IMB-3 detector". In: *Phys. Rev. Lett.* 66 (20 1991), pp. 2561–2564. URL:
3833 <https://link.aps.org/doi/10.1103/PhysRevLett.66.2561>.
- 3834 [60] K. S. Hirata et al. "Observation of a small atmospheric ν_μ/ν_e ratio in
3835 Kamiokande". en. In: *Phys. Lett. B* 280.1-2 (Apr. 1992), pp. 146–152.

- 3836 [61] Z. Li et al. "Measurement of the tau neutrino cross section in atmospheric
3837 neutrino oscillations with Super-Kamiokande". In: *Phys. Rev. D* 98.5 (2018). URL:
3838 <https://doi.org/10.1103/physrevd.98.052006>.
- 3839 [62] K. Abe et al. "Atmospheric neutrino oscillation analysis with external constraints
3840 in Super-Kamiokande I-IV". In: *Phys. Rev. D* 97 (7 2018), p. 072001. URL:
3841 <https://link.aps.org/doi/10.1103/PhysRevD.97.072001>.
- 3842 [63] T2K Collaboration. "Constraint on the matter-antimatter symmetry-violating
3843 phase in neutrino oscillations". en. In: *Nature* 580.7803 (Apr. 2020), pp. 339–344.
- 3844 [64] M. A. Acero et al. "First measurement of neutrino oscillation parameters using
3845 neutrinos and antineutrinos by NOvA". en. In: *Phys. Rev. Lett.* 123.15 (Oct. 2019),
3846 p. 151803.
- 3847 [65] M. G. Aartsen et al. "Measurement of atmospheric neutrino oscillations at 6–56
3848 GeV with IceCube DeepCore". In: *Phys. Rev. Lett.* 120.7 (Feb. 2018).
- 3849 [66] P. Adamson et al. "Combined analysis of $\nu\mu$ Disappearance
3850 and $\nu\mu \rightarrow \nu e$ Appearance in MINOS using accelerator and atmospheric neutrinos".
3851 In: *Phys. Rev. Lett.* 112.19 (May 2014).
- 3852 [67] M. Sajjad Athar et al. "Status and perspectives of neutrino physics". In: *Progress
3853 in Particle and Nuclear Physics* 124 (2022), p. 103947. URL:
3854 <https://doi.org/10.1016/Fj.pppn.2022.103947>.
- 3855 [68] S. B. Kim, T. Lasserre, and Y. Wang. "Reactor Neutrinos". In: *Adv. High Energy
3856 Phys.* 2013 (2013), pp. 1–34.
- 3857 [69] K. Abe et al. "First gadolinium loading to Super-Kamiokande". en. In: *Nucl.
3858 Instrum. Methods Phys. Res. A* 1027.166248 (Mar. 2022), p. 166248.
- 3859 [70] F. P. An et al. "Observation of Electron-Antineutrino Disappearance at Daya Bay".
3860 In: *Phys. Rev. Lett.* 108 (17 2012), p. 171803. URL:
3861 <https://link.aps.org/doi/10.1103/PhysRevLett.108.171803>.
- 3862 [71] J. K. Ahn et al. "Observation of Reactor Electron Antineutrinos Disappearance in
3863 the RENO Experiment". In: *Phys. Rev. Lett.* 108 (19 2012), p. 191802. URL:
3864 <https://link.aps.org/doi/10.1103/PhysRevLett.108.191802>.
- 3865 [72] Y. Abe et al. "Indication of Reactor $\bar{\nu}_e$ Disappearance in the Double Chooz
3866 Experiment". In: *Phys. Rev. Lett.* 108 (13 2012), p. 131801. URL:
3867 <https://link.aps.org/doi/10.1103/PhysRevLett.108.131801>.
- 3868 [73] JUNO Collaboration. "TAO Conceptual Design Report: A Precision
3869 Measurement of the Reactor Antineutrino Spectrum with Sub-percent Energy
3870 Resolution". In: *arXiv* (2020). arXiv: 2005.08745 [physics.ins-det].
- 3871 [74] M. P. Decowski. "KamLAND's precision neutrino oscillation measurements". en.
3872 In: *Nucl. Phys. B*. 908 (July 2016), pp. 52–61.
- 3873 [75] A. Gando et al. "Constraints on θ_{13} from a three-flavor oscillation analysis of
3874 reactor antineutrinos at KamLAND". In: *Phys. Rev. D* 83 (5 2011), p. 052002. URL:
3875 <https://link.aps.org/doi/10.1103/PhysRevD.83.052002>.
- 3876 [76] Particle Data Group. "Review of particle physics". en. In: *Prog. Theor. Exp. Phys.*
3877 2020.8 (Aug. 2020).

- 3878 [77] R. L. Workman et al. "Review of Particle Physics". In: *PTEP* 2022 (2022),
3879 p. 083C01.
- 3880 [78] K. Abe et al. "Precise Measurement of the Neutrino Mixing Parameter θ_{23} from
3881 Muon Neutrino Disappearance in an Off-Axis Beam". In: *Phys. Rev. Lett.* 112 (18
3882 2014), p. 181801. URL:
3883 <https://link.aps.org/doi/10.1103/PhysRevLett.112.181801>.
- 3884 [79] R. Wendell. "Three Flavor Oscillation Analysis of Atmospheric Neutrinos in
3885 Super-Kamiokande". PhD thesis. University of North Carolina, 2008.
- 3886 [80] A. M. Dziewonski and D. L. Anderson. "Preliminary reference Earth model". en.
3887 In: *Phys. Earth Planet. Inter.* 25.4 (June 1981), pp. 297–356.
- 3888 [81] Y. Fukuda et al. "Evidence for oscillation of atmospheric neutrinos". In: *Phys. Rev.*
3889 *Lett.* 81.8 (Aug. 1998), pp. 1562–1567.
- 3890 [82] K. Abe et al. "Calibration of the Super-Kamiokande detector". In: *Nuclear*
3891 *Instruments and Methods in Physics Research Section A* 737 (2014), pp. 253–272. URL:
3892 <https://doi.org/10.1016/j.nima.2013.11.081>.
- 3893 [83] L. Wan. "Atmospheric Neutrino Super-K". In: *Neutrino* 2022 (2022). URL:
3894 <https://zenodo.org/record/6694761>.
- 3895 [84] M. Jiang. "Study of the neutrino mass hierarchy with the atmospheric neutrino
3896 data collected in Super-Kamiokande IV". PhD thesis. Kyoto University, 2019.
- 3897 [85] S. Fukuda et al. "The super-kamiokande detector". en. In: *Nucl. Instrum. Methods*
3898 *Phys. Res. A* 501.2-3 (Apr. 2003), pp. 418–462. eprint:
3899 <http://www.sciencedirect.com/science/article/pii/S016890020300425X>.
- 3900 [86] Y. Itow et al. "The JHF-Kamioka neutrino project". In: *arXiv* (2001).
- 3901 [87] H. Kume et al. "20 inch diameter photomultiplier". In: *Nuclear Instruments and*
3902 *Methods in Physics Research* 205.3 (1983), pp. 443–449. URL:
3903 <https://www.sciencedirect.com/science/article/pii/0167508783900078>.
- 3904 [88] A. Suzuki et al. "Improvement of 20 in. diameter photomultiplier tubes". In:
3905 *Nuclear Instruments and Methods in Physics Research Section A* 329.1-2 (May 1993),
3906 pp. 299–313. URL: [https://doi.org/10.1016/0168-9002\(93\)90949-i](https://doi.org/10.1016/0168-9002(93)90949-i).
- 3907 [89] Y. Nakano et al. "Measurement of the radon concentration in purified water in
3908 the Super-Kamiokande IV detector". en. In: *Nucl. Instrum. Methods Phys. Res. A*
3909 977.164297 (Oct. 2020), p. 164297.
- 3910 [90] Hamamatsu. *Hamamatsu Photonics Photomultiplier Tubes Handbook*. URL:
3911 https://www.hamamatsu.com/content/dam/hamamatsu-photonics/sites/documents/99_SALES_LIBRARY/etd/PMT_handbook_v4E.pdf.
- 3913 [91] J. F. Beacom and M. R. Vagins. "Antineutrino Spectroscopy with Large Water
3914 Čerenkov Detectors". In: *Phys. Rev. Lett.* 93 (17 2004), p. 171101. URL:
3915 <https://link.aps.org/doi/10.1103/PhysRevLett.93.171101>.
- 3916 [92] L. Marti et al. "Evaluation of gadolinium's action on water Cherenkov detector
3917 systems with EGADS". en. In: *Nucl. Instrum. Methods Phys. Res. A* 959.163549
3918 (Apr. 2020), p. 163549.
- 3919 [93] M. Vagins. "Solar/DSNB Neutrino SK-Gd". In: *Neutrino* 2022 (2022). URL:
3920 <https://zenodo.org/record/6696210>.

- 3921 [94] J. Focht. "Dark Noise Calibration of the Super-Kamiokande Outer Detector".
3922 PhD thesis. Massachusetts Institute of Technology, 2004.
- 3923 [95] T. Tanimori et al. "Design and performance of semi-custom analog IC including
3924 two TACs and two current integrators for 'Super-Kamiokande'". In: *IEEE*
3925 *Transactions on Nuclear Science* 36.1 (1989), pp. 497–501.
- 3926 [96] J. Hosaka et al. "Solar neutrino measurements in Super-Kamiokande-I". In: *Phys.*
3927 *Rev. D* 73 (11 2006), p. 112001.
- 3928 [97] H. Nishino et al. "High-speed charge-to-time converter ASIC for the
3929 Super-Kamiokande detector". en. In: *Nucl. Instrum. Methods Phys. Res. A* 610.3
3930 (Nov. 2009), pp. 710–717.
- 3931 [98] S. Yamada et al. "Commissioning of the New Electronics and Online System for
3932 the Super-Kamiokande Experiment". In: *IEEE Transactions on Nuclear Science* 57.2
3933 (2010), pp. 428–432.
- 3934 [99] S. Yamada et al. "New online system without hardware trigger for the
3935 Super-Kamiokande experiment". In: *2007 IEEE Nuclear Science Symposium*
3936 *Conference Record*. Honolulu, HI, USA: IEEE, Oct. 2007.
- 3937 [100] G. Carminati. "The new wide-band solar neutrino trigger for super-kamiokande".
3938 In: *Phys. Procedia* 61 (2015), pp. 666–672.
- 3939 [101] P. A. Čerenkov. "Visible radiation produced by electrons moving in a medium
3940 with velocities exceeding that of light". In: *Phys. Rev.* 52.4 (Aug. 1937),
3941 pp. 378–379.
- 3942 [102] I. Frank and I. Tamm. "Coherent visible radiation of fast electrons passing
3943 through matter". In: *Selected Papers*. Berlin, Heidelberg: Springer Berlin
3944 Heidelberg, 1991, pp. 29–35.
- 3945 [103] The T2K Collaboration. "Letter of Intent: Neutrino Oscillation Experiment at
3946 JHF". In: *KEK Proposal* (2001). eprint:
3947 <http://neutrino.kek.jp/jhfnu/loi/loi.v2.030528.pdf>.
- 3948 [104] The K2K Collaboration and S. H. Ahn. "Detection of Accelerator-Produced
3949 Neutrinos at a Distance of 250 km". In: (Feb. 2001). arXiv: hep-ex/0103001
3950 [hep-ex].
- 3951 [105] The T2K Collaboration. "Tokai-to-Kamioka (T2K) Long Baseline Neutrino
3952 Oscillation Experiment Proposal". In: *KEK Proposal* (2006). eprint: <http://j-parc.jp/researcher/Hadron/en/pac\0606/pdf/p11-Nishikawa.pdf>.
- 3954 [106] K. Abe et al. "Observation of Electron Neutrino Appearance in a Muon Neutrino
3955 Beam". In: *Phys. Rev. Lett.* 112 (6 2014), p. 061802. eprint:
3956 <https://link.aps.org/doi/10.1103/PhysRevLett.112.061802>.
- 3957 [107] T. Fukuda et al. "Proposal for precise measurement of neutrino-water
3958 cross-section in NINJA physics run". Proposal for J-PARC and KEK. 2017.
- 3959 [108] T. Ovsiannikova et al. "New experiment WAGASCI to measure cross sections of
3960 neutrino interactions in water and hydrocarbon using J-PARC beam". In: *Physics*
3961 *of Particles and Nuclei* 48.6 (2017), pp. 1014–1017. eprint:
3962 <https://doi.org/10.1134/S1063779617060478>.

- 3963 [109] M. Antonova et al. "Baby MIND: a magnetized segmented neutrino detector for
3964 the WAGASCI experiment". In: *Journal of Instrumentation* 12.07 (2017), p. C07028.
3965 eprint: <http://stacks.iop.org/1748-0221/12/i=07/a=C07028>.
- 3966 [110] K. Abe et al. "First measurement of the charged current $\bar{\nu}_\mu$ double differential
3967 cross section on a water target without pions in the final state". In: *Phys. Rev. D*
3968 102 (1 2020), p. 012007. URL:
3969 <https://link.aps.org/doi/10.1103/PhysRevD.102.012007>.
- 3970 [111] K. Abe et al. "Measurements of $\bar{\nu}_\mu$ and $\bar{\nu}_\mu + \nu_\mu$ charged-current cross-sections
3971 without detected pions or protons on water and hydrocarbon at a mean
3972 anti-neutrino energy of 0.86 GeV". In: *Progress of Theoretical and Experimental*
3973 *Physics* 2021.4 (Mar. 2021). URL: <https://doi.org/10.1093/ptep/ptab014>.
- 3974 [112] K. Matsuoka et al. "Design and performance of the muon monitor for the T2K
3975 neutrino oscillation experiment". In: *Nuclear Instruments and Methods in Physics*
3976 *Research Section A* 624.3 (2010), pp. 591–600. eprint:
3977 <http://www.sciencedirect.com/science/article/pii/S016890021002098X>.
- 3978 [113] K. Abe et al. "Improved constraints on neutrino mixing from the T2K experiment
3979 with 3.13×10^{21} protons on target". en. In: *Phys. Rev. D.* 103.11 (June 2021).
- 3980 [114] T. Vladisavljevic. *Predicting the T2K neutrino flux and measuring oscillation*
3981 *parameters*. 1st ed. Springer theses. Cham, Switzerland: Springer Nature, Sept.
3982 2020.
- 3983 [115] D. Beavis, A. Carroll, and I. Chiang. "Long baseline neutrino oscillation
3984 experiment at the AGS. Physics design report". In: *Office of Scientific and Technical*
3985 *Information (OSTI)* (Apr. 1995).
- 3986 [116] P.-A. Amaudruz et al. "The T2K fine-grained detectors". In: *Nuclear Instruments*
3987 *and Methods in Physics Research Section A: Accelerators, Spectrometers, Detectors and*
3988 *Associated Equipment* 696 (Dec. 2012), pp. 1–31. URL:
3989 <https://doi.org/10.1016/j.nima.2012.08.020>.
- 3990 [117] N. Abgrall et al. "Time projection chambers for the T2K near detectors". In:
3991 *Nuclear Instruments and Methods in Physics Research Section A: Accelerators,*
3992 *Spectrometers, Detectors and Associated Equipment* 637.1 (May 2011), pp. 25–46. URL:
3993 <https://doi.org/10.1016/j.nima.2011.02.036>.
- 3994 [118] S. Assylbekov et al. "The T2K ND280 off-axis pi-zero detector". In: *Nuclear*
3995 *Instruments and Methods in Physics Research Section A: Accelerators, Spectrometers,*
3996 *Detectors and Associated Equipment* 686 (Sept. 2012), pp. 48–63. URL:
3997 <https://doi.org/10.1016/j.nima.2012.05.028>.
- 3998 [119] D. Allan et al. "The electromagnetic calorimeter for the T2K near detector
3999 ND280". In: *Journal of Instrumentation* 8.10 (2013), P10019–P10019. URL:
4000 <https://doi.org/10.1088%2F1748-0221%2F8%2F10%2Fp10019>.
- 4001 [120] CERN Courier. *UA1 magnet sets off for a second new life*. 2008. URL: <https://cerncourier.com/a/ua1-magnet-sets-off-for-a-second-new-life/>.
- 4002 [121] F. Vannucci. "The NOMAD Experiment at CERN". In: *Advances in High Energy*
4003 *Physics* 2014 (2014), pp. 1–20. URL: <https://doi.org/10.1155/2014/129694>.

- 4005 [122] S. Aoki et al. "The T2K Side Muon Range Detector (SMRD)". In: *Nuclear*
4006 *Instruments and Methods in Physics Research Section A: Accelerators, Spectrometers,*
4007 *Detectors and Associated Equipment* 698 (Jan. 2013), pp. 135–146. URL:
4008 <https://doi.org/10.1016/j.nima.2012.10.001>.
- 4009 [123] K. Suzuki et al. "Measurement of the muon beam direction and muon flux for the
4010 T2K neutrino experiment". In: *Progress of Theoretical and Experimental Physics*
4011 2015.5 (2015), pp. 53C01–0. URL: <https://doi.org/10.1093%2Fptep%2Fptv054>.
- 4012 [124] S. Brooks et al. *Handbook of Markov Chain Monte Carlo*. CRC Press, 2011.
- 4013 [125] W. R. Gilks, S. Richardson, and D. J. Spiegelhalter. *Markov Chain Monte Carlo in*
4014 *Practice*. Chapman & Hall/CRC Interdisciplinary Statistics, 1995.
- 4015 [126] C. Wret. "Minimising systematic uncertainties in the T2K experiment using
4016 near-detector and external data". PhD thesis. Imperial College London, 2018.
- 4017 [127] K. E. Duffy. "Measurement of the Neutrino Oscillation Parameters $\sin^2 \theta_{23}$, Δm_{32}^2 ,
4018 $\sin^2 \theta_{13}$, and δ_{CP} in Neutrino and Antineutrino Oscillation at T2K". PhD thesis.
4019 Oriel College, University of Oxford, 2016.
- 4020 [128] C. Bojeckho and A. Kabooth. "Muon neutrino disappearance simultaneous fit of
4021 ND280 and SK with Run 1+2+3 data using Markov Chain Monte Carlo Analysis".
4022 In: *T2K Technical Note* 140 (2013).
- 4023 [129] T. Bayes. "An essay toward solving a problem in the doctrine of chances". In: *Phil.*
4024 *Trans. Roy. Soc. Lond.* 53 (1764), pp. 370–418.
- 4025 [130] A. Sztuc. "Standard and Non-Standard Neutrino-Antineutrino Oscillation
4026 Analyses and Event Reconstruction Studies using Markov Chain Monte Carlo
4027 Methods at T2K". PhD thesis. Imperial College London, 2021.
- 4028 [131] N. Metropolis et al. "Equation of State Calculations by Fast Computing
4029 Machines". In: *Journal of Chemical Physics* 21.6 (1970).
- 4030 [132] W. K. Hastings. "Monte Carlo Sampling Methods Using Markov Chains and
4031 Their Applications". In: *Biometrika* 57.1 (1970).
- 4032 [133] J. Dunkley et al. "Fast and reliable Markov chain Monte Carlo technique for
4033 cosmological parameter estimation". en. In: *Mon. Not. R. Astron. Soc.* 356.3 (Jan.
4034 2005), pp. 925–936.
- 4035 [134] H. Jeffreys. *The Theory of Probability*. Oxford Classic Texts in the Physical Sciences.
4036 1939.
- 4037 [135] R. E. Kass and A. E. Raftery. "Bayes factors". en. In: *J. Am. Stat. Assoc.* 90.430
4038 (June 1995), pp. 773–795.
- 4039 [136] T.T. Böhlen et al. "The FLUKA Code: Developments and Challenges for High
4040 Energy and Medical Applications". In: *Nuclear Data Sheets* 120 (2014), pp. 211
4041 –214. eprint:
4042 <http://www.sciencedirect.com/science/article/pii/S0090375214005018>.
- 4043 [137] R. Brun et al. *GEANT: Detector Description and Simulation Tool; Oct 1994*. CERN
4044 Program Library. Long Writeup W5013. Geneva: CERN, 1993. eprint:
4045 <http://cds.cern.ch/record/1082634>.

- 4046 [138] C. Zeitnitz and T.A. Gabriel. "The GEANT-CALOR interface and benchmark
4047 calculations of ZEUS test calorimeters". In: *Nuclear Instruments and Methods in*
4048 *Physics Research Section A* 349.1 (1994), pp. 106–111. eprint:
4049 <http://www.sciencedirect.com/science/article/pii/0168900294906130>.
- 4050 [139] A. Fiorentini et al. "Flux Prediction and Uncertainty Updates with NA61 2009
4051 Thin Target Data and Negative Focussing Mode Predictions". In: *T2K Technical*
4052 *Note* 217 (2017).
- 4053 [140] N. Abgrall et al. "Measurements of cross sections and charged pion spectra in
4054 proton-carbon interactions at 31 GeV". In: *Phys. Rev. C* 84.3 (2011). URL:
4055 <https://doi.org/10.1103%2Fphysrevc.84.034604>.
- 4056 [141] N. Abgrall et al. "Measurement of production properties of positively charged
4057 kaons in proton-carbon interactions at 31 GeV". In: *Phys. Rev. C* 85.3 (2012). URL:
4058 <https://doi.org/10.1103%2Fphysrevc.85.035210>.
- 4059 [142] N. Abgrall et al. "Pion emission from the T2K replica target: Method, results and
4060 application". In: *Nuclear Instruments and Methods in Physics Research Section A* 701
4061 (2013), pp. 99–114. eprint:
4062 <http://www.sciencedirect.com/science/article/pii/S016890021201234X>.
- 4063 [143] M. Apollonio et al. "Forward production of charged pions with incident protons
4064 on nuclear targets at the CERN Proton Synchrotron". In: *Phys. Rev. C* 80 (3 2009),
4065 p. 035208. eprint: <https://link.aps.org/doi/10.1103/PhysRevC.80.035208>.
- 4066 [144] B. Blau et al. "The superconducting magnet of AMS-02". In: *Nuclear Physics B -*
4067 *Proceedings Supplements* 113.1-3 (Dec. 2002), pp. 125–132. URL:
4068 [https://doi.org/10.1016/s0920-5632\(02\)01831-5](https://doi.org/10.1016/s0920-5632(02)01831-5).
- 4069 [145] S. Haino et al. "Measurements of primary and atmospheric cosmic-ray spectra
4070 with the BESS-TeV spectrometer". In: *Physics Letters B* 594.1-2 (July 2004),
4071 pp. 35–46. URL: <https://doi.org/10.1016/j.physletb.2004.05.019>.
- 4072 [146] NASA. *U.S. Standard Atmosphere, 1976.* 1976. URL: <https://ntrs.nasa.gov/api/citations/19770009539/downloads/19770009539.pdf>.
- 4074 [147] S. Roesler, R. Engel, and J. Ranft. "The Monte Carlo Event Generator
4075 DPMJET-III". In: *Advanced Monte Carlo for Radiation Physics, Particle Transport*
4076 *Simulation and Applications*. Springer Berlin Heidelberg, 2001, pp. 1033–1038. URL:
4077 https://doi.org/10.1007/978-3-642-18211-2_166.
- 4078 [148] K. Niita et al. "PHITS—a particle and heavy ion transport code system". In:
4079 *Radiation Measurements* 41.9-10 (Oct. 2006), pp. 1080–1090. URL:
4080 <https://doi.org/10.1016/j.radmeas.2006.07.013>.
- 4081 [149] T. Sanuki et al. "Measurements of atmospheric muon spectra at mountain
4082 altitude". In: *Physics Letters B* 541.3-4 (2002), pp. 234–242. URL:
4083 <https://doi.org/10.1016%2Fs0370-2693%2802%2902265-7>.
- 4084 [150] P. Achard et al. "Measurement of the atmospheric muon spectrum from 20 to
4085 3000 GeV". In: *Physics Letters B* 598.1-2 (2004), pp. 15–32. URL:
4086 <https://doi.org/10.1016%2Fj.physletb.2004.08.003>.
- 4087 [151] K. Sato. "Atmospheric Neutrino Reviews on neutrino fluxes (low E atm nu)". In:
4088 *Neutrino 2022* (2022). URL: <https://zenodo.org/record/6695711>.

- 4089 [152] Y. Hayato and L. Pickering. "The NEUT neutrino interaction simulation program
4090 library". In: *The European Physical Journal Special Topics* 230.24 (Oct. 2021),
4091 pp. 4469–4481. URL: <https://doi.org/10.1140/epjs/s11734-021-00287-7>.
- 4092 [153] Y. Hayato. "A Neutrino Interaction Simulation Program Library NEUT". In: *Acta
4093 Physica Polonica B* 40.9 (2009).
- 4094 [154] C. H. Llewellyn Smith. "Neutrino reactions at accelerator energies". In: *Physics
4095 Reports* 3.5 (1972), pp. 261 –379. eprint:
4096 <http://www.sciencedirect.com/science/article/pii/0370157372900105>.
- 4097 [155] O. Benhar, A. Fabrocini, and S. Fantoni. "The nucleon spectral function in infinite
4098 nuclear matter". In: *Nuclear Physics A* 497 (June 1989), pp. 423–430. URL:
4099 [https://doi.org/10.1016/0375-9474\(89\)90484-3](https://doi.org/10.1016/0375-9474(89)90484-3).
- 4100 [156] R. Bradford et al. "A New Parameterization of the Nucleon Elastic Form Factors".
4101 In: *Nuclear Physics B - Proceedings Supplements* 159 (2006). Proceedings of the 4th
4102 International Workshop on Neutrino-Nucleus Interactions in the Few-GeV
4103 Region, pp. 127 –132. eprint:
4104 <http://www.sciencedirect.com/science/article/pii/S0920563206005184>.
- 4105 [157] A. A. Aguilar-Arevalo et al. "First measurement of the muon neutrino charged
4106 current quasielastic double differential cross section". In: *Phys. Rev. D* 81.9 (2010).
4107 URL: <https://doi.org/10.1103/2Fphysrevd.81.092005>.
- 4108 [158] R. Gran et al. "Neutrino-nucleus quasi-elastic and 2p2h interactions up to 10
4109 GeV". In: *Phys. Rev. D* 88 (11 2013), p. 113007. eprint:
4110 <https://link.aps.org/doi/10.1103/PhysRevD.88.113007>.
- 4111 [159] C. Berger and L. M. Sehgal. "Lepton mass effects in single pion production by
4112 neutrinos". In: *Phys. Rev. D* 76 (11 2007), p. 113004. URL:
4113 <https://link.aps.org/doi/10.1103/PhysRevD.76.113004>.
- 4114 [160] C. Berger and L. M. Sehgal. "Partially conserved axial vector current and
4115 coherent pion production by low energy neutrinos". In: *Phys. Rev. D* 79 (5 2009),
4116 p. 053003. eprint: <https://link.aps.org/doi/10.1103/PhysRevD.79.053003>.
- 4117 [161] T. Sjöstrand. "High-energy-physics event generation with PYTHIA 5.7 and
4118 JETSET 7.4". In: *Computer Physics Communications* 82.1 (Aug. 1994), pp. 74–89.
4119 URL: [https://doi.org/10.1016/0010-4655\(94\)90132-5](https://doi.org/10.1016/0010-4655(94)90132-5).
- 4120 [162] C. Bronner and M. Hartz. "Tuning of the Charged Hadrons Multiplicities for
4121 Deep Inelastic Interactions in NEUT". In: *Proceedings of the 10th International
4122 Workshop on Neutrino-Nucleus Interactions in Few-GeV Region (NuInt15)*. Journal of
4123 the Physical Society of Japan, Dec. 2016. URL:
4124 <https://doi.org/10.7566/jpscp.12.010041>.
- 4125 [163] M. Glück, E. Reya, and A. Vogt. "Dynamical parton distributions revisited". In:
4126 *The European Physical Journal C* 5.3 (1998), pp. 461–470. URL:
4127 <https://doi.org/10.1007%2Fs100529800978>.
- 4128 [164] A. Bodek and U. Yang. "Axial and Vector Structure Functions for Electron- and
4129 Neutrino- Nucleon Scattering Cross Sections at all Q^2 using Effective Leading
4130 order Parton Distribution Functions". In: *arXiv* (2010). URL:
4131 <https://arxiv.org/abs/1011.6592>.

- 4132 [165] A. Bodek and U. Yang. "Update to the Bodek-Yang Unified Model for Electron-
4133 and Neutrino- Nucleon Scattering Cross Sections". In: *arXiv* (2010). URL:
4134 <https://arxiv.org/abs/1012.0261>.
- 4135 [166] S. Gollapinni. "Neutrino Cross section Future". In: *arXiv* (2016). URL:
4136 <https://arxiv.org/abs/1602.05299>.
- 4137 [167] E. S. Pinzon Guerra et al. "Using world π^\pm -nucleus scattering data to constrain
4138 an intranuclear cascade model". In: *Phys. Rev. D* 99 (5 2019), p. 052007.
- 4139 [168] S. Agostinelli et al. "GEANT4: A Simulation toolkit". In: *Nucl. Instrum. Meth.*
4140 A506 (2003), pp. 250–303.
- 4141 [169] R. Brun et al. "GEANT3". In: *Cern Document Server* (Sept. 1987). URL:
4142 <https://cds.cern.ch/record/1119728/>.
- 4143 [170] A. Himmel et al. "Super-Kamiokande events and data quality studies for T2K
4144 Runs 5 and 6". In: *T2K Technical Note* 219 (2015).
- 4145 [171] S. Berkman et al. "fiTQun: A New Reconstruction Algorithm for Super-K". In:
4146 *T2K Technical Note* 146 (2013).
- 4147 [172] R.B. Patterson et al. "The extended-track event reconstruction for MiniBooNE".
4148 In: *Nuclear Instruments and Methods in Physics Research Section A* 608.1 (2009),
4149 pp. 206–224. URL: <https://doi.org/10.1016/j.nima.2009.06.064>.
- 4150 [173] M. Shiozawa. "Reconstruction algorithms in the Super-Kamiokande large water
4151 Cherenkov detector". In: *Nuclear Instruments and Methods in Physics Research*
4152 *Section A: Accelerators, Spectrometers, Detectors and Associated Equipment* 433.1-2
4153 (Aug. 1999), pp. 240–246.
- 4154 [174] K. Abe et al. "Search for CP Violation in Neutrino and Antineutrino Oscillations
4155 by the T2K Experiment with 2.2×10^{21} Protons on Target". In: *Phys. Rev. Lett.*
4156 121.17 (Oct. 2018). URL: <https://doi.org/10.1103/physrevlett.121.171802>.
- 4157 [175] K. Abe et al. "Measurements of neutrino oscillation in appearance and
4158 disappearance channels by the T2K experiment with 6.6×10^{20} protons on
4159 target". In: *Phys. Rev. D* 91.7 (Apr. 2015).
- 4160 [176] F. James. "MINUIT Function Minimization and Error Analysis". In: *Reference*
4161 *Manual, Version 94.1, CERN Program Library Long Writeup D506 D.506* (1994).
4162 eprint:
4163 <https://root.cern.ch/sites/d35c7d8c.web.cern.ch/files/minuit.pdf>.
- 4164 [177] X. Li and M. Wilking. "FiTQun Event Selection Optimization". In: *T2K Technical*
4165 *Note* 319 (2017).
- 4166 [178] S. Tobayama. "An Analysis of the Oscillation of Atmospheric Neutrinos".
4167 PhD thesis. British Columbia U., 2016.
- 4168 [179] D. Barrow et al. "Super-Kamiokande Data Quality, MC, and Systematics in Run
4169 10". In: *T2K Technical Note* 399 (2020).
- 4170 [180] A. Maghrabi, A. Aldosari, and M. Almutairi. "Correlation analyses between solar
4171 activity parameters and cosmic ray muons between 2002 and 2012 at high cutoff
4172 rigidity". In: *Advances in Space Research* 68.7 (Oct. 2021), pp. 2941–2952.
- 4173 [181] J. Beringer et al. "Review of Particle Physics". In: *Phys. Rev. D* 86 (1 2012),
4174 p. 010001. URL: <https://link.aps.org/doi/10.1103/PhysRevD.86.010001>.

- 4175 [182] S. Nakayama K. Iyogi and Y. Obayashi. "T2K data acquisition and FC event
4176 selection at Super-Kamiokande". In: *T2K Technical Note* 027 (2011).
- 4177 [183] L. K. Pik. "Study of the neutrino mass hierarchy with the atmospheric neutrino
4178 data observed in Super-Kamiokande". PhD thesis. Tokyo University, 2012.
- 4179 [184] R. Wendell et al. "Atmospheric neutrino oscillation analysis with subleading
4180 effects in Super-Kamiokande I, II, and III". In: *Phys. Rev. D* 81 (9 2010), p. 092004.
- 4181 [185] J. Hosaka et al. "Three flavor neutrino oscillation analysis of atmospheric
4182 neutrinos in Super-Kamiokande". In: *Phys. Rev. D* 74 (3 2006), p. 032002.
- 4183 [186] D. Barrow et al. "Flux and interaction models for the initial T2K-SK atmospheric
4184 joint fit studies". In: *T2K Technical Note* 422 (2022).
- 4185 [187] L. Munteanu et al. "Constraining the Flux and Cross Section Models with Data
4186 from ND280 using FGD1 and FGD2 for the 2020 Oscillation Analysis". In: *T2K*
4187 *Technical Note* 395 (2020).
- 4188 [188] P. Bartet et al. " ν_μ CC event selections in the ND280 tracker using Run 2+3+4
4189 data". In: *T2K Technical Note* 212 (2015).
- 4190 [189] W. Parker. "Constraining Systematic Uncertainties at T2K using Near Detector
4191 Data". PhD thesis. Royal Holloway University of London, 2020.
- 4192 [190] V. Berardi et al. " $\bar{\nu}_\mu$ event selection in the ND280 tracker using Run 5c and Run 6
4193 anti-neutrino beam data". In: *T2K Technical Note* 246 (2015).
- 4194 [191] B. Kirby J. Kim and M. Wilking. "Michel Electron Tagging in FGD1". In: *T2K*
4195 *Technical Note* 104 (2012).
- 4196 [192] J. Misset. "TN-318: Fit to Super-K Atmospheric Neutrino Data for Optimization
4197 of the fiTQun Fiducial Volume Cuts and Estimation of Detector Uncertainties".
4198 In: *T2K Technical Note* 318 (2017).
- 4199 [193] J. Chakrani et al. "NIWG model and uncertainties for 2021 oscillation analysis".
4200 In: *T2K Technical Note* 414 (2022).
- 4201 [194] M. Wascko. "T2K Status, Results, And Plans". In: *Neutrino 2018* (2018). URL:
4202 <https://zenodo.org/record/1286752>.
- 4203 [195] T. Vladislavljevic et al. "Flux Prediction and Uncertainty with NA61/SHINE 2009
4204 Replica-Target Data (TN354 version 3.3)". In: *T2K Technical Note* 354 (2020).
- 4205 [196] G. Ambrosini et al. "K/ π production ratios from 450 GeV/c protons on
4206 beryllium". en. In: *Phys. Lett. B* 420.1-2 (Feb. 1998), pp. 225–232.
- 4207 [197] E. Atkin et al. "NIWG model and uncertainties for 2019-2020 oscillation analysis".
4208 In: *T2K Technical Note* 344 (2019).
- 4209 [198] D. Barrow et al. "SK atmospheric T2K beam joint fit technical note, MaCh3
4210 details". In: *T2K Technical Note* 426 (2022).
- 4211 [199] A. A. Aguilar-Arevalo et al. "Measurement of ν_μ and $\bar{\nu}_\mu$ induced neutral current
4212 single π^0 production cross sections on mineral oil at $E_\nu \sim \mathcal{O} (1 \text{ GeV})$ ". In: *Phys.*
4213 *Rev. D* 81 (1 2010), p. 013005.
- 4214 [200] P. Perio and J. Imber. "Super-K Systematic Uncertainties for RUN1-4 Joint ν_e and
4215 ν_μ Analyses". In: *T2K Technical Note* 186 (2014).

- 4216 [201] P. Perio and J. Imber. "Update of SK ν_e systematic error for 2012a oscillation
4217 analysis". In: *T2K Technical Note* 107 (2012).
- 4218 [202] D. Barrow and C. Vilela. *T2K-SK Detector Matrix Uncertainties - MaCh3 Integration*.
4219 <https://git.t2k.org/t2k-sk/t2ksk-detcovmat/-/tree/feature/MaCh3Integration>. Accessed: 22-06-2022.
- 4220 [203] R. Barlow and C. Beeston. "Fitting using finite Monte Carlo samples". en. In:
4221 *Comput. Phys. Commun.* 77.2 (Oct. 1993), pp. 219–228.
- 4222 [204] J. S. Conway. "Incorporating Nuisance Parameters in Likelihoods for Multisource
4223 Spectra". In: *arXiv* (2011). URL: <https://arxiv.org/abs/1103.0354>.
- 4224 [205] D. Barrow et al. "Oscillation probability calculation for the T2K+SK atmospheric
4225 joint fit". In: *T2K Technical Note* 425 (2022).
- 4226 [206] R. G. Calland, A. C. Kaboth, and D. Payne. "Accelerated event-by-event neutrino
4227 oscillation reweighting with matter effects on a GPU". In: *IOP Journal of
4228 Instrumentation* 9.04 (Apr. 2014), P04016–P04016.
- 4229 [207] R. Wendell. *Prob3++ Oscillation Probability Calculation*. URL:
4230 <http://www.phy.duke.edu/~raw22/public/Prob3++/>.
- 4231 [208] F. Kallenborn et al. "Massively parallel computation of atmospheric neutrino
4232 oscillations on CUDA-enabled accelerators". In: *Computer Physics Communications*
4233 234 (2019), pp. 235–244.
- 4234 [209] L. Warsame. *MaCh3 Analysis Progress*. Implementation of CUDAProb3 in MaCh3
4235 for DUNE. URL: https://indico.fnal.gov/event/50217/contributions/241232/attachments/155318/202209/MaCh3ProgressforDUNELBL_May17%20%282%29.pdf.
- 4236 [210] S. Bourret et al. "Neutrino oscillation tomography of the Earth with
4237 KM3NeT-ORCA". In: *Journal of Physics: Conference Series* 888 (2017), p. 012114.
- 4238 [211] C. Rott, A. Taketa, and D. Bose. "Spectrometry of the Earth using Neutrino
4239 Oscillations". In: *Scientific Reports* 5.1 (Oct. 2015). URL:
4240 <https://doi.org/10.1038/srep15225>.
- 4241 [212] K. Hagiwara, N. Okamura, and K. Senda. "The earth matter effects in neutrino
4242 oscillation experiments from Tokai to Kamioka and Korea". In: *Journal of High
4243 Energy Physics* 2011.9 (Sept. 2011).
- 4244 [213] D. Typinski. *Earth Gravity*.
4245 <http://www.typnet.net/Essays/EarthGravGraphics/EarthGrav.pdf>.
4246 Accessed: 24-06-2022.
- 4247 [214] D. Barrow. *T2K Beam + SK Atmospheric Joint Fit*. Plenary Slides for May 2022 T2K
4248 Collaboration Meeting. 2022. URL:
4249 https://t2k.org/meet/collab/CM_May_2022/Talks/Friday/T2KSKPlenary.
- 4250 [215] E. Atkin et al. "Measuring PMNS parameters in a joint ND280-SK analysis using
4251 MCMC". In: *T2K Technical Note* 393 (2020).
- 4252 [216] K. Abe et al. "Neutron Tagging following Atmospheric Neutrino Events in a
4253 Water Cherenkov Detector". In: *arXiv* (2022). URL:
4254 <https://arxiv.org/abs/2209.08609>.